Sizing up protoplanetary disks

Trapman, L.

Citation

Trapman, L. (2020, November 5). *Sizing up protoplanetary disks*. Retrieved from https://hdl.handle.net/1887/138010

Author: Trapman, L.
Title: Sizing up protoplanetary disks
Issue date: 2020-11-05

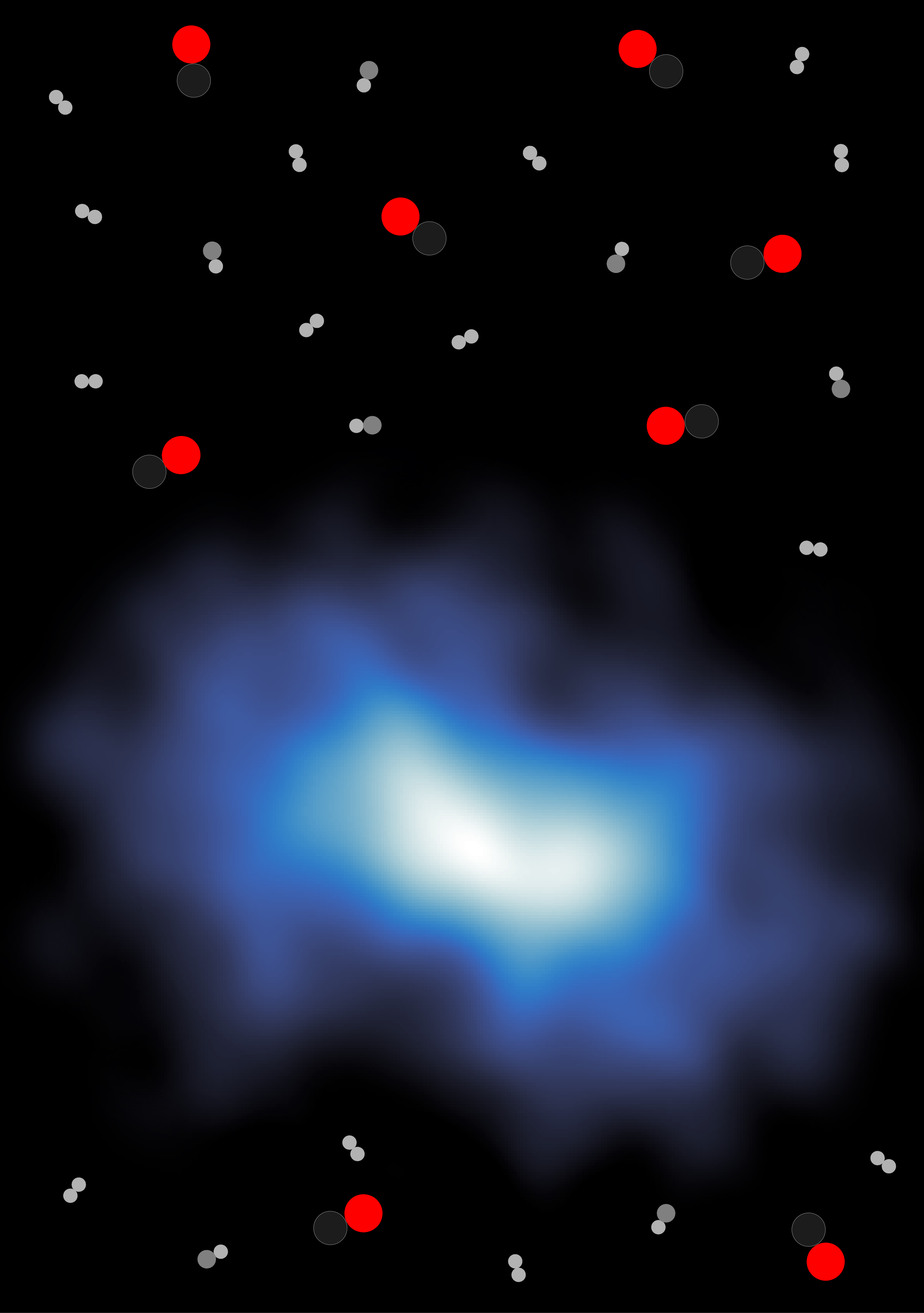

Sizing up protoplanetary disks

Proefschrift

ter verkrijging van
de graad van Doctor aan de Universiteit Leiden,
op gezag van Rector Magnificus prof. mr. C.J.J.M. Stolker,
volgens besluit van het College voor Promoties
te verdedigen op donderdag 5 november 2020
klokke 10.00 uur
door

Leon Trapman

geboren te Amsterdam, Nederland
in 1993

Promotiecommissie

Promotores:	Prof. dr. E. F. van Dishoeck	
	Prof. dr. M. R. Hogerheijde	
Overige leden:	Dr. J. M. Carpenter	Joint ALMA Observatory
	Prof. dr. I. E. E. Kamp	Rijksuniversiteit Groningen
	Prof. dr. G. Lodato	Università degli Studi di Milano
	Dr. P. Pinilla	Max-Planck-Institut für Astronomie
	Prof. dr. S. F. Portegies Zwart	
	Prof. dr. H. J. A. Röttgering	

ISBN: 978-94-641-9049-6

Front cover:
ALMA observations of dust and CO in the protoplanetary disk around CX TAU
Image credits: Stefano Facchini
Cover design by Yvonne Meeuwsen and the author

CONTENTS

1 INTRODUCTION

If there is one thing we can be certain about, it is that planets can be formed. The evidence for that is literally beneath our feet. However, knowing that it can happen and understanding how are two completely different things. The search for understanding planet formation started out focused on our Solar System, arguably with the advent of astronomy itself, but after the discovery of exoplanets orbiting other stars (Mayor & Queloz 1995) has since expanded considerably. The total number of exoplanets found currently stands at 4348[1], a number that will be outdated by the time you read this thesis. Exoplanets are found in a large variety of planetary systems, from multiple terrestrial planets packed inside the central $\sim 0.3 - 1$ AU (e.g., TRAPPIST-1 or Kepler-90, Gillon et al. 2017; Cabrera et al. 2014) to several gas giants spread over ~ 70 AU from the central star (e.g., HR 8799, Marois et al. 2010). The origins of these planetary systems lie in disks of gas and dust that surround young stars while they are being formed. The diverse outcomes of planet formation are intimately linked to these *protoplanetary disks* in which planets form and grow. How much material do disks contain for planet formation? And is this material concentrated close to the star or spread out over a large area? Answering these questions will help us solve the riddle of planet formation.

1.1 From clouds to cores to disks

To be able to discuss under which conditions planets are formed we first have to zoom out to before that process starts, to the giant molecular clouds in which stars form. As the name suggests, these clouds are made up of molecular gas that consists of H_2, CO, N_2 and He. In addition to their gaseous component these molecular clouds also contain small dust grains, with sizes up to 1μm, that make up about one percent of the total mass of the cloud (e.g. Draine 2003). The clouds were first identified and characterized using the background stars they obscured (see, e.g. Barnard 1919; Bok 1948; Cambrésy 1999). At longer wavelengths these clouds become translucent. Observations at far-infrared wavelengths used the blackbody radiation of dust grains of these clouds to study their filamentary internal structure in detail (see, e.g. André et al. 2010; Miville-Deschênes et al. 2010; Ward-Thompson et al. 2010).

The origin of filaments in clouds are still debated, with both turbulence (see, e.g. McKee & Ostriker 2007; Hill et al. 2011; Tafalla & Hacar 2015) and magnetic fields (see, e.g. Nakamura & Li 2008; Peretto et al. 2012; Palmeirim et al. 2013) being proposed

---

[1] `http://www.exoplanet.eu`, as of 24 September 2020

to play a role in their formation. Inside these filaments one can find so-called dense cores, overdensities $\sim 0.01 - 0.1$ parsec in size with a mass between 0.01 and 10 $M_\odot$ that are bound by their own gravity (see, e.g. Bontemps et al. 2010; Könyves et al. 2010; Maury et al. 2011). Internal forces resulting from turbulence and magnetic fields are able to partially balance the inward gravitational force, but eventually gravity will win out and the core will start to collapse, forming one up to a few stars at its center.

When a several 1000 AU size core collapses it contains too much angular momentum for all of the material to be accreted directly onto the forming protostar that is at most a few solar radii across: the rotational speed required would break up the star (see, e.g. Goodman et al. 1993). Some of the angular momentum can be dissipated by magnetic breaking (see e.g. Li et al. 2014) or can go in the orbital angular momentum of a binary in the case where multiple stars form (see, e.g. Reipurth et al. 2014), but observations show that in most cases there is some angular momentum left which goes into the formation of a disk around the young star. Initially the disk is still embedded in an envelope of material from the core that has not yet been accreted onto the disk or star. This envelope feeds material onto the disk, as has been inferred from kinematics (see, e.g. Yen et al. 2015; van 't Hoff et al. 2018) and from the presence of shock-tracing molecular lines detected at the outer edge of the disk (see, e.g. Sakai et al. 2014). Over its lifetime this disk will have its angular momentum transported outward or carried away by disk winds, which drives the accretion flow of material onto the star until internal photoevaporation overcomes the stellar mass accretion and dissipates the disk (see, e.g. Alexander et al. 2014; Ercolano & Pascucci 2017). Mass accretion is likely a violent process, with instabilities in the disk resulting in episodic bursts of accretion (e.g. Zhu et al. 2009). Observationally accretion bursts have been linked to FU Orionis objects which undergo a sudden brightening in stellar luminosity (e.g. Herbig 1977; Hartmann & Kenyon 1996). The accretion onto the star also produces a jet which carves an outflow cavity in the envelope around the disk, which over a time period of $\sim 4 \times 10^5$ yrs disperses the envelope (e.g. Dunham et al. 2014).

Once the envelope has been dispersed the disk can be observed directly. From this point we refer to it as a *protoplanetary disk*. Historically it was thought that planet formation starts in this stage, but over recent years there is increasing evidence that planet formation already started at an early stage (see, e.g Tychoniec et al. 2020) and that protoplanetary disks host the planets and planetesimals that make up the beginnings of a planetary system.

1.2 Inside the disk: physics, chemistry and evolution

1.2.1 Disk (viscous) evolution

At its core a protoplanetary disk is an accretion disk. How the disk evolves therefore depends on the physics that drive the flow of material through the disk and onto the star. As the gas orbiting the star has some amount of angular momentum which has to be conserved, there needs to be a process which can either redistribute or remove angular momentum from the disk in order to drive the stellar mass accretion. There have been two processes proposed that fit this criterion: viscous stresses and magnetohydrodynamical (MHD) disk winds. Which of these processes is the dominant driver of disk evolution remains a topic of active research, as it provides information on the conditions inside the disk. For example, viscous evolution requires the disk to be turbulent, which is not required for a disk-wind driven evolution. It is important to note that these two processes are not mutually exclusive: they can be operating at the same time (see, e.g. Suzuki & Inutsuka 2009; Bai & Stone 2013; Gressel et al. 2015; Béthune et al. 2017; Bai 2017).

Historically, it has commonly been assumed that protoplanetary disks evolve viscously. In the classical approach, where the disk is assumed to be a vertically thin axisymmetric sheet of viscous fluid, a shear causes the inner parts of the disk to lose angular moment to the outer parts of the disk (see, e.g. Lynden-Bell & Pringle 1974; Pringle 1981; Hartmann et al. 1998). This process causes the outermost part of the disk, which makes up only a small fraction of the mass, to expand outward and carry away the angular momentum. The bulk of the mass in the inner disk is instead forced inward where it is accreted onto the star.

Due to the uncertainties in what constitutes the viscosity it is common practice to describe the effects of viscous evolution using an "effective viscosity" also commonly known as the $\alpha-$disk prescription introduced by Shakura & Sunyaev (1973) for accretion disks around black holes. The advantage of this approach is that it describes the evolution of the disk using a single dimensionless parameter α. It should be kept in mind however that implicitly it is assumed here that α is constant with radius and in time, neither of which are guaranteed for the physical processes that constitute the effective viscosity.

What physical process actually makes up this viscosity is still a matter of debate. The molecular viscosity of the gas is too low; a back-of-the-envelope calculation results in a viscous timescale of $\sim 10^{13}$ yr, which is over six orders of magnitude longer than the expected lifespan of protoplanetary disks (see, e.g. Armitage 2019). An alternative proposed by Shakura & Sunyaev (1973) is that turbulence rather than molecular viscosity transports the angular momentum. A rigorous derivation by Balbus & Papaloizou (1999) showed that magnetohydrodynamical turbulence could in principle locally transport angular momentum (see also Balbus & Hawley 1991, 1998). Attempts at measuring turbulence in protoplanetary disks have either found no evidence (HD163296, MWC 480, V4046 Sgr; Flaherty et al. 2015, 2017, 2020) or measured low, subsonic turbulent velocities (TW Hya, DM Tau; Teague et al. 2016; Flaherty et al. 2020).

Viscous stresses are an internal way of redistributing the angular momentum, but it is also possible to do so using external processes. Most important here is the torque exerted by a MHD disk wind on the surface of the disks (see, e.g. Königl & Salmeron 2011; Frank et al. 2014). In the presence of a polodial vertical magnetic field, a disk wind can be launched from the disk surface. Angular momentum is transferred from the disk to the launched material as it is accelerated by the wind, causing the material remaining in the disk to move towards the central star (see, e.g, Blandford & Payne 1982 or Turner et al. 2014 for a review). Theoretical calculations show that these disk winds can remove some or all of the angular momentum required to drive the stellar accretion (see, e.g. Ferreira et al. 2006; Béthune et al. 2017; Zhu & Stone 2018). Observational evidence of this angular momentum removal has proven difficult, as direct observations of disk winds focus on the inner part of the disk (see, e.g. Pontoppidan et al. 2011; Bjerkeli et al. 2016; Tabone et al. 2017, 2020; de Valon et al. 2020).

With direct observations of both turbulence and disk winds proven difficult, another way of studying the physical processes that drive disk evolution is by examining how

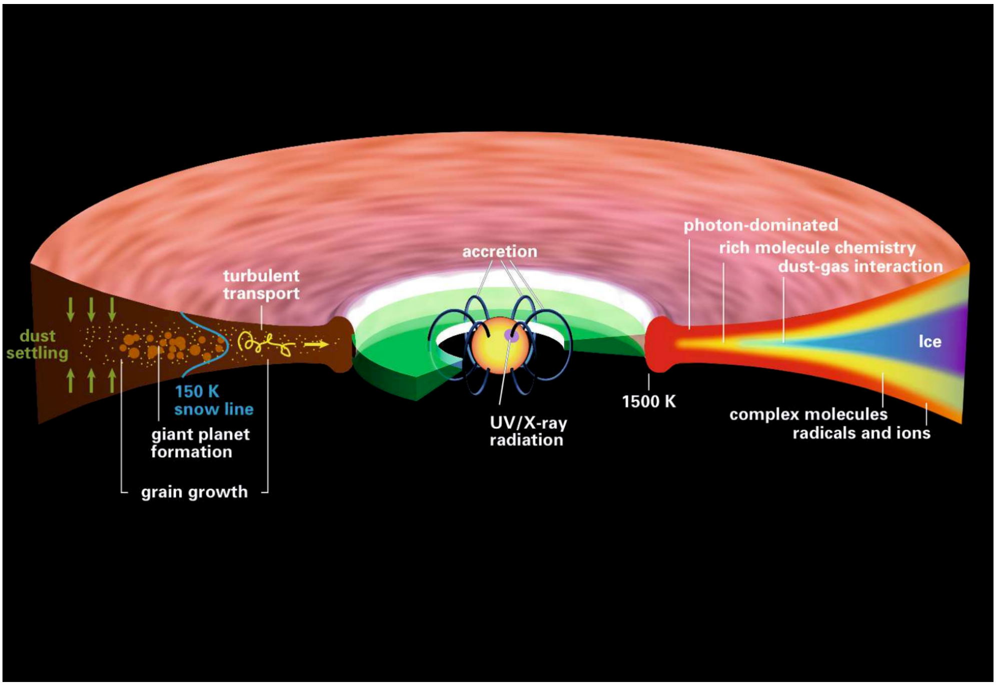

Figure 1.1: Schematic overview of a protoplanetary disk, showing on the left the processes relevant of the evolution of the dust (see also Section 1.2.3). On the right it shows how the chemistry changes from the surface to the midplane of the disk (see also Section 1.2.4). credits: Henning & Semenov (2013)

the disk structure, in particular its radius, reacts to the removal or redistribution of angular momentum. A viscously evolving disk should grow over time as the outer part of the disk expands outward, whereas a for a disk-wind driven evolution this is not the case (see, e.g. Lynden-Bell & Pringle 1974; Hartmann et al. 1998). This will be discussed in more detail in Chapter 4.

1.2.2 Disk structure

It is often assumed that the surface density of a protoplanetary disk follows a powerlaw that at larger radii tapers off exponentially (see, e.g. Hughes et al. 2008; Andrews et al. 2011). This surface density profile is a self-similar solution of a viscously evolving disk, assuming that the viscosity ν varies radially as a powerlaw $\nu \propto R^{\gamma}$ (see, e.g. Hartmann et al. 1998):

$$\Sigma_{\mathrm{gas}}(R) = \frac{(2-\gamma)\,M_{\mathrm{disk}}}{2\pi R_{\mathrm{c}}^{2}} \left(\frac{R}{R_{\mathrm{c}}}\right)^{-\gamma} \exp\left[-\left(\frac{R}{R_{\mathrm{c}}}\right)^{2-\gamma}\right]. \tag{1.1}$$

Here M_{disk} is the total disk mass and the characteristic radius R_{c} defines where the surface density profile transitions from a powerlaw to its exponential taper.

In addition to its link to viscous evolution this surface density profile also provides a natural explanation for the fact that observations show that gas line emission, in

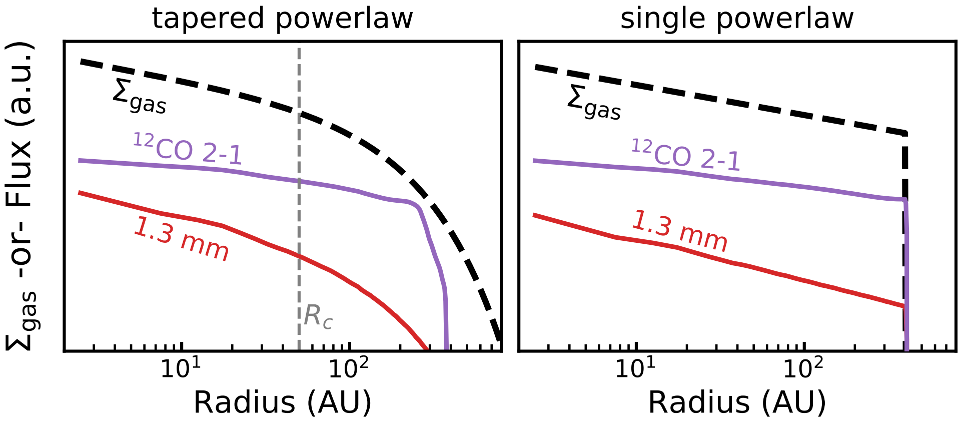

Figure 1.2: Two examples of surface density profiles (black dashed lines) and the corresponding ^{12}CO $J = 2 - 1$ line and 1.3 millimeter continuum radial intensity profiles, shown by the purple and red lines, respectively. The optically thin dust emission follows the surface density, while the optically thick CO emission decreases with the much shallower slope of the temperature profile. For the tapered powerlaw shown on the left the dust emission drops off rapidly at large radii while the CO is approximately at the same brightness.

particular of CO rotational lines, extends further out than continuum emission of the dust, a phenomenon that cannot be explained with only a powerlaw for both the gas and the dust (see, e.g. Panić et al. 2008). The CO emission is optically thick and can be easily detected to far out in the exponential taper of the surface density, down to column densities of $\sim 10^{15}$ cm^{-2}. The continuum emission is predominantly optically thin and therefore falls off rapidly once the surface density starts to decrease exponentially (see Figure 1.2 and e.g. Hughes et al. 2008).

Despite its common usage, it is still not clear how well this profile represents the true radial distribution of the gas, as determining the gas surface density from observations is challenging (see, e.g. Williams & McPartland 2016; Miotello et al. 2018). As an example, there is evidence that the gas profile in the outer disk falls of faster than a exponential taper (see Dullemond et al. 2020). On top of the uncertainties in its general shape it has also become clear that the gas density structure is not smooth. Clear examples are the so-called “transition disks” that show a clear inner cavity in both gas and dust (see, e.g. van der Marel et al. 2016a; Pinilla et al. 2018). High resolution observations at millimeter wavelengths have also shown a wide variation of substructures in the form of asymmetries, rings and dips (see, e.g. van der Marel et al. 2013; ALMA Partnership et al. 2015; Andrews et al. 2016; van Terwisga et al. 2018; Andrews et al. 2018a). Figure 1.4 shows a collage of protoplanetary disks observed at high resolution as part of the ALMA large program Disk Substructures at High Angular Resolution Project (DSHARP; Andrews et al. 2018a and accompanying publications). Most of these features are traced using continuum emission of the dust and therefore do not directly imply variations in the gas density. However, for some of these features a counterpart in the gas has also been revealed using deviations from Keplerian velocity (see, e.g. Teague et al. 2018, 2019; Rosotti et al. 2020).

The vertical structure of the gas is set by the condition that it is in hydrostatic equilibrium, where gas pressure balances out the downward gravity exerted by the central star. Under the assumption that the disk is vertically isothermal the gas density follows a Gaussian distribution with a scale height $h \equiv c_s(T)/\Omega_K$, where $c_s(T)$ is the sound speed and Ω_K is the Keplerian orbital frequency (see, e.g. Chiang & Goldreich 1997; D'Alessio et al. 1998). Being vertically isothermal is a bit of an oversimplification. In truth the vertical temperature gradient requires the gas density to deviate slightly from a Gaussian to remain in hydrostatic equilibrium (see e.g. Armitage 2019). To explain the flat infrared spectra of T-Tauri stars, Kenyon & Hartmann (1987) proposed that disks are flared, where the height of the disk increases super-linearly with radius (see also Dullemond & Dominik 2005). Scattered light observations that trace the small grains at the disk surface show that most disks are indeed flared (see, e.g. Pantin et al. 2005; van Boekel et al. 2017; Avenhaus et al. 2018). These observations also reveal rings and gaps, suggesting that, analogous to the surface density, the scale height has radial variations (see, e.g. de Boer et al. 2016).

1.2.3 Dust evolution

For planets to form in protoplanetary disks, dust grains have to grow approximately thirteen orders from the micron sized grains found in the interstellar medium (see, e.g. Beckwith & Sargent 1991). Luckily, in the more dense environment found in protoplanetary disks these grains can grow efficiently through sticking, as shown in both theoretical calculations (see, e.g. Wada et al. 2008; Paszun & Dominik 2009; Krijt & Kama 2014; Krijt et al. 2015; Birnstiel et al. 2010, 2012) and experimental research (see, e.g. Blum & Wurm 2008; Güttler et al. 2010; Kothe et al. 2010; Weidling et al. 2012; Blum et al. 2014). The evidence for this growth can be seen in the detection of millimeter-sized and even centimeter-sized particles in protoplanetary disks (see, e.g. Rodmann et al. 2006; Ricci et al. 2010). Observations also indicate that grain growth occurs rapidly, with grains of millimeter sizes already present after $\sim 10^5$ yr (e.g. Harsono et al. 2018).

Grain growth is limited by two processes: fragmentation and radial drift. As the grains grow the relative speed at which they collide gets larger (see, e.g. Brauer et al. 2008) increasing the likelihood that these interactions lead to bouncing or fragmentation instead of growth. The exact threshold between growth and fragmentation, called the *fragmentation velocity*, depends on the composition of the grain and its surface. Experiments with silicate grains by Blum & Wurm (2008) show a fragmentation velocity of 1 m s^{-1}. The presence of an icy mantle is expected to increase the fragmentation velocity to ~ 10 m s^{-1} (Wada et al. 2008; Gundlach et al. 2011, but see also Gärtner et al. 2017), allowing grains to efficiently grow to centimeter sizes (Brauer et al. 2008; Windmark et al. 2012). Due to the higher velocities and densities, fragmentation sets the limit for grain growth in the inner disk. Further out the maximum attainable grain size is set by radial drift (see also Birnstiel et al. 2015).

As dust grains grow they start to experience more gas drag, causing them to decouple from the gas. The gas in orbit around the star is partially supported by the inward pressure gradient in the disk, causing it to move at sub-Keplerian velocities. The grains are not similarly supported and therefore move at Keplerian velocities, causing them to experience a "headwind" due to the slower moving gas. This interaction with the gas causes the grains to lose angular momentum, causing them to drift inward (see, e.g. Weidenschilling 1977; Takeuchi & Lin 2002). How quickly grains drift inward depends strongly on the size and mass of the grains and on the density of the surrounding gas. The effect of gas drag on grains can be quantified by their Stokes number, sometimes also referred to as the dimensionless stopping time. The Stokes number compares the time required for the gas drag to stop the particle to the orbital time of said particle. Very small grains, or those that are very porous, have a Stokes number much smaller than one. They are dragged along by the gas and will not drift inward. At the opposite end of the scale, massive boulders that are tens of meters across have a Stokes number much larger than one. For them the angular momentum transfer to the gas is negligible: they simply plough through the gas. In between lie the grains of ~ 0.1 mm - 1 m that have a Stokes number of approximately one, depending on their porosity and the properties of the surrounding gas. These grains experience the most gas drag and rapidly drift inward.

The physics behind radial drift can also provide an explanation for the rings seen in continuum emission at millimeter wavelengths. The gas drag causes dust grains move to where the gas pressure has a maximum, which in a smooth disk is at the position of the central star. However, a local overdensity in the gas will result in a local pressure maximum that can trap drifting dust grains (see, e.g. Whipple 1972; Pinilla et al. 2012). These local gas overdensities are commonly attributed to the presence of a planet in the disk, but other mechanisms such as dead zones have also been proposed (see e.g. Lyra et al. 2009).

Interactions with the gas also change the vertical distribution of the larger dust grains. As discussed in Section 1.2.2, the gas is vertically supported by a vertical pressure gradient which counteracts the vertical component of the stellar gravity. The decoupled larger dust grains are not similarly supported and instead are accelerated until there is enough gas drag to counteract the gravitational force. This *vertical settling* leads to a segregation of dust grains based on their size, with the larger grains being confined to the midplane of the disk (see, e.g. Dubrulle et al. 1995; Dullemond & Dominik 2004, 2005; Mulders & Dominik 2012; Riols & Lesur 2018). Vertical turbulence of the gas in principle counteracts dust settling by lifting grains back up, but it can only do so efficiently for the small grains that are well coupled to the gas (see, e.g. Fromang & Papaloizou 2006).

1.2.4 Chemistry in protoplanetary disks

Conditions in protoplanetary disks are diverse, spreading over a wide range of densities ($10^4 - 10^{12}$ cm^{-3}), temperatures (10-1000 K) and radiation fields, from strongly irradiated with X-ray and ultraviolet at the surface to completely dark in the disk midplane. This diverse environment leads to a diverse chemistry: photodissociation and photoionization, ion-neutral reactions, neutral-neutral reactions and gas-grain surface reactions. The chemistry in turn also affects its environment, as it sets the gas temperature through the changing heating-cooling balance, changes the level of ionization and it ultimately sets the composition of the material that goes into forming planets and their atmosphere.

The remaining chapters in this thesis make extensive use of rotational line emission of CO, emitted in the sub-millimeter, as tracer of the physical structure of the outer disk. As such, the chemistry that will be discussed here focuses on CO chemistry. In the outer disk the temperatures are low (10-100 K) and the chemistry is kick-started by high energy radiation and cosmic rays that are able to ionize various species (see, e.g. Aikawa et al. 1997; van Dishoeck et al. 2006; Walsh et al. 2012). Reactions between these ions and neutral species are mostly barrierless, and thus efficient even at low temperatures, leading to a rapid ion-molecule chemistry (see e.g. Herbst & Klemperer 1973; Woodall et al. 2007). Freeze-out of molecules is another process that becomes important at the low temperatures found in the outer disk. The temperature at which a molecule freezes out onto the grains changes from molecule to molecule and depends on the gas temperature, resulting in temperature dependent variations in the composition of the gas (see, e.g. Öberg et al. 2011; Helling et al. 2014; Eistrup et al. 2016, 2018). Water freezes out at temperatures below ~ 150 K, meaning that beyond the inner few AU all available water is frozen out. The radius where a molecule transitions from predominantly gas phase to frozen out is defined as its iceline. For CO freeze out occurs at a lower temperature ($\sim 15 - 30$ K) and the CO iceline lies therefore further out, at several tens of AU (see e.g. Qi et al. 2013, 2015, 2019; Facchini et al. 2017; van 't Hoff et al. 2017; Zhang et al. 2017). Icelines of dominant carbon and oxygen carriers like H_2O, CO_2 and CO are thought to play an important role in the formation of planets. As discussed in Section 1.2.3, the expected increased stickiness of ice covered grains increases the efficiency of grain growth. Furthermore, Stevenson & Lunine (1988) suggested that water vapor released by ice grains that crossed the water iceline should diffuse back over the snowline and freeze out again, thus locally increasing the density of solids (see also Ciesla & Cuzzi 2006).

Vertically the disk can be divided into three chemically different zones (see Figure 1.3 or e.g. Aikawa et al. 2002; Bergin et al. 2007). High up in the disk, in what we will refer to as the *disk surface layer*, ultraviolet photons from the star can easily ionize and photodissociate molecules. As a result this layer is predominantly populated by neutral or ionized atomic species. The exact composition of this layer depends strongly on the color and strength of the ultraviolet radiation field, as photodissociation is different for different molecules and is sensitive to the shape of the radiation field (see, e.g. Heays et al. 2017). The first molecules that can survive in this layer are H_2, CO and N_2. Photodissociation of these molecules occurs through narrow lines in the far-ultraviolet ($912 - 1200\,\text{Å}$), thus limiting the number of ultraviolet photons that are capable of photodissociating them. This process is referred to as self-shielding and allows these molecules to survive in the gas as soon as they have build up a sufficient column ($\sim 10^{15}$ cm^{-2} in the case of CO, see van Dishoeck & Black 1988). Note here that the dependence of self-shielding on discrete wavelengths results in isotope-selective photodissociation, This leads to less abundant isotopologues like $C^{18}O$ and $C^{17}O$ being destroyed by ultraviolet photons much deeper into the disk (see, e.g., Visser et al. 2009; Miotello et al. 2014).

Below the disk surface layer lies the *warm molecular layer* ($T_{\rm gas} \approx 30 - 70$ K). Here extinction due to e.g. small grains has reduced the ultraviolet radiation field enough that most molecules are no longer being photodissociated, while temperatures are still high enough that most molecules have not frozen out yet. This layer is of a particular interest for observers as most of the detected molecular line emission originates from this layer. In the outer disk H_2O and CO_2 are frozen out in this layer and CO is thought to be the dominant gas-phase carbon carrier. However, recent observations reveal that disks have overall low CO isotopolog line fluxes (see, e.g., Favre et al. 2013; Ansdell et al. 2016; Cleeves et al. 2016; Miotello et al. 2017; Long et al. 2017), and therefore draw into question whether CO is the main carbon carrier in this layer (see also Yu et al. 2017; Molyarova et al. 2017 for discussion).

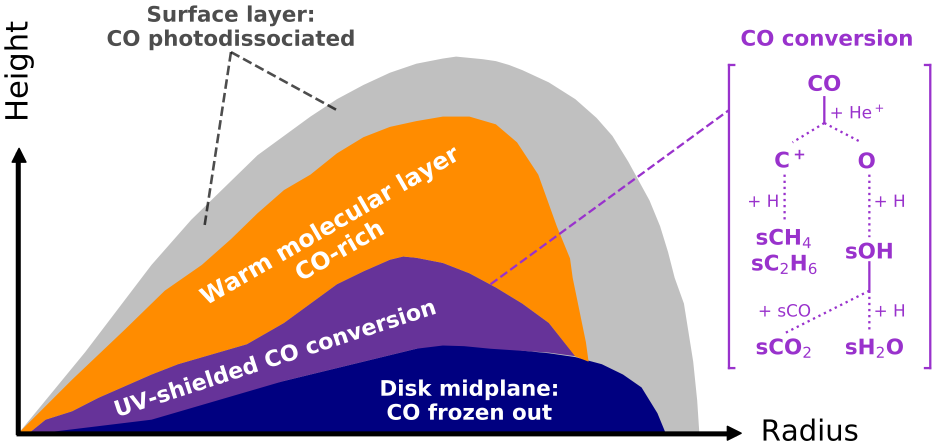

Figure 1.3: 2D sketch of the dominant chemistry affecting CO in different regions of a protoplanetary disk. On the right are the dominant paths through which CO can be converted in the UV-shielded region of the disk (adapted from Figure 2 in Bosman et al. 2018). Molecules frozen out on grains are denoted with an s in front. Note that non-thermal desorption provides a small amount of gas-phase CO in the midplane which can also be converted (see, e.g., Chaparro Molano & Kamp 2012; Helling et al. 2014).

As we move closer to the *disk midplane* the temperature decreases, resulting in the freeze-out of most molecules onto the grains. The previously discussed iceline of a molecule is therefore part of a larger “ice-surface” that marks the transition from gas-phase to solid state in both the radial and vertical direction. This layer is completely shielded from stellar and interstellar ultraviolet photons and X-rays. Instead, gas-phase chemistry is driven by cosmic-ray particles. These high energy particles can collide with molecular hydrogen and ionize it, producing a high energy electron. The H_2^+ can react with another H_2 to produce H_3^+ which starts the ion-molecule chemistry. The high energy electron will collide and excite multiple H_2, which upon de-exciting will produce secondary ultraviolet photons. Similar to higher up in the disk this weak ultraviolet field can dissociate molecules and produce radicals that can partake in chemical reactions. In this environment gas phase CO can be broken apart by He$^+$ into C$^+$ and O. The carbon will go into hydrocarbons like CH_4 and C_2H_6 which freeze out onto the grains. The oxygen that is produced also freezes out and hydrogenates to form H_2O or it reacts with the frozen out CO to form CO_2 (see, e.g. Figure 1.3 here or Figure 2 in Bosman et al. 2018). On the grains simple molecules like CO can also be hydrogenated to form more complex molecules like CH_3OH (see, e.g. Aikawa et al. 1997; Watanabe & Kouchi 2002; Cuppen et al. 2009; Bosman et al. 2018; Schwarz et al. 2018).

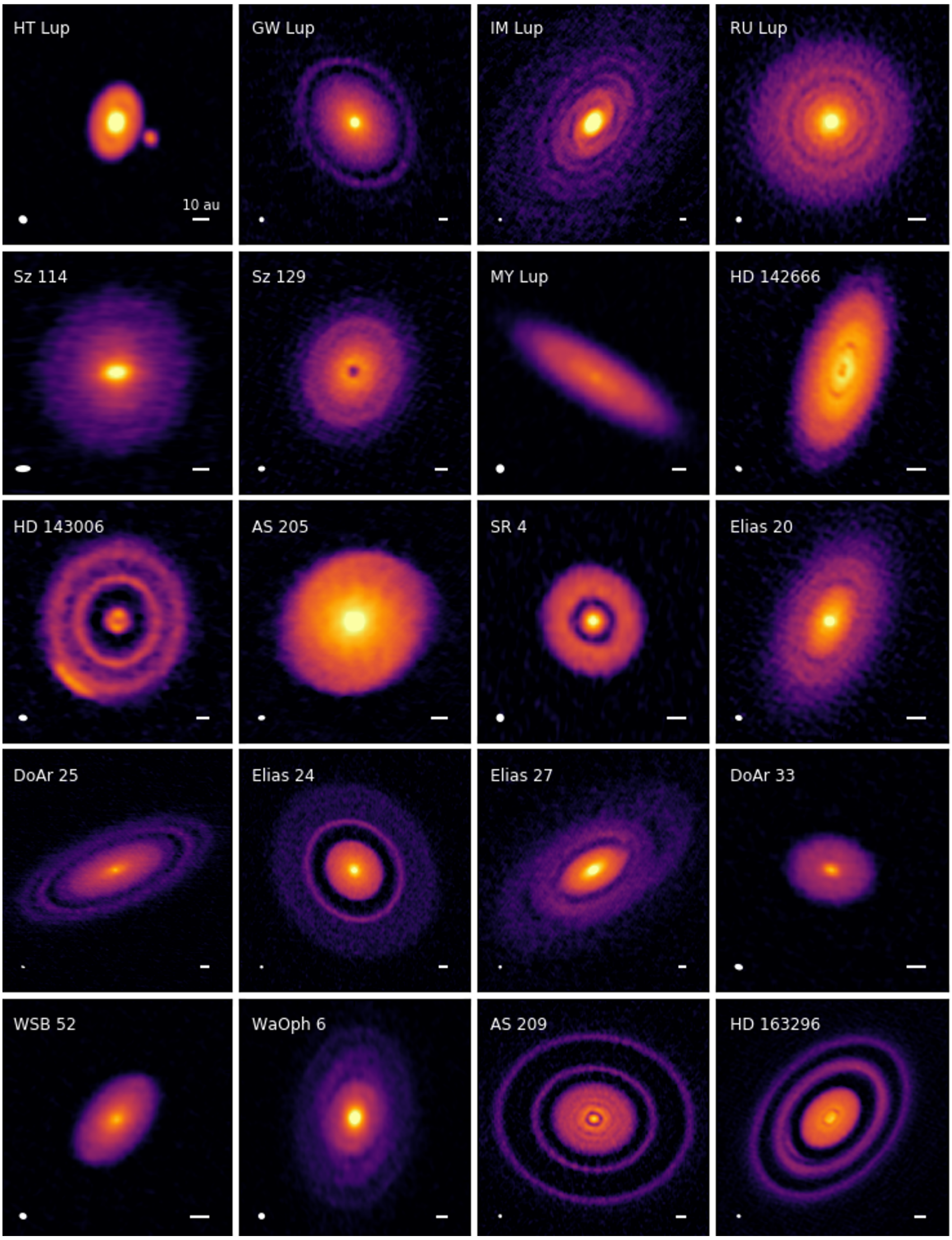

Figure 1.4: Image gallery of high resolution ALMA continuum observations of 25 bright disks (DSHARP large program; Andrews et al. 2018a). These images reveal a wide range of substructures in the dust. Colors show the intensity of the continuum, using an asinh stretch to reduce the dynamic range and accentuate fainter details. Beam sizes and 10 AU scalebars are shown in the lower left and right corners of each panel, respectively. Note that seven of these sources (HT Lup, GW Lup, IM Lup, RU Lup, Sz 114, Sz 129 and MY Lup) lie in the Lupus star-forming region, all of them among the top $\sim 17\%$ brightest disks found in Lupus.

1.3 Millimeter observations of protoplanetary disks: the ALMA era

If weighted by mass, most of the material in the disk resides in cold ($\sim 20-50$ K) molecular gas. This gas emits predominately through rotational line emission at millimeter wavelengths, as the rotational levels of most molecules can be easily excited at these temperatures. The Atacama Large Millimeter/sub-millimeter Array (ALMA) is the preeminent facility for observing protoplanetary disks at millimeter wavelengths, having both the sensitivity needed to detect the faint molecular emission and the sub-arcsecond resolution required to resolve the disk down to a few AU for typical distances to nearby star-forming regions. ALMA has allowed us to study individual objects at high resolution, revealing substructures in the dust in seemingly almost every disks examined in this way (see Figure 1.4 and e.g. ALMA Partnership et al. 2015; Andrews et al. 2016; Andrews et al. 2018a; Long et al. 2019).

Along a different axis, ALMA has allowed for large surveys covering all protoplanetary disks in an entire star forming region to be observed with short ~ 1 minute snap shots at sub-arcsecond resolution (e.g., Taurus, Ward-Duong et al. 2018; Long et al. 2018, 2019; Chamaeleon I, Pascucci et al. 2016; Long et al. 2017; σ-Ori Ansdell et al. 2017; Upper Sco, Barenfeld et al. 2016, 2017; Corona Australis, Cazzoletti et al. 2019; and Ophiuchus, Cox et al. 2017; Cieza et al. 2019; Williams et al. 2019). This has allowed us to study the disk population as a whole, which has shown that the "typical" protoplanetary disk is very different in size and mass from the large and bright individual disks studied previously.

Of particular interest for this thesis is the ALMA survey of the Lupus star-forming region (Ansdell et al. 2016; Ansdell et al. 2018). This program observed all 95 disk candidates in the region in ALMA Band 7 (~ 890 μm at $\sim 0\farcs3$ resolution, covering ^{13}CO $J=3-2$, C^{18}O $J=3-2$ and CN $N=3-2$) and Band 6 (~ 1.3 mm at $\sim 0\farcs25$ resolution, covering ^{12}CO $J=2-1$ ^{13}CO $J=2-1$ and C^{18}O $J=2-1$). Of the 95 disk candidates, $\sim 75\%$ are detected in the continuum. For the gas detection rates are much lower, $\sim 50\%$ for ^{12}CO, $\sim 21-40\%$ for ^{13}CO and $8-12\%$ for C^{18}O. A complementary survey targeted most of these sources with the X-Shooter instrument (Vernet et al. 2011) on the Very Large Telescope (Alcalá et al. 2014, 2017). Combined, these surveys provide a wealth of data on the properties of disks and how these depend on their host star (see, e.g. Manara et al. 2017). Figure 1.5 and 1.6 show overviews of all disks found in the Lupus star-forming region (see also Ansdell et al. 2016; Ansdell et al. 2018). In the next part we focus on two properties: How large is a typical protoplanetary disk? And how much material, i.e. gas and dust, does it contain?

1.3.1 Measuring disk radii

The size of a protoplanetary disks is an important tool for studying the evolution of the gas and the dust in the disk. Do disks grow over time, indicating that they evolve viscously? How much have the larger grains drifted inward with respect to the gas and the small grains? To answer these questions, we need to measure a disk size from the observations and understand how it traces the underlying structure of the disk.

The size of the disk can be measured from the millimeter continuum emission, which shows how extended the millimeter-sized grains are distributed. The continuum emission is easy to detect, making it the most accessible measured disk size. The

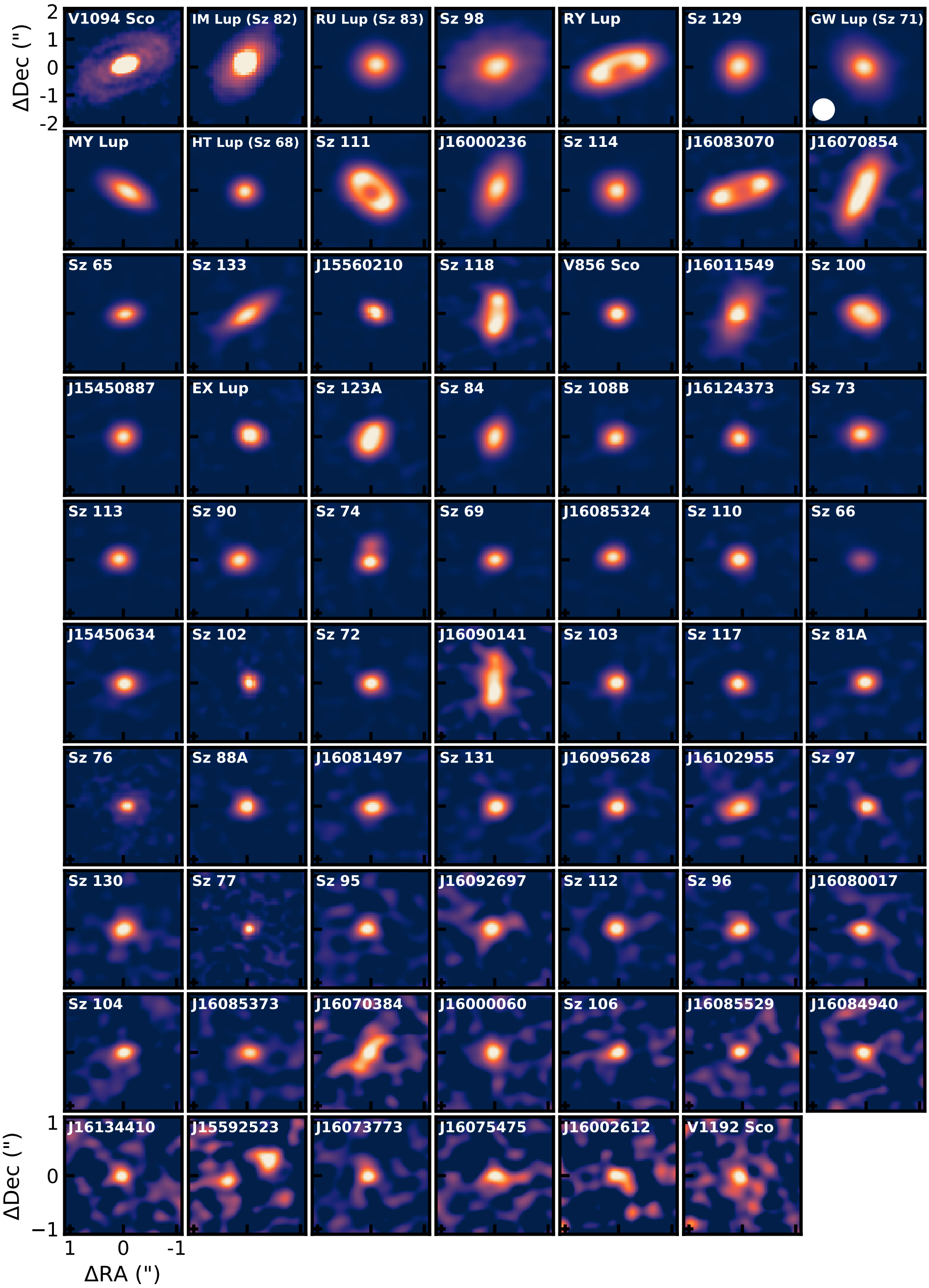

Figure 1.5: Group photo of the disk population in the Lupus star-forming region, located at a distance of $\sim$ 160 pc, showing the 890μm (Band 7) continuum images observed with ALMA (Ansdell et al. 2016). The images are $2''.2 \times 2''.2$ and are ordered by decreasing continuum flux. The color scale in each image runs from the peak flux to zero. V1094 Sco and IM Lup are shown in $4''.2 \times 4''.2$ images and their continuum fluxes in the center have been saturated by 70% to better reveal their faint outer disk.

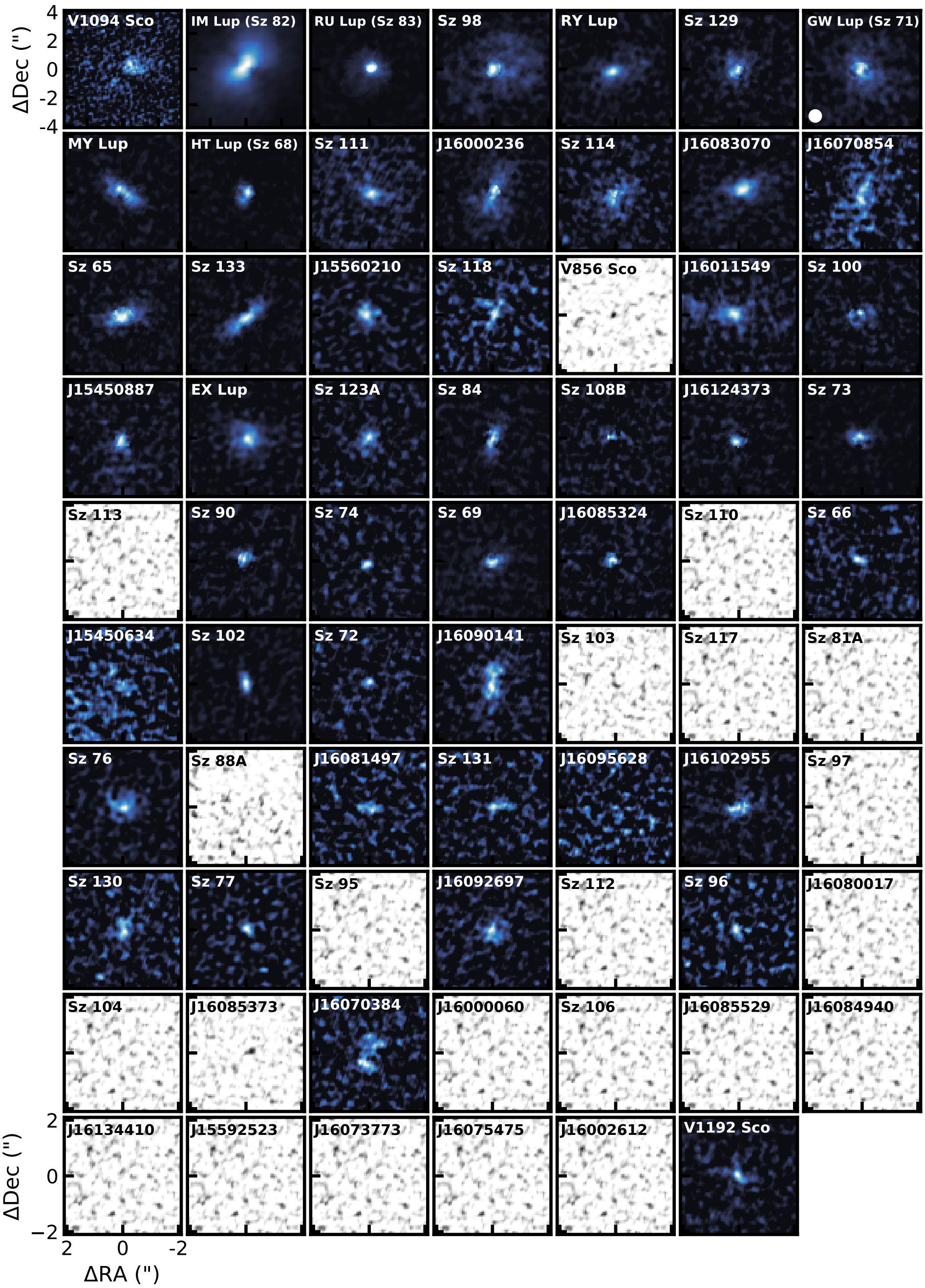

Figure 1.6: As Figure 1.5, but now showing the ^{12}CO $J = 2 - 1$ integrated intensity maps observed with ALMA Band 6. The disks are again ordered by decreasing continuum flux, but the sizes of images have been increased to $4''\!.2 \times 4''\!.2$ ($8''\!.2 \times 8''\!.2$ for V1094 Sco and IM Lup). The color scale in each image runs from the peak intensity to zero. Sources for which ^{12}CO $J = 2 - 1$ was not detected are shown in black and white.

measured dust disk size depends on the wavelength of the continuum emission, with disks becoming more compact at longer wavelengths, likely due to the larger grains having drifted inward more quickly than smaller grains (see, e.g. Tazzari et al. 2016; Tripathi et al. 2018). With the advent of ALMA disk surveys, there is now a large sample of disks for which the dust disk size has been measured (see, e.g. Andrews et al. 2013; Ansdell et al. 2016; Tazzari et al. 2017; Tripathi et al. 2017; Andrews et al. 2018b; Long et al. 2018; Tobin et al. 2020). Overall, it has been found that many protoplanetary disks are small in the dust: only $\sim 2\%$ show continuum emission beyond 200 AU (van Terwisga et al. 2018) and approximately 45% of disks remain unresolved at 0.2 arcsecond resolution, implying radii smaller than 25 AU. This could mean that the bulk of protoplanetary disks is small. However one should keep in mind that these dust disk sizes are measured from continuum emission emitted by millimeter-sized grains which likely have drifted inward (as discussed in Section 1.2.3). The availability of large samples of measured dust disk sizes have allowed us to look for correlations with other disk and stellar parameters (see, e.g. Tazzari et al. 2017; Tripathi et al. 2017; Andrews et al. 2018b; Rosotti et al. 2019a). These studies show that the dust disk size is directly correlated with the dust mass or total millimeter luminosity. This correlation can be reproduced by assuming that the dust is concentrated in optically thick rings that fill $\sim 30\%$ of the disk surface (Tripathi et al. 2017; Andrews et al. 2018b). If this is the case, the millimeter flux would be just a measure of the disk surface area. High resolution observations also show evidence towards a link between presence of rings and the measured dust disk size (see, e.g. Long et al. 2019).

Our understanding of the extent of the gas in protoplanetary disks is more limited compared to the dust. The bulk of the gas is made up by molecular hydrogen, which does not emit in the conditions found throughout most of the disk (this will be discussed in more detail in Section 1.3.2). The gas disk size is therefore measured from the extent of other molecules like CO and CN, whose bright line emission is often detected towards protoplanetary disks (for a non-exhaustive list, see, e.g. Piétu et al. 2005; Schaefer et al. 2009; Piétu et al. 2014; Guilloteau et al. 2014; Simon et al. 2017; Barenfeld et al. 2017; Ansdell et al. 2018). The challenge then lies with understanding what these indirect tracers tell about the underlying bulk distribution of the gas. Line emission from ^{12}CO is optically thick, making it bright and easier to detect out to large radii, but also making it more challenging to link the extent of the emission to how spread out the gas is. Using more optically thin isotopologs like ^{13}CO or C^{18}O would circumvent this, but detecting these lines further out in the disk requires deeper observations that are currently only available for a small number of sources. The CN molecule is a photodissociation tracer that is abundant high up in the disk. When observed at high spatial resolution with ALMA the emission is found to be ring shaped (see, e.g. Teague et al. 2016; van Terwisga et al. 2019). Models by Cazzoletti et al. (2018) show that the location of the ring depends on the radial distribution of the gas and the strength of the ultraviolet radiation field. Based on the same models van Terwisga et al. (2019) showed that the low CN fluxes observed towards many disks can only be explained with small gas disks.

Our understanding of gas disk sizes is still predominantly based on individual objects, most often bright disks around solar mass stars, as obtaining a large sample of measured gas disk sizes comparable to the dust disk sizes has proven difficult to be approved by time allocation committees. Recent ALMA disk surveys in most cases also covered ^{13}CO and C^{18}O, and in some cases ^{12}CO, but the 1 minute snapshots proved too shallow to detect CO at high enough sensitivity to accurately measure the gas disk size.

Ansdell et al. (2018) targeted 95 disks in Lupus with ALMA, detecting ^{12}CO $J = 2 - 1$ in 48 sources ($\sim$ 51%) and was able to measure gas disk sizes for 22 ($\sim$ 23%) sources due to a low signal-to-noise (for more details, see Chapters 2 and 3). They find that gas disk sizes of these 22 disks are universally larger than their dust disk size by a factor of ~ 2 (see Figure 1.7). This could indicate that the millimeter grains have drifted inward, although in Chapters 2 and 3 it will become clear that due its larger optical thickness, the CO line emission will always extend further out than the optically thin dust emission (see also Figure 1.2). They find a tentative correlation between the gas disk size and the total continuum flux but no correlation with stellar mass. Barenfeld et al. (2017) was able to measure gas disk sizes for seven of the 21 disks in Upper Sco where they were able to detect ^{12}CO $J = 2 - 1$. For four of their sources the CO emission is more extended than the dust, although these observations suffer from a low signal-to-noise.

1.3.2 Measuring disk masses

The total mass of protoplanetary disks is a quantity of great interest, as it represents the reservoir of material available to form and grow planets. Measuring the disk mass has proven challenging (see, e.g. Bergin et al. 2019). Most of the disk mass resides in the gas, made up predominantly by molecular hydrogen (H_2), a light, symmetric molecule. The lack of a permanent electric dipole moment limits its rotational transitions to quadrupole transitions ($\Delta J = 2$). To produce significant H_2 emission the $J = 2$ level at $E/k_{\mathrm{B}} = 549.2$ K has to be excited, which requires gas temperatures of at least 100 K (see, e.g. Thi et al. 2001; Carmona et al. 2011). As most of the gas in protoplanetary disks has a much lower temperature, H_2 emission does not trace the bulk of the mass (see, e.g. Pascucci et al. 2013). Even when excited the transitions of H_2 are weak and lie in the mid- and near-infrared where the continuum emission from the dust is also bright, making the detection of H_2 a challenge due to its low line/continuum ratio. Furthermore, the continuum becomes optically thick at these wavelengths very high up in the disk, effectively hiding the H_2 below. Measuring the disk mass thus requires an indirect tracer.

The most common indirect gas mass tracer is carbon monoxide (CO) and its optically thin isotopologues. After molecular hydrogen CO is the second most abundant molecule in the gas. The main isotopolog, ^{12}CO, is optically thick throughout most of the disk, requiring us to go to less abundant isotopologs like ^{13}CO, C^{18}O, C^{17}O and sometimes even ^{13}C^{17}O and ^{13}C^{18}O to measure the total amount of CO in the disk. Relating the total amount of CO to the gas mass requires knowledge of the CO abundance with respect to molecular hydrogen. For this reason, the chemistry of CO in protoplanetary disks has been well studied (see, e.g., van Zadelhoff et al. 2001; Yu et al. 2017; Bosman et al. 2018; Schwarz et al. 2018). Using models that include photodissociation and freeze-out, the dominant processes that affect the CO abundance, the disk gas mass can be derived from observations of ^{13}CO and C^{18}O (see, e.g. Miotello et al. 2014; Miotello et al. 2016; Williams & Best 2014,). Disk surveys carried out with ALMA have used this method to measure gas masses for a large number of protoplanetary disks, although this number is still low compared to the number of measured dust masses (see, e.g. Ansdell et al. 2016; Ansdell et al. 2018;

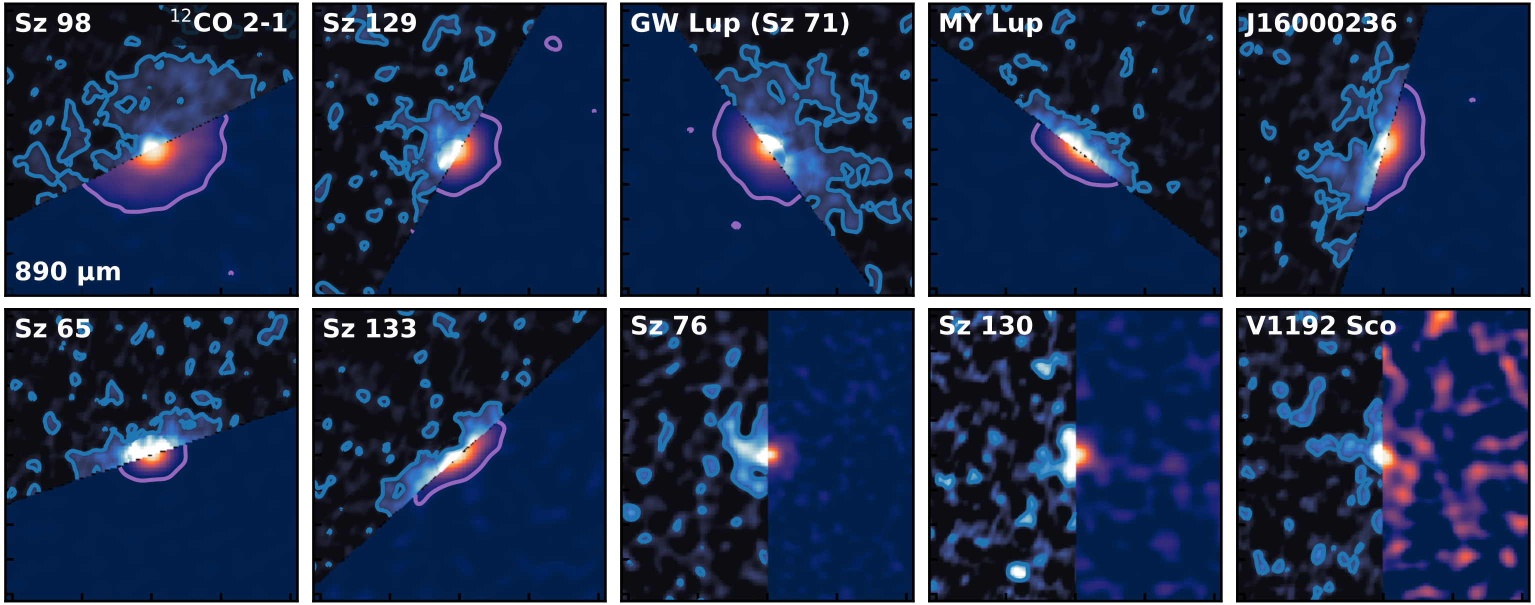

Figure 1.7: A collage of 10 disks in $2''.2 \times 2''.2$ stamps from the Lupus survey, showing the ^{12}CO $J = 2 - 1$ emission in blue on one side of the disk and the 890μm continuum emission in purple on the other side of the disk. The blue contours show a $S/N = 2$ for the CO emission. The purple contours show a $S/N = 3$ for the continuum emission. Note that Sz 76, Sz 130 and V1192 Sco remain unresolved in the continuum. The CO emission is found to be more extended than the continuum emission, but the low S/N of the CO emission also highlights the limitations of the ~ 1 minute snapshots of disk surveys.

Long et al. 2017; Miotello et al. 2017,). These CO-based gas masses are found to be low, with most disks having a gas-to-dust mass ratio $\Delta_{\rm gd} \sim 1-10$, much lower than the ISM value ($\Delta_{\rm gd} \sim 100$). Whether this implies that disks are gas poor or that there exists a process that removes gas-phase CO that currently is not included in the analysis remains an open question, although as will be discussed below the second explanation seems to be favored.

Another promising gas mass tracer is hydrogen deuteride (HD). Being an isotopolog of H_2, HD has been shown to directly follow the distribution of H_2 (see Trapman et al. 2017). The asymmetry of HD gives rise to a small dipole moment and dipole transitions ($\Delta J = 1$). For a gas at a temperature of ~ 20 K it is much easier to excite the first rotational energy level of HD ($E/k_B = 128.5$ K) compared to exciting the second rotational energy level of H_2 ($E/k_B = 549.2$ K), resulting in significantly more emission from HD compared to H_2 in protoplanetary disks. Trapman et al. (2017) show that for low mass disks ($\rm M_{disk} \leq 10^{-3}\ M_\odot$) the HD $J = 1-0$ line flux at 112 μm can be used to directly measure the gas mass to within a factor of two. For more massive disks the gas mass can be measured to within a factor of 3 by combining HD $J = 1-0$ with the HD $J = 2-1$ line flux at 56 μm or a similar tracer of the disk temperature structure.

The energetically lowest transition of HD at 112 μm lies in the far-infrared, where the atmospheric opacity requires going to space-based observatories. Using the PACS (Poglitsch et al. 2010a) instrument on the *Herschel Space Observatory* (Pilbratt et al. 2010a) HD $J = 1-0$ has been detected towards three disks, TW Hya, DM Tau and GM Aur, before the instrument was shut down (Bergin et al. 2013; McClure et al. 2016). Gas masses measured for these sources are higher compared to their CO-based gas masses, finding gas-to-dust mass ratios of $\Delta_{\rm gd} \approx 100$ (Bergin et al. 2013; McClure et al. 2016; Trapman et al. 2017). This has spurred the field to examine chemistry and physical processes that are currently not included in the models that can explain the low CO-based gas masses (see, e.g. chemistry Aikawa et al. 1997; Favre et al. 2013; Bergin et al. 2014; Yu et al. 2017; Schwarz et al. 2018; Bosman et al. 2018, physical processes Bergin et al. 2010; Bergin et al. 2016; Du et al. 2015; Kama et al. 2016b; Krijt et al. 2018 or a combination of the two: Krijt et al. 2020). With the current lack of an observatory capable of detecting HD in protoplanetary disks, we are unable to verify that the results of this small sample of three disks is representative for the full disk population.

Compared to the gas mass, the dust mass is more accessible. Under the assumption that the continuum emission emitted by the dust is optically thin at millimeter wavelengths, there is a simple conversion between the observed flux $F_{\rm mm}$ and the total amount of dust $M_{\rm dust}$ in the disk (see, e.g. Hildebrand 1983; Beckwith et al. 1990)

$$M_{\rm dust} = \frac{d^2}{\kappa_\nu B_\nu(T_{\rm dust})} F_{\rm mm}. \tag{1.2}$$

Here d is the distance to the source, κ_ν is the dust mass opacity, $B_\nu(T_{\rm dust})$ the Planck function at the temperature of the dust, commonly assumed to be $T_{\rm dust} = 20$ K. The conversion from flux to mass is not free from uncertainties. The assumption that the dust is optically thin may not be valid for all parts of the disk, especially if the dust is concentrated in ring-like structures (see, e.g. Dullemond et al. 2018). Another uncertainty is the dust mass opacity. The dust mass opacity depends on the composition of the grains which is not well known (see, e.g. Weingartner & Draine

2001; Draine 2006; Dullemond et al. 2018). A further ingredient that goes into the mass opacity is the grain size distribution, where multi-wavelength observations have put constraints (see, e.g. Tazzari et al. 2016). Finally, scattering at millimeter wavelengths can reduce the flux coming from optically thick regions of the disk, making them appear optically thin, thus leading to an underestimation of the dust mass. In simple models this process is often thought to be negligible, but recent results show that this might not always be case (e.g. Zhu et al. 2019).

To determine the total disk mass requires the ratio of gas to dust in the disk. As discussed previously, the gas-to-dust mass ratio ($\Delta_{\rm gd}$) is found to be approximately 100:1 in the ISM. In disks the ratio is expected to be higher, as the radial drift has caused the large grains to be accreted onto the star (see, e.g. Youdin & Chiang 2004). Furthermore, part of the initial dust mass reservoir has (presumably) been converted into planets or planetary embryos. On the other hand, gas dissipation processes, such as external photo-evaporation, will decrease the $\Delta_{\rm gd}$.

Using ALMA, surveys of multiple star-forming regions have been carried out, which have provided us with an inventory of disk dust masses of the full disk population. These surveys show that the bulk of the disk is less massive than previously thought, with a median disk dust mass of ~ 5 M$_\oplus$ for a 1-3 Myr old star-forming region, assuming a mass opacity of $\kappa_{1.3\rm mm} = 2.3$ cm^2 g^{-1} and a disk-averaged dust temperature of $T_{\rm dust} = 20$ K (see, e.g. Ansdell et al. 2016; Ansdell et al. 2018; Pascucci et al. 2016). This mass already has difficulty explaining the total amount of solids found in exoplanets, without even taking into account that the mass efficiency of planet formation is likely much less than one (see, e.g. Najita & Kenyon 2014; Manara et al. 2018). This discovery has been one of the main drivers for advocating that planet formation already starts in the earlier embedded phase, where disks are found to be more massive (see, e.g. Tychoniec et al. 2018, 2020; Tobin et al. 2020). The surveys also show that the median dust mass decreases with the age of the star-forming region, although recent surveys suggest that this is not a one-to-one correlation (Ansdell et al. 2017; Cazzoletti et al. 2019; Williams et al. 2019).

1.4 Modeling protoplanetary disks

Modeling the emission of protoplanetary disks provides a means of linking what is observed, e.g. the amount, extent and shape of continuum and line emission, to the underlying disk structure and composition. By solving the radiative transfer equation, the dust continuum emission can provide information on the disk dust structure, dust temperature and dust composition. Examples of such 2D/3D continuum radiative transfer codes are `RADMC3D` (Dullemond & Dominik 2004; Dullemond et al. 2012), `TORUS` (Harries et al. 2004; Harries 2014; Harries et al. 2019), `MCFOST` (Pinte et al. 2006), `MCMax` (Min et al. 2009), `Hyperion` (Robitaille 2011) and `POLARIS` (Reissl et al. 2016). Line emission can reveal details on the temperature, distribution and composition of the gas, depending on the molecule used for the analysis. Line radiative transfer codes such as `LIME` (Brinch & Hogerheijde 2010), `FLiTs` (Woitke et al. 2018), `RADlite` (Pontoppidan et al. 2009) and `POLARIS` (Brauer et al. 2017) use inputs such as gas temperature, molecular density and the radiation field to compute line excitation and line emission. In protoplanetary disks gas temperature, line excitation and the chemistry that set molecular abundances are interdependent properties. Several modeling codes have therefore been developed that combine the previously mentioned modeling components into a self-consistent disk model. Examples include `DALI` (Bruderer et al. 2009, 2012; Bruderer 2013), `ProDiMo` (Woitke et al. 2009; Kamp et al. 2010; Thi et al. 2011)(and in extension the DIANA project; Woitke et al. 2016, 2019; Kamp et al. 2017), `RAC2D` (Du & Bergin 2014) and `ANDES` (Akimkin et al. 2013). In these models the dust temperature, gas temperature, chemistry and excitation are calculated self-consistently. In the interest of keeping computation time manageable these models make some simplifications, such as assuming a static, and often parametric, density structure, using a simpler chemical network focused on accurately reproducing the heating and cooling in the disk or making simplifying assumptions about the excitation and radiative transfer such as using an escape probability.

Broadly speaking there are two approaches for modeling, inverse modeling and forward modeling, which have complementary goals. In inverse modeling the aim is to characterize the disk structure, in terms of density, temperature and abundance, that best describes a given set of observations. Briefly, for a given disk model the previously discussed codes can be used to compute the expected emission, which is then compared to the observations, varying the disk parameters to minimize the residuals. To accurately measure formal uncertainties on the parameters that describe the disk structure, for example using a Monte-Carlo Markov Chain method (e.g. Foreman-Mackey et al. 2013), it is necessary to run tens or even hundreds of thousands of models. To make this computationally feasible the approach focuses on radiative transfer codes where running such a number of models is attainable (see, e.g. Andrews et al. 2011; Tazzari et al. 2017; Tazzari et al. 2018; Cieza et al. 2018), although there are also examples of inverse modeling using thermochemical codes (see, e.g. Kama et al. 2016b; Fedele et al. 2017; Woitke et al. 2019).

The alternative approach is forward modeling. In this approach the focus is on accurately portraying the physics and chemistry in protoplanetary disks. By varying the parameters that govern these processes one can inspect the resulting change in observables, such as the amount or distribution of emission. Forward modeling is aimed at characterizing trends between disk properties and observables. Examples include CO isotopolog line fluxes as tracer of disk gas mass (see, e.g. Williams & Best 2014; Miotello et al. 2014; Miotello et al. 2016), the link between CN emission and the size of the disk and far-ultraviolet radiation it is exposed to (Visser et al. 2018; Cazzoletti et al. 2018) and understanding mid-IR and far-IR water features observed in disks with *Spitzer* (Antonellini et al. 2015, 2016).

1.5 This thesis

Over recent years our understanding of protoplanetary disks has grown considerably. However there are still gaps in our knowledge of planet formation. The wide variety of exoplanets and planetary systems is no less than the diversity of the properties of protoplanetary disks they once inhabited. Furthermore, the fact that each star hosts at least one planet (see, e.g. Cassan et al. 2012; Suzuki et al. 2016) on average means the puzzle of planet formation must not only be solved for the previously studied bright, large disks but for the full protoplanetary disk population. The disk surveys with ALMA of entire star-forming regions (e.g. Lupus: Ansdell et al. 2016; Ansdell et al. 2018) have provided the first steps here. This thesis focuses on CO line observations from these surveys, in particular those from the Lupus disk survey. Thermochemical models are used to bridge the gap between observables, such the gas disk size measured from CO, and the underlying bulk properties and distribution of the gas. Based on these observables, the thesis examines physical processes in protoplanetary disks, such as grain growth and radial drift of large dust grains and the viscous evolution of the gas.

Chapter II and III of this thesis look at the effects of radial drift and grain growth on the difference between observed gas and dust disk sizes. The fact that in observations the CO line emission extends further out than the dust continuum is (often solely) attributed to larger grains having radially drifted inward. As discussed previously, the difference in optical depth between the two tracers can produce a similar observational signature. Chapter II examines quantitatively the effects of dust evolution and optical depth on the observed gas-dust size differences. In Chapter III the lessons learned in the previous chapter are applied to the observed gas and dust disk sizes of protoplanetary disks in the Lupus star-forming region. For a sample of ten disks dust-based models without radial dust evolution are used to investigate whether dust evolution is required to reproduce the observations.

Chapter IV examines measured gas outer radii in the context of protoplanetary disks evolving viscously. In viscous evolution theory disks grow over time, an observable feature that distinguishes it from wind-driven disk evolution. This chapter investigates whether the measured gas outer radius is a suitable tracer for viscous spreading and compares models to observations in the Lupus and Upper Sco star forming region to determine if disks evolve viscously.

In chapters V and VI the focus shifts to the gas mass of protoplanetary disks. Chapter V examines the behavior of ^{13}CO and C^{18}O line fluxes of viscously evolving disks. It also investigates whether CO destruction at the disk midplane can reconcile the gas masses required to explain the observed stellar mass accretion rates with the low ^{13}CO and C^{18}O fluxes observed towards protoplanetary disks. In Chapter VI HD $J = 1 - 0$ upper limits obtained from archival *Herschel* observations are examined. Combined with an extensive grid of disks models these upper limits are used to place meaningful constraints on the gas masses of disks around Herbig Ae/Be stars.

The main conclusions of the thesis can be summarized as follows:

Chapter II: The gas disk size measured from models is not affected by dust evolution and traces the radius in the outer disk where the CO column density drops below 10^{15} cm^{-2} and CO becomes photodissociated. To accurately measure the gas outer radius requires a peak signal-to-noise greater than 10 for the ^{12}CO integrated velocity map. A measured gas disk size ($R_{\rm gas}$) that is more than four times as large as the dust disk size ($R_{\rm dust}$) is a clear sign that the disk has undergone grain growth and radial drift. Disks for which the difference in sizes is smaller require modeling of the CO emission to separate optical depth effects from the impact of dust evolution on gas and dust disk sizes.

Chapter III: Out of a sample of ten observed disks in the Lupus star-forming region, all with $R_{\rm gas}/R_{\rm dust} < 4$, five require dust evolution in addition to optical depth effects to explain both their dust structure and the observed gas disk size. For the other five disks the observed gas–dust size ratio can be explained without dust evolution, using only optical depth effects. An additional six disks from the same star-forming region are found to have significant, i.e. $S/N \geq 3$, CO 2-1 emission out beyond four times their dust outer radius. While low S/N prevents detailed analysis, it would be difficult to explain the observations of these six disks without substantial dust evolution.

Chapter IV: Our models show that gas outer radii measured from CO emission are a suitable tracer of viscous expansion: the gas radius increases over time and does so faster if the disk is expanding at a faster rate. However, in the case of a low mass disk expanding rapidly, the gas outer radius measured from our models is found to instead decrease with time as a result of photodissociation in the outer disk. Our models also reveal that quantitatively linking the observed outer radii to viscous evolution is more difficult and can overestimate the amount of viscosity in the disk by up to an order of magnitude. Most observed gas outer radii of disks in Lupus are found to be consistent with viscously evolving disk models that start out small (≤ 10 AU) and evolve with a low viscosity.

Chapter V: For a viscously evolving disk the gas mass decreases over time, but the ^{13}CO and C^{18}O line fluxes of our models, used to trace the gas mass, instead increase over time as their optically thick emitting regions grow in size. Observed ^{13}CO and C^{18}O fluxes of the most massive ($M_{\rm disk} > 5 \times 10^{-3}$ M$_\odot$) disks in Lupus can be reproduced by our viscously evolving disk models. For lower mass disks the observed ^{13}CO and C^{18}O fluxes are up to an order of magnitude fainter compared to the models. CO conversion through cosmic-ray driven chemistry can potentially reconcile the difference for C^{18}O, but it cannot explain this difference for ^{13}CO as CO is predominantly destroyed below the ^{13}CO emitting region. To explain the observed ^{13}CO fluxes and C^{18}O upper limits in Lupus low mass ($M_{\rm dust} \leq 5 \times 10^{-5}$ M$_\odot$) disks either have to be significantly smaller than their more massive counterparts, or they must undergo efficient vertical mixing.

Chapter VI: The HD upper limits constrain the gas masses of nearly all disks to below 0.1 M$_\odot$, thus ruling out that these disks are currently gravitationally unstable. The strongest constraint is obtained for the disk around HD 163296, $M_{\rm gas} \leq 0.07\,$M$_\odot$, which combined with the dust mass suggests that the disk has a global gas-to-dust mass ratio below 100. The HD-based gas mass upper limit lies at the low end of gas masses estimated based on CO isotopologues, suggesting that CO is underabundant by at most a factor of a few. The gas mass upper limits of HD 163296 and HD 100546, two disks that host several massive candidate protoplanets, suggest disk-to-planet mass conversion efficiencies of $\sim 10 - 40\%$ based on current values.

Gas outer radii measured from ^{12}CO emission have a well understood link to the underlying extent of the gas and are therefore a robust measure of the size of the gas disk. As an observable, the gas outer radius is a valuable tool to study radial drift of large grains when combined with the outer radius of the dust. It can also show what physics drive disk evolution if paired with the age of the disk. However, this thesis has shown that modeling is required to accurately interpret observed gas outer radii. Explaining the faint CO isotopolog line fluxes that have been observed likely requires a combination of processes put forward in the literature. With HD remaining our most direct link to the gas mass of protoplanetary disks, a renewed access to the HD rotational lines in the far-infrared would greatly increase our understanding of this elusive quantity.

1.5.1 Future outlook

ALMA has provided some extraordinary and far-reaching results, but, fortunately for us, it is only getting started revealing the intricate inner workings of protoplanetary disks. One area that has remained relatively unexplored is the distribution and composition of the gas in disks. Despite outweighing the dust in disks by a factor ~ 100, after 8 years of ALMA there have been very few deep gas observations in disks compared to the detailed and deep studies of the dust. The recently observed MAPS ALMA (PI: Öberg) large program will provide deep gas observations of a wide range at high ($\sim 0\farcs1$) resolution of five disks. These observations will provide a wealth of information of the gas in disks, but placing them in context of the disk population as a whole requires a revisit of the disk surveys of several star-forming regions carried out with ALMA. These previous disk surveys have been very successful, but they were tailored towards observing the dust continuum and, in hindsight, were too shallow to robustly detect and study the gas emission for the full disk population. One of main next goals of ALMA should therefore be disk surveys that focuses on the gas. As it stands, we know only little of the structure of the gas of disks with low dust mass. Are they as small as their compact dust emission suggest or are we seeing the effect of efficient inward drift of millimeter-sized grains? Using a setup similar to previous surveys but going for 10-30 minutes per source covering CO and its main isotopologs would give us a wealth of information on the properties of the gas of a typical protoplanetary disk.

Currently one of our largest blind spots for in terms of protoplanetary disk research is the lack of a facility capable of observing in the far-infrared, after the *Herschel Space Observatory* shut down. This wavelength range contains the HD rotational lines that are key for measuring disk gas masses and covers several H_2O lines used to detect the presence of cold water in protoplanetary disks. With the recent cancellation of the HIRMES instrument development in April 2020, the future of this wavelength range now lies with the proposed *Space Infrared Telescope for Cosmology and Astrophysics* (SPICA), hopefully to be approved in summer of 2021, and the *Origin Space Telescope* (OST). Both missions will likely not fly before the mid 2030s, but they will be worth the wait.

The *James Webb Space Telescope* (JWST) is closer over the horizon. With its near- and mid-infrared instruments it will focus mostly on the inner few AU of the disk. However, this inner disk and the outer disk are linked. We cannot properly interpret what we see in the outer disk without understanding the structure of the inner disk. For example, if CO is removed from the outer disk through freeze-out and transformation and subsequently transported inward over the CO_2 and H_2O icelines, the enhancement in volatile carbon in the inner disk should be measurable with JWST.

The low average dust mass of protoplanetary disks means that planet formation needs to start already while the disk is still embedded in an envelope. While observations show that the material is there at an early age, we also need to find out if the conditions are favorable for planet formation. For example, can the dust grow fast enough into planetary embryos in the few 10^5 yrs that the disk is embedded? This requires shifting our modeling from building planets in protoplanetary disks to doing so in younger disks. To support this modeling effort we also need observations to uncover the conditions inside these disks. There is already an accepted ALMA large program (PI: Ohashi) to observe 7 Class 0 and 10 Class I disks at AU scale resolution to look for substructure in these young objects. To what extent these substructures are already present will inform us on just how early planets have started to form.

The wealth of new and upcoming observations will bring forth changes and new challenges for our models of protoplanetary disks. For example, observations show that substructures are ubiquitous at least in bright disks, but a large number of models are still run using a smooth density profile Furthermore, it has become increasingly clear that some observations cannot be explained using our static, axisymmetric disk models. A prime example is the riddle of the low CO isotopolog line fluxes, which, as will be discussed later in this thesis, are very difficult to explain using a static disk. It was recently shown that the solution might lie in combining the effects of chemistry with the evolution of the dust (Krijt et al. 2020). This typifies the next major step in disk modeling, where we examine the interplay between the evolution of the dust, the radial and vertical movements of the gas and the chemistry both in the gas as well as on the dust grains. This in itself is not without its challenges, as the complexity of the model increases rapidly with the number of components that are included. We should therefore keep in mind that the goal is to understand the effect of the physics and chemistry that we include and how observations can show us their relative importance. It is tempting to include everything in single model, but remember that we are here to understand what we see, not simply reproduce it.

2 | Gas versus dust sizes of protoplanetary disks: Effects of dust evolution

L. Trapman, S. Facchini, M.R. Hogerheijde, E.F. van Dishoeck and S. Burderer,
2019, A&A, 629, 79

Abstract

Context: The extent of the gas in protoplanetary disks is observed to be universally larger than the extent of the dust. This is often attributed to radial drift and grain growth of the millimeter grains, but line optical depth produces a similar observational signature.

Aims: We investigate in which parts of the disk structure parameter space dust evolution and line optical depth are the dominant drivers of the observed gas and dust size difference.

Methods: Using the thermochemical model `DALI` with dust evolution included we ran a grid of models aimed at reproducing the observed gas and dust size dichotomy.

Results: The relation between R_{dust} and dust evolution is non-monotonic and depends on the disk structure. The quantity R_{gas} is directly related to the radius where the CO column density drops below 10^{15} cm^{-2} and CO becomes photodissociated; R_{gas} is not affected by dust evolution but scales with the total CO content of the disk. While these cases are rare in current observations, $R_{\mathrm{gas}}/R_{\mathrm{dust}} > 4$ is a clear sign of dust evolution and radial drift in disks. For disks with a smaller $R_{\mathrm{gas}}/R_{\mathrm{dust}}$, identifying dust evolution from $R_{\mathrm{gas}}/R_{\mathrm{dust}}$ requires modeling the disk structure including the total CO content. To minimize the uncertainties due to observational factors requires $\mathrm{FWHM}_{\mathrm{beam}} < 1\times$ the characteristic radius and a peak $\mathrm{S/N} > 10$ on the ^{12}CO emission moment zero map. For the dust outer radius to enclose most of the disk mass, it should be defined using a high fraction (90-95%) of the total flux. For the gas, any radius enclosing $> 60\%$ of the ^{12}CO flux contains most of the disk mass.

Conclusions: To distinguish radial drift and grain growth from line optical depth effects based on size ratios requires disks to be observed at high enough angular resolution and the disk structure should to be modeled to account for the total CO content of the disk.

2.1 Introduction

Observations of exoplanetary systems have revealed that they come in a large range of sizes, from multiple planets in the central $\sim 0.3-1$ AU of the system (e.g. TRAPPIST-1 or Kepler-90; Gillon et al. 2017; Cabrera et al. 2014) to systems with Jupiter mass planets in ~ 70 AU orbits around their host star (HR 8799; Marois et al. 2008). The diversity in planetary systems is linked to the diversity in protoplanetary disks from which these planets have formed.

To better understand this link, measurements of the properties of these disks are required. Of particular interest are the spatial extent of the gas, which sets the evolution of the disk, and the behavior of the millimeter grains, which form the building blocks of the planets.

Observations have shown that the gas, traced by the ^{12}CO emission, extends further out than the millimeter grains traced by the (sub)millimeter continuum emission. Two physical processes contribute to the observed size dichotomy. The first is a difference in optical depth, with the line optical depth being much higher than the continuum optical depth (e.g. Dutrey et al. 1998; Guilloteau & Dutrey 1998; Facchini et al. 2017). Depending on how rapidly the density profile drops off in the outer disk, the optically thin continuum emission will drop below the detection limit before the optically thick ^{12}CO emission. Based on the self-similar solution of viscous evolution, an exponentially tapered power law profile has been proposed to simultaneously fit the extent of the gas emission and the extent of the dust emission (e.g. Hughes et al. 2008; Andrews et al. 2009, see also Panić et al. 2008).

The second physical process setting the observed size dichotomy is grain growth and the subsequent inward radial drift of millimeter-sized grains. There is already extensive observational evidence that grains can grow to at least millimeter sizes (e.g. Testi et al. 2003; Natta et al. 2004; Lommen et al. 2007; Andrews & Williams 2005, 2007; Ricci et al. 2010). The large grains have decoupled from the gas. The gas is partly supported by a pressure gradient and therefore moves at slightly sub-Keplerian velocities. Gas drag causes the large grains, moving at Keplerian velocities, to slow down and move inwards. In addition, the maximum grain size seems to be decreasing as function of radial distance from the star, which is supported by both observations (e.g. Guilloteau et al. 2011; Pérez et al. 2012, 2015; Menu et al. 2014; Tazzari et al. 2016; Tripathi et al. 2018) and theoretical modeling results (e.g. Birnstiel et al. 2010, 2012).

Both radial drift and radially dependent grain growth cause the millimeter-sized grains to be confined in the inner regions of the disk, resulting in compact continuum emission at millimeter wavelengths. Dust evolution also affects the CO chemistry and gas temperature and could therefore also change the observed gas disk size, determined from the ^{12}CO emission. Facchini et al. (2017) found that grain growth and settling results in colder gas with respect to the dust at intermediate disk heights, which reduces the CO excitation and emission.

The Atacama Large Millimeter/submillimeter Array (ALMA) is transforming our understanding of disk sizes. High resolution observations have shown that for several disks the dust outer edge drops off too sharply with radius and cannot be explained with the same exponential taper that reproduces the ^{12}CO emission (e.g. Andrews et al. 2011, 2016; de Gregorio-Monsalvo et al. 2013; Piétu et al. 2014; Cleeves et al. 2016).

In addition, complete surveys of disks with ALMA have made it possible to study these disk properties not only for individual disks but also for the full disk population (e.g. Taurus: Andrews et al. 2013; Ward-Duong et al. 2018, Lupus: Ansdell et al. 2016; Ansdell et al. 2018, Chamaeleon I: Pascucci et al. 2016; Long et al. 2017, Upper Sco: Barenfeld et al. 2016, 2017, σ Ori: Ansdell et al. 2017, IC 348: Ruíz-Rodríguez et al. 2018). One of the main findings of these surveys is that most disks have very compact millimeter emission. For example, in the Lupus Survey (Ansdell et al. 2016; Ansdell et al. 2018) $\sim 45\%$ remain unresolved at ~ 20 AU radius resolution. It should be noted that the integration time used by these surveys is short, i.e. 1-2 min per source, resulting in a low signal-to-noise ratio (S/N) on the gas lines.

Observations show that the outer radius of the gas disk, traced by the ^{12}CO emission, is universally larger than the millimeter dust disk, as traced by the millimeter emission. Ansdell et al. (2018) measured gas and dust outer radii for 22 disks from the ^{12}CO 2-1 emission and 1.3 mm continuum emission. They found gas-dust size ratios $R_{\mathrm{gas}}/R_{\mathrm{dust}}$ ranging from 1.5-3.5, with an average $\langle R_{\mathrm{gas}}/R_{\mathrm{dust}}\rangle = 1.96 \pm 0.04|_{\sigma_{\mathrm{obs}}}$. Larger gas-dust ratios ($R_{\mathrm{gas}}/R_{\mathrm{dust}} > 4$) have been found for a few individual disks (e.g. Facchini et al. 2019). It should be noted that measurements of disk sizes are biased towards the most massive disks. Gas-dust sized differences for the faint end of the disk population are not well explored with current sensitivities and angular resolutions.

Both optical depth and radial drift contribute to the observed gas-dust size ratio. Quantitative comparison of how much these two effects affect the gas-dust size ratio has so far been limited to a single disk structure appropriate for the large and massive disk HD 163296 (Facchini et al. 2017).

In this paper, we expand the quantitative analysis of optical depth to a range of disk structures including dust growth and radial drift. In particular we focus on how disk mass, disk size, and dust evolution affect the gas-dust size difference. Additionally, we address what role observational factors such as resolution and sensitivity play in the observed gas-dust size difference. The set-up of the method and the models used in the paper are described in Section 2.2. The results are presented in Section 2.3. In Section 2.4 the connection between dust evolution and the dust outer radius is discussed. The conclusions are presented in Section 2.5.

2.2 Models

2.2.1 `DALI` with dust evolution

To study the effects of radial drift, grain growth, and optical depth on the gas-dust size dichotomy we use the thermo-chemical model `DALI` (Bruderer et al. 2012; Bruderer 2013) with dust evolution included by Facchini et al. (2017).

For a given physical structure, this version of `DALI` first calculates the radial dependence of the grain size distribution following the reconstruction routine from Birnstiel et al. (2015). This semi-analytical prescription provides a good representation of the more complete numerical models in Birnstiel et al. (2010). Birnstiel et al. (2015) divide the dust in the disk into two regimes: In the inner part of the disk, dust evolution is fragmentation dominated and the maximum grain size is set by the fragmentation barrier. In the outer disk, the maximum grain size is set by radial drift. The dust evolution is run for 1 Myr. Tests with models run for 10 Myr showed that the dust evolution timescale has only minimal effect on the dust outer radius (less than 17 %).

Next, dust settling is calculated by solving the advection-diffusion equation in the vertical direction for each grain size bin at every radial point in the model. Opacities are calculated at each (r, z) point of the model using the resulting local grain size distribution.

It should be noted that the local gas-to-dust mass ratio ($\Delta_{\rm gd}$) in the models is kept fixed at $\Delta_{\rm gd} = 100$, i.e. only the dust properties are changed.

The `DALI` thermo-chemical computation can be split into three consecutive steps: First the continuum radiative transfer equation is solved using the input stellar spectrum and the grain opacities calculated in the previous step. This is done using a 3D Monte Carlo method. Next the abundances of atomic and molecular species are calculated by solving the time dependent chemistry at each point in the model. In this step the local grain size distribution is taken into account when computing the dust surface area available for processes such as gas-grain collisions, H_2 formation rate, freeze-out, thermal and non-thermal desorption, and hydrogenation. Using a non-LTE formulation the excitation of levels of the atomic and molecular species are calculated and the resulting gas temperature is determined by balancing the heating and cooling processes. Both the chemistry and the excitation are temperature dependent. The calculation is therefore performed iteratively until a self-consistent solution is found. A more detailed description of `DALI` can be found in Appendix A of Bruderer (2013). The implementation of dust evolution in `DALI` is described in Facchini et al. (2017).

2.2.2 Model set-up

The gas surface density profile of the models is described by a tapered power law that is often used to describe protoplanetary disks (e.g. Hughes et al. 2008; Andrews et al. 2009; Andrews et al. 2011; Tazzari et al. 2017). This simple parametric structure is based on the assumption that the gas structure is set by viscous accretion, where $\nu \propto R^{\gamma}$ (Lynden-Bell & Pringle 1974; Hartmann et al. 1998), i.e.

$$\Sigma_{\rm gas}(R) = \frac{M_{\rm disk}(2-\gamma)}{2\pi R_{\rm c}^2} \left(\frac{R}{R_{\rm c}}\right)^{-\gamma} \exp\left[-\left(\frac{R}{R_{\rm c}}\right)^{2-\gamma}\right]. \tag{2.1}$$

In this case, $R_{\rm c}$ is the characteristic radius where the surface density profile transitions from a power law to an exponential taper.

Under the assumption of vertical isothermality and hydrostatic equilibrium the vertical structure is given by a Gaussian density distribution (Kenyon & Hartmann 1987)

$$\rho_{\rm gas} = \frac{\Sigma_{\rm gas}}{\sqrt{2\pi}Rh} \exp\left[-\frac{1}{2}\left(\frac{z}{Rh}\right)^2\right], \tag{2.2}$$

where $h = h_{\rm c}(R/R_{\rm c})^{\psi}$, ψ is the flaring power-law index and h_c is the disk opening angle at $R_{\rm c}$.

2.2.3 Grid of models

Both the characteristic size $R_{\rm c}$ and the total disk mass $M_{\rm disk}$ are expected to affect the observed extent of the disk. A set of models was run varying both parameters: $R_{\rm c} = 20, 50$ AU and $M_{\rm disk} = 10^{-2}, 10^{-3}, 10^{-4}, 10^{-5}$ $M_{\odot}$. No models with larger

R_c were run as we aim to reproduce the bulk of disk population, most of which are found to be small. For each of these physical structures three models are run with $\alpha = 10^{-2}, 10^{-3}, 10^{-4}$. For reference, a model with the same (R_c, $M_{\rm disk}$) is run using DALI without dust evolution (no drift). In this model the dust is split into two grain populations: small grains with sizes ranging between 5 nm and 1 μm and large grains with sizes between 1 μm and 1 mm. These large grains are restricted to a scale height of χh, where $\chi < 1$, simulating that these grains have settled towards the midplane. The mass ratio of the large to the small grains is given by $f_{\rm large}$.

Standard volatile [C]/[H] $= 1.35 \cdot 10^{-4}$ and [O]/[H] $= 2.88 \cdot 10^{-4}$ are assumed in all models and the chemistry is evolved over a timescale of 1 Myr, which is a representative age for protoplanetary disks. For longer timescales, CO is converted into CH_4/C_2H_2, as shown in Bosman et al. (2018) (see also Schwarz et al. 2018; Dodson-Robinson et al. 2018). This results in a overall underabundance of volatile CO, which has been found in a number of disks (e.g. Favre et al. 2013; Kama et al. 2016b; Cleeves et al. 2016; McClure et al. 2016; Miotello et al. 2017). To investigate how such an underabundance in CO affects the observed gas disk size, a subset of models was run with a lower [C]/[H] and [O]/[H]. These models are discussed in Section 2.4.1.

T Tauri stars are expected to have excess UV radiation as a result of accretion onto the stellar surface. This UV radiation is added to the spectra as a blackbody with T = 10000 K, with a luminosity computed from the accretion rate assuming that the gravitational potential energy is released as radiation with 100% efficiency (see also Kama et al. 2016a).

For analysis, the disks are assumed to be face on ($i = PA = 0°$). The effect of inclination is discussed in Appendix 2.A and is found to be minimal for $i \leq 50°$. In total 32 models are run. Their parameters are found in Table 2.1.

2.2.4 Measuring the outer radius

To investigate the gas-dust size difference we have to measure the size of a disk from observations. A disk size metric that is often adopted for these purposes makes use of the cumulative intensity profile, i.e. the flux is measured in increasingly larger apertures. The outer radius (R_{90}) is defined as the radius that encloses 90% of the total flux ($F_{\rm tot}$) of the disk

$$0.9 = \frac{2\pi}{F_{\rm tot}} \int_0^{R_{90}} I_\nu(r') r' {\rm d}r'. \tag{2.3}$$

This method has the advantage that it can be easily and homogeneously applied to a large number of disks, even if these disks show signs of substructure (see e.g. Tripathi et al. 2017; Ansdell et al. 2018; Andrews et al. 2018a). In addition, the method can be applied to the short integration observations used in recent surveys, where the limited sensitivity hinders a more complex analysis.

It should be noted that the resulting outer radius is an observational outer radius. How well this observational radius is related to underlying physical size of the disk is examined in Section 2.4.3.

In this work, the gas outer radius is measured from the extent of the ^{12}CO 2-1 emission in the moment zero map and the dust outer radius is measured from the extent of the 1300 μm continuum emission. Gas outer radii measured using the ^{12}CO 3-2 emission differ from those measured using the ^{12}CO 2-1 by less than 10%. For

Table 2.1: `DALI` parameters of the physical model.

Parameter	Range
Chemistry	
Chemical age	1 Myr
[C]/[H]	$1.35 \cdot 10^{-4}$
[O]/[H]	$2.88 \cdot 10^{-4}$
Physical structure	
γ	1.0
ψ	0.1
h_c	0.1 rad
$R_{\rm c}$	[20, 50] AU
$M_{\rm gas}$	$[10^{-5},10^{-4},$ $10^{-3},10^{-2}]$ $M_\odot$
Gas-to-dust ratio	100
Dust properties - no dust evolution	
$f_{\rm large}$	0.85
χ	0.2
Dust properties - dust evolution	
$\alpha_{\rm turb}$	$[10^{-2},10^{-3},10^{-4}]$
$\rho_{\rm gr}$	2.5 g $\rm cm^{-3}$
$\rm v_{frag}$	10 m $\rm s^{-1}$
composition	standard ISM[1]
Stellar spectrum	
$T_{\rm eff}$	4000 K + Accretion UV
L_*	0.5 $L_\odot$
Observational geometry	
i	0°
PA	0°
d	150 pc

[1] Weingartner & Draine 2001, see also Section 2.5 in Facchini et al. 2017.

comparison, gas outer radii measured instead from the ^{13}CO 2-1 emission are shown in Appendix 2.B.

We note that the moment zero map is a velocity integrated intensity (in Jy/beam km/s). This puts additional weight at the center of the disk, where the line widths are larger. It would be more comparable to the continuum emission to use the peak intensity map, defined as the peak intensity of the spectrum at each spatial point. In Appendix 2.C we compare gas outer radii derived from the moment 0 and the peak intensity map and find them to be nearly identical.

2.3 Results

In this section we investigate how dust evolution shapes the continuum and line emission and how it affects the dust and gas outer radii. This effect is quantitatively compared to the influence of other disk parameters ($M_{\rm disk}$, $R_{\rm c}$) and observational factors (signal to noise, size of the beam).

2.3.1 Dust radial intensity profiles

Dust evolution changes the distribution of the grains responsible for the millimeter continuum emission, resulting in a different radial intensity profile. Through Equation (2.3) the dust outer radius is affected by the radial profile. In this section we investigate this link.

Figure 2.1 shows the normalized dust radial profiles of the models with $R_\mathrm{c} = 50$ AU on a logarithmic intensity scale. The radial profiles of the models with $R_\mathrm{c} = 20$ AU are shown in Figure 2.20 in Appendix 2.E. Starting with the lowest disk mass ($M_\mathrm{disk} = 10^{-5}$ M$_\odot$), all intensity profiles fall off steeply in the inner 10 AU. For disks with $\alpha_\mathrm{turb} = 10^{-3} - 10^{-4}$ the intensity profile flattens between 10 to 25 AU and then steepens again. The dust outer radii of these two models are located at the second steepening off. For the model with $\alpha_\mathrm{turb} = 10^{-2}$ and the so-called no drift model, the intensity profile is more extended and the dust outer radii of these models are larger.

For the disks with $M_\mathrm{disk} = 10^{-4}$ M$_\odot$ all intensity profiles of the dust evolution models are similar within 25 AU and their outer radii therefore lie close together. At higher disk mass ($M_\mathrm{disk} \geq 10^{-3}$ M$_\odot$) and low viscosity ($\alpha_\mathrm{turb} \leq 10^{-3}$) a plateau of emission can be seen. The prominence of this plateau increases as α_turb decreases. For $M_\mathrm{disk} = 10^{-2}$ M$_\odot$ and $\alpha_\mathrm{turb} = 10^{-4}$ about 75% of the emission is in the plateau and it has a large effect on the cumulative flux and the location of $R_\mathrm{90,dust}$ (cf. Figure 2.22).

The emission plateau is directly linked to the presence of millimeter grains in the outer disk. When α_turb is low, the timescale for collisions that result in fragmentation is longer than the drift timescale and the size of the grains in the outer disk is set by radial drift (cf. Birnstiel et al. 2015). This causes a pile up of millimeter grains in the outer parts of the disk. Thus, the shape of the intensity profile is affected in a complex way by dust evolution.

2.3.2 ^{12}CO radial intensity profiles

The gas outer radius is measured from ^{12}CO 2-1 line emission, which is expected to be mostly optically thick throughout the disk. Dust evolution could affect the ^{12}CO emission by altering the temperature structure (Facchini et al. 2017).

In Figure 2.2 the ^{12}CO 2-1 line emission profiles of the models with $R_\mathrm{c} = 50$ AU are examined. Within each mass bin, the profiles are very similar in shape, suggesting that the effect of dust evolution on the ^{12}CO emission is negligible. The emission profiles drop off relatively slowly, which is expected for optically thick line emission that follows the temperature profile. At a certain radius the emission profile drops off steeply. In the model this radius corresponds to where the CO column (N_CO) density drops below 10^{15} cm^{-2}. Below a CO column density of $N_\mathrm{CO} \leq 10^{15}$ cm^{-2}, CO is no longer able to effectively self-shield against photodissociation and is quickly removed from the gas phase (van Dishoeck & Black 1988). Defining the radius at which $N_\mathrm{CO} = 10^{15}$ cm^{-2} as $R_\mathrm{CO\ disk}$, this radius effectively encloses all of the CO emission and all of the volatile CO in the disk.

Using simple arguments, the observed gas outer radius $R_\mathrm{CO,\ 90\%}$ can be related analytically to $R_\mathrm{CO\ disk}$. Assuming that the CO emission is optically thick ($I_\mathrm{CO} \sim T_\mathrm{gas}(R) \propto R^{-\beta}$) and that $R_\mathrm{CO\ disk}$encloses all ^{12}CO flux, we can write (full derivation

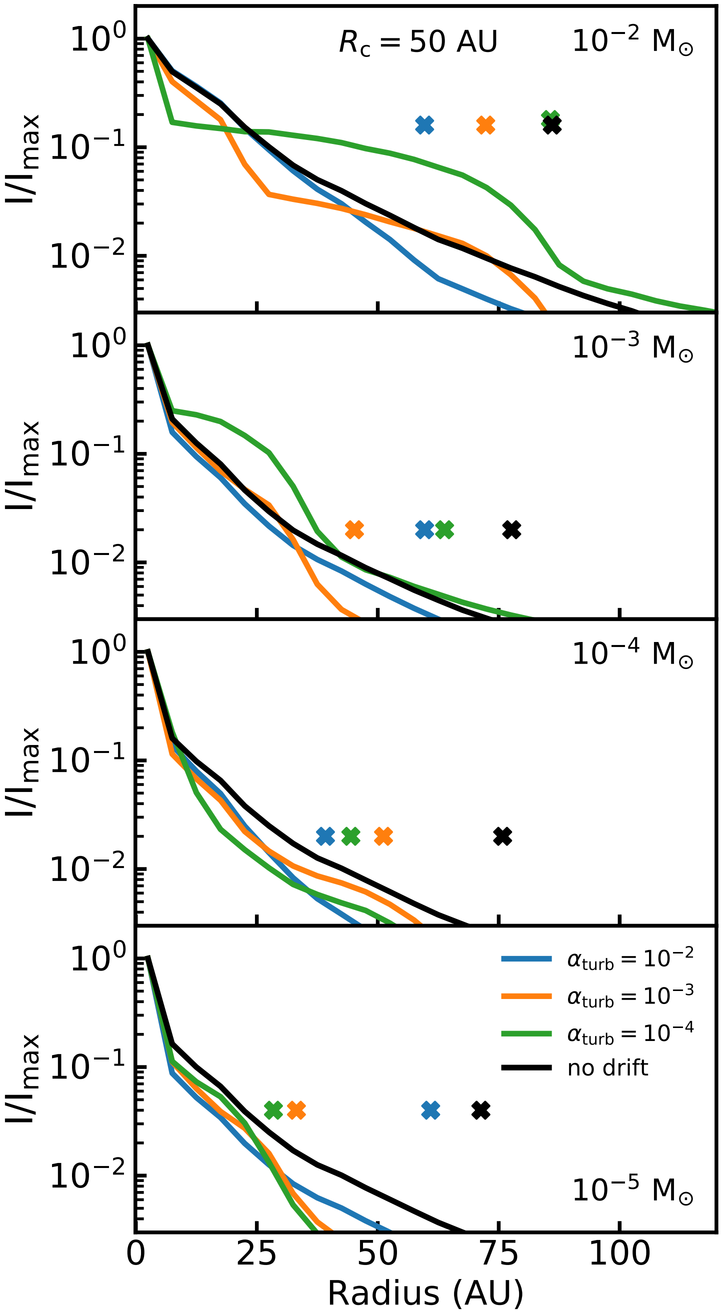

Figure 2.1: Radial intensity profiles of the 1.3 mm continuum emission, normalized to the peak intensity, for the models with $R_c = 50$ AU. Crosses at an arbitrary height above the line denote the dust outer radii, defined as the radii enclosing 90% of the total flux. The resulting cumulative intensity curves are shown in Figure 2.22.

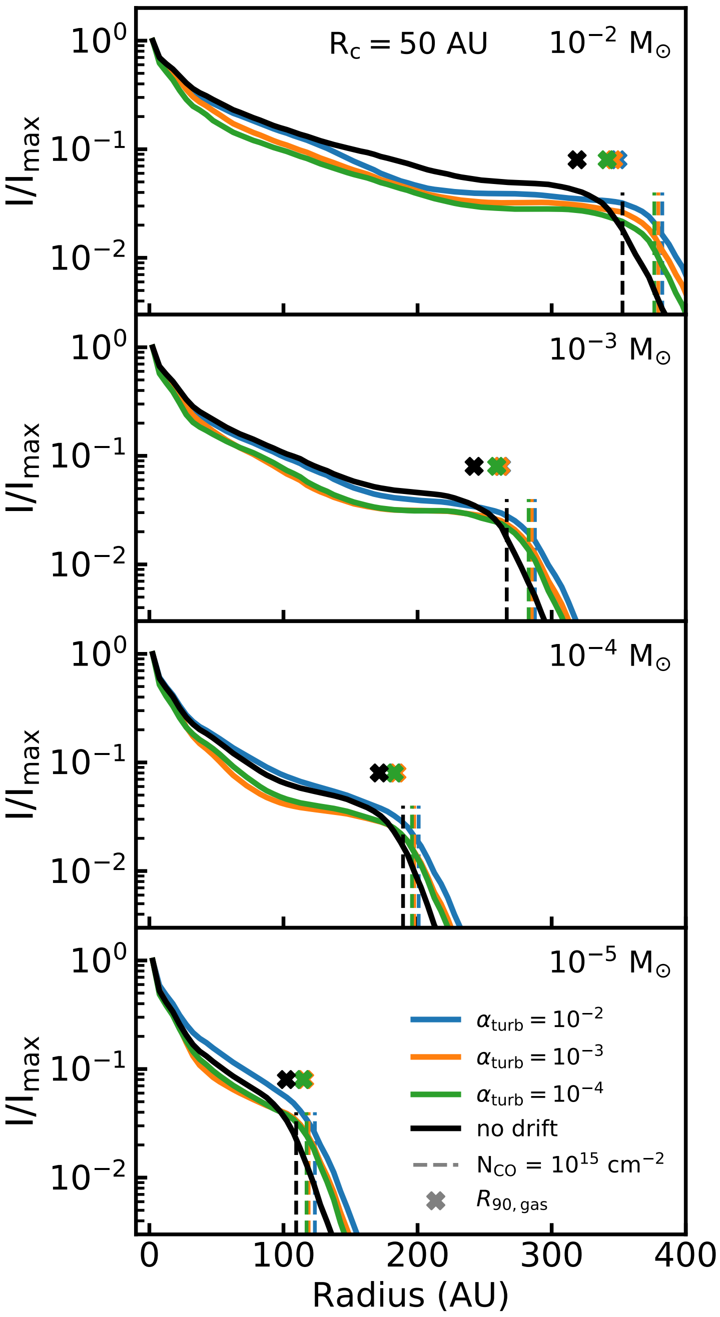

Figure 2.2: Radial intensity profiles of the ^{12}CO 2-1 line emission, normalized to the peak intensity, for models with $R_c = 50$ AU. Crosses above the line denote the dust outer radii, defined as the radii enclosing 90% of the total flux. Vertical dashed lines denote the radius at which the CO column density drops below 10^{15} cm^{-2}, where it can be photodissociated effectively.

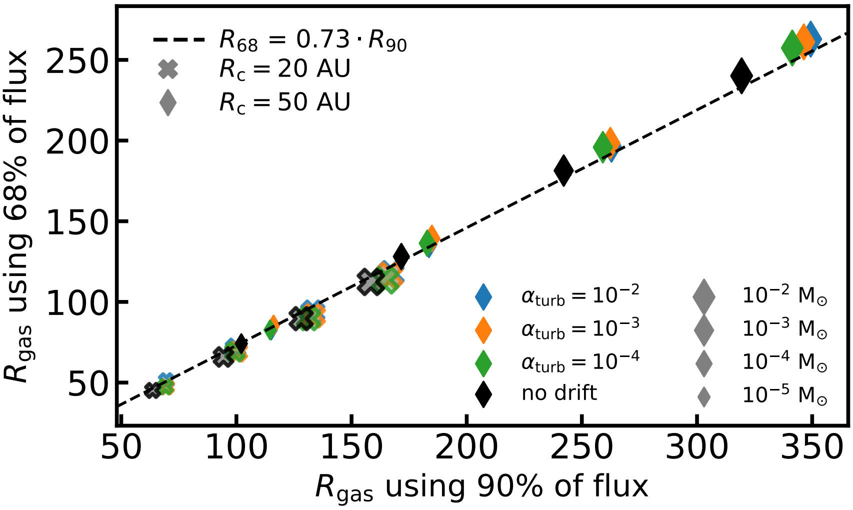

Figure 2.3: Comparison between gas outer radii calculated using 90% of the flux and 68% of the flux. Dashed line shows the expected relation between these two observational outer radii based on Equation (2.4).

can be found in Appendix 2.D)

$$R_{\mathrm{CO,\ 90\%}} = 0.9^{\frac{1}{2-\beta}} R_{\mathrm{CO\ disk}} = f^{\frac{1}{2-\beta}} R_{\mathrm{CO\ disk}}, \tag{2.4}$$

where f represents a more general case where the gas outer radius is defined using a flux fraction f.

Based on Equation (2.4) the fraction of flux f used to define the gas outer radius should not affect the dependence of $R_{\mathrm{f,gas}}$ on disk parameters such as M_{gas} or R_{c}. To highlight this point, Figure 2.3 compares gas outer radii defined using 90% and 68% of the total flux. Independent of M_{gas}, R_{c} , and α_{turb} the models follow a tight linear relation that matches the expected relation $R_{\mathrm{68,gas}} = 0.73 R_{\mathrm{CO,\ 90\%}}$, based on Equation (2.4).

Summarizing, the observational gas outer radius is directly related to the point of the disk where the CO column density reaches $N_{\mathrm{CO}} = 10^{15}$ cm^{-2}. This relation is independent of the flux fraction used to define the gas outer radius.

2.3.3 Effect of dust evolution on $R_{\mathrm{90,dust}}$ and $R_{\mathrm{CO,\ 90\%}}$

In the previous section dust evolution was shown to change the continuum intensity profile and the dust outer radius. Dust evolution also affects the CO chemistry (Facchini et al. 2017) and could therefore change the gas outer radius.

Figure 2.4 shows gas and dust outer radii as function of the turbulent α for different points in our (M_{disk}-R_{c}) parameter space. Compared to the no drift model, the dust radii of the dust evolution models are smaller up to a factor 1.5. No obvious trend of R_{dust} with α_{turb} is found. The dust outer radius scales with α_{visc} at high disk mass of 10^{-2} M$_\odot$, corresponding to a disk dust mass of 10^{-4} M$_\odot$. The trend is negative, with a higher α corresponding to a smaller $R_{\mathrm{90,dust}}$. At high α fragmentation sets the maximum grain size throughout the disk, preventing millimeter grains from forming.

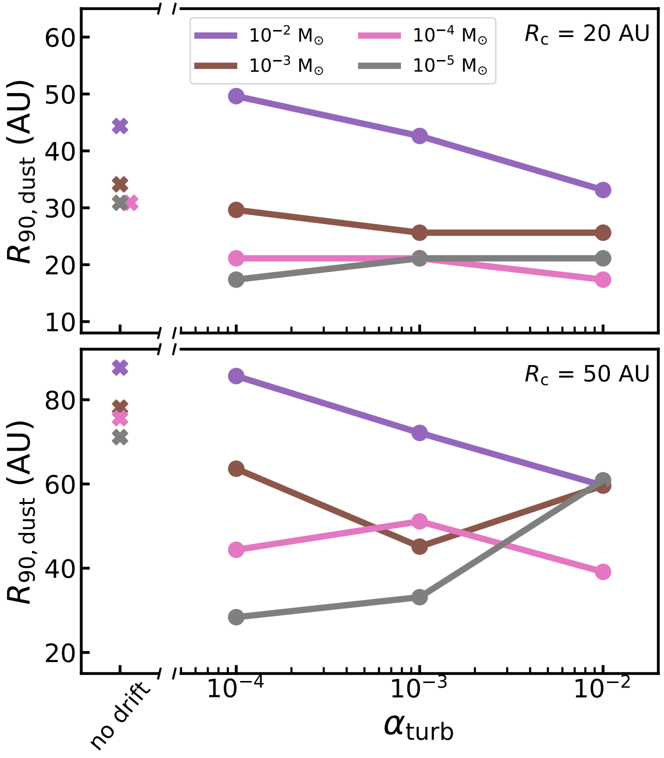

Figure 2.4: For models with different (M_{disk}, R_{c}), $R_{90,\mathrm{dust}}$ as function of α_{turb} . Top panel shows models with $R_{\mathrm{c}} = 20$ AU. Bottom panel shows models with $R_{\mathrm{c}} = 50$ AU. The crosses show the $R_{90,\mathrm{dust}}$ for no drift model.

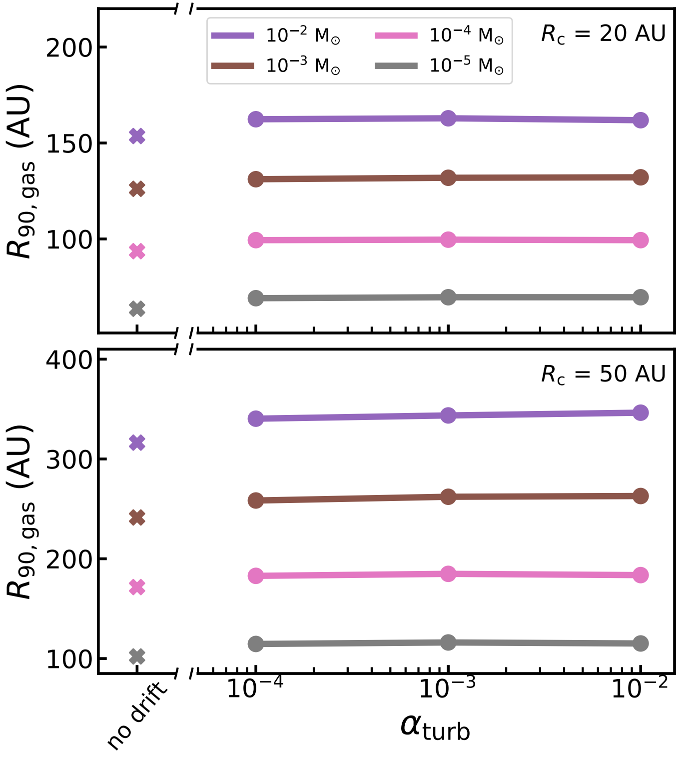

Figure 2.5: For models with different (M_{disk}, R_{c}), $R_{90,\mathrm{gas}}$ as function of α_{turb} . Top panel shows models with $R_{\mathrm{c}} = 20$ AU. Bottom panel shows models with $R_{\mathrm{c}} = 50$ AU. The crosses show the $R_{90,\mathrm{gas}}$ for the no drift model.

For lower disk masses the behavior of $R_{90,\mathrm{dust}}$ as function of α_{turb} depends on the characteristic size of the disk R_{c}. The intensity profile of disks with $R_{\mathrm{c}} = 20$ AU is dominated by an inner core that is largely unaffected by α_{visc}. As a result $R_{90,\mathrm{dust}}$ remains approximately constant with α_{visc}. For the larger disks ($R_{\mathrm{c}} = 50$ AU) $R_{90,\mathrm{dust}}$ varies with α_{visc}, but the trends are not monotonic for $M_{\mathrm{disk}} = 10^{-3} - 10^{-4}$ $\mathrm{M}_{\odot}$. For $M_{\mathrm{disk}} = 10^{-5}$ the trend is monotonic again, but now $R_{90,\mathrm{dust}}$ is larger for higher α_{visc}.

The effect of dust evolution on the gas outer radius is shown in Figure 2.5. There are no noticeable changes in $R_{\mathrm{CO},\ 90\%}$ when α_{turb} is varied, indicating that $R_{\mathrm{CO},\ 90\%}$ is unaffected by dust evolution. The gas radii of the dust evolution models are larger than the gas radius of the no drift model.

A possible explanation is a difference in the amount of small grains in the outer disk. In the no drift model a fixed fraction of the dust is in small grains. In the dust evolution model the maximum grain size decreases with radius, representing the larger grains drifting inwards. However in our model framework no mass is actually transferred inwards. As a result the amount of small grains in the outer disk is enhanced. These small grains can help shield the CO against photodissociation, allowing it to exist further out in the disk.

2.3.4 Effect of disk mass on $R_{\mathrm{CO},\ 90\%}$ and $R_{90,\mathrm{dust}}$

The observed gas-dust size difference is also affected by the difference in optical depth. The value $R_{90,\mathrm{dust}}$ is calculated from the millimeter continuum emission, that is mostly optically thin, whereas $R_{\mathrm{CO},\ 90\%}$ is calculated from the optically thick ^{12}CO line emission. As optical depth is directly related to column density, the mass of the disk is also expected influence the observed outer radii.

Figure 2.6 shows $R_{90,\mathrm{gas}}$ as function of M_{disk} for our standard model and models with different α_{visc}. The gas outer radii increase linearly with $\log_{10} M_{\mathrm{disk}}$, from $\sim 3 \times R_{\mathrm{c}}$ at $M_{\mathrm{disk}} = 10^{-5}$ $\mathrm{M}_{\odot}$ up to $\sim 8 \times R_{\mathrm{c}}$ at $M_{\mathrm{disk}} = 10^{-2}$ $\mathrm{M}_{\odot}$.

This relation can be understood qualitatively using the results from Section 2.3.2. Based on Equation (2.4) and Figure 2.6, we can write $R_{\mathrm{CO\ disk}} \sim R_{\mathrm{CO},\ 90\%} \propto \log_{10} M_{\mathrm{disk}}$. In the outer disk the column density scales as $N_{\mathrm{CO}} \sim \Sigma_{\mathrm{gas}} x_{\mathrm{CO}} \sim M_{\mathrm{disk}} \cdot x_{\mathrm{CO}} \cdot \exp\left(-R/R_{\mathrm{c}}\right)$. At a radius $R_{\mathrm{CO\ disk}}$ the CO column density is known and the equation can be inverted to obtain $R_{\mathrm{CO\ disk}} \sim R_{\mathrm{c}} \log\left(M_{\mathrm{disk}} \cdot x_{\mathrm{CO}}\right)$, similar to the relation found in Figure 2.6.

It should be pointed that the dependence of $R_{\mathrm{CO},\ 90\%}$ on M_{disk} is set by the shape of the density profile in the outer disk. In our models the density profile in the outer parts is described by an exponential, giving rise to the logarithmic dependence of $R_{\mathrm{CO},\ 90\%}$ on M_{disk}. If some process is affecting the density structure of the outer disk (e.g. due to tidal truncation or external photoevaporation; Facchini et al. 2016; Winter et al. 2018), the relation $R_{\mathrm{CO},\ 90\%} \propto \log M_{\mathrm{disk}}$ no longer holds. Instead the relation between $R_{\mathrm{CO},\ 90\%}$ and M_{disk} is set by the altered shape of the density structure in the region where $N_{\mathrm{CO}} = 10^{15}$ cm^{-2}.

The dust radii, shown as solid lines in Figure 2.6, also increase with disk mass, but to a much smaller degree than the gas radii. Over the mass range considered in this work the dust radii increase by up to $1.5 - 2 \times R_{\mathrm{c}}$. This is likely due to the millimeter continuum emission remaining optically thin throughout most of the disk. As the disk mass increases, the total continuum flux also increases, but the shape of the intensity profile and $R_{90,\mathrm{dust}}$ derived from that profile remains largely unchanged. The small

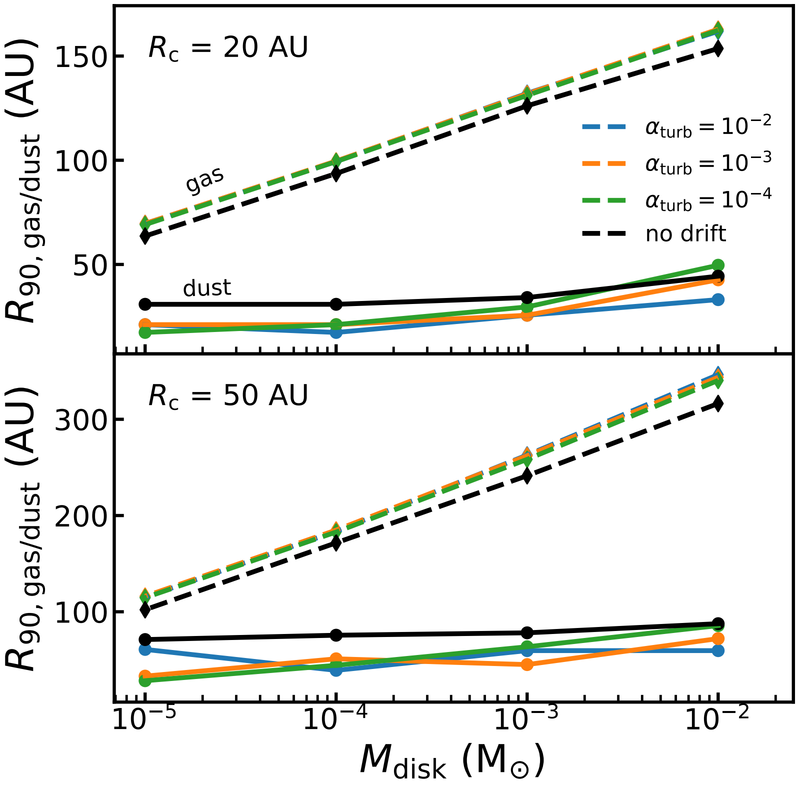

Figure 2.6: Disk outer radii vs. disk mass. Top panel shows models with $R_c = 20$ AU. Bottom panel shows models with $R_c = 50$ AU. Solid lines show dust outer radii. Dashed lines show gas outer radii.

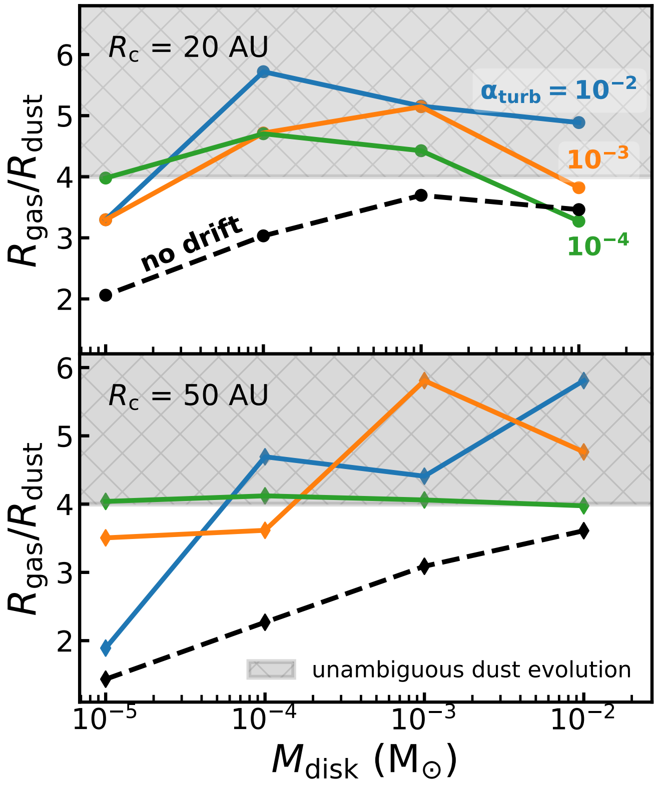

Figure 2.7: Disk mass vs. $R_{90,\rm gas}/R_{90,\rm dust}$. Top panel shows models with $R_c = 20$ AU. Bottom panel shows models with $R_c = 50$ AU. Dashed lines show the no drift model, without dust evolution.

increase with dust mass can be attributed to a core of optically thick emission in the inner part of the disk. For higher disk masses this core increases in size which moves the 90% flux contour outwards. Overall we find that the effect of disk mass and optical depth on $R_{\rm CO,\ 90\%}$ is much larger than the effect of dust evolution on $R_{90,\rm dust}$.

2.3.5 Dust evolution tracer: $R_{90,\rm gas}/R_{90,\rm dust}$

Combining the effects of dust evolution and disk mass (cf. Sections 2.3.3 and 2.3.4), we now look at the gas-dust size dichotomy, quantified by $R_{90,\rm gas}/R_{90,\rm dust}$. Figure 2.7 shows $R_{90,\rm gas}/R_{90,\rm dust}$ as function of $M_{\rm disk}$. The fiducial no drift models show that $R_{90,\rm gas}/R_{90,\rm dust} = 1.5 - 3.5$, with a positive trend between $R_{90,\rm gas}/R_{90,\rm dust}$ and $M_{\rm disk}$. Comparing to Figure 2.6 this trend is a direct result of $R_{\rm CO,\ 90\%}$ increasing with $M_{\rm disk}$.

The dust evolution models all lie above the no drift models, indicating that for a given disk mass a model that includes radial drift and grain growth has a larger $R_{90,\rm gas}/R_{90,\rm dust}$ than a model that only includes the effects of optical depth.

For the dust evolution models with $R_{\rm c} = 50$ AU, an overall positive trend of $R_{90,\rm gas}/R_{90,\rm dust}$ with disk mass is found, but the trend is not monotonic and depends on $\alpha_{\rm visc}$. For the smaller $R_{\rm c} = 20$ AU models the trend becomes negative towards higher disk masses.

From the trends in Figure 2.7 it is clear that the size dichotomy $R_{90,\rm gas}/R_{90,\rm dust}$ can be used to identify dust evolution if the ratio is high enough ($R_{90,\rm gas}/R_{90,\rm dust} \geq 4$). Observationally, these cases are rare (see e.g. Facchini et al. 2019). For the majority of disks, a lower ratio is observed (cf. Ansdell et al. 2018). To identify dust evolution in these disks requires modeling of their ^{12}CO and dust emission, taking into account their total CO and dust content. The results also show that a direct determination of $\alpha_{\rm turb}$ from $R_{90,\rm gas}/R_{90,\rm dust}$ is not possible.

2.3.6 Observational factors affecting $R_{90,\rm gas}/R_{90,\rm dust}$

Effect of beam size

Observational factors such as the size of the beam and the background noise level are also able to influence the gas-dust size dichotomy. Convolution with the beam smears out the intensity profile. For a centrally peaked intensity profile this moves R_{90} outwards. We use the full width at half maximum of the beam (FWHM$_{\rm beam}$) as a measure of the beam size. For a beam size much larger than the observed disk the intrinsic differences between the gas and dust emission are washed out and $R_{90,\rm gas}/R_{90,\rm dust}$ is expected to approach unity.

Figure 2.8 shows the effect of beam size on $R_{90,\rm gas}/R_{90,\rm dust}$ for an example disk with $M_{\rm disk} = 10^{-4}$ M$_\odot$ and $R_{\rm c} = 50$ AU. Similar panels for the other models are shown in Figure 2.23. The quantity $R_{90,\rm gas}/R_{90,\rm dust}$ decreases with beam size, approaching unity when the beam size becomes $\sim 3 \times R_{\rm c}$. At a beam size$\sim 1 \times R_{\rm c}$, $R_{90,\rm gas}/R_{90,\rm dust}$ has dropped below 4 and dust evolution can no longer be unambiguously be identified using only $R_{90,\rm gas}/R_{90,\rm dust}$ (see Section 2.3.5). However, if the uncertainties on $R_{90,\rm gas}/R_{90,\rm dust}$ are sufficiently small and the total CO content of the disk is known, dust evolution can still be inferred from observations with FWHM$_{\rm beam} \leq 2R_{\rm c}$.

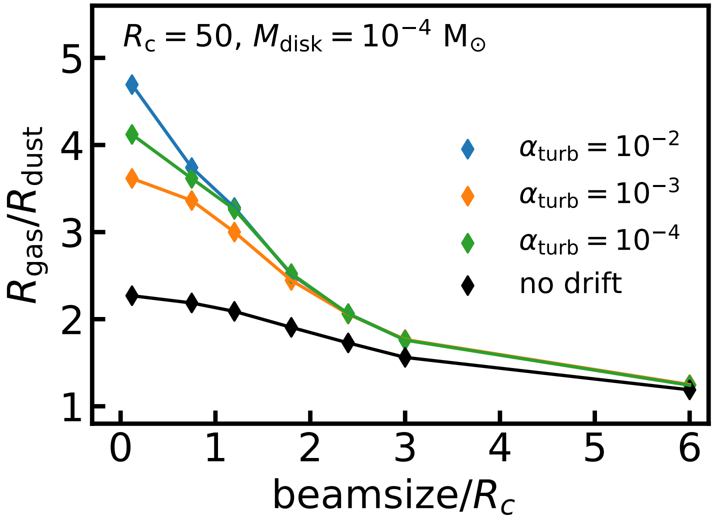

Figure 2.8: Beam size vs. $R_{90,\mathrm{gas}}/R_{90,\mathrm{dust}}$. The effect of the beam scales with its relative size compared to the diameter of the disk. To highlight this, the beam size is expressed in terms of the characteristic size of the disk. Similar figures for various M_{disk} and R_{c} are shown in Figure 2.23

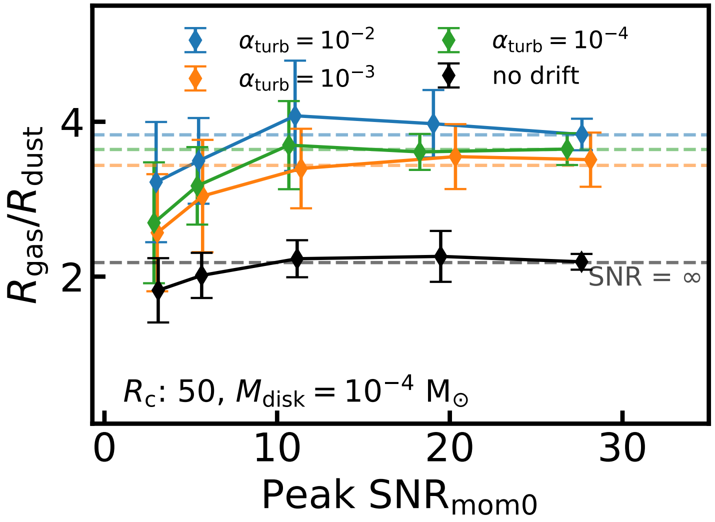

Figure 2.9: Peak S/N in the moment 0 map of the ^{12}CO emission vs. $R_{90,\mathrm{gas}}/R_{90,\mathrm{dust}}$. Similar figures for various M_{disk} and R_{c} are shown in Figure 2.24

Effect of noise level

Noise has two ways in which it can interact with the observational outer radius. Noise affects the shape of the curve of growth, thus changing the radius that encloses 90% of the total flux. In addition, the noise in the image sets the uncertainty on the total flux, which propagates through into the errors on R_{90}. For the gas-dust size difference, the noise on the gas emission is dominant. This is due to a difference in bandwidth: the gas emission is narrow in frequency, typically ~ 0.5km s^{-1}, whereas the continuum emission uses the full bandwidth of the observations. For example, a typical ALMA band 6 observation that has three continuum spectral windows (with a total bandwidth $\Delta\nu_{\rm bandwidth} \simeq 2$ GHz) and 1 line spectral window centered on the ^{12}CO line (with line width $\Delta\nu_{\rm line} \simeq 0.384$ MHz), the noise on the continuum is a factor $\sqrt{\Delta\nu_{\rm bandwidth}/\Delta\nu_{\rm line}} \sim 50$ lower compared to the line emission.

To simulate the effect of noise, empty channels taken from ALMA observations are added to the model image cube after convolution. The size of the convolution beam used for the model was matched to that of observations of Lupus disks (0".25; Ansdell et al. 2018). The rms of the noise was scaled to obtain the requested peak S/N in the moment 0 map for the models.

The results are shown in Figure 2.9 for the same example disk ($M_{\rm disk} = 10^{-4}$ M$_\odot$, $R_{\rm c} =$ 50 AU). The other disks are shown in Figure 2.24. The average $R_{\rm 90,gas}/R_{\rm 90,dust}$ measured at low S/N$_{\rm mom0}$ is smaller than the noiseless case. As the S/N$_{\rm mom0}$ increases it converges to the value measured in the absence of noise. A peak S/N$_{\rm mom0}$ ~ 10 is sufficient to recover the $R_{\rm 90,gas}/R_{\rm 90,dust}$ of the noiseless case. The uncertainties on $R_{\rm 90,gas}/R_{\rm 90,dust}$ are reduced when the peak S/N$_{\rm mom0}$ increases, down to $\leq 10\%$ at a peak S/N$_{\rm mom0}$ of ~ 30. We note however that the noiseless $R_{\rm 90,gas}/R_{\rm 90,dust}$ is recovered within the error bars of the measured $R_{\rm 90,gas}/R_{\rm 90,dust}$ already at peak S/N$_{\rm mom0}$ ~ 5.

Summarizing the effect of the observational factors, two recommendations for future observations can be made. Firstly, differentiating between only optical depth and dust evolution in addition to optical depth requires FWHM$_{\rm beam}$ $\leq 1 \times R_{\rm c}$. For a disk with $R_{\rm c} = 20$ at 150 pc, this means a beam size of $0\farcs14 = 20$ AU. Secondly, to accurately measure the gas-dust size difference requires a peak S/N ≥ 10 in the ^{12}CO moment zero. We note that an increased sensitivity will improve the uncertainty on the measured $R_{\rm 90,gas}/R_{\rm 90,dust}$ and can thus better distinguish cases where $R_{\rm 90,gas}/R_{\rm 90,dust}$ is unambiguously > 4.

2.4 Discussion

2.4.1 CO underabundance and $R_{\rm CO,\ 90\%}$

In our models we have assumed standard interstellar medium (ISM) abundances for carbon and oxygen, resulting in an overall CO abundance of $x_{\rm CO} \sim 10^{-4}$. However, recent observations have found CO to be underabundant by a factor $10 - 100$ with respect to the ISM in several disks (e.g. Favre et al. 2013; Kama et al. 2016b; Cleeves et al. 2016; McClure et al. 2016). The low CO-based disk gas masses found by recent surveys suggest that CO could be underabundant in most disks (see e.g. Ansdell et al. 2016; Miotello et al. 2017; Long et al. 2017). As shown in Section 2.3.4 $R_{\rm CO,\ 90\%}$ is directly related to the CO content of the disk. The observed underabundance of CO in disks causes them to have a smaller observed gas disk size compared to our models.

To quantify the effect of CO underabundance on the measured $R_{\rm CO,\ 90\%}$ the models with $M_{\rm disk} = 10^{-2}$ M$_\odot$ were rerun, but now the total amount of carbon and oxygen in the disk is reduced by a factor $\delta_{C,O} = 0.1 - 0.01$, mimicking the observed underabundance of CO. Figure 2.10 shows that $R_{\rm CO,\ 90\%}$ decreases linearly with $\log_{10}\delta_{C,O}$, similar to the $R_{\rm CO,\ 90\%} \propto \log_{10} M_{\rm disk}$ found earlier. This again highlights the importance of total CO content of the disk. As an example, let us consider two disks with the same total CO content. The first disk has a higher disk mass but is underabundant in CO ($M_{\rm disk}$, $\delta_{\rm C,O}$) = (10^{-2} M$_\odot$, 0.1). The second disk is less massive but has standard ISM abundances ($M_{\rm disk}$, $\delta_{\rm C,O}$) = (10^{-3} M$_\odot$, 1). For both disks we obtain the same $R_{\rm CO,\ 90\%}$, indicating that the gas outer radius depends on the total CO content of the disk.

A lower $R_{\rm CO,\ 90\%}$ also results in a lower $R_{\rm 90,gas}/R_{\rm 90,dust}$. Figure 2.11 shows $R_{\rm 90,gas}/R_{\rm 90,dust}$ as function of CO underabundance $\delta_{\rm C,O}$. In the case of no CO underabundance ($\delta_{C,O} = 1$), $R_{\rm 90,gas}/R_{\rm 90,dust} = 2.5 - 5.5$. By decreasing the amount of CO in the disk by a factor of 100, the gas disk size decreases leading to $R_{\rm 90,gas}/R_{\rm 90,dust} = 1.5$ for the no drift model and $R_{\rm 90,gas}/R_{\rm 90,dust} = 2 - 3.5$ for the dust evolution models. We note that these values are for a disk with $M_{\rm disk} = 10^{-2}$ M$_\odot$. For a less massive disk that is also underabundant in CO $R_{\rm 90,gas}/R_{\rm 90,dust}$ is lower (cf. Section 2.3.4).

For a sample of 22 disks Ansdell et al. (2018) measured $R_{\rm CO,\ 90\%}$ from the ^{12}CO 2-1 emission and $R_{\rm 90,dust}$ from the 1.3 mm continuum emission and found $R_{\rm 90,gas}/R_{\rm 90,dust} = 1.5 - 3.5$. The sample is skewed towards the most massive disks in their sample, where $M_{\rm dust} = 0.5 - 2.7 \times 10^{-4}$ M$_\odot$. This makes these massive disks comparable in dust content to the models discussed in this section ($M_{\rm dust} = 10^{-4}$ M$_\odot$). A simple, first order comparison between the models and the observations can therefore be made. CO underabundances of the disks in the Lupus sample are calculated by assuming a gas-to-dust mass ratio of 100 and comparing that to the ratio of $M_{\rm CO\ based}/M_{\rm dust}$, where $M_{\rm CO\ based}$ is the CO-based gas mass estimate from Miotello et al. (2017). For example, a disk with $M_{\rm CO\ based} = 10^{-3}$ M$_\odot$ and $M_{\rm dust} = 10^{-4}$ M$_\odot$ is interpreted as having a CO underabundance of $\delta_{\rm C,O} = \frac{M_{\rm CO\ based}}{M_{\rm dust}}/100 = 0.1$.

The calculated CO abundances show that several disks in the sample have $\delta_{C,O} \leq 10^{-2}$. For the same CO underabundance, the no drift model has $R_{\rm 90,gas}/R_{\rm 90,dust} = 1.5 - 2.0$, which is at the low end or below the observed range, suggesting that a least for some of the sources in the sample explaining the observed $R_{\rm 90,gas}/R_{\rm 90,dust}$ requires dust evolution. Modeling of the individual sources is required to provide a definitive identification of dust evolution, which is beyond the scope of this work (but see Trapman et al. 2019).

2.4.2 Effect of the surface density slope on outer radii

The surface density is governed by three parameters: $R_{\rm c}$, $M_{\rm disk}$, and γ (cf. Eq. 2.1). The slope γ sets how the material is distributed in the disk and therefore affects the outer radius of the disk. In addition, the physical processes involved in dust evolution are also affected by γ. The slope of the gas surface density is not well constrained, having been observational constrained only for a few disks (e.g. Cleeves et al. 2016; Williams & McPartland 2016; Zhang et al. 2017; Miotello et al. 2018). Most of these studies find a value of $\gamma \sim 1.0$. In this section we investigate how much $R_{\rm 90,gas}/R_{\rm 90,dust}$ depends on γ. Figure 2.12 shows $R_{\rm 90,gas}/R_{\rm 90,dust}$ versus $\gamma =$

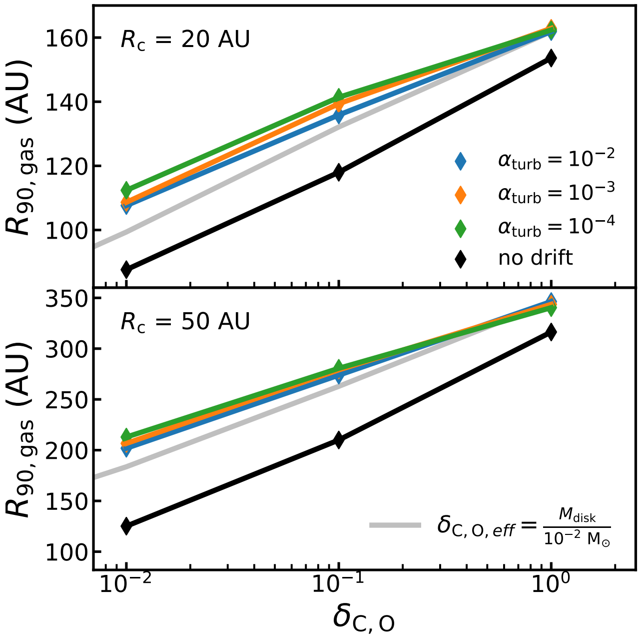

Figure 2.10: Disk outer radii vs. CO underabundance. For comparison, the outer radii for the no drift model is shown in grey. Top panel shows models with $R_c = 20$ AU. Bottom panel shows models with $R_c = 50$ AU.

Figure 2.11: CO underabundance vs. $R_{90,\mathrm{gas}}/R_{90,\mathrm{dust}}$. Middle panel shows models with $R_c = 20$ AU. Bottom panel shows models with $R_c = 50$ AU. The observed range of $R_{90,\mathrm{gas}}/R_{90,\mathrm{dust}}$ from Ansdell et al. (2018) is shown in gray. Top panel shows a histogram of the gas-to-dust ratios measured in Lupus (Ansdell et al. 2016; Miotello et al. 2017). These have been converted into an effective CO underabundance using $\delta_{\mathrm{C,O,eff}} = \Delta_{\mathrm{gd}}/100$, where Δ_{gd} is the gas-to-dust mass ratio.

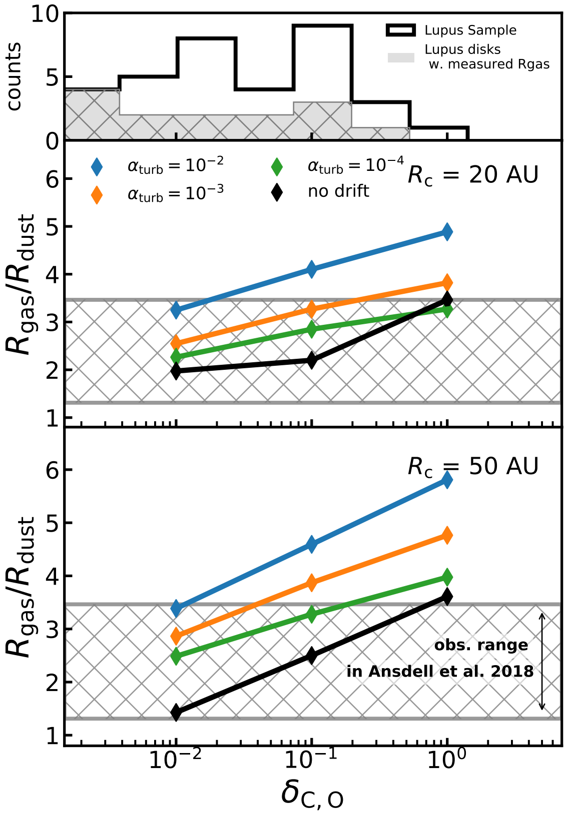

$[0.5, 1.0, 1.5]$ for a set of low mass and high mass models. For low mass disks ($M_{\rm disk} = 10^{-5}$ M$_\odot$), $R_{90,{\rm gas}}/R_{90,{\rm dust}}$ increases drastically when γ is increased from 1.0 to 1.5 and has values of $R_{90,{\rm gas}}/R_{90,{\rm dust}} \simeq 24$ for models with dust evolution.

For the disks with dust evolution and $\gamma = 1.5$, millimeter-sized grains have been removed from the disk except for the inner few AU. As a result, the continuum emission is concentrated in this inner region and a very small dust outer radius is inferred. For the no drift model the dust radius is not similarly affected and the gas-dust size difference only increases to $R_{90,{\rm gas}}/R_{90,{\rm dust}} = 3.7$.

Increasing γ for the high mass disk does not have a significant effect on $R_{90,{\rm gas}}/R_{90,{\rm dust}}$. For the high mass disk the trends are similar for the no drift model and the dust evolution models. Here dust evolution is not significantly affected by the change in γ. For both low and high mass disks, decreasing γ from 1.0 to 0.5 results in a $R_{90,{\rm gas}}/R_{90,{\rm dust}}$ that is lower by a factor ~ 2.

2.4.3 Match of observed R$_{\rm out}$ to physical size of the disk

In this work we have quantified the radial extent of the disk using R_{90}, a flux based measure of the size of the disk. For this radius to be the outer edge of the disk in a physical sense, we could require that it encloses most (e.g. $\geq 90\%$) of the total mass of the disk.

In the cumulative intensity method used to define $R_{\rm CO,\ 90\%}$ and $R_{90,{\rm dust}}$, a free parameter is the fraction of total flux f used (cf. Eq. 2.3). In this work the outer radius is set at 90% of the total flux under the assumption that this radius encloses most of the disk. We investigate the requirement on f if we want the outer radius to enclose $\geq 90\%$ of the mass.

Figure 2.13 shows, for a given f used to compute $R_{90,{\rm gas}}$ and $R_{90,{\rm dust}}$, what fraction of the total disk mass is enclosed within this outer radius. Similar figures for the other disks in the model grid are shown in Appendix 2.I.

For the dust emission, show in the top panel of Figure 2.13, the fraction of enclosed disk mass ($f_{\rm mass}$) correlates with the fraction of total flux ($f_{\rm flux}$) used to define the outer radius. The relation between $f_{\rm mass}$ and $f_{\rm flux}$ is roughly linear, however the exact trend depends on $\alpha_{\rm visc}$, $M_{\rm disk}$, and $R_{\rm c}$. Using a flux fraction of $f_{\rm flux} = 0.9$, between 75% and 90% of the total mass is enclosed with the exact fraction depending on $\alpha_{\rm visc}$. At $f_{\rm flux} = 0.68$ this has dropped to between 60% and 84% of the total mass.

The bottom panel of Figure 2.13 shows that for the ^{12}CO emission, any gas outer radius $R_{90,{\rm gas}}$ defined using a fraction of total flux $f_{\rm flux} > 60\%$ encloses almost all ($> 98\%$) of the total disk mass and would thus meet our criterion of a physical outer radius (i.e. enclosing $\geq 90\%$ of $M_{\rm disk}$). According to the definition of Eq. (2.3), these observational outer radii are not the same size. For example, a radius enclosing 90% of the flux has to be larger than a radius enclosing 75% of the flux. These observational outer radii are all related through Equation (2.4) to the same physical point in the disk, where the CO column density equals 10^{15} cm^{-2} (cf. Section 2.3.2).

Summarizing, the fraction of mass enclosed by $R_{\rm dust}$ scales roughly linearly with the fraction of continuum flux used to define $R_{\rm dust}$. To have the dust radius enclose most of the disk mass, the outer radius should be defined using a high fraction ($90 - 95\%$) of the total flux. For the gas, any radius enclosing $> 60\%$ of the flux contains most of the mass.

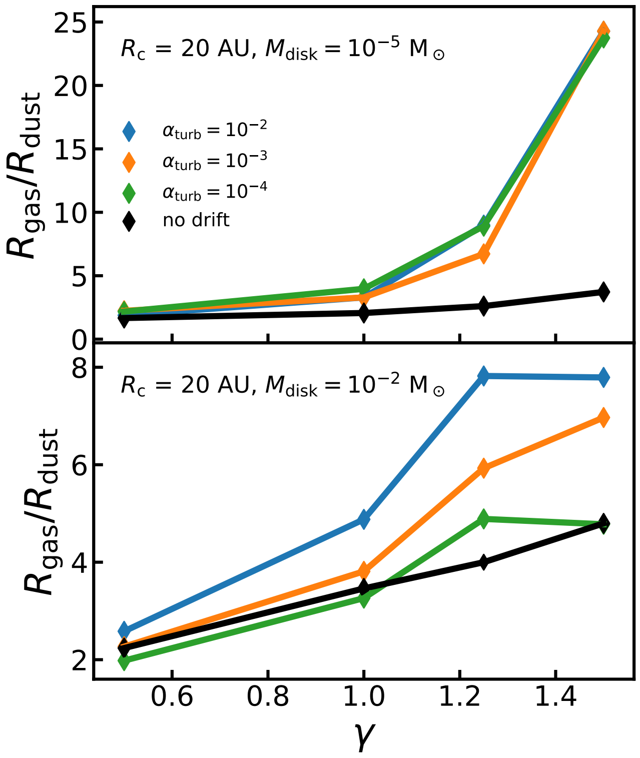

Figure 2.12: $R_{90,\mathrm{gas}}/R_{90,\mathrm{dust}}$ as function of the slope of the gas surface density. Top panel shows models with $M_{\mathrm{disk}} = 10^{-5}$ M$_\odot$. Bottom panel shows models with $M_{\mathrm{disk}} = 10^{-2}$ M$_\odot$.

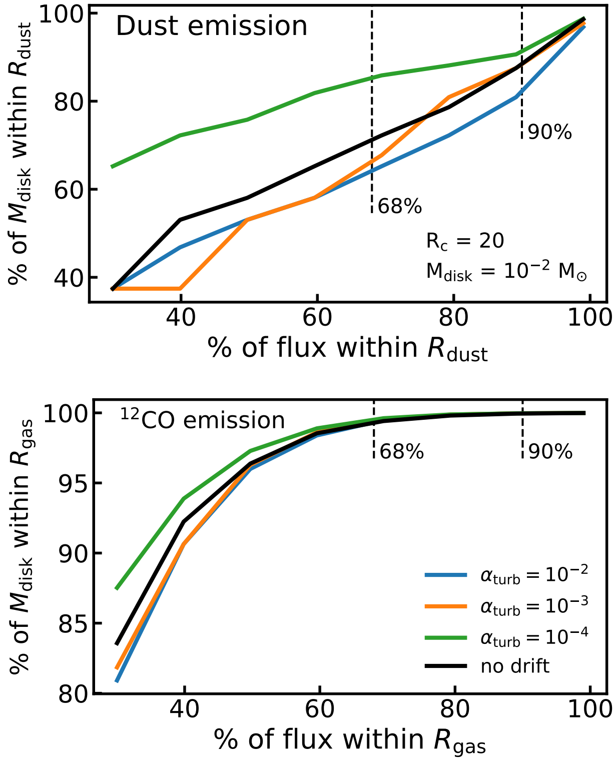

Figure 2.13: Fraction of flux f used to calculate R_{dust} and $R_{90,\mathrm{gas}}$ compared to the fraction of M_{disk} within R_{dust} and $R_{90,\mathrm{gas}}$. Top panel shows the dust emission and the bottom panel shows the gas emission.

2.5 Conclusions

The gas in protoplanetary disks is found to be universally more extended than the dust. This effect can result from grain growth and subsequent inward drift of millimeter-sized grains. However, the difference in line optical depth between the optically thick ^{12}CO emission of the gas and the optically thin continuum emission of the dust also produces a gas-dust size dichotomy. In this work the thermochemical code DALI (Bruderer et al. 2012; Bruderer 2013), extended to include dust evolution (Facchini et al. 2017), is used to run a grid of models. Using these models, the impact of dust evolution, optical depth, and disk structure parameters on the observed gas-dust size difference are investigated. Our main conclusions can be summarized as follows:

- Including dust evolution leads to smaller observationally derived dust radii and larger gas radii. Dust evolution, as quantified by $\alpha_{\rm visc}$, has a complex effect on the dust radius, which also depends on the disk mass and the characteristic radius. The gas outer radius is unaffected by changes in $\alpha_{\rm visc}$.

- The gas outer radius $R_{\rm CO,\ 90\%}$ is directly related to the radius at which the CO column density drops below 10^{15} cm^{-2} where CO becomes photodissociated. The value $R_{\rm CO,\ 90\%}$ scales with the product $M_{\rm disk} \cdot x_{\rm CO}$, the total CO content of the disk; $R_{\rm gas}$ is directly related to the radius where ^{12}CO no longer is able to self-shield.

- The quantity $R_{\rm 90,gas}/R_{\rm 90,dust}$ increases with the total CO content and is higher for disks that include dust evolution. Disks with $R_{\rm 90,gas}/R_{\rm 90,dust} > 4$ are difficult to explain without dust evolution. For $R_{\rm 90,gas}/R_{\rm 90,dust} < 4$, deducing whether or not a disk is affected by dust evolution from the size ratio requires a measure of the total CO content. However, constraining $\alpha_{\rm turb}$ using $R_{\rm 90,gas}/R_{\rm 90,dust}$ is not possible.

- Increasing the beam size and lowering the peak S/N of the ^{12}CO moment 0 map both decrease the measured $R_{\rm 90,gas}/R_{\rm 90,dust}$. To minimize the effect of these observational factors requires $\text{FWHM}_{\rm beam} \leq 1 \times R_{\rm c}$ and $\text{S/N}_{\rm peak,mom0} > 10$.

- $R_{\rm 90,gas}/R_{\rm 90,dust}$ increases with the slope of the surface density γ. In low mass disks with high γ, dust evolution removes almost all grains from the disk, resulting in large gas-dust size differences ($R_{\rm 90,gas}/R_{\rm 90,dust} \sim 24$).

- To have the dust radius enclose most of the disk mass, the outer radius should be defined using a high fraction ($90 - 95\%$) of the total flux. For the gas, any radius enclosing $> 60\%$ of the flux contains most of the mass.

The gas-dust size dichotomy is predominantly set by the structure and CO gas content of the disk, which can produce size differences up to $R_{\rm 90,gas}/R_{\rm 90,dust} \sim 4$. Disks with $R_{\rm 90,gas}/R_{\rm 90,dust} > 4$ can be directly identified as having undergone dust evolution, provided the gas and dust radii were measured with $\text{FWHM}_{\rm beam} \leq 1 \times R_{\rm c}$. However, these disks are rare in current observations. For disks with a smaller gas-dust size difference, modeling of the disk structure including the total CO gas content is required to identify radial drift and grain growth.

Appendix

2.A Effect of inclination

In the analysis in this work all disk radii were measured from disks with an inclination of 0 degrees. Inclination increases the optical depth along the line of sight. This can affect the measured size of the disk, especially for the gas, which is determined from optically thick emission (cf. Section 2.2.4).

Figures 2.14 and 2.15 show gas and dust radii measured from images with an inclination of $i = 0, 30, 60$ degrees. For the inclined images, the cumulative flux is instead calculated using elliptical apertures to account for the projection. Between $i = 0°$ and $i = 30°$ there is no noticeable difference in the outer radii. For 60 degrees outer radii have become slightly larger, but even at the most extreme the effect is smaller than a 50% increase. Thus the effect of inclination should only be considered for disks with high inclination ($i > 60°$) when trying to identify dust evolution.

2.B Measuring $R_{\mathrm{CO,\ 90\%}}$ from ^{13}CO 2-1 moment zero maps

In this Appendix, we investigate how the gas outer radius would differ, if instead it had been defined as the radius enclosing 90% of the ^{13}CO 3-2 flux. ^{13}CO is added to the model parametrically, by taking the CO abundances and scaling them with the ^{12}C/^{13}C elemental ratio, assumed to be $^{12}\mathrm{C}/^{13}\mathrm{C} = 77$.

Figure 2.16 shows $R_{\mathrm{CO,\ 90\%}}(^{13}\mathrm{CO})$ and $R_{\mathrm{CO,\ 90\%}}(^{12}\mathrm{CO})$ as function of disk mass. The value $R_{\mathrm{CO,\ 90\%}}(^{13}\mathrm{CO})$ also with disk mass in a similar manner to $R_{\mathrm{CO,\ 90\%}}(^{12}\mathrm{CO})$, i.e. $R_{\mathrm{CO,\ 90\%}}(^{13}\mathrm{CO}) \sim \log_{10} M_{\mathrm{disk}}$. As a result, using the ^{13}CO emission does not change the qualitative results seen in this work.

Figure 2.17 shows the ratio $R_{\mathrm{CO,\ 90\%}}(^{12}\mathrm{CO})/R_{\mathrm{CO,\ 90\%}}(^{13}\mathrm{CO})$ for different disk masses. On average, $R_{\mathrm{CO,\ 90\%}}(^{12}\mathrm{CO})$ is 30-45% larger than $R_{\mathrm{CO,\ 90\%}}(^{13}\mathrm{CO})$ and has variations because α_{visc}, R_{c} , or M_{disk} are small. However we do not consider the effects of isotope-selective photodissociation, which become relevant in the outer part of the disk (cf. Miotello et al. 2014).

2.C Measuring $R_{\mathrm{CO,\ 90\%}}$ from peak intensity maps

The extent of the gas emission is measured from the moment zero map, which is constructed by integrating in spectral image cube over the frequency axis. As a result the gas emission has units [Jy/beam km/s]. This method places extra emphasis on the inner part of the disk, where the Keplerian velocity structure of the gas produces the widest line profiles (in velocity).

Another method would be to measure the gas radius using the peak intensity map, which is the intensity at peak velocity. This map has units identical to the continuum emission ([Jy/beam]). Compared to the moment 0 map more weight is placed in the outer parts of the disk, moving $R_{\mathrm{CO,\ 90\%}}$ outwards. By removing the dependence on the line width the peak intensity map might also be less affected by inclination (cf. Section 2.A).

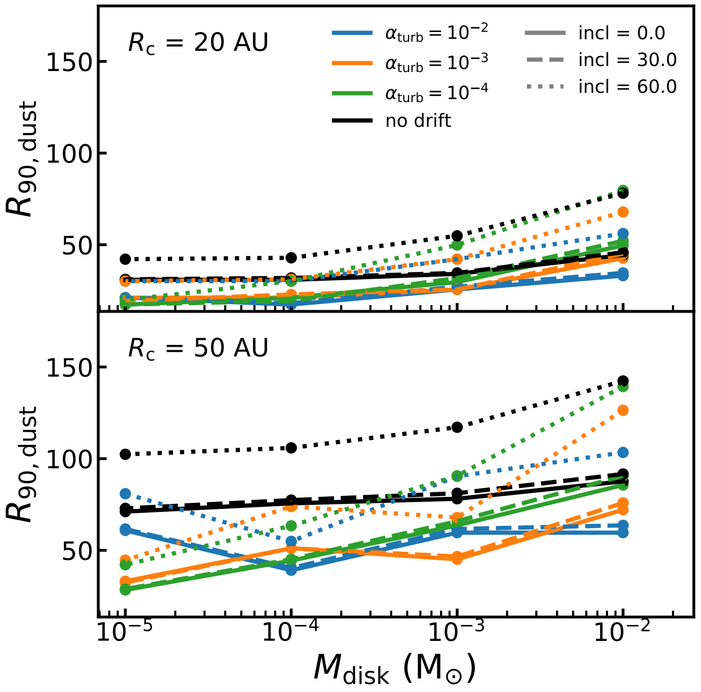

Figure 2.14: Effect of inclination on measuring the dust outer radius. Disks with a R_C = 20 AU and R_C = 50 AU are shown in the top and bottom panel, respectively.

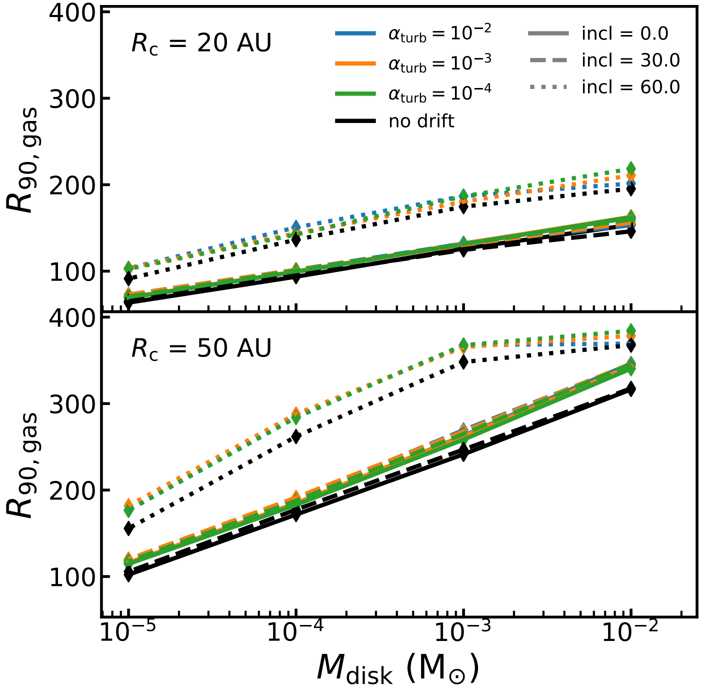

Figure 2.15: Effect of inclination on measuring the gas outer radius. Disks with a R_C = 20 AU and R_C = 50 AU are shown in the top and bottom panel, respectively.

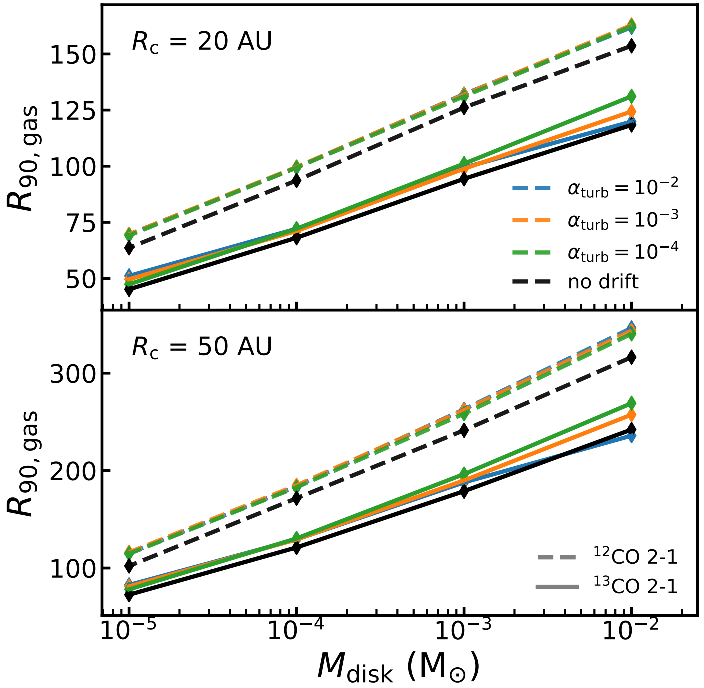

Figure 2.16: Comparison of gas outer radii measured from ^{13}CO 2-1 emission (solid lines) and ^{12}CO 2-1 emission (dashed lines).

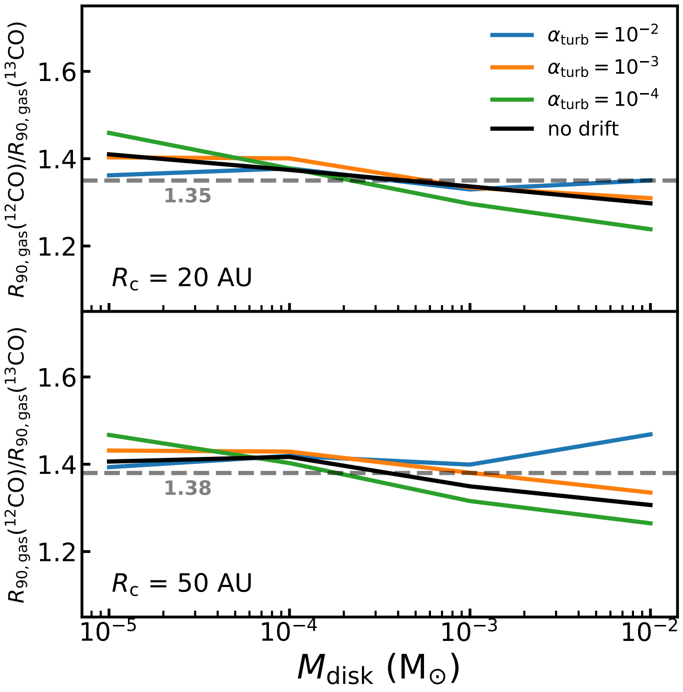

Figure 2.17: Ratio of gas outer radii measured from ^{12}CO 2-1 emission ($R_{CO,\,90\%}(^{12}CO)$) over ^{13}CO 2-1 emission ($R_{CO,\,90\%}(^{13}CO)$). The mean ratio of all models is shown in grey.

Figure 2.18 shows a comparison between gas outer radii derived from the moment 0 map (shown on the left) and the peak intensity map (shown on the right) for three different inclinations. For the inclined disks ($i = 30, 60°$), there is indeed more emission in the outer disk for the peak intensity map. In all cases $R_{\mathrm{CO},\ 90\%}$(peak int.) is larger than the $R_{\mathrm{CO},\ 90\%}$(mom 0).

In Figure 2.19 $R_{\mathrm{CO},\ 90\%}$(peak int.) and $R_{\mathrm{CO},\ 90\%}$(mom 0) are compared as functions of disk mass and inclination. Over the mass range examined we find that $R_{\mathrm{CO},\ 90\%}$(peak int.) $>$ $R_{\mathrm{CO},\ 90\%}$(mom 0). However, apart from this offset, $R_{\mathrm{CO},\ 90\%}$(peak int.) follows the same trend with disk mass as $R_{\mathrm{CO},\ 90\%}$(mom 0) and is also similarly affected by inclination.

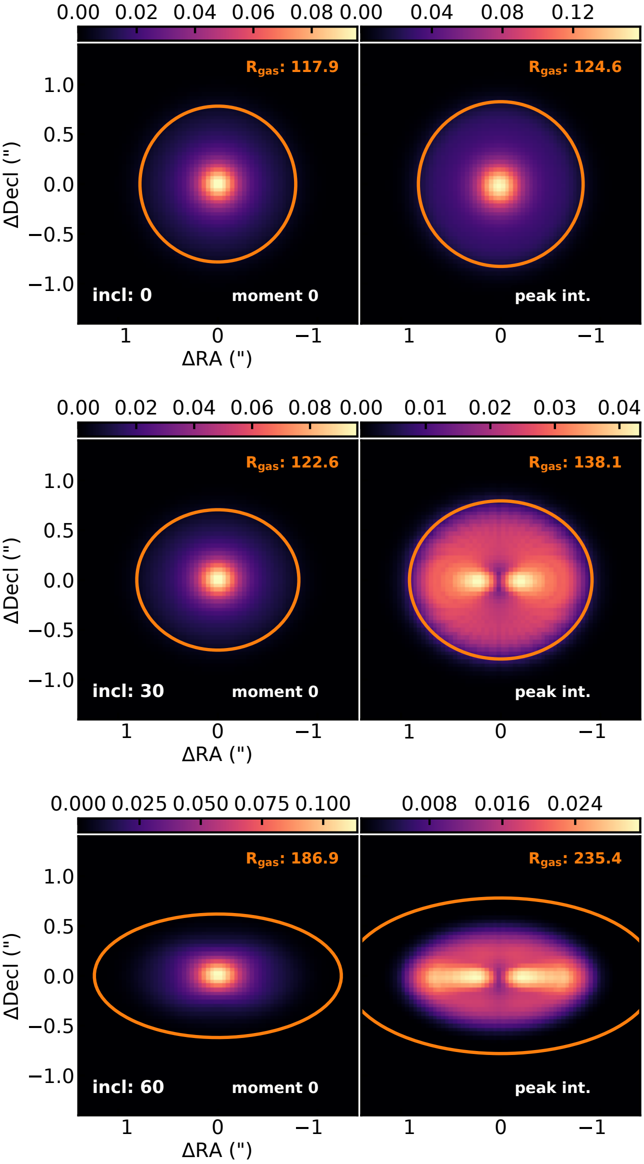

Figure 2.18: Comparison between outer radii derived from ^{12}CO moment 0 map (left) and the peak intensity (moment 8) map (right). The model shown has $M_{\mathrm{disk}} = 10^{-3}$ M$_\odot$, R_c = 50 AU, and α_{visc} = 10^{-4}.

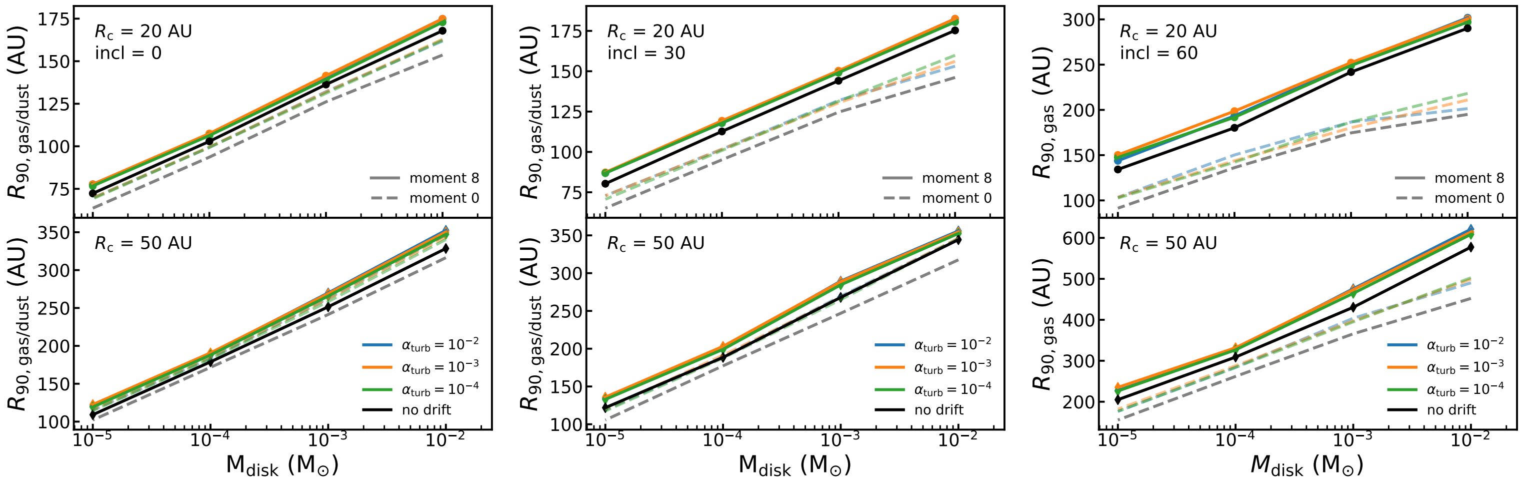

Figure 2.19: Gas radii measured from the peak intensity map vs. disk mass. The top, middle, and bottom figures show disks with inclinations of 0, 30, and 60 degrees, respectively

2.D Deriving a relation between $R_{\mathrm{CO,\ 90\%}}$ and the CO column density

In Section 2.3.2 the ^{12}CO emission profile was found to quickly drop off at a point very close to where the CO column density (N_{CO}) drops below 10^{15} cm^{-2}. Defining $R_{\mathrm{CO\ disk}}$ as the radius where $N_{\mathrm{CO}} = 10^{15}$ cm^{-2}, we can derive an analytical relation between $R_{\mathrm{CO,\ 90\%}}$ and $R_{\mathrm{CO\ disk}}$.

Using equation (2.3), $R_{\mathrm{CO,\ 90\%}}$ is defined as

$$0.9 = \frac{2\pi}{F_{\mathrm{tot}}} \int_0^{R_{\mathrm{CO,\ 90\%}}} I_{\mathrm{CO}}(r') r' \mathrm{d}r' \tag{2.5}$$

$$= \frac{\int_0^{R_{\mathrm{CO,\ 90\%}}} I_{\mathrm{CO}}(r') r' \mathrm{d}r'}{\int_0^{R_{\mathrm{CO\ disk}}} I_{\mathrm{CO}}(r') r' \mathrm{d}r'}. \tag{2.6}$$

In this case we used the fact that $R_{\mathrm{CO\ disk}}$ effectively encloses all of the ^{12}CO flux (cf. Figure 2.2). If we assume that the ^{12}CO emission is optically thick, $I_{\mathrm{CO}}(R) = \frac{2\nu^2}{c^2} k_{\mathrm{B}} T(R)$, the equation can be rewritten

$$0.9 = \frac{\int_0^{R_{\mathrm{CO,\ 90\%}}} T(r') r' \mathrm{d}r'}{\int_0^{R_{\mathrm{CO\ disk}}} T(r') r' \mathrm{d}r'}, \tag{2.7}$$

where T_{gas} is the gas temperature in the CO emitting layer. The temperature profile can often be well described by a power law, $T(R) = T_c (R/R_{\mathrm{c}})^{-\beta}$, which can be substituted in the integrals

$$0.9 = \frac{\int_0^{R_{\mathrm{CO,\ 90\%}}} \left(\frac{r'}{R_c}\right)^{-\beta} r' \mathrm{d}r'}{\int_0^{R_{\mathrm{CO\ disk}}} \left(\frac{r'}{R_c}\right)^{-\beta} r' \mathrm{d}r'} \tag{2.8}$$

$$= \frac{\left[\frac{1}{2-\beta} r'^{2-\beta}\right]_0^{R_{\mathrm{CO,\ 90\%}}}}{\left[\frac{1}{2-\beta} r'^{2-\beta}\right]_0^{R_{\mathrm{CO\ disk}}}} \tag{2.9}$$

$$= \frac{R_{\mathrm{CO,\ 90\%}}^{2-\beta}}{R_{\mathrm{CO\ disk}}^{2-\beta}}, \tag{2.10}$$

where we assumed $0 < \beta < 2$.

We find that $R_{\mathrm{CO,\ 90\%}}$ and $R_{\mathrm{CO\ disk}}$ are related through

$$R_{\mathrm{CO,\ 90\%}} = 0.9^{\frac{1}{2-\beta}} R_{\mathrm{CO\ disk}} = f^{\frac{1}{2-\beta}} R_{\mathrm{CO\ disk}}, \tag{2.11}$$

where f represents a more general case where the gas outer radius is defined using a flux fraction f.

2.E Continuum intensity profiles for $R_c = 20$ AU

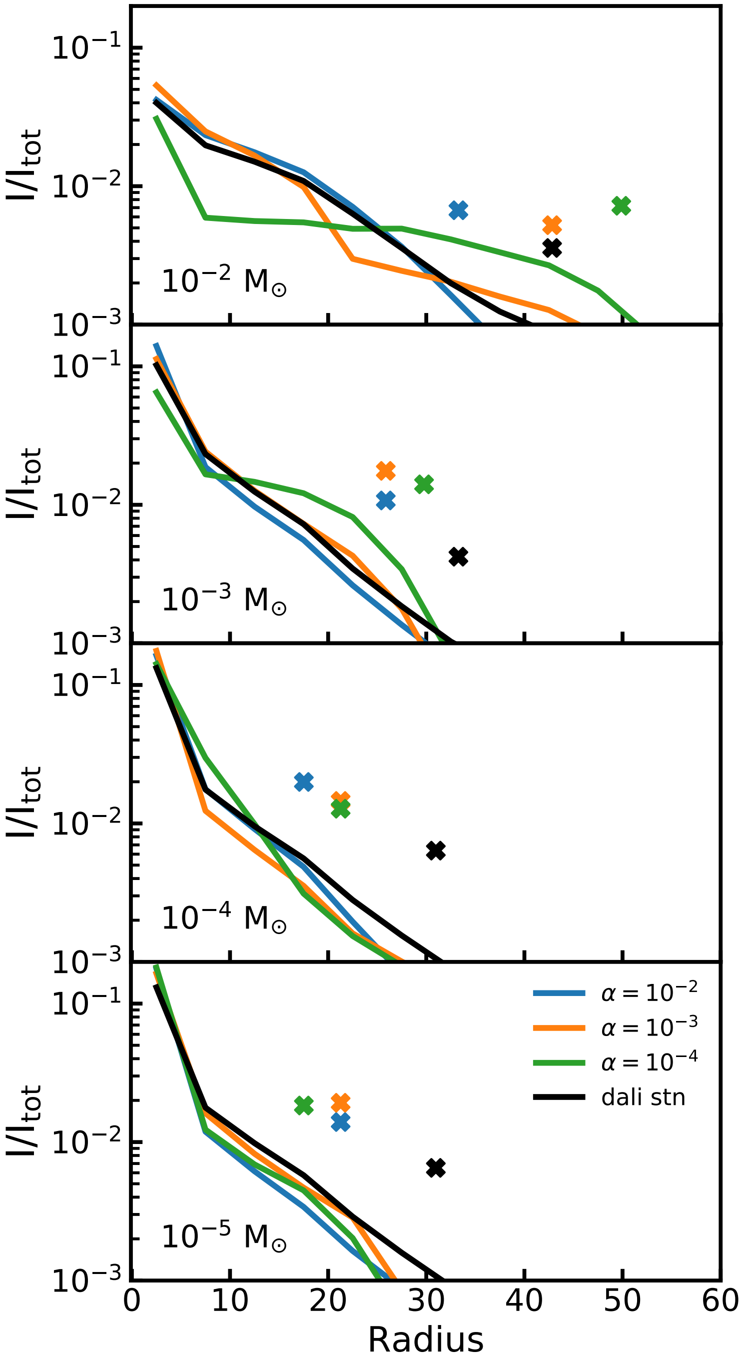

Figure 2.20: Radial profiles of 1300 μm normalized to the total flux. Crosses above the line denote the radii enclosing 90% of the flux (heights of the crosses are arbitrary).

2.F Curves of growth for the $R_c = 50$ AU dust profiles

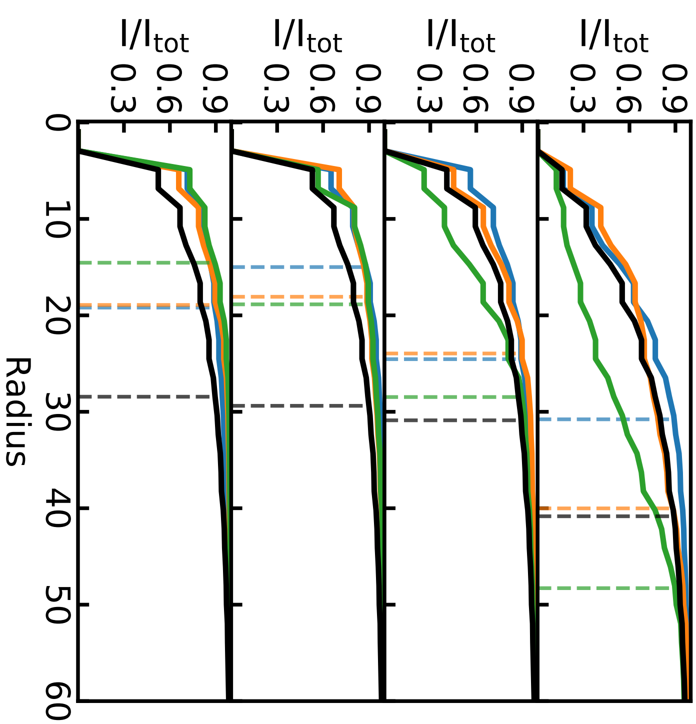

Figure 2.21: 1300 μm curve of growth of the profiles seen in Figure 2.20. Dashed vertical line denote the radii enclosing 90% of the flux.

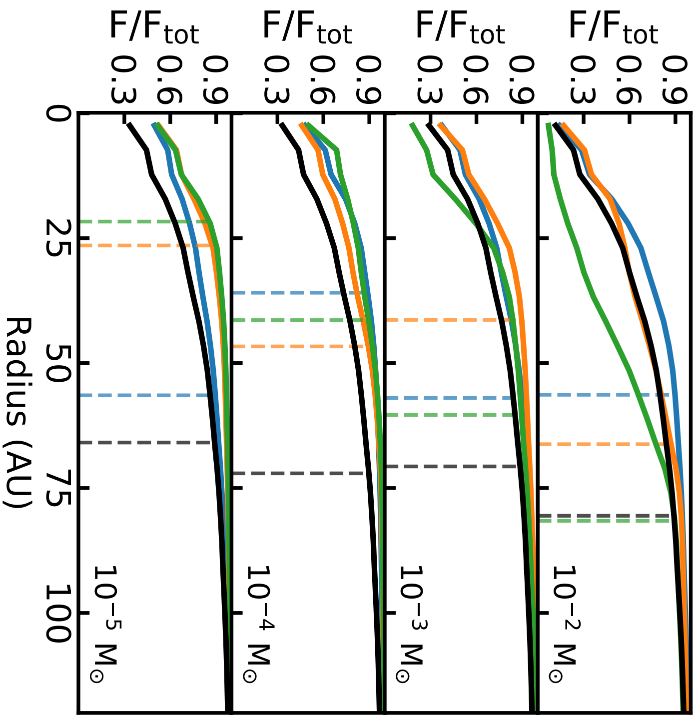

Figure 2.22: 1300 μm curve of growth of the profiles seen in Figure 2.1. Dashed vertical line denote the radii enclosing 90% of the flux.

2.G Beam size and peak S/N for all disk masses vs. $R_{90,\mathrm{gas}}/R_{90,\mathrm{dust}}$

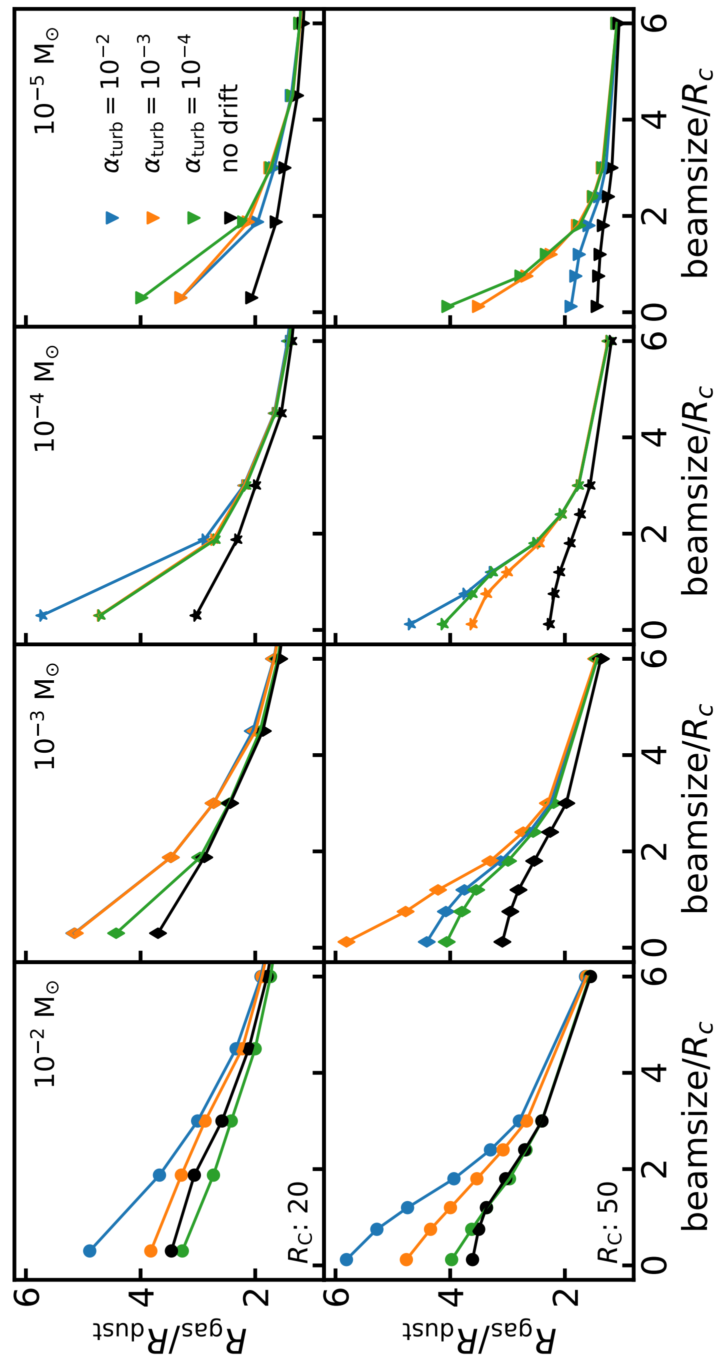

Figure 2.23: Beam size vs. $R_{90,\mathrm{gas}}/R_{90,\mathrm{dust}}$. The effect of the beam scales with its relative size compared to the size of the disk. To highlight this, the beam size is expressed in terms of the characteristic size of the disk.

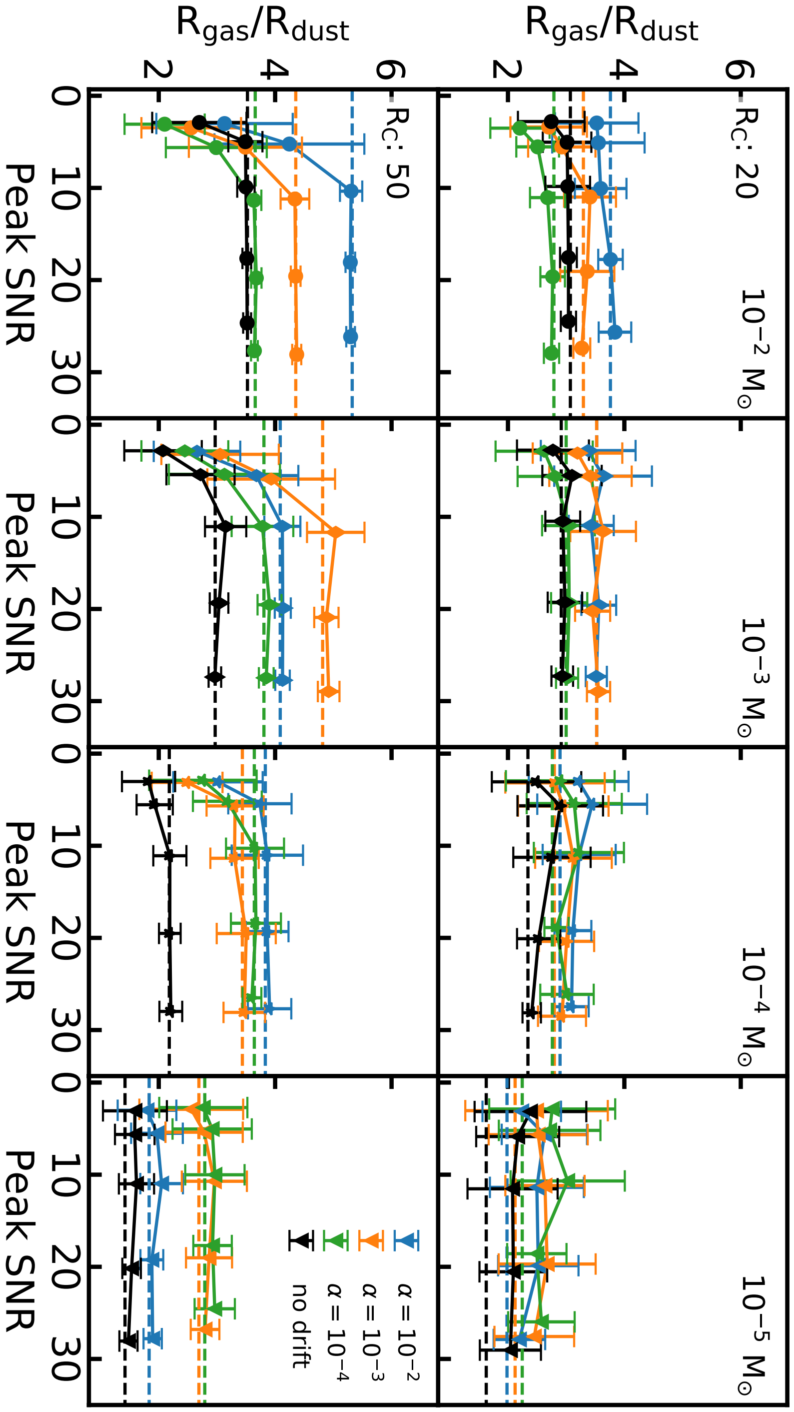

Figure 2.24: Peak S/N in the moment 0 map of the ^{12}CO vs. $R_{90,\mathrm{gas}}/R_{90,\mathrm{dust}}$.

2.H Gas radii vs. peak S/N

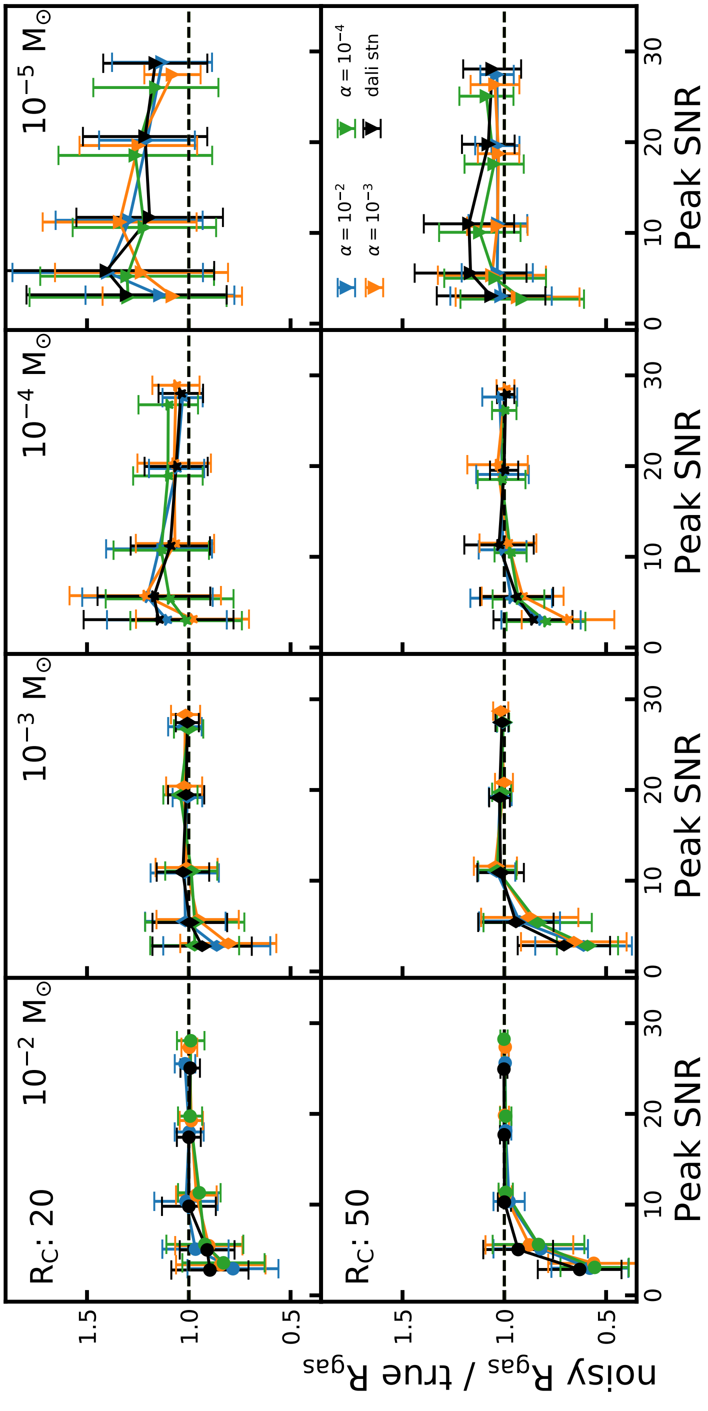

Figure 2.25: Peak S/N normalized to the $R_{\rm CO,\,90\%}$ obtained from the noiseless case vs. $R_{\rm CO,\,90\%}$.

2.I Mass fractions and flux fractions for the remaining disks

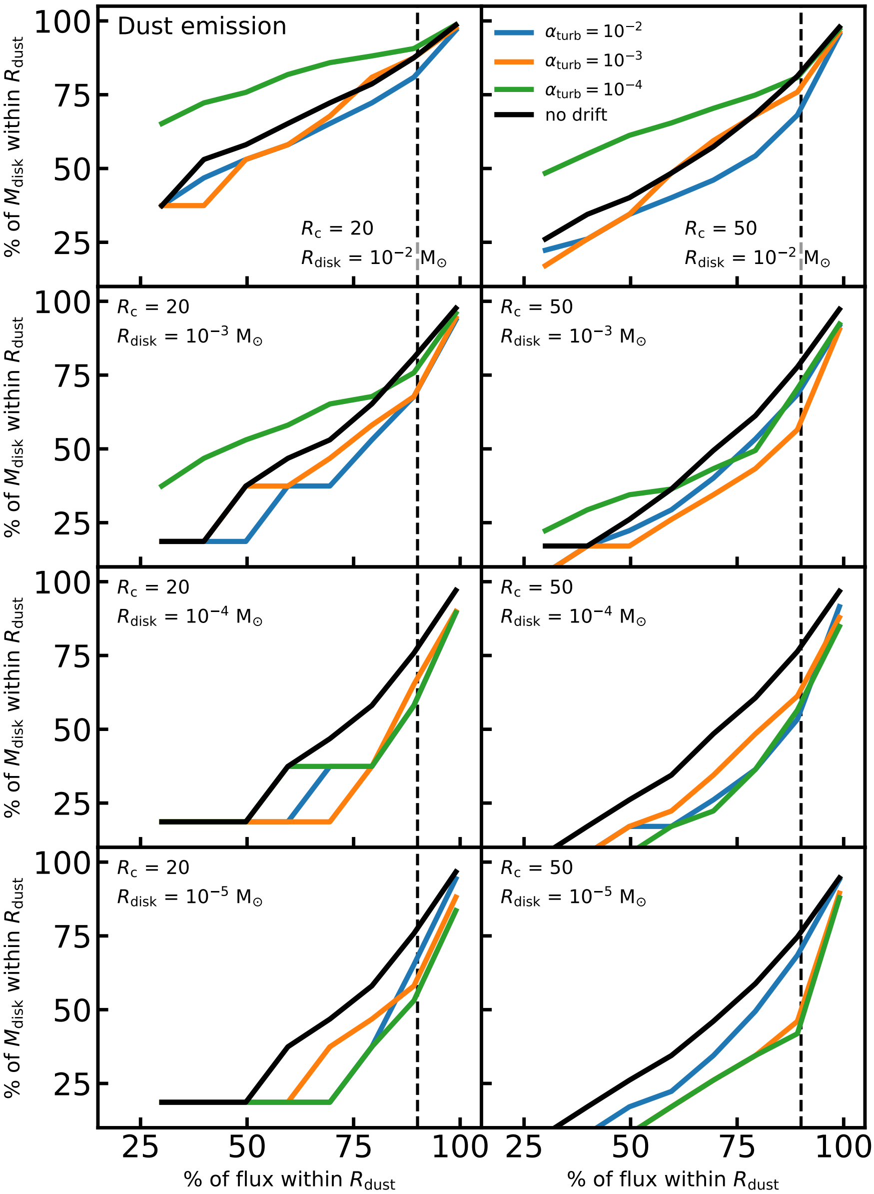

Figure 2.26: Fraction of continuum flux used to calculate $R_{90,\rm dust}$ compared to the fraction of $M_{\rm disk}$ within $R_{\rm CO,\ 90\%}$. Dashed vertical line indicates 90 % of the flux.

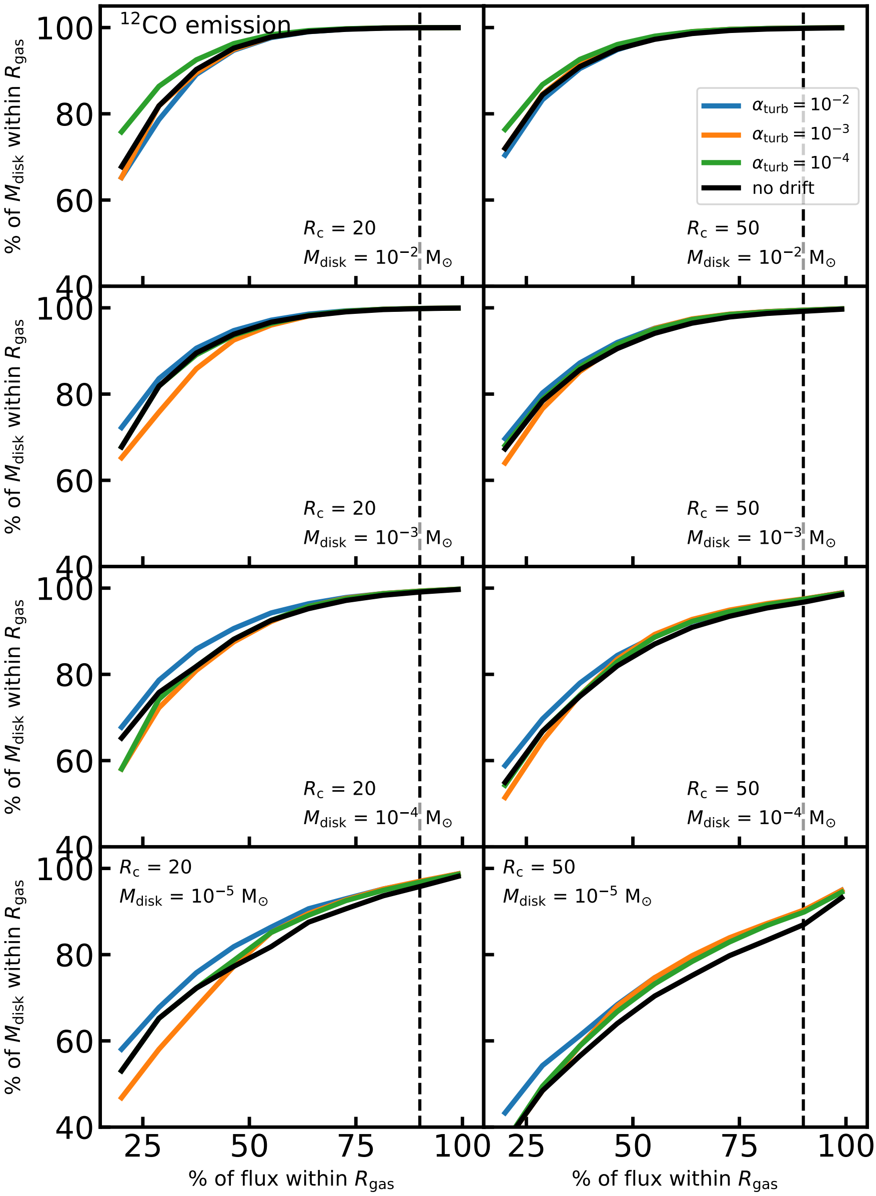

Figure 2.27: Fraction of ^{12}CO flux used to calculate $R_{\mathrm{CO},\ 90\%}$ compared to the fraction of M_disk within $R_{\mathrm{CO},\ 90\%}$. Dashed vertical line indicates 90 % of the flux.

3

Constraining the radial drift of millimeter-sized grains in the protoplanetary disks in Lupus

L. Trapman, M. Ansdell, M.R. Hogerheijde, S. Facchini, C.F. Manara, A. Miotello, J.P. Williams and S. Bruderer, 2020, A&A, 638, 38

Abstract

Context: Recent ALMA surveys of protoplanetary disks have shown that for most disks the extent of the gas emission is greater than the extent of the thermal emission of millimeter-sized dust. Both line optical depth and the combined effect of radially dependent grain growth and radial drift may contribute to this observed effect. To determine whether or not radial drift is common across the disk population, quantitative estimates of the effect of line optical depth are required.

Aims: For a sample of ten disks from the Lupus survey we investigate how well dust-based models without radial dust evolution reproduce the observed ^{12}CO outer radius, and determine whether radial dust evolution is required to match the observed gas–dust size difference.

Methods: Based on surface density profiles derived from continuum observations we used the thermochemical code DALI to obtain ^{12}CO synthetic emission maps. Gas and dust outer radii of the models were calculated using the same methods as applied to the observations. The gas and dust outer radii ($\mathrm{R_{CO}}, \mathrm{R_{mm}}$) calculated using only line optical depth were compared to observations on a source-by-source basis.

Results: For five disks, we find $\mathrm{R_{CO,\ obs}/R_{mm,\ obs} > R_{CO,\ mdl}/R_{mm,\ mdl}}$. For these disks we need both dust evolution and optical depth effects to explain the observed gas–dust size difference. For the other five disks, the observed $\mathrm{R_{CO}/R_{mm}}$ lies within the uncertainties on $\mathrm{R_{CO,\ mdl}/R_{mm,\ mdl}}$ due to noise. For these disks the observed gas–dust size difference can be explained using only line optical depth effects. We also identify six disks not included in our initial sample but part of a survey of the same star-forming region that show significant (S/N $\geq$ 3) ^{12}CO $J = 2 - 1$ emission beyond $4 \times \mathrm{R_{mm}}$. These disks, for which no $\mathrm{R_{CO}}$ is available, likely have $\mathrm{R_{CO}/R_{mm}} \gg 4$ and are difficult to explain without substantial dust evolution.

Conclusions: Most of the disks in our sample of predominantly bright disks are consistent with radial drift and grain growth. We also find six faint disks where the observed gas–dust size difference hints at considerable radial drift and grain growth, suggesting that these are common features among both bright and faint disks. The effects of radial drift and grain growth can be observed in disks where the dust and gas radii are significantly different, while more detailed models and deeper observations are needed to see this effect in disks with smaller differences.

3.1 Introduction

Over recent years the number of detected exoplanet systems has exploded, with several thousand exoplanets found around a wide range of stars. The link between these exoplanet systems and the protoplanetary disks from which they formed is still not fully understood (see e.g., Benz et al. 2014; Morton et al. 2016).

The behavior of the dust in protoplanetary disks is an important piece in this puzzle. In order for planets to form, dust grains have to grow from the micron sized particles in the interstellar medium to millimeter sized grains, centimeter sized pebbles, meter sized boulders, and kilometer sized planetary embryos. The rate of growth of the dust depends on both the gas and the dust surface densities, leading to radial variations (see, e.g Birnstiel et al. 2010, 2012). As the grains grow, they start to decouple from the gas. As a result of gas drag, these larger dust grains lose angular momentum and start to drift inward. Radially dependent grain growth and inward radial drift, the combination of which we refer to here as “dust evolution” , together result in a decrease of the maximum grain size with distance from the star (see, e.g., Guilloteau et al. 2011; Miotello et al. 2012; Pérez et al. 2012, 2015; Menu et al. 2014; Tazzari et al. 2016). As a consequence of dust evolution, we expect the millimeter grains to be confined in a more compact disk than the smaller grains and the gas.

The difference between the extent of the gas emission and the extent of the millimeter continuum emission has been put forward as one of the observational signatures of dust evolution. Observations almost universally show that the gas disk, traced most often by ^{12}CO emission, is larger than the extent of the millimeter grains traced by (sub)millimeter continuum emission (see, e.g., Dutrey et al. 1998; Guilloteau & Dutrey 1998; Panić et al. 2008; Hughes et al. 2008; Andrews et al. 2011). These observations support the idea that radial drift and grain growth are common in protoplanetary disks.

However, the observed gas–dust size difference can also be explained by the difference in optical depth between the two tracers (see also Hughes et al. 2008). Dust disk size ($\mathrm{R_{mm}}$) is measured from (sub)millimeter continuum emission, which is mostly optically thin at large radii. In contrast, the size of the gas disk ($\mathrm{R_{CO}}$) is measured using optically thick ^{12}CO line emission. If a disk has the same radial distribution of both gas and millimeter dust, the difference in optical depth will result in an observed gas–dust size difference ($\mathrm{R_{CO}} > \mathrm{R_{mm}}$). Even when dust evolution has resulted in a disk of compact millimeter grains, optical depth effects on the observed gas–dust size difference will further increase $\mathrm{R_{CO}}/\mathrm{R_{mm}}$.

To quantify the relative importance of optical depth effects and dust evolution, Trapman et al. (2019) measured $\mathrm{R_{CO}}/\mathrm{R_{mm}}$ for a series of models with and without dust evolution (see also Facchini et al. 2017). Trapman et al. found that optical depth effects alone can create gas–dust size differences of up to $\mathrm{R_{CO}}/\mathrm{R_{mm}} \simeq 4$. A gas–dust size difference $\mathrm{R_{CO}}/\mathrm{R_{mm}} \geq 4$ is a clear sign for radial drift. Sources showing a gas–dust size difference of $\mathrm{R_{CO}}/\mathrm{R_{mm}} \geq 4$ are rare in current observations, but one example is CX Tau, for which Facchini et al. (2019) measured $\mathrm{R_{CO}}/\mathrm{R_{mm}} \simeq 5$.

With the advent of the Atacama Large Millimeter/sub-Millimeter Array (ALMA) it has become possible to do surveys of entire star-forming regions, taking ~ 1 minute snapshots of each disk at moderately high resolution ($\sim 0\farcs25-0\farcs40$). This has allowed us to study the properties of the complete disk population (e.g., Taurus, Andrews et al. 2013; Ward-Duong et al. 2018; Long et al. 2018, 2019; Lupus, Ansdell et al.

2016; Ansdell et al. 2018; Chamaeleon I, Pascucci et al. 2016; Long et al. 2017; σ-Ori Ansdell et al. 2017; Upper Sco, Barenfeld et al. 2016, 2017; Corona Australis, Cazzoletti et al. 2019; and Ophiuchus, Cox et al. 2017; Cieza et al. 2019; Williams et al. 2019). In the survey of the Lupus star forming region, Ansdell et al. (2018) measured the gas and dust outer radii ($\mathrm{R_{gas}}$, $\mathrm{R_{dust}}$) for a sample of 22 disks. These latter authors found that the extent of the gas exceeds the extent of the dust, with an average ratio of $\mathrm{R_{gas}/R_{dust}} = 1.96 \pm 0.04|_{\sigma_{\mathrm{obs}}} \pm 0.57|_{\sigma_{\mathrm{dispersion}}}$. Here, σ_{obs} is the uncertainty due to the errors on the observed outer radii, whereas $\sigma_{\mathrm{dispersion}}$ is the standard deviation of the sample.

The average gas–dust size difference $\langle \mathrm{R_{CO}/R_{mm}} \rangle = 1.96$ is much lower than the value of $\mathrm{R_{CO}/R_{mm}} \sim 4$ found by Trapman et al. (2019) to be a clear indication of dust evolution. This would suggest that almost none of the 22 disks show signs of having undergone dust evolution. However, low ^{13}CO and C^{18}O line fluxes observed for these sources indicate that they also have a low CO content, which lowers the contribution of optical depth effects to the gas–dust size difference. A more detailed analysis is required to determine whether the $\mathrm{R_{CO}/R_{mm}}$ observed for the disks in Lupus is a sign of radial drift and grain growth or can be reproduced using only optical depth effects.

In this work, the gas structure of a sample of ten disks taken from the Lupus survey is modeled using the thermochemical code DALI (Bruderer et al. 2012; Bruderer 2013) under the assumption that gas and dust follow the same density structure. The resulting $\mathrm{R_{CO}/R_{mm}}$, set only by optical depth, are compared to observations on a source-by-source basis, and conclusions are drawn on whether or not dust evolution, that is, radial drift and radially dependent grain growth, is needed to match the observed $\mathrm{R_{CO}/R_{mm}}$.

Section 3.2 describes the observations and sample selection. The models are described in Section 3.3 and we describe how the gas and dust outer radii are measured. In Section 3.4 the gas models are compared to the observations in terms of the extent of the gas as traced by ^{12}CO and the gas–dust size difference. The role of noise in measuring $\mathrm{R_{CO}/R_{mm}}$ is also discussed. In Section 3.5 we examine the Lupus disks with unresolved dust emission that were detected in ^{12}CO and discuss whether $\mathrm{R_{CO}/R_{mm}}$ could be larger for more compact dust disks.

3.2 Observations and sample selection

3.2.1 Observations

The disks analyzed in this paper are a subsample of the ALMA Lupus disk survey (Ansdell et al. 2016; Ansdell et al. 2018) (id: ADS/JAO.ALMA#2013.1.00220.S, Band 7, and ADS/JAO.ALMA#2015.1.00222.S, Band 6) and the Lupus Completion Survey (id: ADS/JAO.ALMA#2016.1.01239.S Band 6 and 7).

The band 7 observations were taken with an array configuration covering baselines between 21.4 and 785.5 m. The resulting average beamsize for the continuum is $0\farcs34 \times 0\farcs28$. The bandwidth-weighted mean continuum frequency was 335.8 GHz (890 μm). The spectral setup included two windows covering the ^{13}CO $J = 3-2$ and C^{18}O $J = 3-2$ transitions centered at 330.6 GHz and 329.3 GHz, respectively. Both windows have channel widths of 0.122 MHz, corresponding to a velocity resolution of 0.11 km s^{-1}. Further details on the observational setup and data reduction can be found in Ansdell et al. (2016).

The targets of the observations consist of a sample of sources selected from the Lupus star-forming complex (clouds I to IV) that were classified as Class II or Flat IR spectra disks (Merín et al. 2008). The sample totaled 93 objects of which 61 were detected in the continuum at $\geq 3\sigma$. The ALMA observations are complemented by a VLT/X-shooter spectroscopic survey by Alcalá et al. (2014, 2017). These latter authors derive fundamental stellar parameters for the Class II objects of the region.

The Band 6 observations were taken with a more extended configuration, covering baselines between 15 and 2483 m. As a result, the average beam size for the continuum is $0\farcs25 \times 0\farcs24$, slightly smaller than the one for the Band 7 observations. The bandwidth-weighted mean continuum frequency of these observations was 225.66 GHz (1.33 mm). Three windows were included in the spectral setup, covering the ^{12}CO $J = 2 - 1$, ^{13}CO $J = 2 - 1$ and C^{18}O $J = 2 - 1$ transitions centered at 230.51, 220.38, and 219.54 GHz respectively. Each spectral window has a bandwidth of 0.12 GHz, a channel width of 0.24 MHz, and velocity resolution of 0.3 km s^{-1}. More details of the observations can be found in Ansdell et al. (2018). We note that the sample in Ansdell et al. (2018) covered four additional sources while also excluding two sources later found to be background red giants (Frasca et al. 2017). Neither of these changes affect our sample selection.

3.2.2 Sample selection

In total, 48 of the 95 targets were detected both in 1.33 mm continuum and ^{12}CO $J = 2 - 1$ line emission. For 22 of these sources, the signal-to-noise ratio (S/N) in the channel maps was high enough to measure the gas outer radius defined as the radius enclosing 90% of the ^{12}CO flux (Ansdell et al. 2018). For our sample, we select 10 of these 22 disks that have dust surface density profiles derived by Tazzari et al. (2017), which is a prerequisite for our analysis. IM Lup formally meets our selection criteria, but it is excluded due to its structural complexity.

Of the remaining 11 disks with an observed gas outer radius that were not included in our sample, two sources were covered by the Lupus completion survey (ID: 2016.1.01239.S, PI: van Terwisga) and were not included in the analysis by Tazzari et al. (2017). The remaining 9 were also not included in the analysis by Tazzari et al. (2017) due to the presence of a clear cavity in the image plane. We note that several other disks in the sample (e.g., Sz 84, Sz 100, MY Lup) have been identified as transition disks, either in the higher resolution band 6 observations or in the visibilities (cf. Tazzari et al. 2017; van der Marel et al. 2018). We also excluded Sz 73 from our analysis as it was not detected in ^{13}CO, preventing us from calibrating its CO content.

Our final sample consists of ten disks (in order of decreasing dust mass): Sz 133, Sz 98, MY Lup, Sz 71, J16000236-4222115, Sz 129, Sz 68, Sz 100, Sz 65 and Sz 84. Their properties are shown in Table 3.1.

Table 3.1: Source properties

Name	Stellar properties[1,†]				Disk properties[2,3,†]						
	L_* ($L_\odot$)	$T_{\rm eff}$ (K)	M_* ($M_\odot$)	d (pc)	γ	$M_{\rm dust}$ ($\times 10^{-4} M_\odot$)	R_c (AU)	PA (deg)	i (deg)	$R_{\rm dust}$ (AU)	$R_{\rm gas}$ (AU)
Sz 133	0.07	4350	0.63	153	-0.17	2.9	68.1	126.29	78.53	145.9	225.5
Sz 98	1.53	4060	0.67	156	0.11	2.8	155.4	111.58	47.1	148.4	279.6
MY Lup	0.85	5100	1.09	156	-0.59	2.8	63.3	58.94	72.98	114.8	204.6
Sz 71	0.33	3632	0.41	155	0.25	2.6	88.0	37.51	40.82	98.7	229.7
J16000236	0.18	3270	0.23	164	-0.2	2.6	98.1	160.45	65.71	122.6	301.0
Sz 129	0.43	4060	0.78	161	-0.33	2.5	54.2	154.94	31.74	73.3	141.2
Sz 68	5.42	4900	2.13	154	-0.39	1.3	14.4	175.78	32.89	39.1	73.0
Sz 100	0.08	3057	0.14	136	-1.52	0.6	41.1	60.2	45.11	56.1	121.9
Sz 65	0.89	4060	0.7	155	0.12	0.5	29.0	108.63	61.46	67.3	191.5
Sz 84	0.13	3125	0.17	152	-0.98	0.4	41.3	167.31	73.99	81.4	148.6

Notes.[1]: Alcalá et al. (2014, 2017). [2] Dust and gas radii from Ansdell et al. (2018). [3]: Other disk parameters from Tazzari et al. (2017) [†]: Both stellar and disk parameters were recalculated using the Gaia DR2 distances (Brown et al. 2018; Bailer-Jones et al. 2018; cf. Appendix A in Manara et al. 2018) and Appendix A in Alcalá et al. 2019

Figure 3.1 shows the comparison between our sample and the full survey (Ansdell et al. 2016; Ansdell et al. 2018). We note that our sample is biased towards the most massive disks (in dust). This is likely due to the fact that both resolving the dust and being able to measure the gas outer radius biases the sample to the brightest, most easily detected and therefore most massive disks.

3.3 Methods

The observed difference in extent between gas and dust (gas–dust size difference), quantified by the ratio of the radii enclosing 90% of the ^{12}CO $J = 2 - 1$ and 1.3 millimeter emission ($\mathrm{R_{CO,\ obs}/R_{mm,\ obs}}$), is set by a combination of line optical depth effects and dust evolution, that is, radial drift and radially dependent grain growth. We can use $\mathrm{R_{CO,\ obs}/R_{mm,\ obs}}$ to identify whether or not a disk has undergone dust evolution provided that we know the contribution of optical depth to the gas–dust size difference. To find out if the disks in Lupus show signs of dust evolution, our approach is the following. Based on observational constraints, we set up source-specific models for the ten disks in our sample, where we assume that dust evolution has not occurred. We use the thermochemical code `DALI` (Bruderer et al. 2012; Bruderer 2013) to create synthetic dust continuum and CO line emission maps. Gas and dust outer radii of the model ($\mathrm{R_{CO,\ mdl}}$,$\mathrm{R_{mm,\ mdl}}$) are measured from the emission using the same methods that were applied to the observations. Combining $\mathrm{R_{CO,\ mdl}}$ and $\mathrm{R_{mm,\ mdl}}$, we calculate $\mathrm{R_{CO,\ mdl}/R_{mm,\ mdl}}$, which for our models is only based on optical depth effects. In this context, sources for which $\mathrm{R_{CO,\ mdl}/R_{mm,\ mdl}}$ is smaller than $\mathrm{R_{CO,\ obs}/R_{mm,\ obs}}$ would indicate that some combination of radial drift and grain growth has occurred.

We should note here that both radial drift and grain growth produce a similar radial distribution of dust grain sizes, that is, that larger grains are concentrated closer to the star, and therefore these two effects lead to a similar observed $\mathrm{R_{CO,\ obs}/R_{mm,\ obs}}$. Birnstiel & Andrews (2013) showed that a sharp outer edge of the dust emission is a clear signature of radial drift. Unfortunately our observations lack the sensitivity to detect this sharp edge. Throughout this work we therefore use the term “dust evolution” to refer to the combined effect of radial drift and grain growth.

3.3.1 DALI

To calculate CO line fluxes and produce images, we use the thermochemical code Dust And LInes (`DALI`; Bruderer et al. 2012; Bruderer 2013). `DALI` takes a physical 2D disk model and calculates the thermal and chemical structure self-consistently. Using the stellar spectrum, the UV radiation field inside the disk is calculated. The computation is split into three steps. At the start the dust temperature structure and the internal radiation field are calculated by solving the radiative transfer equation using a 2D Monte Carlo method. For each point, the abundances of the molecular and atomic species are calculated by solving the time-dependent chemistry. The excitation levels of the atomic and molecular species are computed using a nonlocal thermodynamic equilibrium (NLTE) calculation. Based on these excitation levels, the gas temperature can be calculated by balancing the heating and cooling processes. Since both the chemistry and the excitation depend on temperature, an iterative calculation is used to find a self-consistent solution. Finally, the model is ray-traced to construct spectral

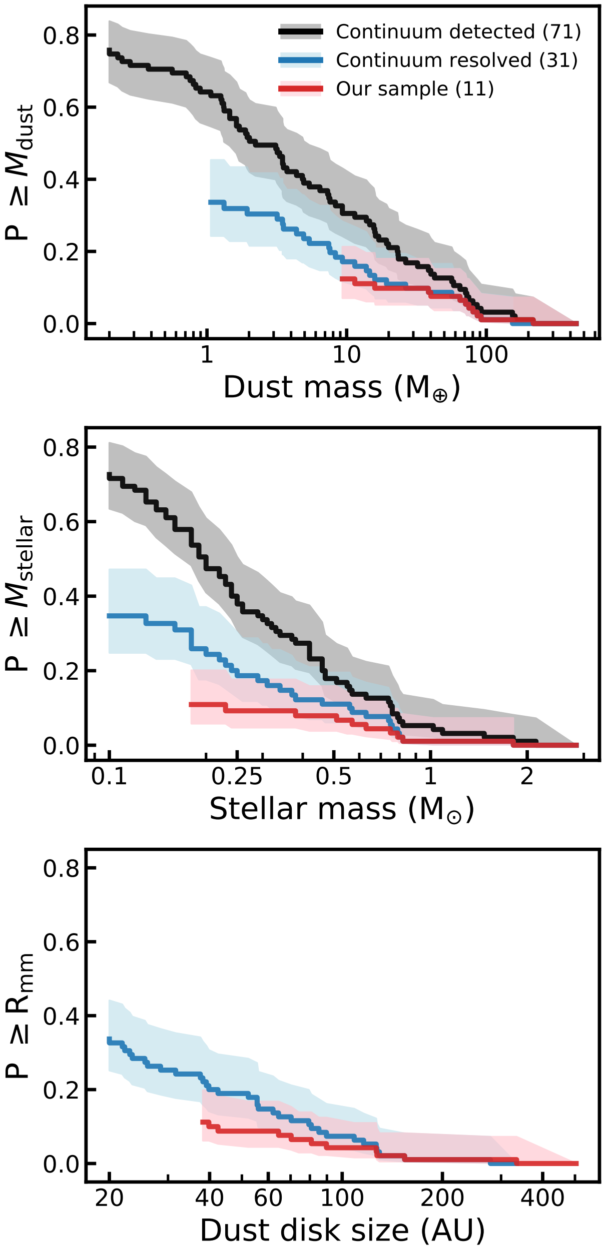

Figure 3.1: Cumulative distribution of our sample in relation to the full Lupus disk population. **Top panel:** Dust masses taken from Ansdell et al. 2016 of all Lupus disks detected in continuum (gray), Lupus disks resolved in continuum (blue) and our sample (red; see Section 3.2.2). **Middle panel:** Same as above, but showing stellar masses derived from X-SHOOTER spectra Alcalá et al. (2017), but recalculated using the new Gaia DR2 distances (see Appendix A in Alcalá et al. 2019) **Bottom panel:** Same as above, but showing dust outer radii ($R_{\rm mm}$).

image cubes and line profiles. A more detailed description of the code can be found in Appendix A of Bruderer et al. (2012).

3.3.2 Chemical network

We use the CO isotopolog chemical network from Miotello et al. (2014) which includes both CO freeze-out and photodissociation of ^{12}CO and its ^{13}CO, C^{17}O, and C^{18}O isotopologs individually. This is an extension of the standard chemical network in DALI, which is based on the UMIST 06 network (Woodall et al. 2007; Bruderer et al. 2012; Bruderer 2013). Reactions included in the network are H_2 formation on the grains, freeze-out, thermal and non-thermal desorption, hydrogenation of simple species on ices, gas-phase reactions, photodissociation, X-ray- and cosmic-ray-induced reactions, polycyclic aromatic hydrocarbon (PAH) grain charge exchange and/or hydrogenation, and reactions with vibrationallly excited H_2^*. The implementation of these reactions can be found in Appendix A.3.1 of Bruderer et al. (2012). Miotello et al. (2014) expanded the chemical network to include CO isotope-selective processes such as photodissociation (see also Visser et al. 2009).

3.3.3 The physical model

For the surface density of the model, we use the surface density profiles from Tazzari et al. (2017). These latter authors fitted the 890 μm visibilities of each source in our sample using a simple disk model with a tapered power law surface density and a two-layer temperature structure (see Chiang & Goldreich 1997). The tapered power law surface density is given by Lynden-Bell & Pringle (1974); Hartmann et al. (1998)

$$\Sigma = \frac{(2-\gamma)\,M_{\rm disk}}{2\pi R_{\rm c}^2}\left(\frac{R}{R_{\rm c}}\right)^{-\gamma}\exp\left[-\left(\frac{R}{R_{\rm c}}\right)^{2-\gamma}\right], \tag{3.1}$$

where $M_{\rm disk}$ is the total disk mass, γ is the slope of the surface density, and $R_{\rm c}$ is the characteristic radius of the disk.

By using this surface density for the gas in our model, the gas and millimetre-sized grains follow the same surface density profile. Our null hypothesis is thus that no radial-dependent dust evolution has occurred.

Vertical structure

In their original fit, Tazzari et al. (2017) use a two-layer vertical structure to calculate the temperature structure of their models (see Chiang & Goldreich 1997). This vertical structure consists of a thin upper layer that intercepts and is superheated by the stellar radiation. This upper layer re-emits in the infrared and heats the interior of the disk. To correctly calculate the CO chemistry and emission, we instead need to run a full two-dimensional physical-chemical model. Assuming hydrostatic equilibrium and a vertically isothermal disk, the vertical density structure is given by a Gaussian distribution

$$n(R,z) = \frac{1}{\sqrt{2\pi}}\frac{1}{H}\exp\left[-\frac{1}{2}\left(\frac{z}{H}\right)^2\right], \tag{3.2}$$

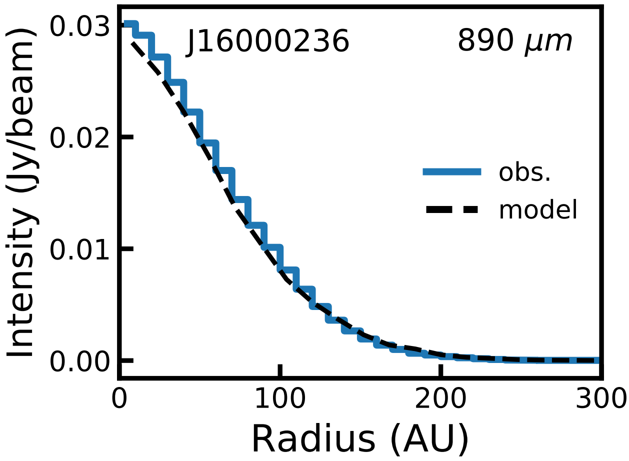

Figure 3.2: Example comparison between model and observed 890 μm continuum intensity profile for J16000236-4222115. Similar comparisons for the other disks can be found in Figure 3.10.

where $H = Rh$ is the physical height of the disk and the scale height h is parametrized by

$$h = h_c \left(\frac{R}{R_c} \right)^{\psi} . \tag{3.3}$$

Here, h_c is the scale height at R_c and ψ is known as the flaring angle. In this work, $(h_c, \psi) = (0.1, 0.1)$ is assumed for all disks.

Compared to the models fitted by Tazzari et al. (2017), our models have a different vertical structure and their temperature structure is calculated differently (cf. Section 3.3.1). It is therefore worthwhile to confirm that our models still reproduce the observed 890 μm continuum emission. As an example, Figure 3.2 compares the model and observed 890 μm radial intensity profile for J16000236 - 4222115. As shown in the figure, our model matches the observation. Similar figures for all ten disks are shown in Figure 3.10. Except for Sz 133, our models reproduce the observed 890 μm radial intensity profile.

Total CO content

The gas outer radius is measured from ^{12}CO emission and increases with the total CO content (see, e.g., Trapman et al. 2019). Observations revealed low ^{13}CO and C^{18}O line fluxes for most disks in Lupus, indicating that they have a low total CO content (see, e.g., Ansdell et al. 2016; Ansdell et al. 2018; Miotello et al. 2017).

Two explanations have been suggested to explain the low CO isotopolog line fluxes. CO isotopologs ^{13}CO and C^{18}O are often used to measure the total gas mass. The low ^{13}CO and C^{18}O line fluxes could indicate that these disks have low gas masses, suggesting low gas-to-dust mass ratios ($\Delta_{\rm gd}$) of the order of $\Delta_{\rm gd} \simeq 1 - 10$.

Alternatively, the low ^{13}CO and C^{18}O line fluxes could be due to an overall underabundance of volatile CO. In this case the disks do not have a low gas mass, but instead some process not currently accounted for has removed CO from the gas phase. Several processes have been suggested to explain the underabundance of CO. One possibility is linked to grain growth, where CO freezes out and becomes locked up in larger bodies, preventing it from re-entering the gas-phase chemistry (see, e.g., Bergin et al.

2010; Bergin et al. 2016; Du et al. 2015; Kama et al. 2016b). Alternatively, CO can be removed by converting it into more complex organics such as CH_3OH that have higher freeze-out temperatures or turning it into CO_2 and/or CH_4 ice (see, e.g., Aikawa et al. 1997; Favre et al. 2013; Bergin et al. 2014; Bosman et al. 2018; Schwarz et al. 2018). We note that neither of these processes is included in `DALI`. Recent C_2H observations in a subsample of Lupus disks are in agreement with this second hypothesis, that is, with C and O being underabundant in the gaseous outer disk (Miotello et al. 2019).

It should be noted here that the two explanations for the low total CO content discussed here have very different implications for the evolution of dust in the disk. If the low CO fluxes are indicative of low gas-to-dust mass ratios, dust grains will not be well coupled to the gas, increasing the effects of fragmentation and thus limiting the maximum grain size in the disk. If disks are underabundant in CO but have $\Delta_{\rm gd} \sim 100$, dust grains stay well coupled to the gas for longer and grow to larger sizes, and for most of the disks radial drift will set the maximum grain size.

For each source in our sample we examine both scenarios. We run a gas depleted disk model, where $\Delta_{\rm gd}$ is lowered until the model reproduces the observed ^{13}CO 3 - 2 line flux. In addition, we run a CO underabundant model for each source, where we lower the C and O abundances until the ^{13}CO 3 - 2 line flux matches the observations. Our tests show that both approaches yield near identical results. In this work we therefore only show the CO underabundant models.

Dust properties

Dust settling is included parametrically in the model by splitting the grains into two populations:

- Small grains (0.005-1 μm) are included with a (mass) fractional abundance $1 - f_{\rm large}$ and are assumed to be fully mixed with the gas.
- Large grains (1-10^3 μm) are included with a fractional abundance $f_{\rm large}$. To simulate the large grains settling to the midplane, these grains are constrained to a vertical region with scale height χh; $\chi < 1$.

The opacities are computed using a standard interstellar medium (ISM) dust composition following Weingartner & Draine (2001), with a MNR (Mathis et al. 1977) grain size distribution between the grain sizes listed above.

In our models, we set $f_{\rm large} = 0.99$ and $\chi = 0.2$, thus assuming that the majority of the dust mass is in the large grains that have settled to the midplane of the disk.

We note that in our analysis we keep the disk flaring structure and dust settling fixed and identical for all ten sources in our sample. In practice these parameters will likely vary between different disks. In Appendix 3.B we show that varying these parameters changes $R_{\rm CO,\ mdl}$ by less than 10 %.

Stellar spectrum

Alcalá et al. (2014, 2017) used VLT X-Shooter spectra to derive stellar properties for all our sources. Using their stellar luminosity and effective temperature, re-scaled to account for the new Gaia DR2 distances (see also Appendix A in Alcalá et al. 2019), we calculate the blackbody spectrum to use as the stellar spectrum for each source. Excess UV radiation that is expected as a result of accretion is added to the

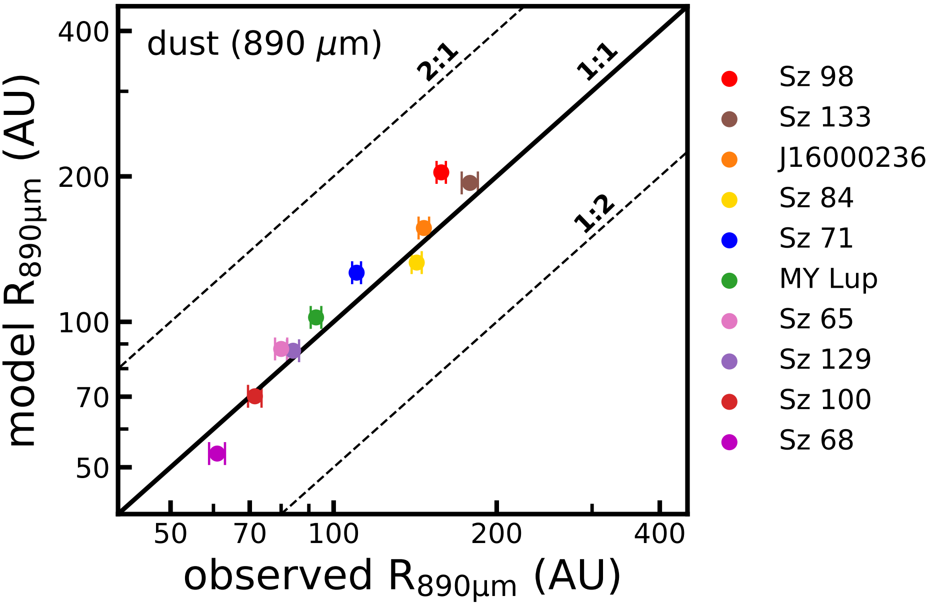

Figure 3.3: Comparison between model and observed dust outer radii based on the 890 μm continuum emission. Differences are within 15% with the exception of Sz 98 (30%).

stellar spectrum as blackbody emission with T = 10000 K. The total luminosity of this component is set to the observed accretion luminosity (Alcalá et al. 2017). For three sources (Sz 65, Sz 68 and MY Lup) only an upper limit of the accretion luminosity is known. We use this upper limit as the accretion luminosity in the models for these sources.

Some of the sources in our sample have anomalously low stellar luminosities, which could be linked to the high inclination of their disk. The main consequence of underestimating the stellar luminosity will be that our disk model is too cold. Increasing the stellar luminosity will have a very similar effect to increasing the flaring of the disk, as both increase the temperature in the disk. In Appendix 3.B we show that increasing the flaring has only a minimal effect on the gas outer radius and therefore we do not expect an underestimation of the stellar luminosity to affect our results.

3.3.4 Measuring model outer radii

We follow the same approach as Ansdell et al. (2018) to measure the gas and dust outer radii from our models. These latter authors define the outer radius as that which encloses 90 % of the total flux. In both the observations the gas outer radius (R_{CO}) is measured from the ^{12}CO 2 - 1 line emission and the dust outer radius (R_{mm}) is measured from the 1.3 millimeter continuum emission. The outer radius is measured using a curve of growth method where the flux is measured in increasingly larger elliptical apertures until the measured flux reaches 90 % of the total flux. The inclination (i) and position angle (PA) of the apertures are chosen to match the orientation of the continuum emission (see Tazzari et al. 2017). A Keplerian masking technique is applied to the line emission to increase the S/N of the CO emission in the outer parts of the disk (for details, see Appendix 3.A). Uncertainties on R_{CO} and R_{mm} are determined by taking the uncertainties on the total flux and using the curve of growth method to propagate these uncertainties into the observed outer radius.

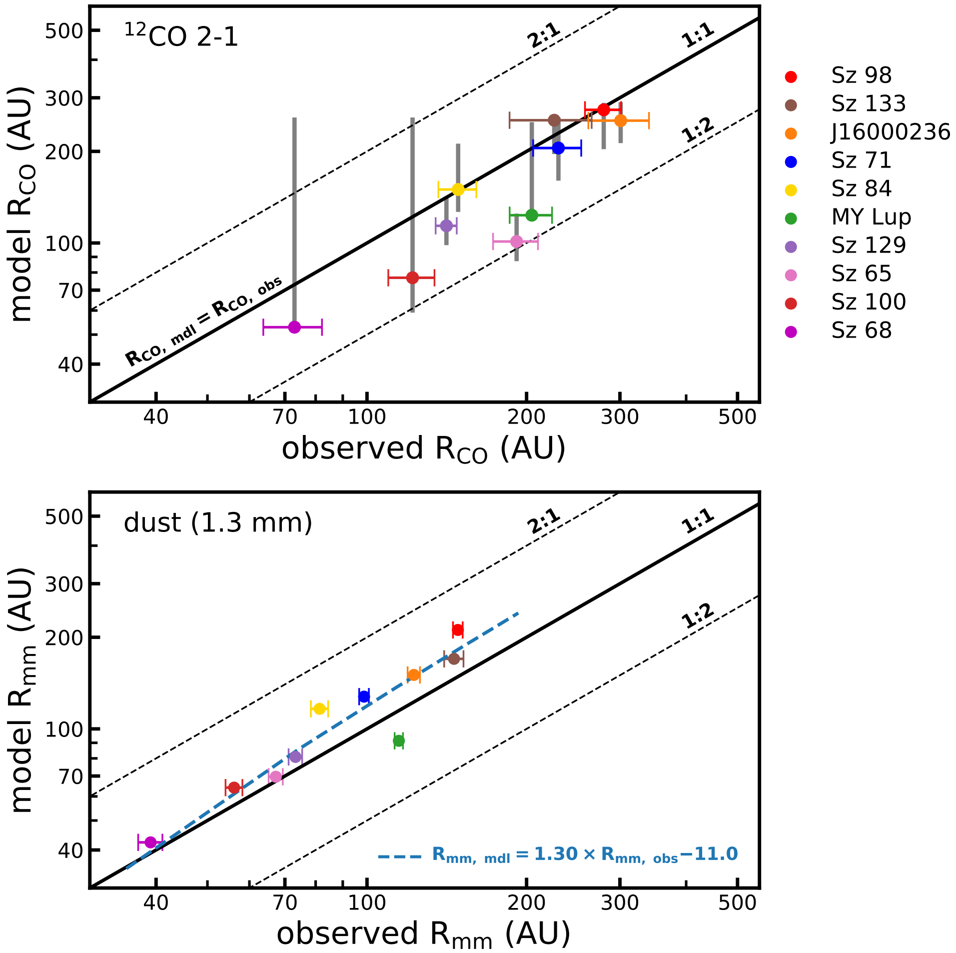

Figure 3.4: Disk size comparison of the models and the observations. **Top panel:** Gas disk size (R_{CO}), defined as the radius enclosing 90% of the ^{12}CO $J = 2-1$ flux. Observed R_{CO}, including uncertainties, are shown as a colored error bar (Ansdell et al. 2018). Gray vertical lines denote the range of $R_{CO,\ mdl}$ measured after noise is included (see Appendix 3.D). The upper and lower points of the gray line show the 84th and 16th quantiles, respectively, of the noisy R_{CO} distribution (cf. Appendix 3.F). **Bottom panel:** As above, but showing the dust disk size, defined as the radius that encloses 90% of the 1.3 mm continuum flux. The blue dashed line shows the best fit of the offset between $R_{mm,\ mdl}$ and $R_{mm,\ obs}$ (see Section 3.4.2).

We measure $\mathrm{R_{CO}}$ and $\mathrm{R_{mm}}$ from our models following the same procedure. First, our models are raytraced at the observed inclination and the resulting synthetic ^{12}CO line emission cubes and 1.3 millimeter continuum emission maps are convolved with the beam of the Band 6 observations (see Section 3.2.1; Ansdell et al. 2018). We note that this approach is a simplification of producing full synthetic observations of our models by sparsely sampling the Fourier transform of our model and reconstructing it in the image plane with the CLEAN algorithm. However, tests show that both methods yield approximately the same measured gas and dust outer radii.

For the CO, we add noise to the synthetic ^{12}CO $J = 2-1$ spectral cube following the procedure outlined in Appendix 3.D and we apply the Keplerian mask that was used for the observations before collapsing the spectral cube along the spectral axis to create a moment-zero map. The outer radii are measured using the curve of growth method, also using i and PA of the continuum for the elliptical apertures. Figure 3.3 shows a comparison between model and observed outer radii based on the 890 μm continuum emission. The models and observations agree to within 15 % except for Sz 98 ($\sim$ 29%). Figures 3.2 and 3.3 show that our models are able to reproduce the continuum intensity profile and the extent of the 890 μm continuum observations.

3.4 Results

3.4.1 Observed versus modeled disk sizes

Having measured the gas and dust outer radii of our models, we can compare them to the observations. In Figure 3.4 we compare the gas and dust outer radii of the model ($\mathrm{R_{CO,\ mdl}}$, $\mathrm{R_{mm,\ mdl}}$) to the observed gas and dust outer radii ($\mathrm{R_{CO,\ obs}}$,$\mathrm{R_{mm,\ obs}}$).

The top panel of Figure 3.4 shows that all models are either equal in size to or smaller than the observations in terms of the measured gas outer radius. If we account for the uncertainty on $\mathrm{R_{CO,\ obs}}$ shown in the figures as the colored error bar, we find that for six of the ten models ($\sim$ 60%) the modeled gas outer radius ($\mathrm{R_{CO,\ mdl}}$) is smaller than the observed gas outer radius ($\mathrm{R_{CO,\ obs}}$). These are predominantly the smaller disks ($\mathrm{R_{CO,\ obs}} \lessapprox 200$ AU).

The gray bars in Figure 3.4 show the range of $\mathrm{R_{CO,\ mdl}}$ that we measure after adding noise to the synthetic ^{12}CO $J = 2-1$ spectral cube following the procedure outlined in detail in Appendix 3.D. Briefly, we take a noise map from the observed spectral cube at random and add it to the model spectral cube, apply the Keplerian mask, and measure $\mathrm{R_{CO,\ mdl}}$ using the curve of growth method outline in Section 3.3.4. This process is repeated for approximately 1000 noise realisation and gives us a distribution of possible $\mathrm{R_{CO,\ mdl}}$ that could be measured from our models in the presence of noise (see Figure 3.9).

For most of our sources we see that the uncertainty on $\mathrm{R_{CO,\ mdl}}$, which is represented by the range of noisy $\mathrm{R_{CO,\ mdl}}$, is smaller than or similar to the uncertainty on $\mathrm{R_{CO,\ obs}}$. This shows that propagating the uncertainty in the total flux through the curve of growth into the observed outer radius is in most cases a conservative estimate of the effect of noise on measuring the outer radius.

The range of noisy $\mathrm{R_{CO,\ mdl}}$ is the largest of the two smallest disks in the sample, Sz 68 and Sz 100 (see Figure 3.4). Within our sample, these disks are also among the faintest in ^{12} CO $J = 2-1$ emission. The compact, faint emission makes their curve of growth more susceptible to the effects of noise. These results show that care should be taken when measuring the gas disk size of faint, compact disks using a curve of growth method.

The bottom panel of Figure 3.4 compares modeled dust outer radius ($\mathrm{R_{mm,\ mdl}}$) and observed dust outer radius ($\mathrm{R_{mm,\ obs}}$), both measured from the 1.3 millimeter continuum emission. In the figure we can see that the $\mathrm{R_{mm,\ mdl}}$ of four disk models are significantly larger than $\mathrm{R_{mm,\ obs}}$: namely Sz 84 (43%), Sz 71 (29%), J16000236 (23%), and Sz 98 (42%), and the disk model for MY Lup is significantly smaller (20%). The differences of $\mathrm{R_{mm}}$ between the model and the observations are larger than the differences seen at 890 μm (cf. Figure 3.3). This indicates that our models overproduce the extent of the 1.3 millimeter continuum emission despite reproducing the extent of the continuum emission at 890 μm. A potential explanation for this is the lack of dust evolution in our models. Based on dust evolution, the larger 1.3 millimeter grains should be more concentrated toward the star compared to the 890 μm grains, which should be reflected by dust outer radii decreasing with wavelength (see, e.g., Tripathi et al. 2018). In our models we do not take this into account. Instead, we base our models on the 890 μm continuum emission, and thus the extent of the 890 μm grains, and assume the same radial extent for the 1.3 millimeter grains. The fact that $\mathrm{R_{mm,\ mdl}}$ is larger than $\mathrm{R_{mm,\ obs}}$ would therefore suggest that without including dust evolution we are overestimating the radial extent of the 1.3 millimeter grains.

3.4.2 Gas–dust size difference: models versus observations

The ratio between $\mathrm{R_{CO}}$ and $\mathrm{R_{mm}}$ of a disk encodes whether it has undergone dust evolution. From the gas and dust outer radii of the models we can calculate their gas–dust size ratio ($\mathrm{R_{CO,\ mdl}/R_{mm,\ mdl}}$). We note that, as the models do not include radial drift or radially dependent grain growth, these gas–dust size differences are set only by optical depth. Here we compare $\mathrm{R_{CO,\ mdl}/R_{mm,\ mdl}}$ to the observed gas–dust size difference ($\mathrm{R_{CO,\ obs}/R_{mm,\ obs}}$), to identify which disks in our sample have undergone radial drift and radially dependent grain growth.

Our analysis of $\mathrm{R_{CO}/R_{mm}}$ is based on the fact that our models reproduce the extent of the continuum emission. However, in the previous section we found a seemingly systematic offset in $\mathrm{R_{mm}}$, namely $\mathrm{R_{mm,\ mdl} > R_{mm,\ obs}}$, which might affect our interpretation of $\mathrm{R_{CO,\ obs}/R_{mm,\ obs}}$versus $\mathrm{R_{CO,\ mdl}/R_{mm,\ mdl}}$. We therefore elect to propagate the effect of this offset into $\mathrm{R_{CO,\ mdl}/R_{mm,\ mdl}}$. We fit the offset with a straight line ($\mathrm{R_{mm,\ mdl}} = a \times \mathrm{R_{mm,\ obs}} + b$, see Figure 3.4) and use the best-fit values to scale $\mathrm{R_{mm,\ mdl}}$ when calculating $\mathrm{R_{CO,\ mdl}/R_{mm,\ mdl}}$. We note that for the disks where $\mathrm{R_{mm,\ mdl} > R_{mm,\ obs}}$ this will increase $\mathrm{R_{CO,\ mdl}/R_{mm,\ mdl}}$ and enhance the perceived effect of optical depth on $\mathrm{R_{CO}/R_{mm}}$. Therefore, for any disk showing $\mathrm{R_{CO,\ obs}/R_{mm,\ obs} > R_{CO,\ mdl}/R_{mm,\ mdl}}$, we can confidently say that optical depth cannot explain their observed gas–dust size ratio.

Figure 3.5 shows $\mathrm{R_{CO}/R_{mm}}$ of the models and the observations. The gas–dust size ratios were calculated using the gas and dust outer radii shown in Figure 3.4. The uncertainties on $\mathrm{R_{CO,\ obs}/R_{mm,\ obs}}$ were calculated using the uncertainties on $\mathrm{R_{CO,\ obs}}$ and $\mathrm{R_{mm,\ obs}}$. The uncertainties on $\mathrm{R_{CO,\ mdl}/R_{mm,\ mdl}}$ were calculated using the 16th and 84th quantile of the noisy $\mathrm{R_{CO,\ mdl}}$ distribution (see Appendix 3.F).

For five of the ten disks in our sample (50%) we find $\mathrm{R_{CO,\ obs}/R_{mm,\ obs} > R_{CO,\ mdl}/R_{mm,\ mdl}}$ even after the effects of noise are included, indicating this is a solid result considering the uncertainties on the measurements. These disks are Sz 65, Sz 71, J1600236, Sz 98,

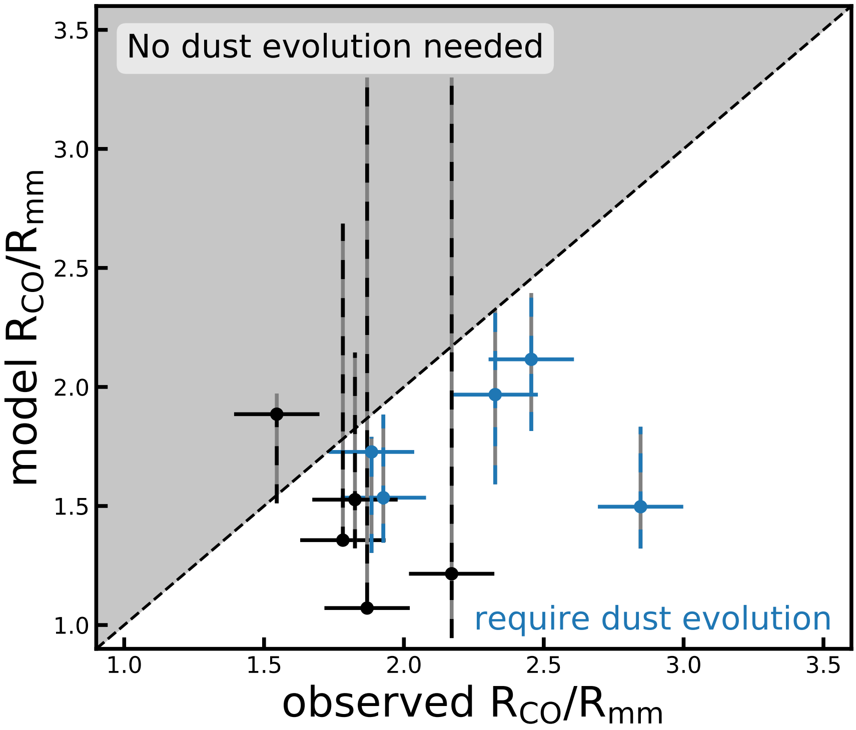

Figure 3.5: Disk gas–dust size ratio comparison of the models with noise and the observations. Uncertainties of the model $R_{CO,\ mdl}/R_{mm,\ mdl}$ were computed using the 16th and 84th quantile of the R_{CO} distribution. Sources where $R_{CO,\ mdl}/R_{mm,\ mdl} < R_{CO,\ obs}/R_{mm,\ obs}$ are shown in blue. To reproduce the observed $R_{CO,\ obs}/R_{mm,\ obs}$ these sources require a combination of dust evolution and optical depth.

and Sz 129. For these disks, we need both dust evolution and optical depth effects to explain the observed $R_{CO,\ obs}/R_{mm,\ obs}$.

For the other five disks in the sample, Sz 133, Sz 100, MY Lup Sz 84, and Sz 68, the observed $R_{CO,\ obs}/R_{mm,\ obs}$ lies within the uncertainty on $R_{CO,\ mdl}/R_{mm,\ mdl}$. For these disks, it is possible that our model would reproduce the observed $R_{CO,\ obs}/R_{mm,\ obs}$ if it were observed at similar sensitivity to the band 6 observations. We are however not able rule out that the $R_{CO,\ obs}/R_{mm,\ obs}$ measured for these five sources are only due to optical depth effects.

Among these latter five disks is Sz 68, also known as HT Lup, which has been observed at high spatial resolution as part of the DSHARP program (Andrews et al. 2018a, see also Kurtovic et al. 2018). Sz 68 is a multiple star system and the high-resolution observations were able to individually detect both the primary disk around Sz 68 A and the disks around Sz 68 B and C located at 25 and 434 AU in projected separation from Sz 68 A (Kurtovic et al. 2018), respectively. In our observations with a resolution of ~39 AU the disks around Sz 68 A and B are not resolved separately. The observed $R_{CO,\ obs}/R_{mm,\ obs}$ is therefore not likely to reflect the evolution of dust in this system.

It should be noted that of these five disks, three show large uncertainties towards large $R_{CO,\ mdl}/R_{mm,\ mdl}$, which can be traced back to similarly large uncertainties on $R_{CO,\ mdl}$. Trapman et al. (2019) showed that a peak S/N ≥ 10 on the moment-zero map of ^{12}CO is required to measure R_{CO} to within 20% (see, e.g., their Figure H.1). To compare this to our observations, the peak S/N in our sample varies from ~ 6 (Sz 100) to ~ 12 (Sz 133). This suggests that for these three disks our comparison between $R_{CO,\ obs}/R_{mm,\ obs}$ and $R_{CO,\ mdl}/R_{mm,\ mdl}$ is probably not reliable due to observational effects. Observations with a factor two higher sensitivity, equivalent to increasing the integration time from 1 to 4 minutes per source, would be sufficient to remove these observational effects.

3.5 Discussion

3.5.1 Fast dust evolution candidates in Lupus

In the present study, we look at the gas–dust size differences for a sample of 10 of the 48 disks in Lupus where ^{12}CO $J = 2 - 1$ is detected. Our sample makes up $\sim 15\%$ of the Lupus disk population and is biased towards the most massive ($\geq 10\mathrm{M}_{\oplus}$) dust disks (see Figure 3.1). Notably, the ^{12}CO detections are not similarly biased, with ^{12}CO $J = 2 - 1$ being detected for some of the faintest continuum sources.

Here we examine the 38 disks in Lupus where ^{12}CO $J = 2 - 1$ was detected, but which did not meet our selection criteria; we refer to these as the “low-S/N sample”. As discussed in Section 3.2.2, most of these sources were excluded from our analysis because the S/N of the ^{12}CO $J = 2 - 1$ was too low to measure R_{CO}. Analyzing them in the same manner as the “high S/N sample” is not possible with the current observations. The disks in the high S/N sample show that R_{CO} approximately coincides with a contour showing S/N = 3 ^{12}CO $J = 2 - 1$ emission. For the disks in the low S/N sample we can therefore use the S/N = 3 contour of ^{12}CO $J = 2 - 1$ as a proxy for R_{CO}, giving us some idea of their gas disk sizes. We note that this approximation is likely to underestimate R_{CO}, as observing these sources at a sensitivity matching the high S/N sample would move the S/N = 3 contour outward.

With this proxy for R_{CO}, we can investigate whether the disks in the low S/N sample show signs of dust evolution. Using `DALI`, Trapman et al. (2019) compared the $R_{CO,\ mdl}/R_{mm,\ mdl}$ of a series of models with and without dust evolution. These latter authors found that $R_{CO}/R_{mm} \geq 4$ is a clear sign of dust evolution, giving us a clear criterion with which we can identify signs of dust evolution. If a disk in the low S/N sample has a S/N = 3 contour for its ^{12}CO emission that reaches beyond $4 \times R_{mm}$, it is likely that this disk would have $R_{CO}/R_{mm} \geq 4$ if observed at higher sensitivity. We therefore identify it as a disk showing clear signs of having undergone dust evolution, where it would be difficult to explain the observations using only optical depth and without any radial drift or radially dependent grain growth.

As shown in Figure 3.6 we identify six disks where the S/N = 3 contour of their ^{12}CO emission reaches beyond $4 \times R_{mm}$ Of these, three have marginally resolved 1.3 mm continuum emission, namely J15450887 - 3417333, J16085324 - 3914401, and Sz 69. Although R_{CO} could not be measured for these sources, it is difficult to explain the difference between the extent of the CO and the extent of the continuum without including dust evolution. It should be noted that the ^{12}CO channel maps of J15450887

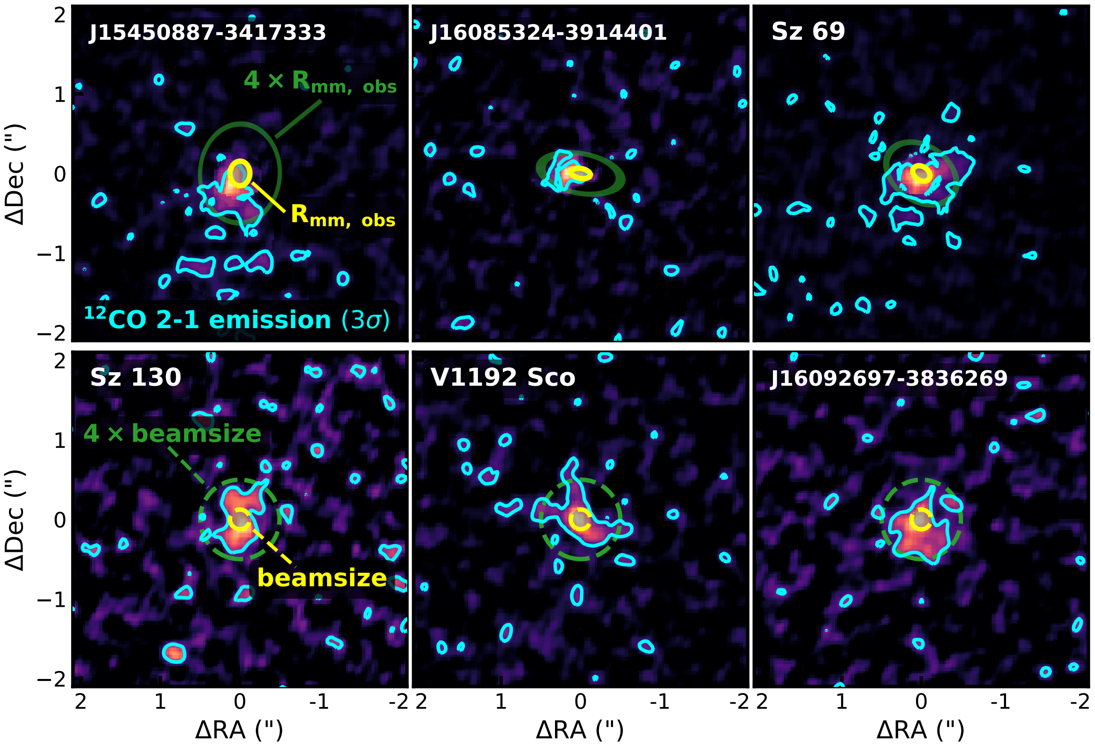

Figure 3.6: ^{12}CO moment-zero maps of the six sources from the "low S/N sample" (see Section 3.5.1) where the S/N = 3 contour of their ^{12}CO emission, shown in cyan, reaches beyond $4 \times \mathrm{R}_{\mathrm{mm}}$. Using this contour as a proxy for R_{CO}, these disks likely have $\mathrm{R}_{\mathrm{CO}}/\mathrm{R}_{\mathrm{mm}} \geq 4$ and are therefore clear candidates for having undergone dust evolution (cf. Trapman et al. 2019). The top three disks have resolved continuum emission and their $\mathrm{R}_{\mathrm{mm,\ obs}}$ is shown by the yellow ellipse. For these sources, Keplerian masking was applied to the ^{12}CO $J = 2 - 1$ emission (see Appendix 3.A). The bottom three disks have unresolved continuum emission. The dashed yellow circle shows the size of the beam ($0\overset{\prime\prime}{.}25$) as an upper limit to the dust disk size. Similarly, the dashed green circle shows four times the beam size.

show some cloud emission. Most of this emission is removed by the Keplerian mask but some of it could still be present in the moment-zero map.

The other three disks remain unresolved in the continuum at a resolution of $0\farcs25$. As an upper limit for the dust disk size we use $0\farcs125$ which is approximately the radius of the beam. These three disks, Sz 130, V1192 Sco, and J16092697-3836269, show significant CO emission outside $4 \times \frac{1}{2} \times$ beamwidth $= 4 \times 0\farcs125$. Taking into account that the dust disk of these sources is unresolved, it is very likely that these disks have undergone substantial dust evolution. Noteworthy here is the inclusion of V1192 Sco, which has the faintest detected continuum flux of the disks in Lupus. Several studies have shown that there exists a relation between the millimeter luminosity and the dust disk size (see, e.g., Tazzari et al. 2017; Tripathi et al. 2017; Andrews et al. 2018b). If we extrapolate this relation down to the observed millimeter flux of V1192 Sco, we find a dust disk size of 4-8 AU ($0\farcs025 - 0\farcs05$). With ^{12}CO $J = 2 - 1$ emission extending out up to $0\farcs75$, V1192 Sco would seemingly have a gas–dust size difference of $\mathrm{R_{CO,\ obs}/R_{mm,\ obs}}$ $15 - 30$, which would make it one of the most extreme cases of grain growth and radial drift. Deeper observations of ^{12}CO and higher resolution observations of the continuum are required to confirm this. We should note here that these disks could have faint, extended continuum emission that was undetected in our current observations. However, given the sensitivity of our current observations this faint emission can at most increase $\mathrm{R_{mm}}$ by a factor of two for our faintest source, V1192 Sco.

3.5.2 Are compact dust disks the result of runaway radial drift?

The discovery of six disks that likely have $\mathrm{R_{CO,\ obs}/R_{mm,\ obs}} \geq 4$ highlights an interesting property of the ten disks analyzed in detail in here, namely that they all have relatively low gas–dust size differences. The disks in our sample have $\langle \mathrm{R_{CO,\ obs}/R_{mm,\ obs}} \rangle_{\mathrm{obs}} = 2.06 \pm 0.37$ where the second number specifies the standard deviation of the sample. As discussed in Section 3.2.2, these disks represent the massive end of the Lupus disk population (see Figure 3.1). In contrast, there are at least six disks with low dust masses that have $\mathrm{R_{CO,\ obs}/R_{mm,\ obs}} \geq 4$. These are all disks with compact continuum emission ($\mathrm{R_{mm}} \leq 24\,\mathrm{AU}$). We would expect more massive disks to have a higher $\mathrm{R_{CO}/R_{mm}}$ (see, e.g., Trapman et al. 2019). As a result of their higher disk mass, these disks have a greater total CO content which results in a larger observed gas outer radius ($\mathrm{R_{CO}}$). In addition, these disks have a higher dust mass, resulting in more efficient grain growth and inward radial drift.

The low $\mathrm{R_{CO,\ obs}/R_{mm,\ obs}}$ in our sample could be linked to the rings and gaps observed in large disks (see, e.g., Andrews et al. 2018a; Huang et al. 2018). These rings are the result of a local pressure maximum that acts as a dust trap for the millimeter-sized grains (see, e.g., Whipple 1972; Klahr & Henning 1997; Kretke & Lin 2007; Pinilla et al. 2012). These dust traps stop the millimeter-sized grains from drifting inward, effectively halting the radial dust evolution. As a result, the disks stay both large and bright in terms of the millimeter continuum emission. This hypothesis is also in line with recent results from a high-resolution ALMA survey in Taurus (Long et al. 2018, 2019). Of the 32 disks observed at ∼16 AU resolution, all disks with a dust outer radius of at least 55 AU show detectable substructures (Long et al. 2019), whereas all disks without substructures are found to be small. Long et al. (2019) hypothesize that fast radial drift could be the cause of this dichotomy.

The disks in our sample are massive ($M_{\rm dust} = 10 - 200$ $\rm M_{\oplus}$) and should have been capable of forming gap-opening planets in the outer part of the disk. Using high-resolution observations of GW Lup (Sz 71), Zhang et al. (2018) inferred the presence of a $\sim$ 10 $\rm M_{\oplus}$ planet at 74 AU based on a gap in the continuum emission. The six disks of our sample with $\rm R_{CO,\ obs}/R_{mm,\ obs} \geq 4$ have a much lower dust mass ($M_{\rm dust} = 0.4 - 10$ $\rm M_{\oplus}$) and could have been unable to form a gap-opening planet in their outer disk. Without these gaps acting as dust traps, radial drift would be unimpeded, leading to a compact disk of millimeter-sized grains and a large gas–dust size difference.

Alternatively, the disks in our sample could have a higher level of CO underabundance, and therefore a lower total CO content, which would explain their low $\rm R_{CO,\ obs}/R_{mm,\ obs}$ (see, e.g., Section 3.3.3; Trapman et al. 2019). Being both large and massive, the disks in our sample are expected to be cold, leading to a larger fraction of CO being frozen out. A lower total CO content leads to a smaller $\rm R_{CO}$ and a lower $\rm R_{CO}/R_{mm}$.

Being compact and less massive, the six disks with $\rm R_{CO,\ obs}/R_{mm,\ obs} \geq 4$ are expected to be warmer. In these disks it would be harder to keep CO frozen out on the grains, lowering the effectiveness of the processes suggested to be responsible for the observed CO underabundance (see Section 3.3.3 and references therein). The lack of a CO underabundance would result in larger $\rm R_{CO}$ and a higher $\rm R_{CO}/R_{mm}$. However, Miotello et al. 2017 showed that Sz 90, J15450887 - 3417333, Sz 69, and Sz 130 have $\Delta_{\rm gd} \geq 10$, indicating that they have a similar level of CO underabundance to the ten disks in our sample.

3.6 Conclusions

In the present study, the observed gas and dust size dichotomy in protoplanetary disks was studied in order to investigate the occurrence of common radial drift and radially dependent grain growth across the Lupus disk population. The gas structure of a sample of ten disks in the Lupus star-forming regions was modeled in detail using the thermochemical code DALI (Bruderer et al. 2012; Bruderer 2013), incorporating the effects of CO isotope-selective processes (Miotello et al. 2014). Surface density structures were based on modeling of the continuum emission by Tazzari et al. (2017). The total CO content of the models was fitted using integrated ^{13}CO fluxes to account for either gas depletion or CO underabundance. Noise was added to the synthetic ^{12}CO emission maps and gas and dust outer radii were measured from synthetic ^{12}CO and 1.3 millimeter emission maps using the same steps used to measure these quantities from the observations. From comparisons of our model gas and dust outer radii to the observations, we draw the following conclusions:

- For five disks (Sz 98, Sz 71, J16000236 - 4222115, Sz 129 and Sz 65) we find $\rm R_{CO,\ obs}/R_{mm,\ obs} > R_{CO,\ mdl}/R_{mm,\ mdl}$. For these disks we need both dust evolution and optical depth effects to explain the observed gas–dust size difference.

- For five disks (Sz 133, MY Lup, Sz 68, Sz 84 and Sz 100), the observed $\rm R_{CO,\ obs}/R_{mm,\ obs}$ lies within the uncertainties on $\rm R_{CO,\ mdl}/R_{mm,\ mdl}$ due to noise. For these disks the observed gas–dust size difference can be explained using optical line effects only.

- We identify six disks without a measured $\mathrm{R_{CO}}$ that show significant ($\mathrm{S/N} \geq 3$) ^{12}CO $J = 2 - 1$ emission beyond $4 \times \mathrm{R_{mm}}$. These disks likely have $\mathrm{R_{CO}/R_{mm}} \gg 4$, which would be difficult to explain without substantial dust evolution.

- The wide range of noisy $\mathrm{R_{CO,\ mdl}}$ measured for the two smallest disks in our sample show that care should be taken when measuring the gas disks size of faint compact disks using a curve of growth method.

Our analysis shows that most of the disks in our sample, which represent the bright end of the Lupus disk population, are consistent with radial drift and grain growth. Furthermore, we also find six faint disks with ^{12}CO emission beyond four times their dust disk size, suggesting that radial drift is a common feature among bright and faint disks. For both cases, our analysis is limited by the sensitivity of current disk surveys. More sensitive disk surveys that integrate 5 - 10 minutes per source are required to obtain a complete picture of radial drift and grain growth in “typical disks” in young star-forming regions.

Appendix

3.A Keplerian masking

Analysis of the gas emission of protoplanetary disks is often performed using the moment-zero map, which is obtained by integrating the observed spectral cube along the velocity axis. The velocity range for the integration is set by the maximum velocity offset (positive and negative) relative to the source velocity where emission of the disk is still observed. This leads to broad velocity integration range, whereas in the outer regions of the disk line emission is coming from a much more narrower velocity range. The S/N in these regions can therefore be improved if the integration is limited to only those channels containing emission.

This method of improving the S/N of moment-zero maps has already been used (e.g., Salinas et al. 2016; Carney et al. 2017; Bergner et al. 2018; Loomis et al. 2018). Yen et al. (2016) developed a similar method whereby spectra are aligned at different positions in the disk by shifting them by the projected Keplerian velocities at their positions and are then stacked. Their method produces an aligned spectrum with increased S/N, well suited for detecting emission not seen in individual channels (e.g., Yen et al. 2018).

The masking method works for observed line emission from a source with a known, ordered velocity pattern. In the case of protoplanetary disks, this is the Keplerian rotation around the central star. Using prior knowledge of this rotation pattern, voxels of the spectral cube can be selectively included in the analysis of the data, for example when making a moment-zero map, based on the criterion

$$|V_{\mathrm{kep}}(\alpha, \delta) - V_{\mathrm{voxel}}| \leq \frac{1}{2} \cdot \text{channel width.} \tag{3.4}$$

Here, V_{kep} is the Keplerian velocity at the coordinates (RA, Dec) $= (\alpha, \delta)$ and V_{voxel} is the velocity coordinate of the voxel.

3.A.1 Implementation

Calculate the projected Keplerian velocity pattern

In order to calculate the Keplerian velocities at a given point p with coordinates (α, δ) in the observed image, the coordinates of p first have to be projected onto the 2D local frame of the source. For a source with an observed position angle PA and inclination i at a distance d this coordinate transformation is given by

$$x = \frac{1}{\cos i}\left((\alpha - \alpha_0)\cos PA + (\delta - \delta_0)\sin PA\right) \cdot d \tag{3.5}$$

$$y = \left(-(\alpha - \alpha_0)\sin PA + (\delta - \delta_0)\cos PA\right) \cdot d. \tag{3.6}$$

Here α, δ are the right ascension and declination of the point p and (α_0, δ_0) is the location of the center of the source.

Using the local coordinates x, y the Keplerian velocity at p can be calculated using

$$V_{\text{kep}} = \sqrt{\frac{GM_*}{r}}; \quad r = \sqrt{x^2 + y^2}. \tag{3.7}$$

Here G is the gravitational constant, M_* is the stellar mass, and r is the deprojected radial distance from the star.

To convert the Keplerian velocity back to the velocity at which the emission will be observed, it has to be projected along the line of sight:

$$V_{\text{proj}} = -V_{\text{kep}} \sin i \frac{y}{r} + V_{\text{sys}}, \tag{3.8}$$

where V_{sys} is the systematic velocity of the source.

Selecting voxels containing emission

For a given point $p = (\alpha, \delta)$ equation (3.8) gives the expected velocity of the emission. Based on this information a Keplerian mask can be created by selecting a voxel nml for the Keplerian mask if

$$|V_{\text{proj}}(\alpha_n, \delta_m | M_*, PA, i, \alpha_0, \delta_0, V_{\text{sys}}) - V_l| \leq \frac{1}{2}\Delta V_{\text{width}} + \Delta V_{int}. \tag{3.9}$$

Here α_n, δ_m, V_l are the coordinates of the voxel and ΔV_{width} is the channel width. Further, ΔV_{int} is introduced in Eq. (3.9) to compensate for the fact that using a Keplerian rotation profile is a simplification that is only valid if the disk is geometrically thin and the rotation is purely Keplerian. In reality, the line emission is more likely to originate from layers higher in the (often flared) disk (e.g., Dutrey et al. 2014). As a result a single pixel, representing a single line of sight through the disk, contains contributions from different vertical layers at project velocities that are offset from the Keplerian rotation velocity of the midplane.

Here ΔV_{int} is left as a free parameter with no radial dependence in order to make no assumptions on the vertical structure of the disk. However, such a dependence could be introduced. For example Yen et al. (2016) use the empirically fitted description for ΔV_{int} from Piétu et al. (2007).

Convolving the mask

After the mask is set up, it is convolved with the beam to include the effects of resolution on the channel maps. We note that this effect is only relevant if the smearing by the beam is much larger than the width of the channel.

Clipping the mask

In order to ensure flux conservation in the masked region, a final step has to be made. After the convolution in the previous step, the pixels of the mask now have weights ≤ 1. The mask is therefore converted back into a boxcar function according to

$$M_{\text{clipped}}(\alpha_n, \delta_m, V_l) = \begin{cases} 1 & M(\alpha_n, \delta_m, V_l) \leq \text{cutoff} \\ 0 & \text{else}, \end{cases} \tag{3.10}$$

where M is the mask after step 3 and the cutoff is set to 0.05 of the peak value.

3.A.2 Making moment-zero maps and calculating noise

After the mask has been produced following the steps mentioned above, it can be applied to the data. The moment-zero map can be calculated following

$$\text{Mom } 0(\alpha_n, \delta_m) = \sum_{l=0}^{L} M_{\text{clipped}}(\alpha_n, \delta_m, V_l) \times I(\alpha_n, \delta_m, V_l), \tag{3.11}$$

where $I(\alpha_n, \delta_m, V_l)$ is the observed spectral cube and V_0 and V_L are the minimum and maximum velocities of the spectral cube respectively.

In a similar manner, a map of the expected noise levels in the moment-zero map can be calculated. As a result of the masking, individual pixels will have different noise characteristics depending on how many nonzero voxels in the mask are summed over (cf. Eq. (3.11). Using the fact that the noise between individual channels is independent, a 2D noise map can be created using

$$N(\alpha_n, \delta_m) = \text{RMS} \times \sqrt{\sum_{l=0}^{L} \left(M_{\text{clipped}}(\alpha_n, \delta_m, V_l)\right)^2}, \tag{3.12}$$

where RMS is the root mean square noise taken from an empty channel.

As a result of the term in the square root, the S/N defined as $\text{S/N} \equiv \text{Mom } 0/N$ can be increased by not clipping the mask (Section 3.A.1), but this comes at the cost of a reduced total flux in the moment-zero map. This difference can be understood by the fact that the convolved mask provides lower weights (w_{nml}) for voxels that are expected to contain very little flux with respect to the noise in that pixel. In the noise, these voxels are almost excluded due to the term w_{nml}^2 in Eq (3.12), resulting in a lower noise for that pixel. In the moment-zero map however, the flux in these voxels is also scaled down by a factor w_{nml}. As $w_{nml} \leq 1$, flux is no longer conserved in this case.

3.A.3 Caveats

In step one of making the mask (Section 3.A.1), a simplification is made in that a single velocity can be assigned to a pixel, i.e., that the velocity gradient over the length of pixel is small. At the center this simplification breaks down. To circumvent this problem the center pixel can be included in all channels.

We note that as a consequence the S/N in the center part decreases to the pre-masked values. For most sources this is not a significant problem, as the S/N is usually highest at the center where the source is brightest.

3.A.4 The Keplerian mask parameters of our sample

Here we outline the Keplerian mask used in this work. As shown in Eq. (3.9) the Keplerian mask is described by seven parameters: the stellar mass (M_*), the orientation of the disk (PA, i), the three coordinate centroids ($\alpha_0, \delta_0, V_{\rm sys}$), and the free parameter $\Delta V_{\rm int}$. For the stellar masses we use the observations and methods presented in Alcalá et al. (2014, 2017), but rescaled to the new *Gaia* DR2 distances (Brown et al. 2018, see also Appendix A of Manara et al. 2018). The position angle, inclination, and centroid were taken from the observations of the millimeter continuum (cf. Tables 1 and 2 in Tazzari et al. 2017). The final two parameters, $V_{\rm sys}$ and $\Delta V_{\rm int}$, were obtained by varying them to maximize the total S/N in the moment-zero map. The mask parameters of the ten sources in our sample plus the eight sources with resolved continuum emission described in Section 3.5.1 are presented in Table 3.2

Table 3.2: Keplerian masks

Name	M_* ($M_\odot$)	PA (deg)	i (deg)	α_0 (J2000)	δ_0 (J2000)	$V_{\rm sys}$ (km s^{-1})	$\Delta V_{\rm int}$ (km s^{-1})
Sz 133	0.63	126	79	16:03:29.4	-41:40:02.1	4.22	0.83
Sz 98	0.67	112	47	16:08:22.5	-39:04:46.8	2.81	0.62
MY Lup	1.09	59	73	16:00:44.5	-41:55:31.3	4.5	1.11
Sz 71	0.41	38	41	15:46:44.7	-34:30:36.1	3.2	0.7
J16000236	0.23	160	66	16:00:02.3	-42:22:15.0	4.0	0.65
Sz 129	0.78	155	32	15:59:16.5	-41:57:10.7	4.2	0.36
Sz 68	2.13	176	33	15:45:12.8	-34:17:31.0	4.9	0.6
Sz 100	0.14	60	45	16:08:25.7	-39:06:01.6	1.9	1.2
Sz 65	0.7	109	61	15:39:27.8	-34:46:17.6	4.4	0.89
Sz 84	0.17	167	74	15:58:02.5	-37:36:03.1	5.2	1.6
J15450887	0.14	2	36	15:45:08.9	-34:17:33.8	4.5	0.9
J16085324	0.02	100	61	16:08:53.2	-39:14:40.5	3.0	1.0
Sz 69	0.2	124	44	15:45:17.4	-34:18:28.7	5.3	0.8
Sz 83	0.67	164	3	15:56:42.3	-37:49:15.8	4.23	0.2
Sz 90	0.78	123	61	16:07:10.1	-39:11:03.6	3.2	0.83
Sz 73	0.78	95	50	15:47:56.9	-35:14:35.2	4.1	0.93
Sz 114	0.19	149	16	16:09:01.8	-39:05:12.8	5.0	0.28
J16124373	0.45	23	44	16:12:43.7	-38:15:03.4	4.0	0.75
J16102955	0.2	119	67	16:10:29.5	-39:22:14.8	3.5	1.2

3.B Influence of dust settling and flaring

In our models we have kept the disk vertical structure fixed. In addition we assume a single height and mass fraction of large grains (cf. Section 3.3.3 and 3.3.3). The vertical structure and the distribution of the large grains set both the temperature structure and the chemistry. Varying them could therefore change the ^{13}CO 3 - 2 flux used to determine the total CO content and the shape of ^{12}CO intensity profile from which we measure $\mathrm{R_{CO}}$. We examine the effect of varying the vertical structure and the distribution of the large grains on $\mathrm{R_{CO}}$ for two disks in our sample that represent two completely different physical structures: Sz 68 (compact, strong CO flux, ^{13}CO optically thick) and Sz 98 (large, weak CO flux, ^{13}CO optically thin).

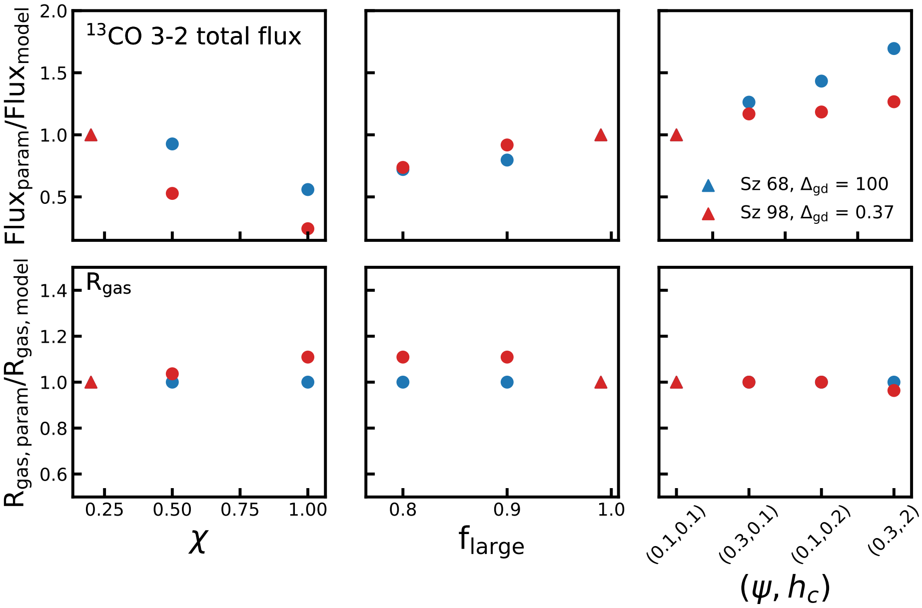

Figure 3.7: Effects of vertical structure and the large grains. **Top panels:** Integrated ^{13}CO flux as function of large grain settling (χ), fraction of large grains (f_{large}) and disk vertical structure ($h = h_c(R/R_c)^{\psi}$). The models for Sz 98 and Sz 68 are shown in red and blue respectively. Triangle markers denote the value used in the rest of this work (cf. Sections 3.3.3 and 3.3.3). **Bottom panels:** As top panels, but showing the variations of the gas outer radius $\mathrm{R_{CO}}$.

The results are shown in Figure 3.7. The top three panels show the effect on the ^{13}CO integrated flux used to determine the total CO content of the disk (cf Section 3.3.3). Increasing the vertical extent of the large grains (χ) lowers the ^{13}CO flux by up to ~40% for the optically thin Sz 98 and up to ~80% for the optically thick Sz 68. This is likely due to the dust becoming optically thick at millimeter wavelengths higher up in the disk. Decreasing the mass fraction of large grains (f_{large}) also lowers the ^{13}CO flux, up to ~25% for both disks. Changing either χ or f_{large} would require increasing the total CO content to reproduce the ^{13}CO flux, which would increase $\mathrm{R_{CO}}$.

Changing the vertical structure of the disk by either increasing the amount of flaring or increasing the scale height of the disk will lead by to an increase in the observed ^{13}CO integrated flux. Both parameters directly affect the amount of stellar light intercepted by the disk, leading to a higher temperature. The ^{13}CO flux is increased by up to ∼20% for Sz 68 and up to ∼65% for Sz 98. Increasing either the flaring or the scale height would mean a lower total CO content is needed to match the observed ^{13}CO flux, leading to a smaller $R_{\rm CO}$ (cf. Trapman et al. 2019).

The bottom three panels of Figure 3.7 show how $R_{\rm CO}$ is affected by changes in $f_{\rm large}$, χ, h_c, Ψ. For Sz 98 the gas outer radius increases by less than 10% if either $f_{\rm large}$ or χ is changed and the $R_{\rm CO}$ of Sz 68 is not affected at all. Changing the vertical structure of either disk changes the derived $R_{\rm gas}$ by less than 5%. The vertical structure does affect the ^{12}CO intensity profile, but the relative changes remain nearly constant over the extent of the disk. As a result the curve of growth and the inferred $R_{\rm gas}$ remain unaffected.

3.C ^{12}CO $J = 2 - 1$ emission maps of 17 sources

In total, 48 disks in Lupus were detected in ^{12}CO $J = 2 - 1$. In this work we analyzed ten of these disks in detail (referred to as the high S/N sample) and showed ^{12}CO $J = 2 - 1$ emission maps of six more disks (part of the low S/N sample; see Section 3.5.1). Here we show the ^{12}CO $J = 2 - 1$ emission maps of the remaining disks of the low S/N sample. From our analysis we exclude transition disks with clear resolved cavities. For a detail analysis of these disks, see van der Marel et al. (2018).

The remaining 17 disks with detected ^{12}CO emission can be divided into two groups. For 6 of the 17 disks the 1.3 millimeter continuum emission was resolved and we were able to measure $R_{\rm mm}$ (see also Tazzari et al. 2017). The top two rows of Figure 3.8 show the ^{12}CO 2 - 1 moment-zero maps for these six sources. Keplerian masking was applied to the data before making the moment-zero maps (cf. Section 3.3.4 and Appendix 3.A).

Sz 83, also known as RU Lup, is a notable inclusion here. This disk is the third-most brightest continuum source in Lupus and has been readily detected in ^{12}CO, ^{13}CO, and C^{18}O. Furthermore, RU Lup has also been observed at high spatial resolution as part of the DSHARP program (Andrews et al. 2018a). It seems therefore odd that $R_{\rm CO}$ has not been measured for this source. A closer inspection of the ^{12}CO channel maps reveals that a component of the emission is nonKeplerian and could be a possible outflow (see Appendix C in Ansdell et al. 2018). Keplerian masking has removed part of the emission but enough remains in the moment-zero map to prevent us from measuring $R_{\rm CO}$.

There are 11 disks that are detected in ^{12}CO but for which the 1.3 millimeter continuum emission is not resolved at a resolution of $0\farcs25$. These are shown in the bottom four rows of Figure 3.8. We exclude three disks from our analysis: J16011549 - 4152351 is resolved in the continuum, but the ^{12}CO channel maps show significant cloud emission even after applying Keplerian masking. J16070384 - 3911113 and J16090141 - 3925119 are resolved but have irregular shaped continuum emission and are possibly unresolved binary sources (cf. Tazzari et al. 2017).

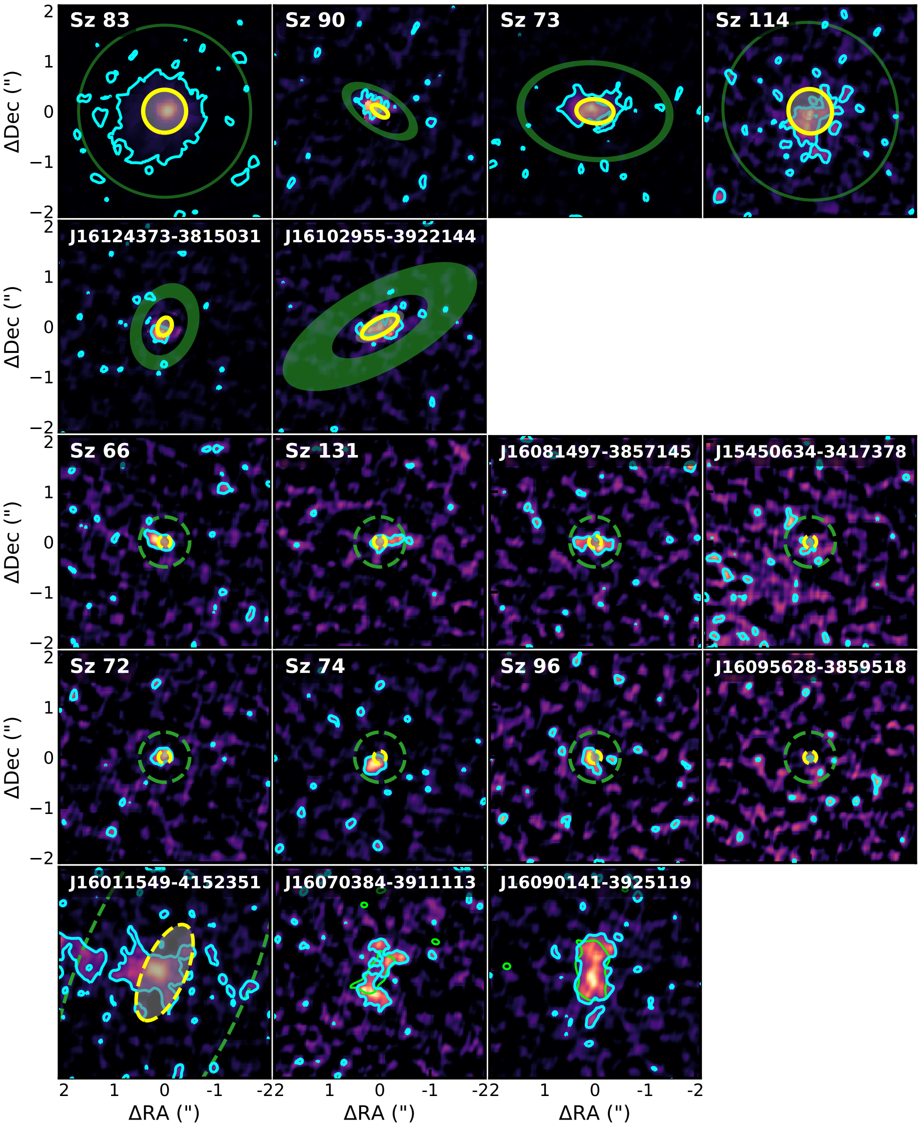

Figure 3.8: ^{12}CO moment-zero maps of the 17 sources that were detected at low S/N, referred to as the low S/N sample in this work. Cyan contours show significant (S/N ≥ 3) ^{12}CO emission. The top six disks have resolved continuum emission and their $R_{\mathrm{mm,\ obs}}$ is shown by the yellow ellipse. For these sources, Keplerian masking was applied to the ^{12}CO $J = 2-1$ emission (see Appendix 3.A). The middle eight disks (Sz 66 to J16095628) have unresolved continuum emission. The dashed yellow circle shows the size of the beam ($0\farcs25$) as an upper limit to the dust disk size. Similarly, the dashed green circle shows four times the beamsize. For J16011549 the continuum is resolved and R_{dust} was calculated from 90% of the total flux. The continuum emission of J16070384 and J16090141 is resolved but irregular in shape. Here, we show the 3σ contours of the continuum in green.

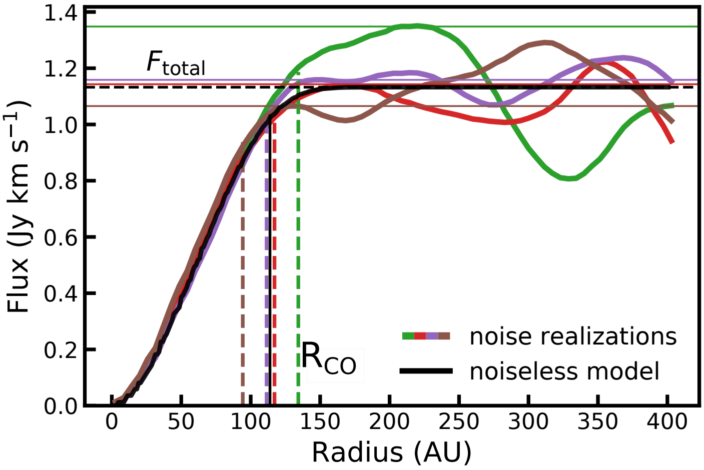

Figure 3.9: Curve of growth of the ^{12}CO 2 - 1 emission for the Sz 129 model for four different and extreme noise realizations chosen to show the range of effects that noise can have on measuring the outer radius. For each noise realization, the horizontal lines show the total flux and the dashed vertical line shows the calculated outer radius. The curve of growth, total flux, and outer radius of the noiseless model are shown in black.

3.D Measuring $\mathrm{R_{CO}}$ from noisy spectral cube

Here, we outline how noise was added to models to simulate its effect on measuring $\mathrm{R_{CO}}$ from our models. The procedure can be outlined in three steps. First a random patch of noise is added to each of the channels in the synthetic ^{12}CO spectral cube. The patch of noise is taken from one of the emission free channels in observed spectral cube. Care is taken to avoid the outer edges of the observed field of view in the random selection, as the noise levels there are not representative for the center of the observations.

Next, we construct a Keplerian mask using the same parameters that are used for the observations (cf. Table 3.2). By applying the Keplerian mask to the noisy model spectral cube we increase the S/N in the outer parts of the disk in the same manner as in the observations (cf. Section 3.3.4). The masked spectral cube is summed over the velocity axis to create the ^{12}CO moment-zero map.

Finally, the gas outer radius is measured from the noisy moment-zero map. By definition, $\mathrm{R_{CO}}$ is the radius that encloses 90% of the total flux ($F_{\rm tot}$). In noiseless case, the curve of growth converges to $F_{\rm tot}$ at large radii. In the presence of noise the curve of growth can show variations at large radii, making it difficult to determine $F_{\rm tot}$ (cf. Figure 3.9). Empirically, we find that using the flux at the first peak in the curve of growth in most cases most closely matches $F_{\rm tot}$ of the noiseless case. At an average peak S/N$\sim$ 8 of the ^{12}CO moment-zero map, noise has a significant effect on measuring $\mathrm{R_{CO}}$. As an example, Figure 3.9 shows the curve of growths for four noise realizations for the Sz 129 disk model. As shown in the figure, the curve of growth varies between each noise realization and all four have different $F_{\rm tot}$ and different $\mathrm{R_{CO}}$.

3.E Radial 890 μm continuum profiles

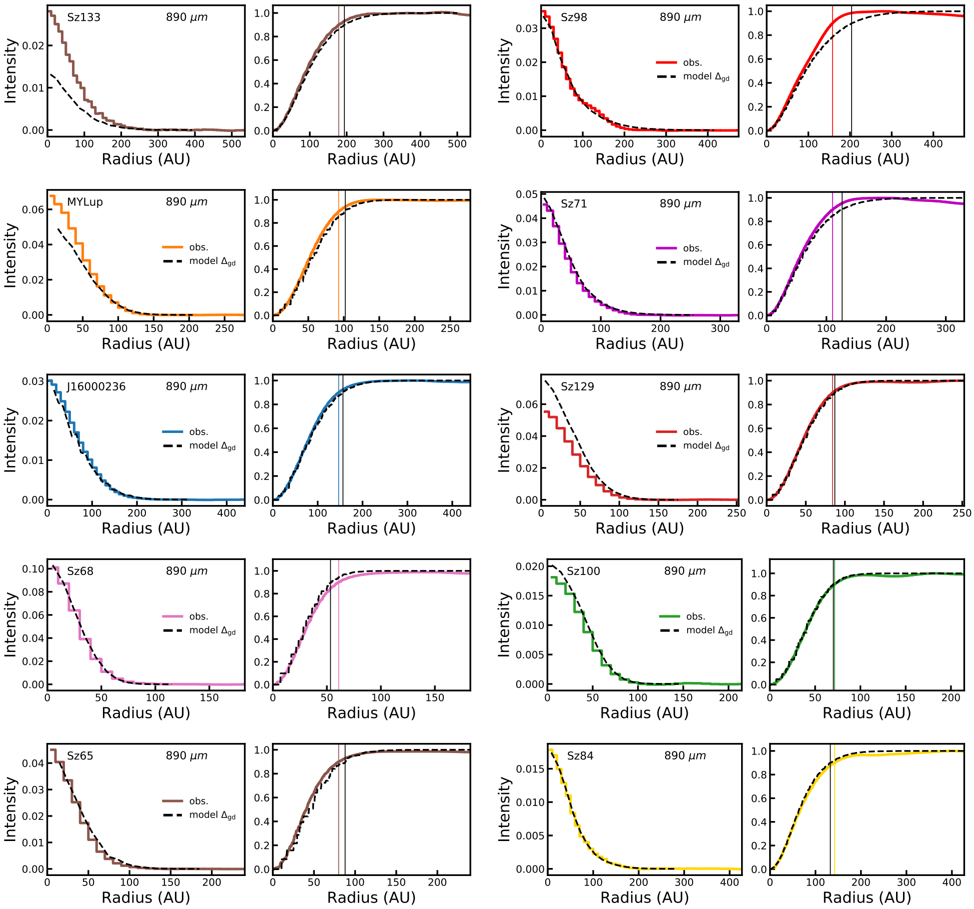

Figure 3.10: Comparison between model and observed 890 μm continuum intensity profiles for the ten sources in our sample. For each source, the left panel shows the intensity profile and the right panel shows the matching normalized curve of growth for both the model (black, dashed) and the observation (colored, solid). Vertical lines in the right panels show the radius that encloses 90% of the total flux ($\mathrm{R}_{890\,\mu\mathrm{m}}$). We note that the curve of growth of the model and the observation are normalized separately as the total flux is unimportant when measuring $\mathrm{R}_{890\,\mu\mathrm{m}}$.

3.F Noisy R$_{\mathrm{CO}}$ distributions for the disks in our sample

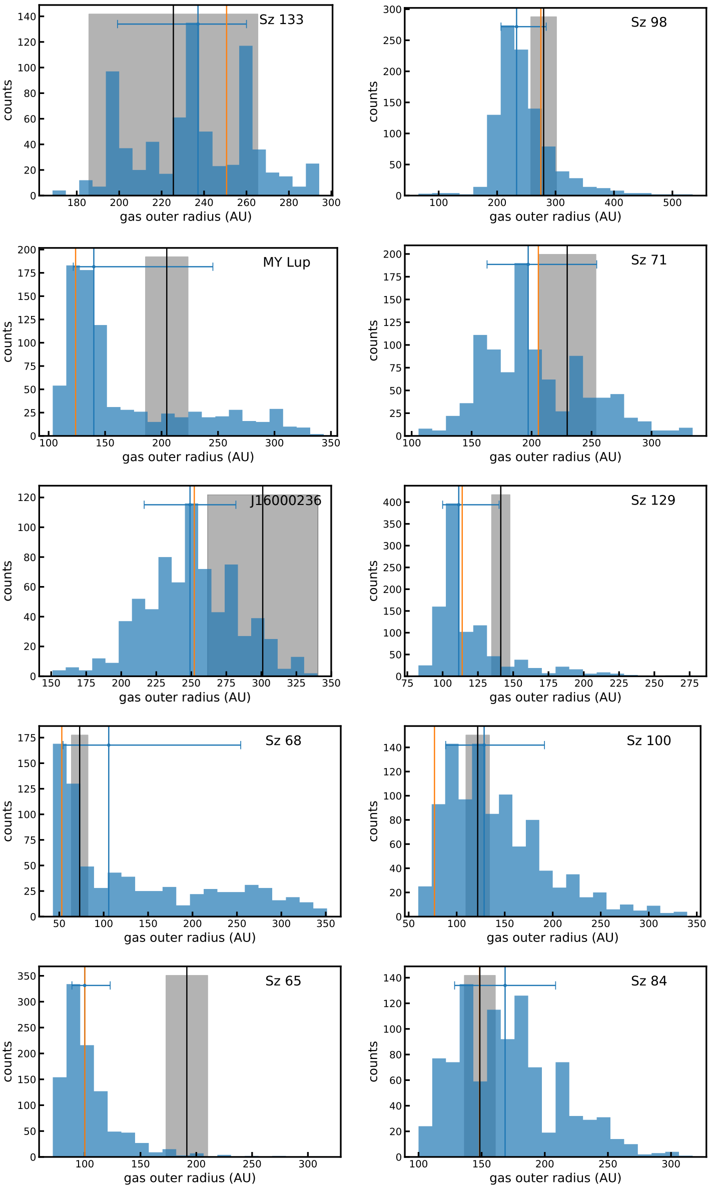

Figure 3.11: Histogram of possible R$_{\mathrm{CO}}$ if noise is included in the model. The 16$^{\mathrm{th}}$ quantile and the 84$^{\mathrm{th}}$ quantile are shown by the blue errorbar, with the median shown as a blue vertical line. Orange vertical line shows R$_{\mathrm{CO}}$ of the noiseless model. The observed R$_{\mathrm{CO}}$ and uncertainties are shown in black.

4

Observed sizes of planet-forming disks trace viscous spreading

L. Trapman, G. Rosotti, A. D. Bosman, M. R. Hogerheijde and E. F. van Dishoeck,
2020, A&A, 640, 4

Abstract

Context: The evolution of protoplanetary disks is dominated by the conservation of angular momentum, where the accretion of material onto the central star is fed by the viscous expansion of the outer disk or by disk winds extracting angular momentum without changing the disk size. Studying the time evolution of disk sizes therefore allows us to distinguish between viscous stresses or disk winds as the main mechanism of disk evolution. Observationally, estimates of the size of the gaseous disk are based on the extent of CO submillimeter rotational emission, which is also affected by the changing physical and chemical conditions in the disk during the evolution.

Aims: We study how the gas outer radius measured from the extent of the CO emission changes with time in a viscously expanding disk. We also investigate to what degree this observable gas outer radius is a suitable tracer of viscous spreading and whether current observations are consistent with viscous evolution.

Methods: For a set of observationally informed initial conditions we calculated the viscously evolved density structure at several disk ages and used the thermochemical code `DALI` to compute synthetic emission maps, from which we measured gas outer radii in a similar fashion as observations.

Results: The gas outer radii ($R_{\mathrm{CO,\ 90\%}}$) measured from our models match the expectations of a viscously spreading disk: $R_{\mathrm{CO,\ 90\%}}$ increases with time and, for a given time, $R_{\mathrm{CO,\ 90\%}}$ is larger for a disk with a higher viscosity α_{visc}. However, in the extreme case in which the disk mass is low ($M_{\mathrm{disk}} \leq 10^{-4}$ M$_{\odot}$) and α_{visc} is high ($\geq 10^{-2}$), $R_{\mathrm{CO,\ 90\%}}$ instead decreases with time as a result of CO photodissociation in the outer disk. For most disk ages, $R_{\mathrm{CO,\ 90\%}}$ is up to$\sim$ 12× larger than the characteristic size R_{c} of the disk, and $R_{\mathrm{CO,\ 90\%}}/R_{\mathrm{c}}$ is largest for the most massive disk. As a result of this difference, a simple conversion of $R_{\mathrm{CO,\ 90\%}}$ to α_{visc} overestimates the true α_{visc} of the disk by up to an order of magnitude. Based on our models, we find that most observed gas outer radii in Lupus can be explained using viscously evolving disks that start out small ($R_{\mathrm{c}}(t = 0) \simeq 10$ AU) and have a low viscosity ($\alpha_{\mathrm{visc}} = 10^{-4} - 10^{-3}$).

Conclusions: Current observations are consistent with viscous evolution, but expanding the sample of observed gas disk sizes to star-forming regions, both younger and older, would better constrain the importance of viscous spreading during disk evolution.

4.1 Introduction

Planetary systems form and grow in protoplanetary disks. These disks provide the raw materials of gas and dust to form the increasingly diverse population of exoplanets and planetary systems that has been observed (see, e.g. Benz et al. 2014; Morton et al. 2016; Mordasini 2018). The formation of planets and the evolution of protoplanetary disks are closely related. While planets are forming, the disk is evolving around them, affecting the availability of material and providing constantly changing physical conditions around the planets. In a protoplanetary accretion disk, material is transported through the disk and accreted onto the star. We are still debating exactly which physical process dominates the angular momentum transport and drives the accretion flow, which is a crucial part of disk evolution.

It is commonly assumed that disks evolve under the influence of an effective viscosity, where viscous stresses and turbulence transport angular moment to the outer disk (see, e.g. Lynden-Bell & Pringle 1974; Shakura & Sunyaev 1973). As a consequence of the outward angular momentum transport, the bulk of the mass moves inward and is accreted onto the star. The physical processes that constitute this effective viscosity are still a matter of debate, magnetorotional instability being the most accepted mechanism (see, e.g. Balbus & Hawley 1991, 1998).

An alternative hypothesis is that angular momentum can be removed by disk winds rather than being transported through the disk (see, e.g. Turner et al. 2014 for a review). The presence of a vertical magnetic field in the disk can lead to the development of a magnetohydrodynamic (MHD) disk wind. These disk winds remove material from the surface of the disk and are thus able to provide some or all of the angular momentum removal required to fuel stellar accretion (see, e.g. Ferreira et al. 2006; Béthune et al. 2017; Zhu & Stone 2018). Direct observational evidence of such disk winds focuses on the inner part of the disk, but it is unclear whether winds dominate the transport of angular momentum and therefore how much winds affect the evolution of the disk (see, e.g. Pontoppidan et al. 2011; Bjerkeli et al. 2016; Tabone et al. 2017; de Valon et al. 2020).

Observationally these two scenarios make distinctly different predictions on how the sizes of protoplanetary disks evolve over time. In the viscous disk theory, conservation of angular momentum ensures that some parts of the disk move outward. As a result, disk sizes should grow with time. If instead disk sizes do not grow with time, disk winds are likely to drive disk evolution. To distinguish between viscous evolution and disk winds we need to define a disk size, which has to be measured or inferred from observed emission, and we must examine how it changes as a function of disk age.

With the advent of the Atacama Large Millimeter/sub-Millimeter Array (ALMA) it has become possible to perform large surveys of protoplanetary disks at high angular resolution. This has resulted in a large number of disks for which the extent of the millimeter continuum emission, the dust disk size, can be measured (see, e.g. Barenfeld et al. 2017; Cox et al. 2017; Tazzari et al. 2017; Ansdell et al. 2018; Cieza et al. 2018; Long et al. 2019). However, this continuum emission is predominantly produced by millimeter-sized dust grains, which also undergo radial drift as a result of the drag force from the gas, an inward motion that complicates the picture. Moreover, radial drift and radially dependent grain growth lead to a dependence between the extent of the continuum emission and the wavelength of the observations; emission at longer wavelengths is more compact (see e.g. Tripathi et al. 2018).

Rosotti et al. (2019b) used a modeling framework to study the combined effect of radial drift and viscous spreading on the observed dust disk sizes. They determined that to measure viscous spreading, the dust disk size has to be defined as a high fraction ($\geq$ 95%) of the total continuum flux. To ensure that this dust disk size is well characterized, the dust continuum has to be resolved a signal-to-noise ratio (S/N). These authors show that existing surveys lack the sensitivity to detect viscous spreading.

To avoid having to disentangle the effects of radial drift from viscous spreading, we can instead measure a gas disk size from rotational line emission of molecules such as CO and CN, which are commonly observed in protoplanetary disks. An often used definition for the gas disk size is the radius that encloses 90% of the total CO $J = 2 - 1$ flux ($R_{\rm CO,\ 90\%}$; see, e.g. Ansdell et al. 2018). This radius encloses most ($>$ 98%) of the disk mass and it has been shown that $R_{\rm CO,\ 90\%}$ is not affected by dust evolution (Trapman et al. 2019). The longer integration time required to detect this emission in the outer disk means that significant samples of measured gas disk sizes are only now becoming available (see, e.g. Barenfeld et al. 2017; Ansdell et al. 2018). Using a sample of measured gas disk sizes collated from literature, Najita & Bergin (2018) show tentative evidence that older Class II sources have larger gas disk sizes that the younger Class I sources; this is consistent with expectations for viscous spreading. It should be noted however that the gas disk sizes in their sample were measured using a variety of different tracers and observational definitions of the gas disk size.

When searching for viscous spreading using measured gas disk sizes it is important to keep in mind that these gas disk sizes are an observed quantity that are measured from molecular line emission. As the disk evolves, densities and temperatures change, affecting the column densities and excitation levels of the gas tracers used to measure the disk size. How well the observed gas outer radius traces viscous expansion has not been investigated in much detail.

Time-dependent chemistry also affects the gas tracers such as CO that we use to measure gas disk sizes. At lower densities CO, found in the outer disk and at a few scale heights above the midplane of the disk, is destroyed through photodissociation by UV radiation. Trapman et al. (2019) show that $R_{\rm CO,\ 90\%}$ traces the point in the outer disk where CO becomes photodissociated. Deeper in the disk, around the midplane where the temperature is low, CO freezes out onto dust grains. Once frozen out, CO can be converted into other molecules such as $\rm CO_2$, $\rm CH_4$ and $\rm CH_3OH$ (see, e.g. Bosman et al. 2018; Schwarz et al. 2018). These molecules have higher binding energies than CO and therefore stay frozen out at temperatures at which CO would normally desorb back into the gas phase. Through this process gas-phase CO can be more than an order of magnitude lower than the abundance of 10^{-4} with respect to molecular hydrogen, which is the expected abundance at which most of the volatile carbon is contained in CO (see, e.g. Lacy et al. 1994).

In this work, we set up disk models with observationally informed initial conditions, let the surface density evolve viscously, and use the thermochemical code `DALI` (Bruderer et al. 2012; Bruderer 2013) to study how the CO $J = 2 - 1$ intensity profiles, and the gas disk sizes derived from these profiles, change over time. We then compare these values with existing observations to see if the observations are consistent with viscous evolution. This work is structured as follows: We introduce the setup and assumptions in our modeling in Section 4.2. In Section 4.3 we show how well observed gas outer radii trace viscous evolution both qualitatively and quantitatively.

In Section 4.4 we compare our models to observations. We also study how chemical CO depletion through grain-surface chemistry affects our results. We discuss whether external photo-evaporation could explain the small observed gas disk sizes, compare our results to disk evolution driven by magnetic disks winds, and we discuss whether including episodic accretion would affect our results. We conclude in Section 4.5 that measured gas outer radii can be used to trace viscous spreading in disks.

4.2 Model setup

The gas disk size is commonly obtained from CO rotational line observations, for example, by measuring the radius that encloses 90% of the CO flux (e.g. Ansdell et al. 2018) or by fitting a power law to the observed visibilities (e.g. Barenfeld et al. 2017). In this work we used the radius that encloses 90% of the ^{12}CO 2-1 flux ($R_{\mathrm{CO},\ 90\%}$) as the definition of the observed gas disk size. Trapman et al. (2019) show that $R_{\mathrm{CO},\ 90\%}$ traces a fixed surface density in the outer disk, where CO becomes photodissociated. To see if $R_{\mathrm{CO},\ 90\%}$ is a suitable tracer of viscous evolution, we are therefore interested in how the extent of the ^{12}CO intensity changes over time in a viscously evolving disk.

Our approach for setting up our models is the following. First, we obtained a set of initial conditions that reproduce current observed stellar accretion rates, assuming that the disks feeding the stellar accretion have evolved viscously. Next we calculated the time evolution of the surface density. For each set of initial conditions, we analytically calculated the surface density profile ($\Sigma(R,t)$) at ten different disk ages. For each of these time steps we used the thermochemical code Dust and Lines (`DALI`; Bruderer et al. 2012; Bruderer 2013) to calculate the current temperature and chemical structure of the disk at that age and created synthetic emission maps of ^{12}CO, from which we measured $R_{\mathrm{CO},\ 90\%}$.

4.2.1 Viscous evolution of the surface density

Accretion disks in which the disk structure is shaped by viscosity are often described using a $\alpha-$disk formalism (Shakura & Sunyaev 1973), parameterizing the kinematic viscosity as $\nu = \alpha c_s H$, where c_s is the sound speed and H is the height above the midplane (Pringle 1981). For an $\alpha-$disk, the self-similar solution for the surface density Σ is given by (Lynden-Bell & Pringle 1974; Hartmann et al. 1998)

$$\Sigma_{\mathrm{gas}}(R) = \frac{(2-\gamma)\,M_{\mathrm{disk}}(t)}{2\pi R_{\mathrm{c}}(t)^2}\left(\frac{R}{R_{\mathrm{c}}(t)}\right)^{-\gamma}\exp\left[-\left(\frac{R}{R_{\mathrm{c}}(t)}\right)^{2-\gamma}\right], \tag{4.1}$$

where γ is set by assuming that the viscosity varies radially as $\nu \propto R^{\gamma}$ and M_{disk} and R_{c} are the disk mass and the characteristic radius, respectively.

Following Hartmann et al. (1998), the time evolution of M_{disk} and R_{c} is described by

$$M_{\mathrm{disk}}(t) = M_{\mathrm{disk}}(t=0)\left(1+\frac{t}{t_{\mathrm{visc}}}\right)^{-\frac{1}{[2(2-\gamma)]}} = M_{\mathrm{init}}\left(1+\frac{t}{t_{\mathrm{visc}}}\right)^{-\frac{1}{2}} \tag{4.2}$$

$$R_{\mathrm{c}}(t) = R_{\mathrm{c}}(t=0)\left(1+\frac{t}{t_{\mathrm{visc}}}\right)^{\frac{1}{(2-\gamma)}} = R_{\mathrm{init}}\left(1+\frac{t}{t_{\mathrm{visc}}}\right), \tag{4.3}$$

where $t_{\rm visc}$ is the viscous timescale and we defined short hands for the initial disk mass $M_{\rm init} \equiv M_{\rm disk}(t=0)$, the initial characteristic size $R_{\rm init} \equiv R_{\rm c}(t=0)$. For the second step and the rest of this work, we assumed $\gamma = 1$ since for a typical temperature profile it corresponds to the case of a constant $\alpha_{\rm visc}$.

Combining equations (4.1), (4.2), and (3) we obtain the time evolution of the surface density profile

$$\Sigma_{\rm gas}(t,R) = \frac{M_{\rm disk}(t)}{2\pi R_{\rm c}(t)^2}\left(\frac{R}{R_{\rm c}(t)}\right)^{-1} \exp\left[-\left(\frac{R}{R_{\rm c}(t)}\right)\right] \tag{4.4}$$

$$= \frac{M_{\rm init}}{2\pi R_{\rm init}^2}\left(1+\frac{t}{t_{\rm visc}}\right)^{-\frac{3}{2}}\left(\frac{R}{R_{\rm init}\left(1+\frac{t}{t_{\rm visc}}\right)}\right)^{-1} \tag{4.5}$$

$$\times \exp\left[-\left(\frac{R}{R_{\rm init}\left(1+\frac{t}{t_{\rm visc}}\right)}\right)\right]. \tag{4.6}$$

4.2.2 Initial conditions of the models

For a viscous disk the initial disk mass $M_{\rm init}$ is related to the stellar accretion rate through (Hartmann et al. 1998)

$$M_{\rm init} = 2t_{\rm visc}\dot{M}_{\rm acc}(t)\left(\frac{t}{t_{\rm visc}}+1\right)^{3/2}. \tag{4.7}$$

Under the assumption that the disk evolved viscously, we calculated $M_{\rm init}$ given the stellar accretion rate measured at a time t and the viscous timescale of the disk. For various star-forming regions, for example, Lupus and Chamaeleon I, stellar accretion rates were determined from observations (see, e.g. Alcalá et al. 2014, 2017; Manara et al. 2017). A correlation was found between the stellar mass M_* and the stellar accretion rate $\dot{M}_{\rm acc}$, best described by a broken power law. Based on equation (4.7) a disk around a more massive star therefore has a higher initial disk mass for the same viscous timescale.

For our models we considered three stellar masses: $0.1, 0.32,$ and $1.0\ \rm M_\odot$. For each stellar mass, we used the observations, presented in Figure 6 of Alcalá et al. (2017), to pick the average stellar accretion rate associated with that stellar mass. For each stellar accretion rate, we calculated the initial disk mass using equation (4.7) for three different viscous timescales. The viscous timescale is computed for three values of the dimensionless viscosity $\alpha_{\rm visc} = 10^{-2}, 10^{-3}, 10^{-4}$, assuming a characteristic radius of 10 AU (which is the radius we employed; see below) and a disk temperature $T_{\rm disk}$ of 20 K (see, e.g. equation 37 in Hartmann et al. 1998)

$$\frac{t_{\rm visc}}{\rm yr} = \frac{R_{\rm c}^2}{\nu} \simeq 8\times10^4\left(\frac{\alpha_{\rm visc}}{10^{-2}}\right)^{-1}\left(\frac{R_{\rm c}}{10\ \rm AU}\right)\left(\frac{M_*}{0.5\ \rm M_\odot}\right)^{1/2}\left(\frac{T_{\rm disk}}{10\ \rm K}\right)^{-1}. \tag{4.8}$$

The combination of three stellar accretion rates and three viscous timescales results in nine different disk models (see Table 4.1). Figure 4.1 shows how disk parameters such as $\dot{M}_{\rm acc}$, $R_{\rm c}$, and $M_{\rm disk}$ evolve with time for the models with $M_* = 0.1\ \rm M_\odot$. Similarly, Figure 4.9 shows how $M_{\rm disk}$ evolves for the models with $M_* = 0.32\ \rm M_\odot$ and

1.0 $M_\odot$. We note that the trends for $M_{\rm disk}$(t) are very similar, apart from starting at a higher initial $M_{\rm disk}$ ($\sim 10^{-2}$ $M_\odot$ for $M_* = 0.32$ $M_\odot$ and $\sim 10^{-1}$ $M_\odot$ for $M_* = 1.0$ $M_\odot$; cf. Table 4.1).

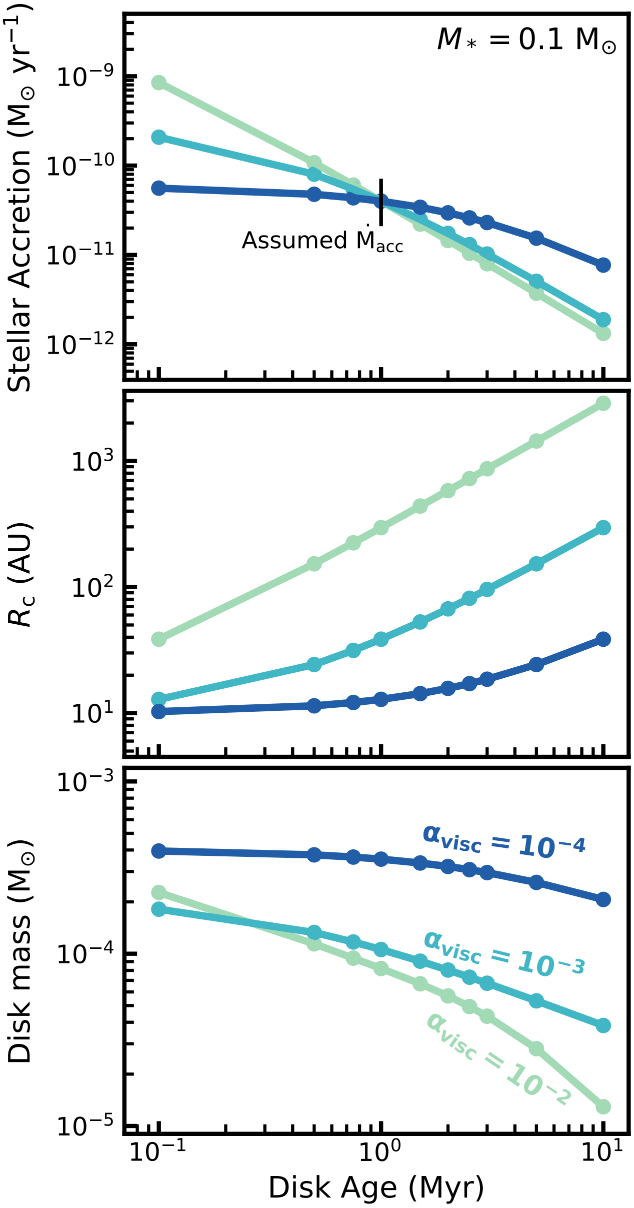

Figure 4.1: Evolution of the disk parameters for the models with $M_* = 0.1$ $M_\odot$. The colors show different $\alpha_{\rm visc}$. For reference, the viscous timescales are 0.046, 0.46, and 4.6 Myr for $\alpha_{\rm visc} = 10^{-2}, 10^{-3}$, and 10^{-4}, respectively. The evolution of the disk mass for the models with $M_* = 0.32$ $M_\odot$ and 1.0 $M_\odot$ is shown Figure 4.9. For the model with $\alpha_{\rm visc} = 10^{-2}$, $M_{\rm disk}$ starts out at higher mass compared to the model with $\alpha_{\rm visc} = 10^{-3}$, but this model also loses mass at a faster rate.

The initial size of disks is less well constrained, predominately because of a lack of high-resolution observations for younger Class 1 and 0 objects. Recently, Tobin et al. 2020 present the VANDAM II survey: 330 protostars in Orion observed at 0.87 millimeter with ALMA at a resolution of $\sim 0\farcs1$ ($\sim$ 40 AU in diameter). By fitting a 2D Gaussian to their dust millimeter observations, the authors determined median dust disk radii of $44.9^{+5.8}_{-3.4}$ AU and $37.0^{+4.9}_{-3.0}$ AU for their Class 0 and Class 1 protostars, suggesting that the majority of disks are initially very compact. It should be noted that it is unclear whether the extent of the dust emission can be directly related to the gas disk size. However, there is also similar evidence from the gas that Class 1 and 0 objects are compact. As part of the CALYPSO large program, Maret et al. (2020) observed 16 Class 0 protostars and found that only two sources show Keplerian rotation at $\sim$ 50 AU scales, suggesting that Keplerian disks larger than 50 AU, such as found for VLA 1623 (Murillo et al. 2013), are uncommon. We therefore adopted an initial disk size of $R_{\rm init} = 10$ AU for our models. In Section 4.4.2 we discuss the impact of this choice.

Table 4.1: Initial conditions of our `DALI` models

M_*	($\mathrm{M_\odot}$)	0.1	0.32	1.0
$\dot{M}_{\rm acc}$	($\mathrm{M_\odot\ yr^{-1}}$)	4×10^{-11}	2×10^{-9}	1×10^{-8}
			$\alpha_{\rm visc} = 10^{-2}$	
$t_{\rm visc}$	($\times10^6$ yr)	0.035	0.046	0.115
$M_{\rm init}$	($\mathrm{M_\odot}$)	4.5×10^{-4}	1.99×10^{-2}	6.9×10^{-2}
			$\alpha_{\rm visc} = 10^{-3}$	
$t_{\rm visc}$	($\times10^6$ yr)	0.35	0.46	1.15
$M_{\rm init}$	($\mathrm{M_\odot}$)	2.1×10^{-4}	1.0×10^{-2}	5.9×10^{-2}
			$\alpha_{\rm visc} = 10^{-4}$	
$t_{\rm visc}$	($\times10^6$ yr)	3.5	4.6	11.5
$M_{\rm init}$	($\mathrm{M_\odot}$)	4.1×10^{-4}	2.5×10^{-2}	2.6×10^{-1}

4.2.3 `DALI` models

Based on our nine sets of initial conditions, we calculated $M_{\rm disk}$ and $R_{\rm c}$ at ten disk ages between 0.1 and 10 Myr using equations (4.2) and (3) (see Figure 4.1 for an example). From $M_{\rm disk}$(t) and $R_{\rm c}$(t), we calculated $\Sigma_{\rm gas}$(t) and used that as input for the thermochemical code `DALI` (Bruderer et al. 2012; Bruderer 2013). Based on a 2D physical disk structure, `DALI` calculates the thermal and chemical structure of the disk self-consistently. First, the dust temperature structure and the internal radiation field are computed using a 2D Monte Carlo method to solve the radiative transfer equation. In order to find a self-consistent solution, the code iteratively solves the time-dependent chemistry, calculates molecular and atomic excitation levels, and computes the gas temperature by balancing heating and cooling processes. The model can then be ray traced to construct synthetic emission maps. A more detailed description of the code is provided in Appendix A of Bruderer et al. (2012).

For the vertical structure of our models we assumed a Gaussian density distribution, with a radially increasing scale height of the form $h = h_c\,(R/R_{\rm c})^{\psi}$. In this equation, h_c is the scale height at $R_{\rm c}$ and ψ is the flaring angle. The stellar spectrum used in our models is a black body with $T_{\rm eff} = 4000$ K. To this black body we added excess UV radiation, resulting from accretion, in the form of 10000 K black body. For the luminosity of this component, we assume that the gravitational potential energy of the accreted mass is released with 100% efficiency (see, e.g. Kama et al. 2015). For the external UV radiation we assumed a standard interstellar radiation field of 1 G_0 (Habing 1968)). These parameters are summarized in Table 4.2.

Table 4.2: Fixed `DALI` parameters of the physical model.

Parameter	Range
Chemistry	
Chemical age	0.1-$10^{*,\dagger}$ Myr
[C]/[H]	$1.35 \cdot 10^{-4}$
[O]/[H]	$2.88 \cdot 10^{-4}$
Physical structure	
γ	1.0
ψ	0.15
h_c	0.1
$R_{\rm c}$	$10 - 3 \times 10^{3,\dagger}$ AU
$M_{\rm gas}$	$10^{-5} - 10^{-1,\dagger}$ $M_\odot$
Gas-to-dust ratio	100
Dust properties	
$f_{\rm large}$	0.9
χ	0.2
composition	standard ISM[1]
Stellar spectrum	
$T_{\rm eff}$	4000 K + Accretion UV
L_*	0.28 $L_\odot$
$\zeta_{\rm cr}$	10^{-17} s^{-1}
Observational geometry	
i	0°
PA	0°
d	150 pc

Notes.*The age of the disk is taken into account when running the time-dependent chemistry. †These parameters evolve with time (see Figure 4.1 and Sect. 4.4.3). [1]Weingartner & Draine 2001, see also Section 2.5 in Facchini et al. 2017.

In our models we included the effects of dust settling by subdividing our grains into two populations. A population of small grains (0.005-1 μm) follows the gas density distribution both radially and vertically. A second population of large grains (1-10^3 μm), making up 90% of the dust by mass, follows the gas radially but has its scale height reduced by a factor $\chi = 0.2$ with respect to the gas. We computed the dust opacities for both populations using a standard interstellar medium (ISM) dust composition following Weingartner & Draine (2001), with a Mathis-Rumpl-Nordsieck (MRN) (Mathis et al. 1977) grain size distribution. We did not include any radial drift or radially varying grain growth in our `DALI` models (cf. Facchini et al. 2017). However, we note that Trapman et al. (2019) show that dust evolution does not affected measured gas outer radii.

4.3 Results

4.3.1 Time evolution of the ^{12}CO emission profile

To first order, the evolution of ^{12}CO intensity profile is determined by three time-dependent processes as follows:

1. Viscous spreading moves material, including CO, to larger radii resulting in more extended CO emission.
2. The disk mass decreases with time, lowering surface density, which in the outer disk allows CO to be more easily photodissociated. This removes CO from the outer disk and lowers the CO flux coming from these regions.
3. Over longer timescales, time-dependent chemistry results in CO being converted into CH_4, CO_2, and CH_3OH. This is discussed separately in more detail in Section 4.4.3.

The combined effect of the first two processes on the ^{12}CO emission profile can be seen in Figure 4.2 for disks with a stellar mass of $M_* = 0.1$ $M_\odot$. Similar profiles for the remaining disks are shown in Figure 4.12

For a high $\alpha_{\rm visc}$ of 0.01 the viscous timescale is short compared to the disk age and viscous evolution is happening fast. This is reflected in the ^{12}CO emission, which spreads quickly (within 1 Myr) from $\sim$ 200 AU to $\sim$ 400 AU. After $\sim$ 2 Myr the ^{12}CO emission in the outer parts of the disk starts to decrease. At this point the total column densities in the outer disk are low enough that CO is removed through photodissociation. As a reference, by 2 Myr the disk mass of the models has dropped to $M_{\rm disk} = 5 \times 10^{-5}$ $M_\odot$ and its characteristic size has increased to $R_{\rm c} = 400$ AU (see Figure 4.1).

For models with $\alpha_{\rm visc} = 10^{-3}$, shown in the middle panel of Figure 4.2, viscous spreading of the disk dominates the evolution of the ^{12}CO emission profile. Compared to the $\alpha_{\rm visc} = 10^{-2}$ models the column density in the outer disk never becomes low enough for CO to be efficiently photodissociated.

The models with $\alpha_{\rm visc} = 10^{-4}$, presented in the right panel of Figure 4.2, shows only small changes in the emission profile. For these models the viscous timescale is $\sim$ 3.5 Myr, meaning that within the 10 Myr lifetime considered the surface density does not go through much viscous evolution.

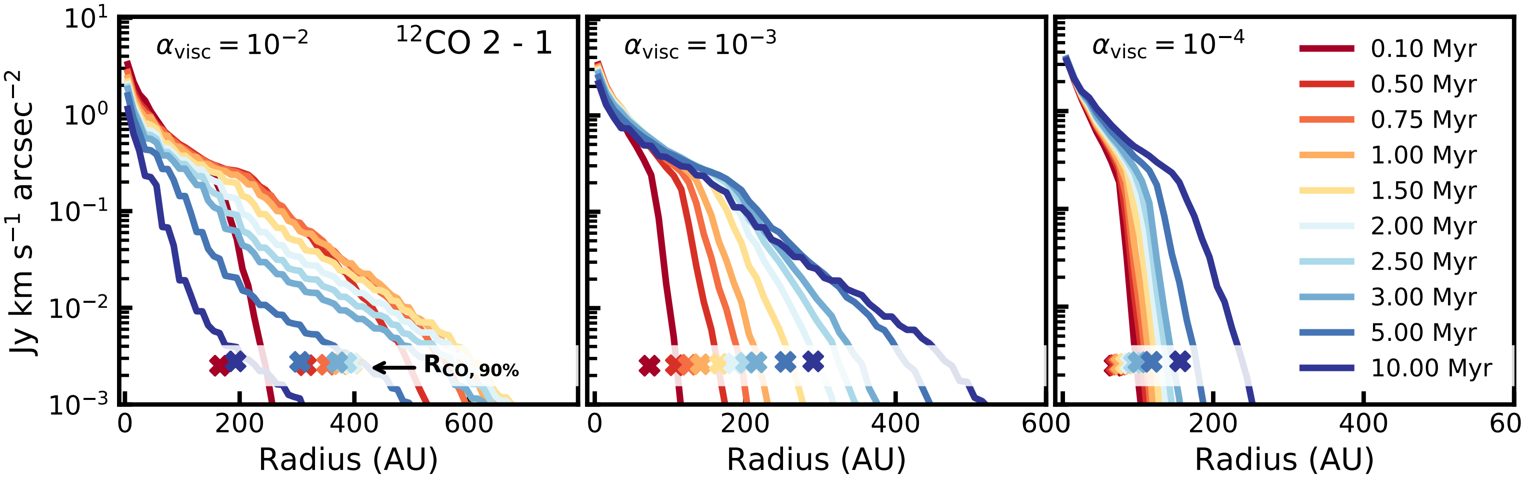

Figure 4.2: Evolution of the ^{12}CO 2 - 1 radial intensity profiles for models with $M_* = 0.1$ M$_\odot$. The colors indicate various disk ages between 0.1 and 10 Myr. The crosses at the bottom of each panel show the gas outer radius, defined as the radius that encloses 90% of the total ^{12}CO 2 - 1 flux.

4.3.2 Evolution of the observed gas outer radius

From the ^{12}CO emission maps we can calculate the outer radius that would be obtained from observations. We define the observed gas outer radius, $R_{\rm CO,\ 90\%}$, as the radius that encloses 90% of the total ^{12}CO flux. A gas outer radius defined this way encloses most ($> 98\%$) of the disk mass and traces a fixed surface density in the outer disk (Trapman et al. 2019). We note that we do not include observational factors, such as noise, which affect the $R_{\rm CO,\ 90\%}$ that is measured. To accurately retrieve $R_{\rm CO,\ 90\%}$ from observations requires a peak S/N > 10 on the moment zero map of the ^{12}CO emission (cf. Trapman et al. 2019). The radii discussed in this work are measured from ^{12}CO $J = 2-1$ emission, but tests show that gas outer radii measured from ^{12}CO $J = 3-2$ are the same to within a few percent.

Figure 4.3 shows how the observed outer radius changes as a result of viscous evolution. The top panel shows $R_{\rm CO,\ 90\%}$ for models with $M_* = 0.1$ M$_\odot$. For $\alpha_{\rm visc} = 10^{-2}$ the gas outer radius first increases until it starts to decrease at ~ 2 Myr. The decrease in $R_{\rm CO,\ 90\%}$ is due to decreasing column densities in the outer disk, allowing CO to be more easily photodissociated (for details, see Section 4.3.1). For $\alpha_{\rm visc} = 10^{-3}$, $R_{\rm CO,\ 90\%}$ increases monotonically from ~ 70 AU to ~ 280 AU. The trend is similar for $\alpha_{\rm visc} = 10^{-4}$ but $R_{\rm CO,\ 90\%}$ increases at a slower rate, ending up at $R_{\rm CO,\ 90\%} \sim 150$ AU after 10 Myr.

For models with $M_* = 0.32$ M$_\odot$ and 1.0 M$_\odot$, the initial and final disk masses are much higher compared to the models with $M_* = 0.1$ M$_\odot$. As a result, photodissociation does not have a significant effect on $R_{\rm CO,\ 90\%}$ and $R_{\rm CO,\ 90\%}$ does not significantly decrease with age. In addition, the disk sizes for these two groups of models are very similar. For $\alpha_{\rm visc} = 10^{-2}$, $R_{\rm CO,\ 90\%}$ instead rapidly increases from $\sim 180-250$ AU at 0.1 Myr to $1500-1800$ AU at 10 Myr. For $\alpha_{\rm visc} = 10^{-3}$ the growth of $R_{\rm CO,\ 90\%}$ is less extreme in comparison, but observed disk sizes still reach $500-700$ AU after 10 Myr. Owing to the long viscous timescales of $5-10$ Myr for the models with $\alpha_{\rm visc} = 10^{-4}$, $R_{\rm CO,\ 90\%}$ does not increase significantly (i.e., by less than a factor of ~ 2) over a disk lifetime of ~ 10 Myr.

For more embedded star-forming regions, the ^{12}CO emission from the disk can be contaminated by the cloud, either by having ^{12}CO emission from the cloud mixed in with the emission from the disk or through cloud material along the line of sight absorbing the ^{12}CO emission from the disk. This can prevent using ^{12}CO to accurately measure disk sizes. We therefore also examined disk sizes measured using 90% of the ^{13}CO 2-1 flux, which are shown in Figure 4.14. Apart from being a factor $\sim 1.4-2$ smaller than the ^{12}CO outer radii, the ^{13}CO outer radii evolve similarly as $R_{\rm CO,\ 90\%}$. The ^{13}CO outer radii are smaller than $R_{\rm CO,\ 90\%}$ because the less abundant ^{13}CO is more easily removed in the outer parts of the disk through photodissociation. Our conclusions for $R_{\rm CO,\ 90\%}$ are therefore also applicable for gas disk sizes measured from ^{13}CO emission. However, see Section 4.4.3 on how chemical depletion of CO through grain-surface chemistry affects this picture.

Overall we find that the observed outer radius increases with time and is larger for a disk with a higher $\alpha_{\rm visc}$. The exception to this rule are the models with low stellar mass ($M_* = 0.1$ M$_\odot$) and high viscosity ($\alpha_{\rm visc} = 10^{-2}$). These highlight the caveat that if the disk mass becomes too low, CO becomes photodissociated in the outer disk and the observed outer radius decreases with time.

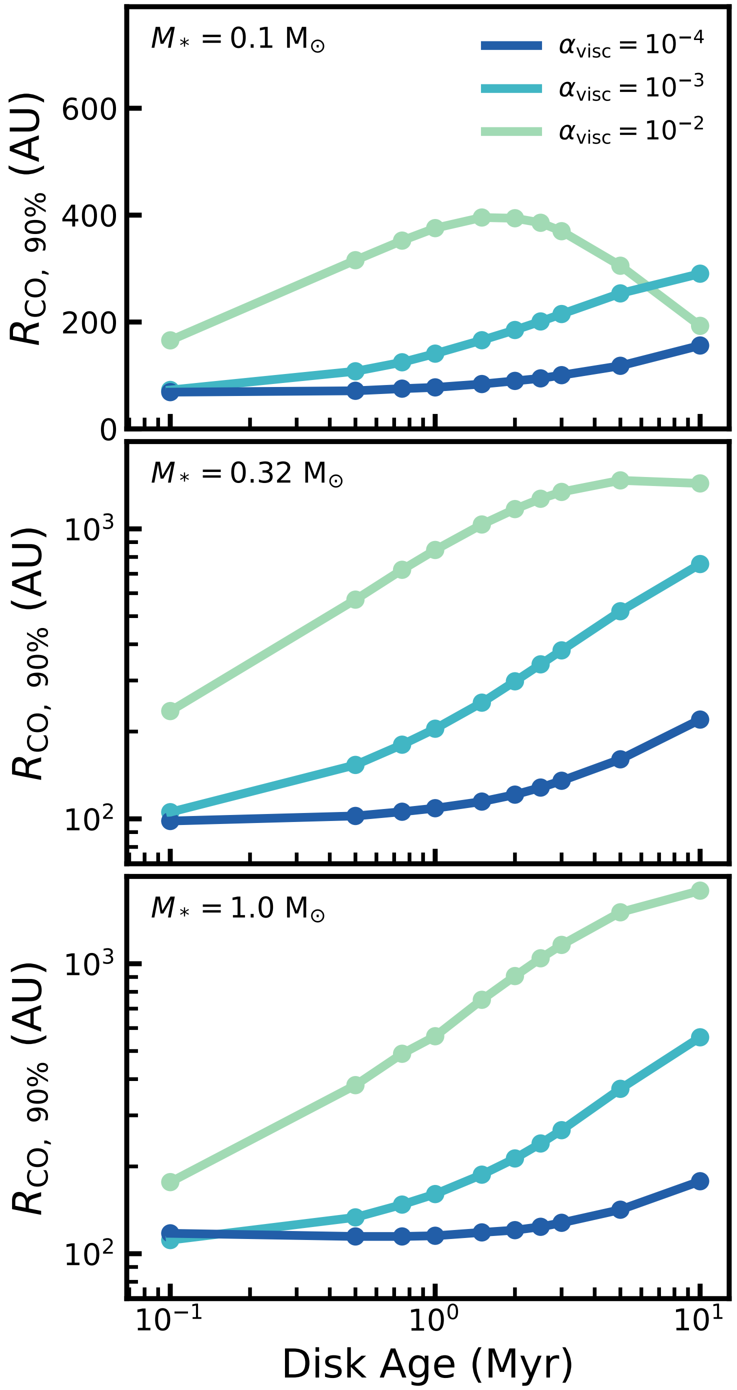

Figure 4.3: Gas outer radius vs. disk age, defined as the radius that encloses 90% of the ^{12}CO 2 - 1 flux. The top, middle, and bottom panels show models with various stellar masses (cf. Table 4.1). The colors correspond to the $\alpha_{\rm visc}$ of the model.

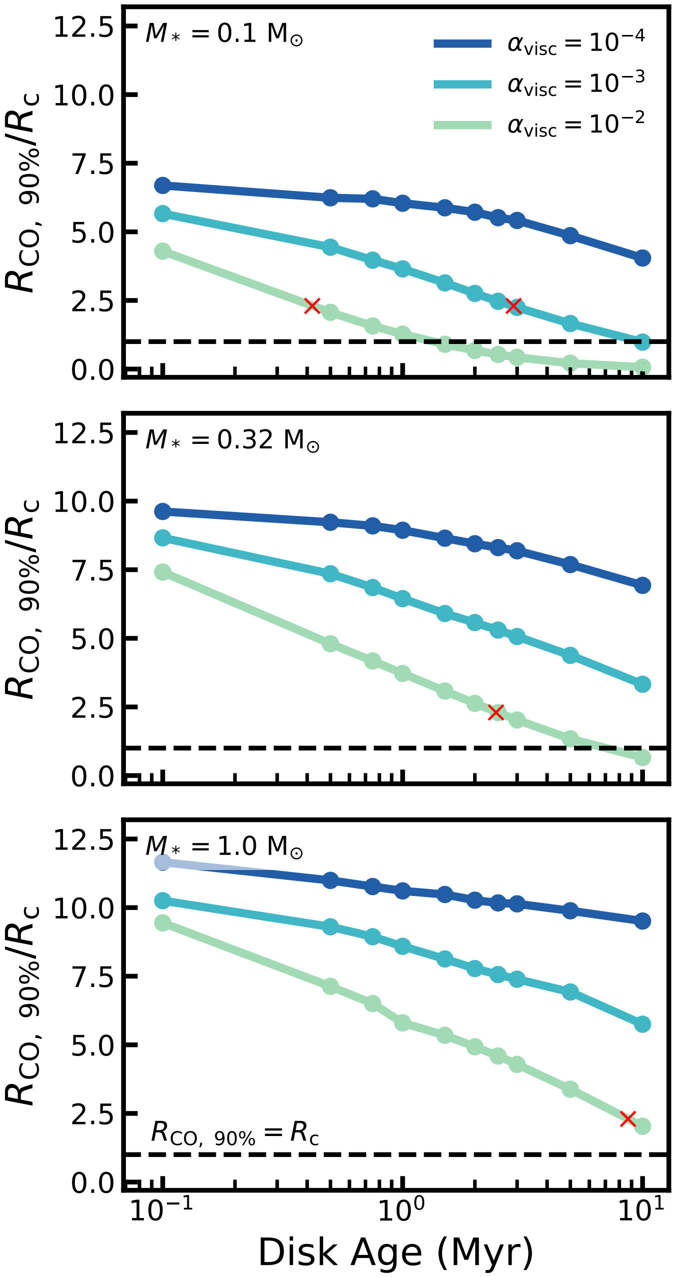

Figure 4.4: Ratio of gas outer radius over characteristic radius vs. disk age. The black dashed line shows where $R_{\rm CO,\ 90\%} = R_{\rm c}$. The top, middle, and bottom panels show models with various stellar masses (cf. Table 4.1). The colors correspond to the $\alpha_{\rm visc}$ of the model. The red crosses denote where $R_{\rm CO,\ 90\%}/R_{\rm c} = 2.3$, that is, where $R_{\rm CO,\ 90\%}$ encloses 90% of the total disk mass (see Section 4.3.4)

4.3.3 Gas outer radius traces viscous evolution

The previous section has shown that disks with higher $\alpha_{\rm visc}$, which evolve over a shorter viscous timescale, are overall larger at a given disk age. To quantify this, it is worthwhile to examine how well the observed gas outer radius $R_{\rm CO,\ 90\%}$ traces the characteristic size $R_{\rm c}$ of the disk.

Figure 4.4 shows the ratio $R_{\rm CO,\ 90\%}/R_{\rm c}$ as a function of disk age for the three sets of stellar masses. If $R_{\rm CO,\ 90\%}$ were only affected by viscous spreading it would grow at the same rate as the characteristic radius, $R_{\rm CO,\ 90\%} \propto R_{\rm c}$, represented by a horizontal line in Figure 4.4. Instead we see $R_{\rm CO,\ 90\%}/R_{\rm c}$ decreasing with disk age, indicating that the observed outer radius grows at a slower rate than the viscous spreading of the disk. The main cause for the slower growth rate of $R_{\rm CO,\ 90\%}$ is the decreasing disk mass over time because $R_{\rm CO,\ 90\%}$ traces a fixed surface density. As shown in Trapman et al. (2019), $R_{\rm CO,\ 90\%}$ coincides with the location in the outer disk, where CO is no longer able to effectively self-shield against photodissociation and is quickly removed from the gas. The CO column density threshold for CO to self-shield is $N_{\rm CO} \geq 10^{15}$ cm^{-2} (van Dishoeck & Black 1988). Thus, given that $R_{\rm CO,\ 90\%}$ traces a point of fixed column density, it scales with the total disk mass. As a result of angular momentum transport via viscous stresses, material is accreted onto the star, causing the total disk mass to decrease following equation (4.2) (see, e.g, Figure 4.1), which limits the growth of $R_{\rm CO,\ 90\%}$.

Figure 4.4 also shows that $R_{\rm CO,\ 90\%}/R_{\rm c}$ is larger for models with a lower $\alpha_{\rm visc}$; this difference becomes larger for older disks. This behavior can also be related to disk mass. As shown in Figure 4.1 disk models with a lower $\alpha_{\rm visc}$ have a higher disk mass. For the same $R_{\rm c}$ a higher disk mass, to first order, results in higher CO column densities in the outer disk. As a result CO is able to self-shield against photodissociation further out in the disk, increasing the difference between $R_{\rm CO,\ 90\%}$ and $R_{\rm c}$.

In conclusion, we find that $R_{\rm CO,\ 90\%}/R_{\rm c}$ is between 0.1 and 12 and is mainly determined by the time evolution of the disk mass, which is set by the assumed viscosity. To infer $R_{\rm c}$ directly from $R_{\rm CO,\ 90\%}$ requires information on the total disk gas mass.

4.3.4 Possibility of measuring $\alpha_{\rm visc}$ from observed $R_{\rm CO,\ 90\%}$

A useful definition for an outer radius of a disk is that it encloses most of the mass in the disk. In this case, using a few simple assumptions, we can relate the outer radius directly to $\alpha_{\rm visc}$. If we assume that the viscous timescale at the outer radius of the disk, given by $t_{\rm visc} \approx R_{\rm out}^2 \nu^{-1}$, is approximately equal to the age of the disk, given by $\dot{M}_{\rm acc} \approx M_{\rm disk}/t_{\rm visc}$, we can write $\alpha_{\rm visc}$ as (see, e.g. Hartmann et al. 1998; Jones et al. 2012; Rosotti et al. 2017)

$$\alpha_{\rm visc} = \frac{\dot{M}_{\rm acc}}{M_{\rm disk}} \cdot c_s^{-2} \cdot \Omega_K \cdot R_{\rm out}^2, \tag{4.9}$$

where $\dot{M}_{\rm acc}$ is the stellar accretion rate, $M_{\rm disk}$ is the total disk mass, c_s is the sound speed, Ω_K is the Keplerian orbital frequency, and $R_{\rm out}$ is the physical outer radius of the disk.

In absence of this physical outer radius, Ansdell et al. (2018) used the observed gas outer radius $R_{\rm CO,\ 90\%}$, based on the ^{12}CO 2-1 emission, to measure $\alpha_{\rm visc}$ for 17 disks in Lupus finding a wide range of $\alpha_{\rm visc}$, spanning two orders of magnitude between 3×10^{-4} and 0.09.

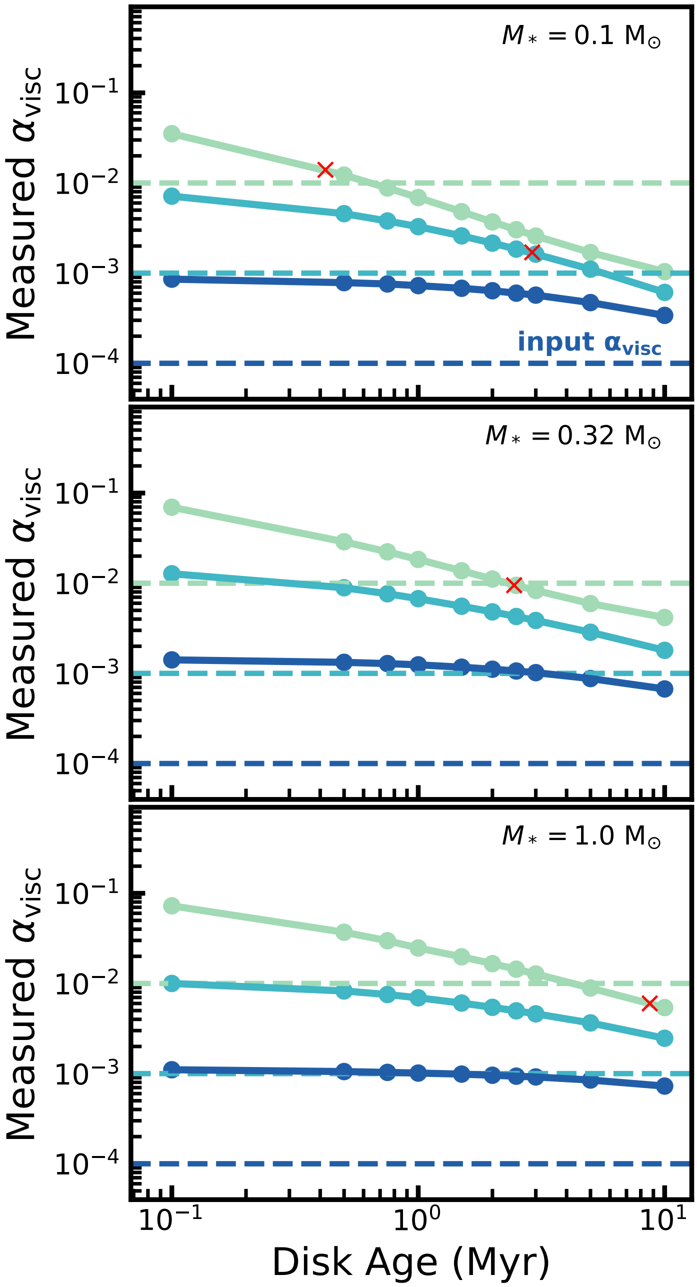

Figure 4.5: Comparison between $\alpha_{\rm visc}$ measured from $R_{\rm CO,\ 90\%}$ (solid line) and the input $\alpha_{\rm visc}$ (dashed line). The colors correspond to the input $\alpha_{\rm visc}$ of the model. The top, middle, and bottom panels show models with different stellar masses (cf. Table 4.1). The red crosses denote where $R_{\rm CO,\ 90\%}/R_{\rm c} = 2.3$ and $R_{\rm CO,\ 90\%}$ encloses 90% of $M_{\rm disk}$ (cf. Section 4.3.4 and Figure 4.4). The red crosses denote where $R_{\rm CO,\ 90\%}/R_{\rm c} = 2.3$, that is, where $R_{\rm CO,\ 90\%}$ encloses 90% of the total disk mass (see Section 4.3.4).

For our models we have both $R_{\mathrm{CO},\ 90\%}$, measured from our models, and input α_{visc}, thus we can examine how well α_{visc} can be retrieved from the observed gas outer radius $R_{\mathrm{CO},\ 90\%}$. As we are mainly interested in the correlation between α_{visc} and $R_{\mathrm{CO},\ 90\%}$, we assume that M_*, $\dot{M}_{\mathrm{acc}}$, and M_{disk} are known, and c_s is calculated assuming a disk temperature of 20 K, which is the same temperature used to calculate t_{visc} in Section 4.2.2.

Figure 4.5 shows α_{visc} measured using $R_{\mathrm{CO},\ 90\%}$, for our models and compares this value to the α_{visc} that was used as input for the models. For all disk models the measured α_{visc} decreases with age and, for most ages, we find $\alpha_{\mathrm{visc}}(\mathrm{measured}) > \alpha_{\mathrm{visc}}(\mathrm{input})$. Both of these observations can be traced back to which radius is used in Equation (4.9) to calculate $\alpha_{\mathrm{visc}}(\mathrm{measured})$. In the assumptions going into deriving Equation (4.9), R_{out} is defined as the radius that encloses all (100 %) of the mass of the disk. In our models in which the surface density follows a tapered power law the radius that encloses 100 % of the mass is infinite, but we can instead take R_{out} as a radius that encloses a large, fixed fraction of the disk mass. For a tapered power law, this R_{out} is directly related to R_{c}. As an example, for a tapered power law where $\gamma = 1$, the radius that encloses 90% of the disk mass is $2.3 \times R_{\mathrm{c}}$. For $R_{\mathrm{out}} = 2.3 \times R_{\mathrm{c}}$ in Equation (4.9) we obtain approximately the same α_{visc} that was put into the model. Ideally we would therefore like $R_{\mathrm{CO},\ 90\%}$ to also enclose a large, fixed fraction of the disk mass, or continuing our example, we would like $R_{\mathrm{CO},\ 90\%} \approx 2.3 \times R_{\mathrm{c}}$, independent of disk age and mass. However, in Section 4.3.3 we show that $R_{\mathrm{CO},\ 90\%}/R_{\mathrm{c}}$ lies between 0.1 and 10 and decreases with disk age. Figure 4.4 shows that $R_{\mathrm{CO},\ 90\%}/R_{\mathrm{c}} \gg 2.3$ for most disk ages, leading us to overestimate α_{visc} when measured from $R_{\mathrm{CO},\ 90\%}$. Taking the example discussed before, if we compare Figures 4.5 and 4.4 we find that at disk ages where $R_{\mathrm{CO},\ 90\%}/R_{\mathrm{c}} \approx 2.3$ our α_{visc} measured from $R_{\mathrm{CO},\ 90\%}$ is within a factor of 2 of the input α_{visc}.

Summarizing we find that in most cases, $R_{\mathrm{CO},\ 90\%}/R_{\mathrm{c}} \gg 2.3$ and we measure an α_{visc} much larger than the input α_{visc}, up to an order of magnitude higher, especially if the input α_{visc} is low. Given that at 1 Myr the measured α_{visc} is $5 - 10\times$ larger than the input α_{visc}, this implies that the α_{visc} determined by Ansdell et al. (2018) likely overestimates the true α_{visc} of the disks in Lupus by a factor 5-10.

4.4 Discussion

4.4.1 Comparing to observations

Gas disk sizes have now been measured consistently for a significant number of disks. In contrast with Najita & Bergin (2018), in this paper we chose to select homogeneous samples (in terms of analysis and tracer). These samples are Ansdell et al. (2018) and Barenfeld et al. (2017), who measured $R_{\mathrm{CO},\ 90\%}$ for 22 sources in Lupus and 7 sources in Upper Sco. Between them, these disks span between 0.5 and 11 Myr in disk ages. In Figure 4.6 we compare our models to these observations, where sources with $M_* \leq 0.66\ \mathrm{M}_\odot$ are compared to models with $M_* = 0.32\ \mathrm{M}_\odot$ and those with $M_* > 0.66\ \mathrm{M}_\odot$ are compared to models with $M_* = 1.0\ \mathrm{M}_\odot$. Ansdell et al. (2018) define the gas outer radius as the radius that encloses 90% of the ^{12}CO 2 - 1 emission, so we take their values directly. For the disks in Upper Sco we calculate $R_{\mathrm{CO},\ 90\%}$ from their fit to the observed ^{12}CO intensity (cf. Barenfeld et al. 2017). Stellar ages and masses were determined by comparing pre-main-sequence evolutionary models to X-shooter observations of these sources (Alcalá et al. 2014, 2017). Lacking such observations for Upper Sco, we instead use the 5-11 Myr stellar age of Upper Sco (see, e.g. Preibisch et al. 2002; Pecaut et al. 2012) for all sources in this region. The observations are summarized in Table 4.3.

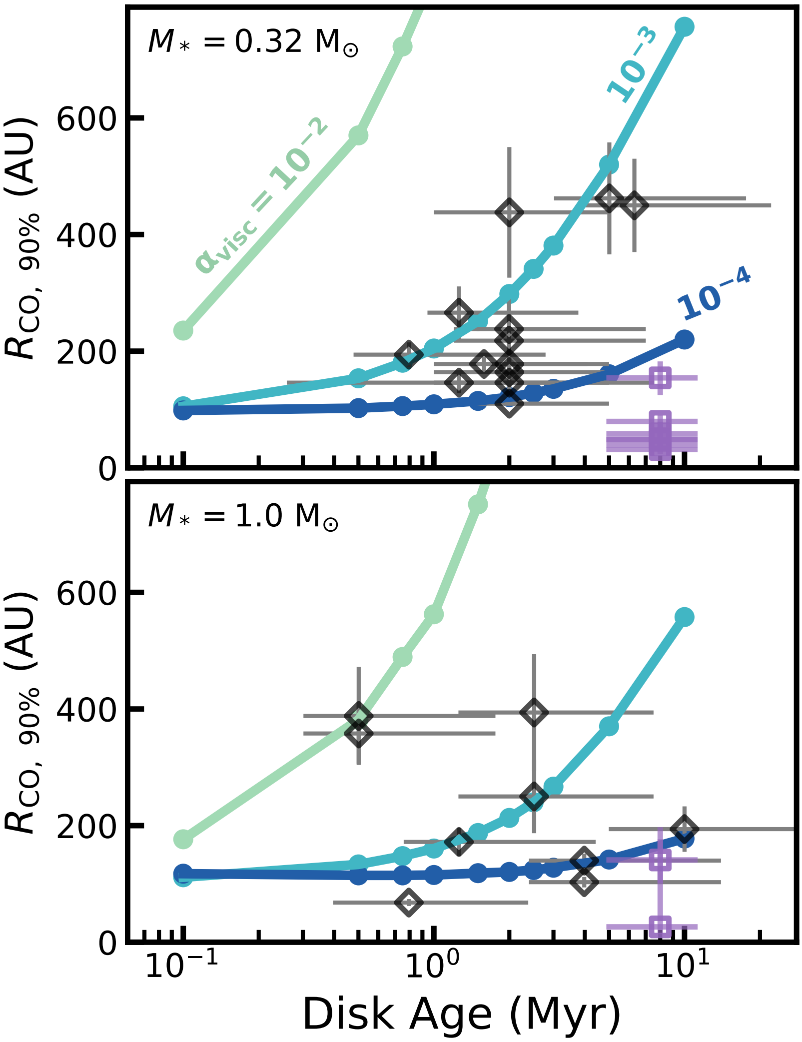

Figure 4.6: Gas outer radii of our models ($R_{\rm CO,\ 90\%}$) compared to observations. The colors correspond to the $\alpha_{\rm visc}$ of the model. The black open diamonds show observed gas outer radii in Lupus (Ansdell et al. 2018) and the purple open squares denote observed gas outer radii in Upper Sco (Barenfeld et al. 2017). The Upper Sco outer radii shown are 90% outer radii, calculated from their fit to the observed ^{12}CO intensity. The top and bottom panels split models and observations based on stellar mass. The sources with $M_* \leq 0.66$ M$_\odot$ are compared to models with $M_* = 0.32$ M$_\odot$; those with $M_* > 0.66$ M$_\odot$ are compared to models with $M_* = 1.0$ M$_\odot$. Only panels for $M_* = 0.32$ and 1.0 M$_\odot$ are shown because the sample of observations considered in this work does not contain any objects with $M_* \sim 0.1$ M$_\odot$.

As shown in Figure 4.6, most of the Lupus observations lie between the models with $\alpha_{\rm visc} = 10^{-3}$ and $\alpha_{\rm visc} = 10^{-4}$. Most of the disks can therefore been explained as viscously spreading disks with $\alpha_{\rm visc} = 10^{-4}$–$10^{-3}$ that start out small ($R_{\rm init} = 10$ AU). Only two sources with $M_* = 1.0$ M$_\odot$, IM Lup and Sz 98 (also known as HK Lup), require a larger $\alpha_{\rm visc} \simeq 10^{-2}$ to explain the observed gas disk size given their age.

It is interesting to note that Lodato et al. (2017) reached a similar conclusion using a completely different method. They show that a simple viscous model can reproduce the observed relation between stellar mass accretion and disk mass in Lupus (see Manara et al. 2016a). To match both the average disk lifetime and the observed scatter in the $\dot{M}_{\rm acc}$-$M_{\rm disk}$ relation, disk ages in Lupus have to be comparable to the viscous timescale, on the order of ~ 1 Myr (see also Jones et al. 2012; Rosotti et al. 2017). This viscous timescale is comparable to our models with $\alpha_{\rm visc} = 10^{-3}$ (cf. Table 4.1).

As we made no attempt to match our models to individual observations, it is worthwhile to discuss if it is possible to explain the large disks in our sample, such as IM Lup and Sz 98, by other means than a large $\alpha_{\rm visc}$. A quick comparison with Table 4.1 shows that increasing the disk mass does not help to explain their large $R_{\rm CO,\ 90\%}$. Our models with $M_* = 1.0$ M$_\odot$ and $\alpha_{\rm visc} = 10^{-3} - 10^{-4}$ differ by an order of magnitude in initial disk mass, but at 0.75 Myr they differ by less than 5% in terms of $R_{\rm CO,\ 90\%}$. Another possibility would be increasing the initial disk size $R_{\rm c}(t = 0)$, which we discuss in Section 4.4.2.

Interestingly, five of the seven Upper Sco disks have gas outer radii that lie well below our models with $\alpha_{\rm visc} = 10^{-4}$, indicating that their small $R_{\rm CO,\ 90\%}$ cannot be explained by our models, even when taking into account the uncertainty on their age. As the viscous timescale for our models with $\alpha_{\rm visc} = 10^{-4}$ is already ~ 10 Myr, decreasing $\alpha_{\rm visc}$ does not allow us to reproduce the observed $R_{\rm CO,\ 90\%}$. At face value, these small disk sizes would thus seem to rule out that these disks have evolved viscously. We note, however, that there are processes which, in combination with viscous evolution, could explain these small disk sizes. The first would consist in reducing the CO content of these disks; we discuss this option in Section 4.4.3. Given that the disks in Upper Sco are highly irradiated as members of the Sco-Cen OB association (see e.g. Sections 4.4.4 and Appendix 4.B), another option is that external photo-evaporation is the culprit for their small disk sizes, but we cannot rule out a contribution of MHD disks winds to their evolution.

We have shown that the current observations in Lupus are consistent with viscous disk evolution with a low effective viscosity of $\alpha_{\rm visc} = 10^{-3} - 10^{-4}$ (viscous timescales of $1 - 10$ Myr). However, the current available data do not provide sufficient evidence for viscous spreading, which is the proof that viscosity is driving disk evolution. We stress that this is mostly because most of the available data come from the same star-forming region (Lupus), and therefore most of the disks are concentrated around a disk age range from 1 Myr to 3 Myr. Only a few disks lie outside this range. The inclusion of the Upper Sco disks would help constrain the importance of viscous spreading, but we already commented in the previous paragraph about the caveats with this region. Thus, we conclude that the current sample of radii is insufficient to confirm or reject the hypothesis that disks are viscously spreading. To overcome this problem, future observational campaigns should focus on expanding the observational sample of well-measured disk CO radii in other star-forming regions with a different age than Lupus.

4.4.2 Larger initial disk sizes

In our analysis we assumed that disks start out small, with $R_{\rm init} = 10$ AU, as motivated by recent ALMA observations of disks around young Class 0 and 1 protostars (Maury et al. 2019; Maret et al. 2020; Tobin et al. 2020). However, these observations also show a spread in disk size for these young objects. Increasing the initial disk size would potentially also allow us to explain the larger disks, for example, IM Lup and Sz 98 (see van Terwisga et al. 2018), which have a lower $\alpha_{\rm visc}$.

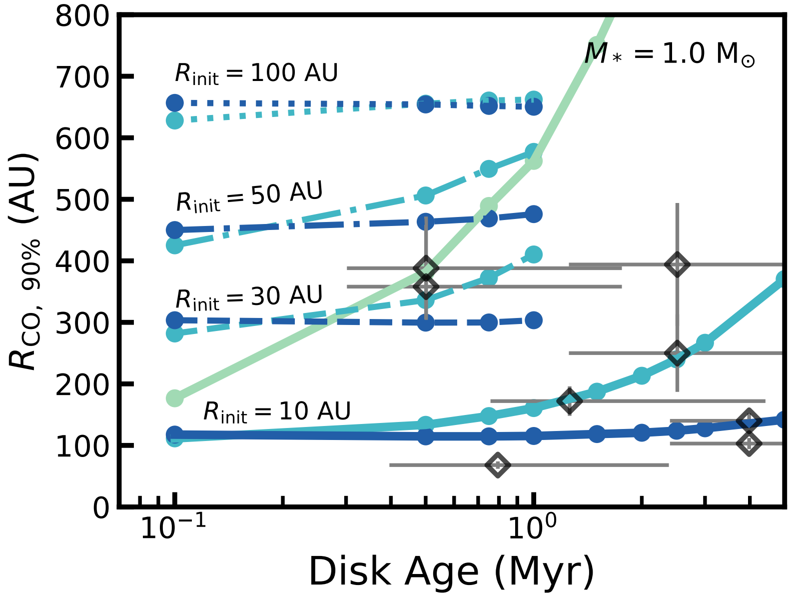

Figure 4.7: Zoom in of the bottom panel of Figure 4.6, showing gas outer radii of our models ($R_{\rm CO,\ 90\%}$) compared to observations. Also added are models with $M_* = 1.0\ \mathrm{M}_\odot$ (see Section 4.2.2) but with $R_{\rm init} = 30, 50$, and 100 AU denoted with dotted, dashed-dotted, and dashed lines, respectively. The colors indicated different values for $\alpha_{\rm visc}$. The new models were only run for $\alpha_{\rm visc} = [10^{-3}, 10^{-4}]$.

Figure 4.7 presents $R_{\rm CO,\ 90\%}$ measured from three sets of models with $M_* = 1.0\ \mathrm{M}_\odot$ (see Section 4.2.2), but with an increased $R_{\rm init} = [30, 50, 100]$ AU. Since our models with $R_{\rm init} = 10$ AU and $\alpha_{\rm visc} = 10^{-2}$ already have $R_{\rm CO,\ 90\%}$ much larger than what is observed, we only run these new models for $\alpha_{\rm visc} = [10^{-3}, 10^{-4}]$. These models have much larger gas disk sizes than models with $R_{\rm init} = 10$ AU; $R_{\rm CO,\ 90\%}$ is at least three times larger ($R_{\rm CO,\ 90\%} \geq 300$ AU). As such, they show that the large disks in the sample ($R_{\rm CO,\ 90\%,obs.} \geq 300$ AU) can also be explained with a larger initial size ($R_{\rm init} = 30$) and a low viscous alpha ($\alpha_{\rm visc} = 10^{-4}$). Extrapolating our results beyond 1 Myr and to models with $M_* = 0.32\ \mathrm{M}_\odot$ there are six examples of such large disks in Lupus that can be explained with $R_{\rm init} \approx 30$ AU (c.f. Figure 4.6). In particular these models show that the observed gas disk sizes of IM Lup and Sz 98 can be explained by either a high viscous alpha ($R_{\rm init} = 10\ \mathrm{AU}, \alpha_{\rm visc} = 10^{-2}$) or a larger initial disk size ($R_{\rm init} \simeq 30 - 50\ \mathrm{AU}, \alpha_{\rm visc} = 10^{-3} - 10^{-4}$). Given the similarities in terms of $R_{\rm CO,\ 90\%}$ between models with $M_* = 1.0\ \mathrm{M}_\odot$ and $M_* = 0.32\ \mathrm{M}_\odot$ seen in Figure 4.3, we expect that increasing $R_{\rm init}$ from 10 AU to 30 AU for models with $M_* = 0.32\ \mathrm{M}_\odot$

would similarly increase their $R_{\mathrm{CO,\ 90\%}}$ by a factor of at least 3.

However, our models show that disks with $R_{\mathrm{init}} = 30$ AU start out at $R_{\mathrm{CO,\ 90\%}} \sim 300$ AU, which is already much larger than most observed $R_{\mathrm{CO,\ 90\%}}$ in Lupus (Ansdell et al. 2018). This indicates that, even if a larger R_{init} can provide an explanation for these six disks, the bulk of the disks in Lupus cannot have had a large R_{init} and they must have started out small ($R_{\mathrm{init}} \simeq 10$ AU). This could be in line with the observations of Tobin et al. (2020), although their measured dust radii should be multiplied by a factor of typically two to three to get the gas radii due to optical depth effects (Trapman et al. 2019).

4.4.3 Effect of chemical CO depletion on measurements of viscous spreading

Over the recent years it has become apparent in observations that protoplanetary disks are underabundant in gaseous CO with respect to the expected abundance of $\mathrm{CO/H_2} = 10^{-4}$ (see, e.g. Favre et al. 2013; Du et al. 2015; Kama et al. 2016b; Bergin et al. 2016; Trapman et al. 2017). Several authors have shown that grain-surface chemistry is able to lower the CO abundance in disks, by converting CO into $\mathrm{CO_2}$ and $\mathrm{CH_3OH}$ on the grains on a timescale of several million years (see, e.g. Bosman et al. 2018; Schwarz et al. 2018). In this work we refer to this process as chemical depletion of CO to distinguish it from simple freeze out of CO, which is included in our models presented in Section 4.3. As the chemical depletion of CO operates on similar timescales as viscous evolution, it can have a large impact on the use of ^{12}CO as a probe for viscous evolution. We implement an approximate description for grain surface chemistry and examine its effects on observed gas outer radii. A more detailed description can be found in Appendix 4.F.

Figure 4.8 shows ^{12}CO 2 - 1 and ^{13}CO 2 - 1 intensity profiles, with and without including chemical CO depletion, for two models at different disk ages. The ^{12}CO 2 - 1 radial intensity profile remains unchanged until 10 Myr, at which point the intensities start to drop between $\sim$ 100 AU and $\sim$ 300 AU, seemingly carving a small "dip" in the intensity profile. With our current definition of the outer radius at 90% of the total flux, this dip lies within $R_{\mathrm{CO,\ 90\%}}$. The decreasing intensity due to chemical CO depletion causes $R_{\mathrm{CO,\ 90\%}}$ to move outward, although the change is small ($\leq 2\%$). The chemical depletion of CO does not affect the CO abundance beyond 300 AU (see, e.g. Figure 4.16), so the ^{12}CO 2 - 1 flux originating from > 300 AU now makes up a larger fraction of the total ^{12}CO flux when comparing models with and without chemical CO depletion. It should therefore be noted that if we were to change our definition of the gas outer radius such that it lies within the "dip", for example, by defining $R_{\mathrm{CO,\ X\%}}$ using a lower percentage of the total flux, $R_{\mathrm{CO,\ X\%}}$ would decrease if we include chemical depletion of CO.

In contrast, the ^{13}CO 2 - 1 intensity profile, shown in the right panels of Figure 4.8, is significantly affected by chemical CO depletion at 10 Myr. Between $\sim$100 AU and $\sim$300 AU the ^{13}CO intensity profile has dropped by more than an order of magnitude. Again, as an consequence of the infinite S/N of our synthetic emission maps, the decrease in the intensity profile has moved the radius enclosing 90% of flux outward. For real observations, in which the S/N is limited, chemical depletion of CO instead significantly decreases the observed outer radius if measured from ^{13}CO emission. Figure 4.8 shows that gas disk sizes measured from ^{13}CO can only be interpreted correctly if CO depletion is taken into account in the analysis. The figure also highlights the importance of high S/N observations when measuring gas disk sizes from ^{13}CO emission. Given the lack of a significant sample of observed ^{13}CO outer radii, we do not investigate this aspect in this paper further. We note however that once such a sample becomes available, an analysis quantifying the effect of chemical depletion on ^{13}CO outer radii will become possible.

As shown in Figure 4.16, there exists a vertical gradient in CO abundances. Vertical mixing, not included in our models, would move CO rich gas from the ^{12}CO emission layer toward the midplane and exchange it with CO-poor gas. If we were to include vertical mixing, the CO abundance in the ^{12}CO emitting layer would decrease and thus the effect of CO depletion on $R_{\mathrm{CO},\ 90\%}$ measured from ^{12}CO would increase. The effect would be similar to what is seen for ^{13}CO, indicating that in this case chemical CO depletion could also affect gas disk sizes measured from ^{12}CO emission and should thus be taken into account in the analysis (see, e.g. Krijt et al. 2018; Krijt et al. 2020)

4.4.4 Caveats

Photo-evaporation: In this paper we considered a disk evolving purely under the influence of viscosity. In reality, it is well known that pure viscous evolution cannot account for the observed timescale of a few million years on which disks disperse (see Alexander et al. 2014 for a review). Internal photo-evaporation is commonly invoked as a mass-loss mechanism to solve this problem. Because photo-evaporation preferentially removes mass from the inner disk (a few AUs), it is unlikely to change our conclusions. We note however that some photo-evaporation models (Gorti & Hollenbach 2009) have an additional peak in the mass-loss profile at a scale of 100-200 AU, which might influence our results.

Another potential concern is the effect of external photo-evaporation, that is, mass loss induced by the high-energy radiation emitted by nearby massive stars. In this case, the mass-loss preferentially affects the outer part of the disk (Adams et al. 2004) and might therefore have an influence on the evolution of the outer disk radius, likely moving $R_{\mathrm{CO},\ 90\%}$ inward. The importance of this effect is region-dependent. A region like Lupus is exposed to relatively low levels of irradiation (see the appendix in Cleeves et al. 2016) and neglecting external photo-evaporation is probably safe in this case, although the effect can still be important for the largest disks (Haworth et al. 2017). For other regions, such as Upper Sco, the impact of external photo-evaporation is potentially more severe since the region is part of the nearest OB association, Sco-Cen (Preibisch & Mamajek 2008). According to the catalog of de Zeeuw et al. (1999), the earliest spectral type in the region is B0 and there are 49 B stars in the complex, suggesting that the level of irradiation can be significantly higher than in Lupus. A simple calculation, outlined in Appendix 4.B, suggests that the disks in Upper Sco are currently subjected to a far-ultraviolet (FUV) radiation field of $10-300$ G$_0$. For these levels of external UV radiation the mass-loss rate due to external photo-evaporation at radii of $\sim$ 100 AU is $\sim 10^{-9}-10^{-8}$ M$_\odot$yr^{-1}, which is of the same order of magnitude as the accretion rate (see, e.g. Facchini et al. 2016; Haworth et al. 2017, 2018). Given the age of the region, stars with even earlier spectral types might have been present but are now evolved, as shown by the red supergiant Antares, implying that in the past the region was subject to a more intense UV flux than it is at the present.

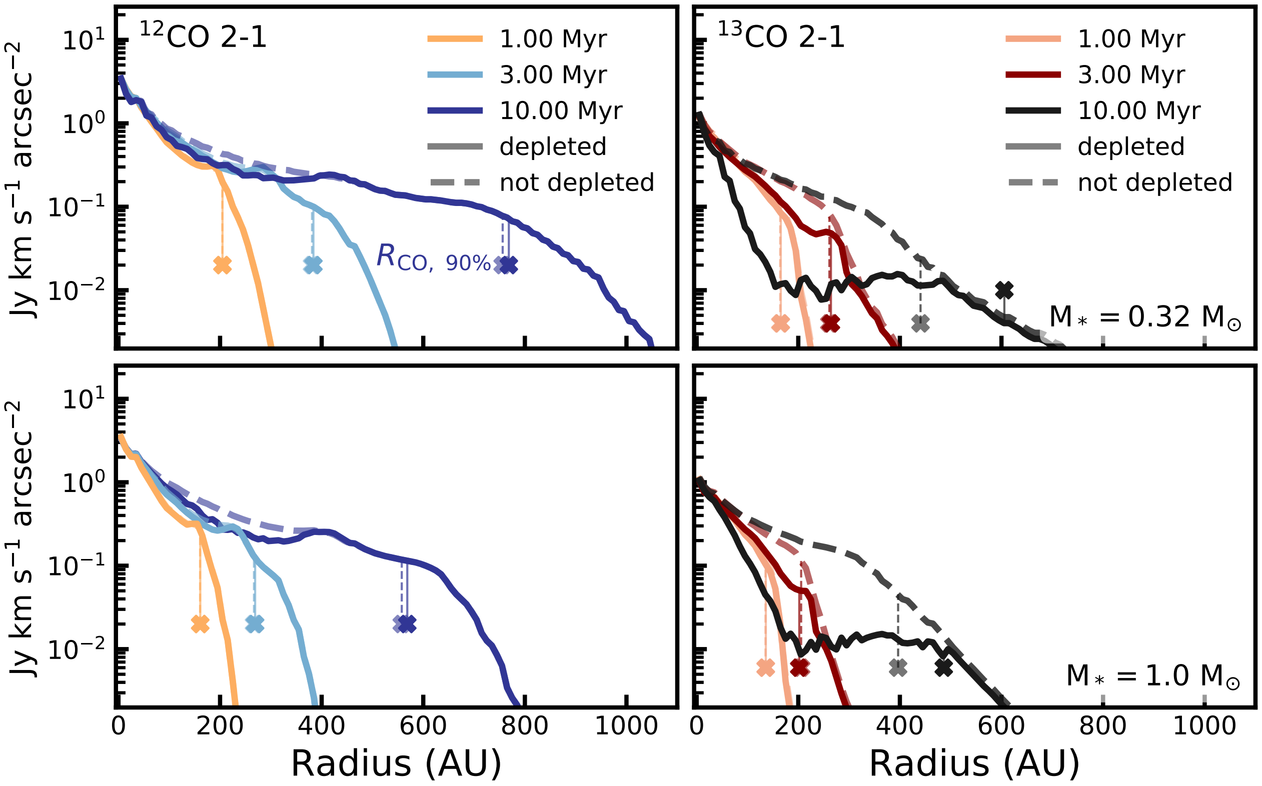

Figure 4.8: Effect of chemical CO depletion through grain-surface chemistry on the ^{12}CO 2-1 intensity profile (left panels) and ^{13}CO 2-1 intensity profile (right panels) after 1 Myr (orange), 3 Myr (light blue/dark red), and 10 Myr (blue/black). The top and bottom rows show models with $M_* = 0.32$ M$_\odot$ and $M_* = 1.0$ M$_\odot$, respectively. The profile without chemical CO depletion is shown as a dashed line. The gas outer radii ($R_{\mathrm{CO},\ 90\%}$) are shown as a cross at arbitrary height below the profile. After 1 Myr the chemical CO depletion is not significant enough to change the intensity profile and $R_{\mathrm{CO},\ 90\%}$. After 10 Myr chemical CO depletion causes $R_{\mathrm{CO},\ 90\%}$ to increase (for details, see Section 4.4.3). Figures 4.13 and 4.17 give a full overview of the ^{13}CO 2-1 intensity profile of the models without and with chemical CO depletion.

Magnetic disk winds versus viscous evolution: In Section 4.4.1 we have shown that the observations in Lupus match with our viscously spreading disk models with $\alpha_{\rm visc} = 10^{-3} - 10^{-4}$. However, we cannot exclude an alternative interpretation in which the observed $R_{\rm CO,\ 90\%}$ and stellar ages of individual disks could be reproduced by models in which disk evolution is driven by disk winds with a suitable choice of parameters. Figure 4.6 should therefore not be considered a confirmation of viscous evolution in disks. To properly distinguish between whether viscous stresses or disk winds are the dominant driver of disk evolution requires an observation of viscous spreading (or lack thereof), that is, that the average disk grows in size over time. Additionally, a search for disk winds in the objects discussed in this paper could allow us to quantitatively compare how much specific angular momentum is extracted by disk winds and how much is transported outward by viscous stresses.

Episodic accretion: In this work we have assumed a simple prescription of viscous evolution, where viscosity in the disk is described by a single parameter $\alpha_{\rm visc}$, which is kept constant in time and does not vary with radius. In reality this is likely to be a too simplistic view. For example, there is an increasing amount of evidence that stellar accretion is episodic rather than the smooth process assumed in this work (see, e.g. Audard et al. 2014 for a review). It is likely however that episodic accretion is most important in the early phases when the star is being assembled, and probably less in the later Class II phase (see, e.g. Costigan et al. 2014; Venuti et al. 2015).

If accretion were also episodic in the Class II phase, the growth of the disk size is likely also to be episodic, rather than the smooth curves shown in this work. However, to reproduce the average observed accretion rate, the episodic accretion rate averaged over time should still match the smooth accretion rate assumed in this work. Observationally, we cannot perform an average over time since the variational timescales, if any exists in the class II phase, are longer than what can be practically measured; observational studies find that accretion is modulated on the rotational period of the star (Costigan et al. 2014; Venuti et al. 2015), but that there is no variation on longer timescales. However, averaging over a sample of similar sources is mathematically equivalent to the average over time since they are at different stages of their duty cycle. Overall, the values for $\alpha_{\rm visc}$ discussed in this work thus should be intended as some kind of average over its variations in space and time.

Related to the topic of episodic accretion is the connection, at an early age, between the disk and its surrounding envelope. Material is accreted from this envelope onto the disk; current evidence indicates that this could still be ongoing into the Class I phase (see, e.g. Yen et al. 2019). While this might affect our results at early ages (0.1-0.5 Myr) it is unlikely to change our results at a later age when accretion from the envelope onto the disk has stopped, and this would be equivalent to changing the initial disk mass or the initial disk size.

4.5 Conclusions

In this work we used the thermochemical code `DALI` to examine how the extent of the CO emission changes with time in a viscously expanding disk model and investigate how well this observed measure of the gas disk size can be used to trace viscous evolution. We summarize our conclusions as follows:

- Qualitatively the gas outer radius $R_{\rm CO,\ 90\%}$ measured from the ^{12}CO emission of our models matches the signatures of a viscously spreading disk: $R_{\rm CO,\ 90\%}$ increases with time and does so at a faster rate if the disk has a higher viscous $\alpha_{\rm visc}$ (i.e., when it evolves on a shorter viscous timescale).

- For disks with high viscosity ($\alpha_{\rm visc} \geq 10^{-2}$), the combination of a rapidly expanding disk with a low initial disk mass ($M_{\rm disk} \leq 2 \times 10^{-4}$ $\mathrm{M}_{\odot}$) can result in the observed outer radius decreasing with time because CO is photodissociated in the outer disk.

- For most of our models, $R_{\rm CO,\ 90\%}$ is up to ~12 × larger than the characteristic size $R_{\rm c}$ of the disk, with the difference being larger for more massive disks. As a result, measuring $\alpha_{\rm visc}$ directly from observed $R_{\rm CO,\ 90\%}$ overestimates the true $\alpha_{\rm visc}$ of the disk by up to an order of magnitude.

- Current measurements of gas outer radii in Lupus can be explained using viscously expanding disks with $\alpha_{\rm visc} = 10^{-4} - 10^{3}$ that start out small ($R_{\rm init} = 10$ AU). The exceptions are IM Lup (Sz 82) and HK Lup (Sz 98), which require either a higher $\alpha_{\rm visc} \approx 10^{-2}$ or a larger initial disk size of $R_{\rm init} = 30 - 50$ AU to explain their large gas disk size.

- Chemical depletion of CO through grain-surface chemistry has only minimal impact on the $R_{\rm CO,\ 90\%}$ if measured from ^{12}CO emission, but can significantly reduce $R_{\rm CO,\ 90\%}$ at 5-10 Myr if measured from more optically thin tracers such as ^{13}CO.

We have shown that measured gas outer radii can be used to trace viscous spreading of disks and that models that fully simulate the observations play an essential role in linking the measured gas outer radius to the underlying physical size of the disk. Our analysis shows that current observations in Lupus are consistent with most disks starting out small and evolving viscously with low $\alpha_{\rm visc}$. However, most sources lie within an age range between 1Myr and 3 Myr, which is too narrow to confirm that disk evolution is only driven by viscosity. We therefore cannot rule out that disk winds are contributing to the evolution of the disk. Future observations should focus on expanding the available sample of observe gas disk sizes to other star-forming regions, both younger and older than Lupus, to conclusively show whether disks are viscous spreading and confirm whether viscosity is the dominant physics driving disk evolution.

Appendix

4.A Disk mass evolution

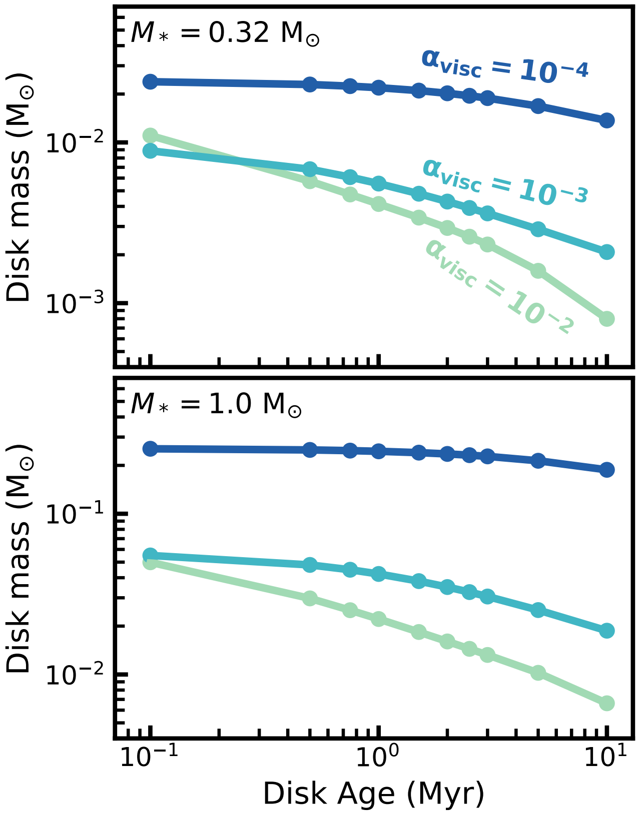

Figure 4.9: Evolution of the disk mass for the models with $M_* = 0.32$ M$_\odot$ and 1.0 M$_\odot$. Evolution of the disk mass for models with $M_* = 0.1$ M$_\odot$ is shown in Figure 4.1. The colors show models with different $\alpha_{\rm visc}$. The order of magnitude difference between the $M_* = 0.32$ M$_\odot$ models (top panel) and $M_* = 1.0$ M$_\odot$ models (bottom panel) are shown.

4.B Local UV radiation field in Upper Sco

Because they belong to the nearest OB association, the disks in Upper Sco are likely to be subjected to high levels of irradiation. In this appendix, we quantify this these irradiation levels using the locations of known B stars (de Zeeuw et al. 1999) and the disks in Upper Sco (see Figure 4.10).

Barenfeld et al. (2016) present ALMA observations of a sample of 106 stars in Upper Sco between spectral types of M5 and G2, selected based on the excess infrared emission observed by *Spitzer* or *WISE* (Carpenter et al. 2006; Luhman & Mamajek 2012). Parallaxes for 96 of these 106 stars were measured with *Gaia* as part of its DR2 data release (Brown et al. 2018). We use these parallaxes to calculate the distance to each of the stars. For the 10 stars in which no parallax is available, we instead assume the distance to be 143 pc, which is the median distance to Upper Sco based on the DR2 data (see, e.g. Bailer-Jones et al. 2018; Wright & Mamajek 2018; Damiani et al. 2019).

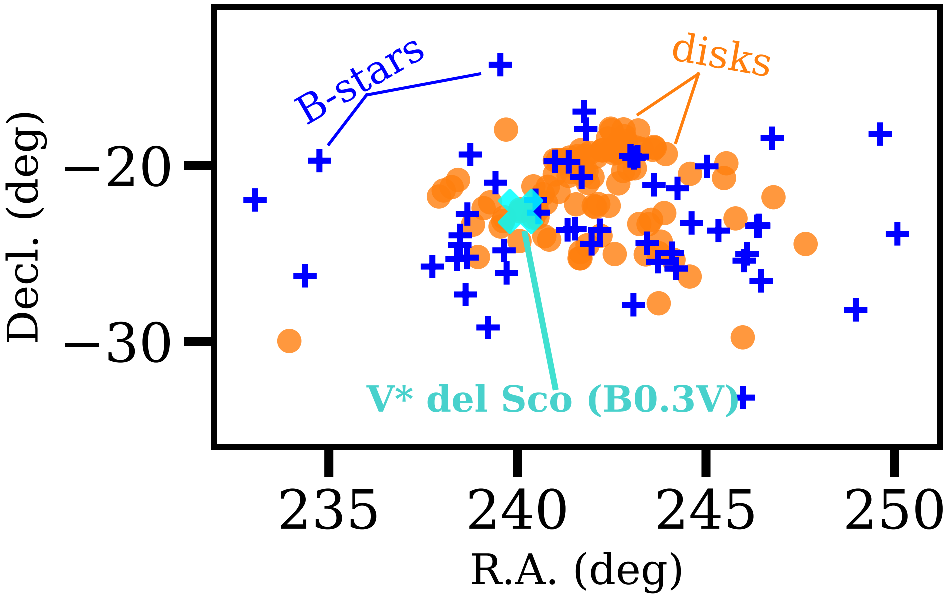

Figure 4.10: Spatial distribution of the disks in Upper Sco (colored circles) and the 49 B stars (blue crosses). The light blue cross denotes the location of V* del Sco, a B0.3V star that contributes significantly to the UV radiation in the region.

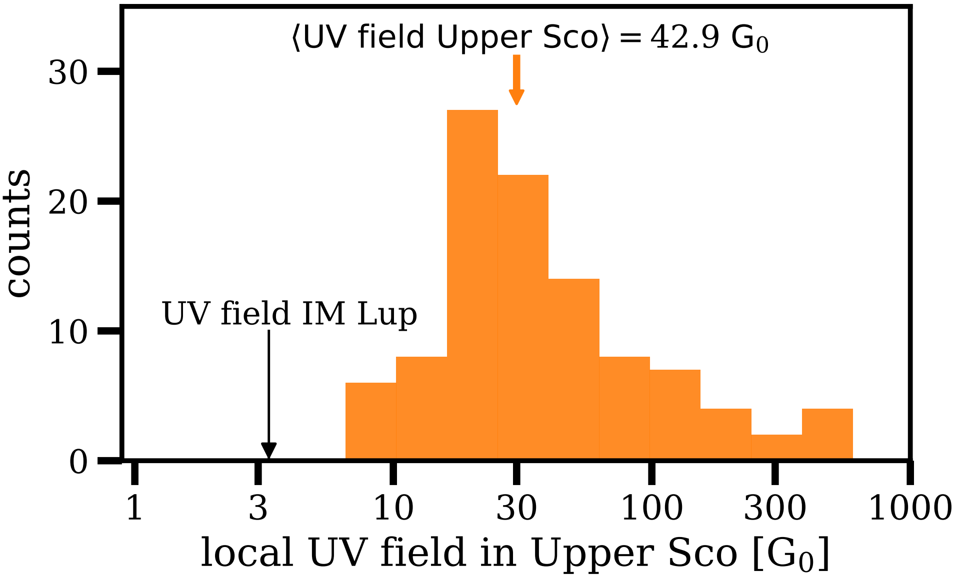

Figure 4.11: Histogram of the local UV radiation field for disks in Upper Sco. Radiation fields were calculated for each disk using Equation (4.10). The orange arrow denotes the median UV radiation field. For comparison, the black arrow shows the external UV radiation field of IM Lup (Cleeves et al. 2016).

In close proximity to these disk-hosting stars there are 49 stars with spectral type B1 and the region hosts one B0.3V star (V* del Sco) (see, e.g. de Zeeuw et al. 1999; de Bruijne 1999). With the exception of the B0 star, these stars are also part of *Gaia* DR2, allowing us to determine distances to these stars based on their parallaxes. The B0 star, V* del Sco, is too bright to be part of *Gaia* DR2. For this star we use a distance of 224 ± 24 pc, which was calculated by Megier et al. (2009) based on interstellar Ca II lines. Combining these positions and distances, we can now calculate, for each disk-hosting star, the relative distances between it and each of the B stars.

To calculate the local FUV radiation field, we take the following approach: We collect the spectral types of the 49 B stars from the catalog of de Bruijne (1999) and use them to compute their effective temperatures following Hillenbrand & White (2004). Based on these effective temperature we fit stellar masses using the stellar models from Schaller et al. (1992). Using the stellar masses we calculate the UV luminosity $L_{\rm UV,\ B\ star}$ produced by each star based on the relation presented in Buser & Kurucz (1992). Finally, for each disk in the sample from Barenfeld et al. (2016), we calculate the local UV radiation ($F_{\rm UV,\ disk}$) by adding up the relative contributions of each of the nearby B stars, that is,

$$F_{\rm UV,\ disk} = \sum_{\rm B\ stars} \frac{L_{\rm UV,\ B\ star}}{|x_{\rm disk} - x_{\rm B\ star}|^2}, \tag{4.10}$$

where $|x_{\rm disk} - x_{\rm B\ star}|$ denotes the relative distance between the disk and the B star.

Figure 4.11 shows a histogram of the local UV radiation $F_{\rm UV,\ disk}$ for the disks in Upper Sco. Levels range from $\sim$ 8 G$_0$ to $\sim$7 $\times$ 10^3 G$_0$, with a median $F_{\rm UV,\ disk} =$ 42.9 G$_0$, confirming that these disks are subjected to high levels of external UV radiation. Even the lowest $F_{\rm UV,\ disk}$ ($\sim$8 G$_0$) is several times higher than the external UV field in Lupus ($\sim$ 3 G$_0$; Cleeves et al. 2016).

Owing to the age of Upper Sco (5-11; see Preibisch et al. 2002; Pecaut et al. 2012), stars with spectral types earlier than B0.3, with lifetimes of a few up to 10 Myr might have been present in the region but are now evolved. It is therefore likely that external UV radiation in Upper Sco was higher in the past, suggesting that the $F_{\rm UV,\ disk}$ calculated in this work is a lower limit of what the disks in Upper Sco experienced during their lifetime.

4.C ^{12}CO radial intensity profiles

Figure 4.12: Time evolution of the ^{12}CO intensity profiles for our grid of models. The rows show models with equal stellar mass; the columns show models with equal $\alpha_{\rm visc}$. The colors, going from red to blue, show the different time steps. For each model, the radius enclosing 90% of the total flux is denoted by a cross. A low stellar mass corresponds to a low stellar accretion rate, using the observational relation shown in Figure 6 in Alcalá et al. (2017). Also owing to the setup, a low $\alpha_{\rm visc}$ corresponds to a high viscous time ($t_{\rm visc}$) and a high initial mass ($M_{\rm init}$).

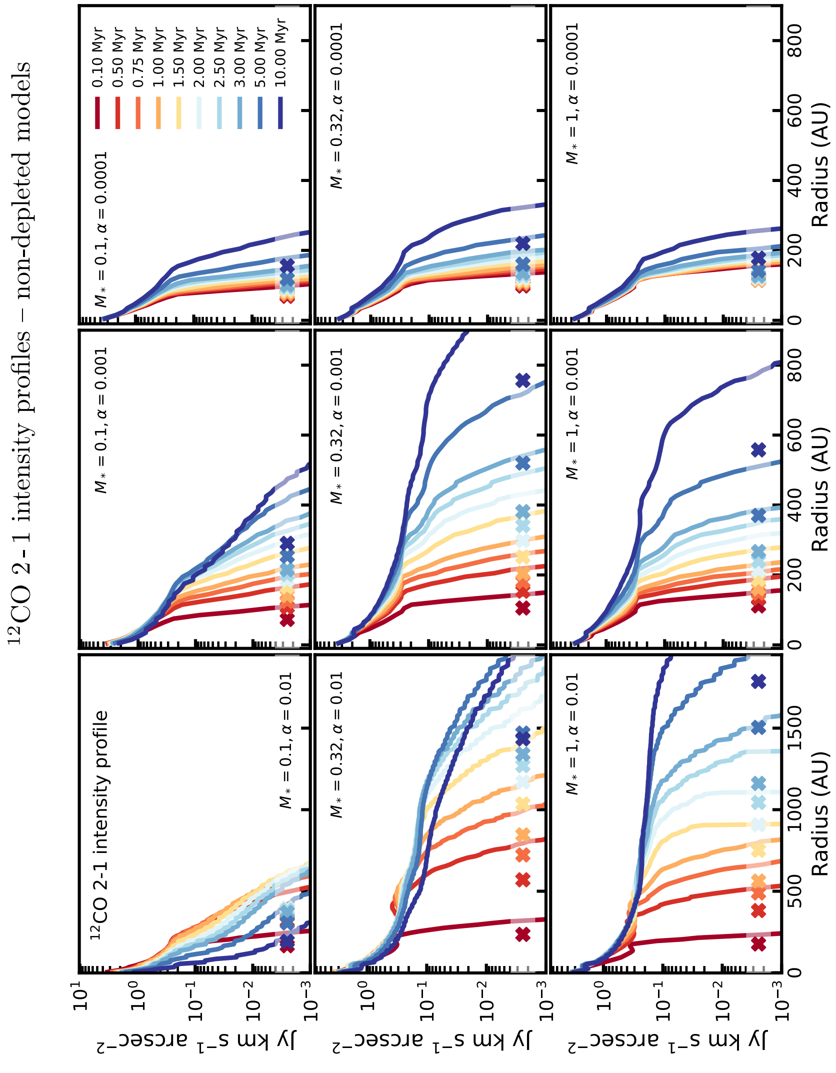

4.D Outer radii based ^{13}CO emission

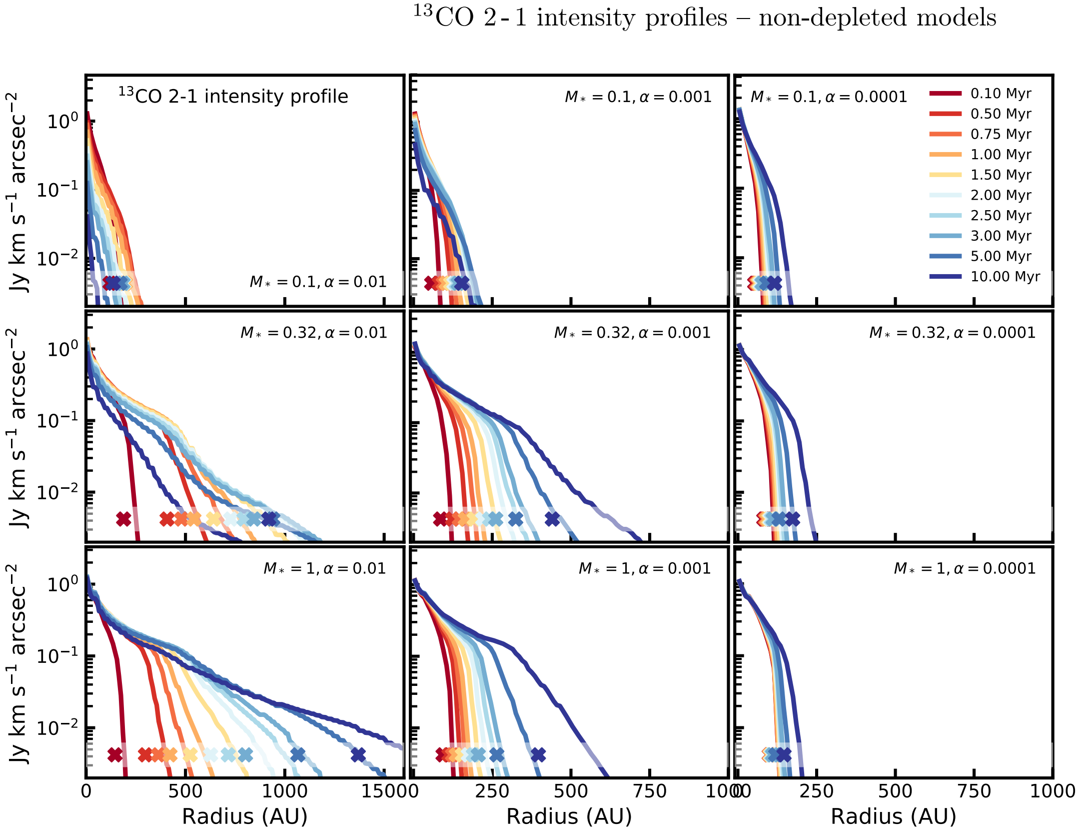

Figure 4.13: Time evolution of the ^{13}CO intensity profiles for our grid of models. The rows show models with equal stellar mass; the columns show models with equal $\alpha_{\rm visc}$. The colors, going from red to blue, show the different time steps. For each model, the radius enclosing 90% of the total flux is denoted by a cross. A low stellar mass corresponds to a low stellar accretion rate, using the observational relation shown in Figure 6 in Alcalá et al. (2017). Also owing the setup, a low $\alpha_{\rm visc}$ corresponds to a high viscous time ($t_{\rm visc}$) and a high initial mass ($M_{\rm init}$).

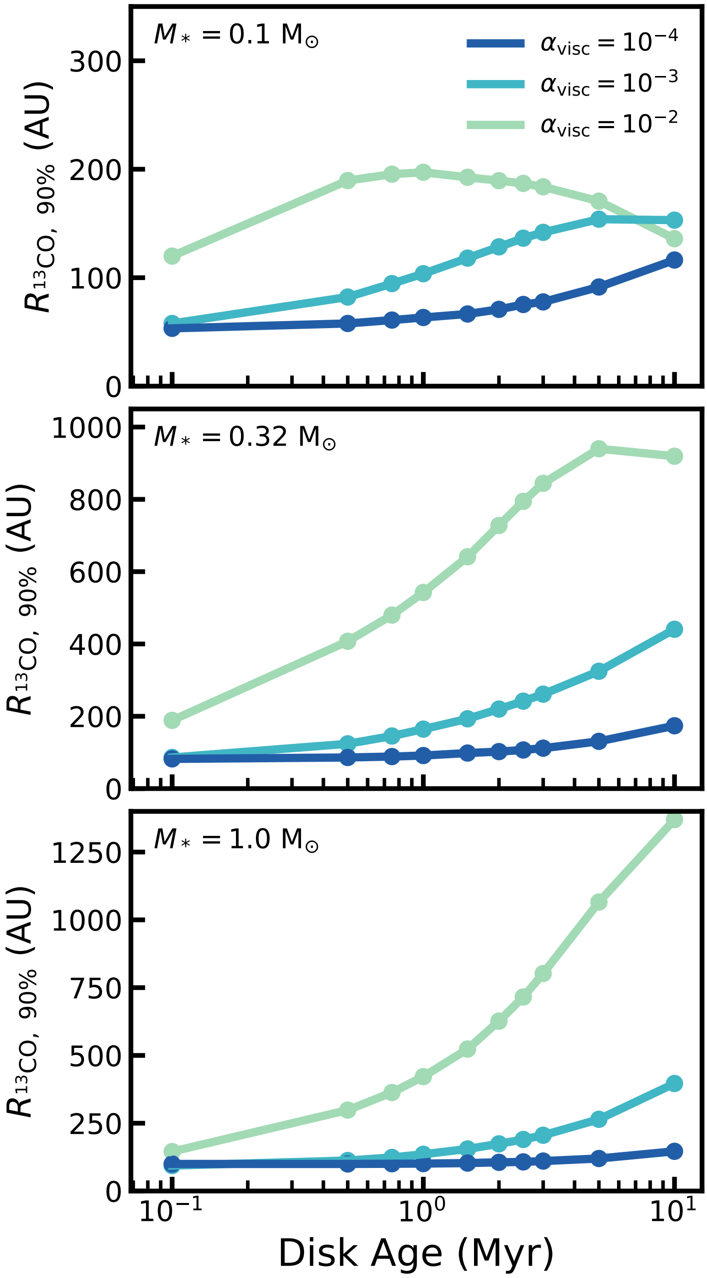

Figure 4.14: Disk ages vs. gas outer radii ($R_{\rm CO,\ 90\%}$), measured from ^{13}CO 2 - 1 emission. The top, middle, and bottom panels show models with different stellar masses. The colors indicate the $\alpha_{\rm visc}$ of the model.

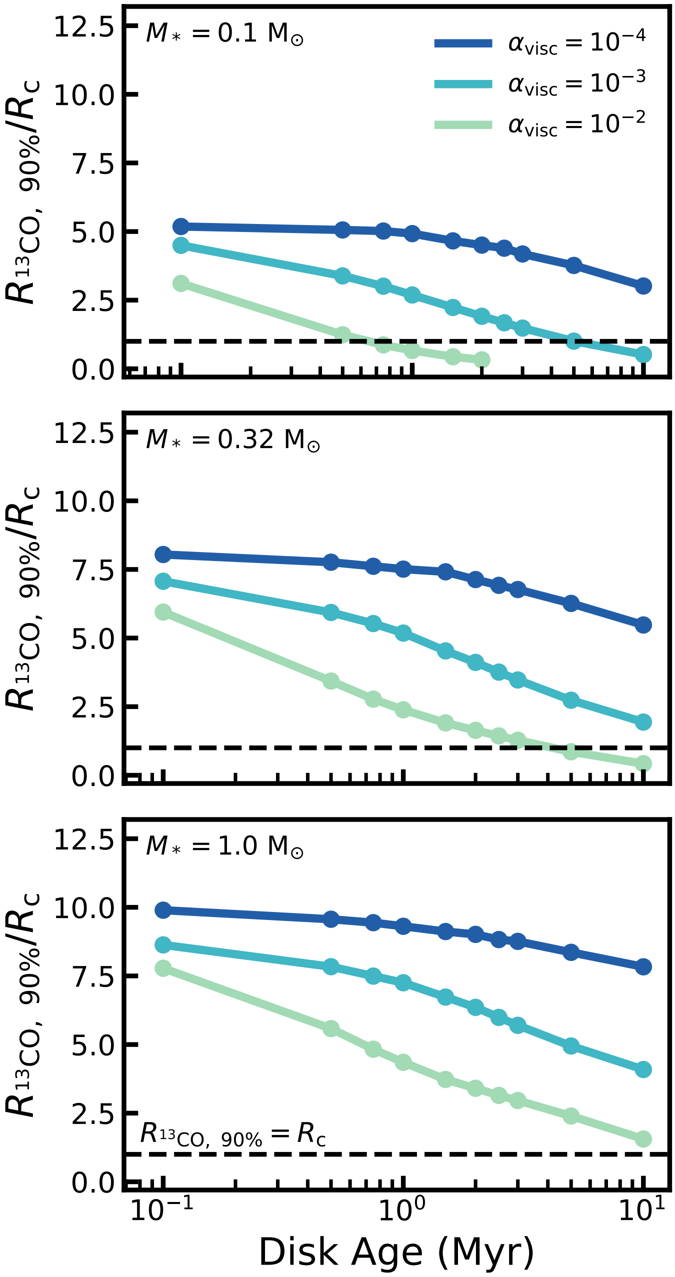

Figure 4.15: Ratio of gas outer radius ($R_{^{13}\rm CO}$) over characteristic radius ($R_{\rm c}$) vs. disk age. The gas outer radii are measured from ^{13}CO 2 - 1 emission of our models. The black dashed line indicates where $R_{^{13}\rm CO} = R_{\rm c}$. The top, middle, and bottom panels show models with different stellar masses. The colors represent models with different $\alpha_{\rm visc}$.

4.E Observed sample

Table 4.3: Observations in Lupus and Upper Sco

Name	M_* ($M_\odot$)	age (Myr)	$R_{\mathrm{CO},\ 90\%}$ (AU)
		Lupus	
Sz 65	0.70 ± 0.16	$1.3^{+1.9}_{-0.8}$	172 ± 24
Sz 68	2.13 ± 0.34	$0.8^{+0.8}_{-0.4}$	68 ± 6
Sz 71	0.42 ± 0.11	$2.0^{+3.0}_{-1.2}$	218 ± 54
Sz 73	0.82 ± 0.16	$4.0^{+6.0}_{-2.4}$	103 ± 9
Sz 75	0.51 ± 0.14	$0.8^{+1.2}_{-0.5}$	194 ± 21
Sz 76	0.25 ± 0.03	$2.0^{+1.0}_{-1.0}$	164 ± 6
J15560210-3655282	0.46 ± 0.12	$2.0^{+1.0}_{-1.0}$	110 ± 3
IM Lup	1.10 ± 0.0	$0.5^{+0.8}_{-0.3}$	388 ± 84
Sz 84	0.18 ± 0.03	$1.3^{+5.1}_{-0.3}$	146 ± 18
Sz 129	0.80 ± 0.15	$4.0^{+6.0}_{-2.4}$	140 ± 12
RY Lup	1.47 ± 0.22	$2.5^{+2.5}_{-1.3}$	250 ± 63
J16000236-4222145	0.24 ± 0.03	$1.3^{+1.3}_{-0.9}$	266 ± 45
MY Lup	1.02 ± 0.13	$10.0^{+29.8}_{-5.0}$	194 ± 39
EX Lup	0.56 ± 0.14	$2.0^{+1.0}_{-1.0}$	178 ± 12
Sz 133	0.63 ± 0.05	$2.0^{+3.0}_{-1.2}$	238 ± 66
Sz 91	0.47 ± 0.12	$6.3^{+9.5}_{-3.8}$	450 ± 80
Sz 98	0.74 ± 0.20	$0.5^{+0.8}_{-0.3}$	358 ± 52
Sz 100	0.18 ± 0.03	$1.6^{+0.9}_{-1.3}$	178 ± 12
J16083070-3828268	1.81 ± 0.28	$2.5^{+2.5}_{-1.3}$	394 ± 100
V1094 Sco	0.47 ± 0.14	$2.0^{+1.0}_{-1.0}$	438 ± 112
Sz 111	0.46 ± 0.12	$5.0^{+7.6}_{-3.0}$	462 ± 96
Sz 123A	0.46 ± 0.11	$2.0^{+1.0}_{-1.0}$	146 ± 12
	Upper Sco		
J15534211-2049282	$0.27^{+0.07}_{-0.05}$	$(5 - 11)$	$48.3^{+9.6}_{-10.5}$
J16001844-2230114	$0.19^{+0.07}_{-0.04}$	$(5 - 11)$	$58.2^{+16.1}_{-13.4}$
J16020757-2257467	$0.34^{+0.07}_{-0.06}$	$(5 - 11)$	$48.9^{+14.1}_{-11.2}$
J16035767-2031055	$1.05^{+0.13}_{-0.11}$	$(5 - 11)$	$26.3^{+166.3}_{-7.0}$
J16035793-1942108	$0.36^{+0.07}_{-0.07}$	$(5 - 11)$	$39.4^{+7.7}_{-6.0}$
J16075796-2040087	$0.45^{+0.12}_{-0.09}$	$(5 - 11)$	$31.3^{+6.4}_{-2.6}$
J16082324-1930009	$0.66^{+0.08}_{-0.06}$	$(5 - 11)$	$141.1^{+30.8}_{-34.9}$
J16123916-1859284	$0.51^{+0.09}_{-0.08}$	$(5 - 11)$	$154.2^{+23.5}_{-24.7}$
J16142029-1906481	$0.56^{+0.05}_{-0.06}$	$(5 - 11)$	$79.4^{+6.3}_{-6.1}$

Table 4.4: Stellar parameters derived from observations presented in Alcalá et al. (2014, 2017) (For the stellar age estimation, see Andrews et al. 2018b). Gas radii for Lupus from Ansdell et al. (2018). Stellar masses for Upper Sco taken from Barenfeld et al. (2016). For the stellar age, the 5-11 Myr stellar age of Upper Sco is used (see, e.g. Preibisch et al. 2002; Pecaut et al. 2012). For sources in Upper Sco $R_{\mathrm{CO},\ 90\%}$ were calculated from the fit to the observed ^{12}CO intensity in Barenfeld et al. (2017).

4.F Implementing CO chemical depletion through grain-surface chemistry

Based on the results from Bosman et al. (2018), we developed an approximated description for CO grain surface chemistry. The description only traces the main carbon carriers, that is, CO, CH_3OH, CO_2, and CH_4. Briefly, the approximation splits reactions into two groups, fast and slow reactions, and assumes that fast reactions can be calculated by equilibrium chemistry and that only the slow reactions need to be integrated explicitly. A more detailed description is provided in appendix A of Krijt et al. (2020). The approximation breaks down in the upper regions of the disk, where photodissociation of CO by UV photons becomes important. In these regions the chemistry included in `DALI` provides more accurate CO abundances. We therefore split our disk models into two regions based on the outward CO column:

$N_{\rm CO} < 10^{16}$ cm^{-2}; the outward CO column is too low for CO to self-shield against photodissociation. As a result the CO chemistry is accurately described by the photochemistry included in DALI and we therefore do not recompute the CO abundances.

$N_{\rm CO} \geq 10^{16}$ cm^{-2}: Deeper in the disk CO is able to self-shield against photodissociation. Grain-surface chemistry is able to convert CO into other species, thus lowering the gas-phase abundance of CO. For this region we recompute the CO abundances using the approximate grain-surface chemistry from Krijt et al. (2020)

Figure 4.16 presents the CO abundance structure with and without including CO depletion through grain-surface chemistry. At 1 Myr, shown in left panels, the inclusion of grain-surface chemistry has little impact on the CO abundance. However, at 10 Myr CO has become significantly depleted ($X[CO] \leq 10^{-8}$) around the midplane of the disk. We obtain the same conclusion as Bosman et al. (2018), namely that CO depletion only becomes significantly long timescales. Among our models we are only starting to see its effects after $\geq$ 5 Myr, indicating this process is most important for older star-forming regions such as Upper Sco.

Figure 4.16 also shows the emitting layers of ^{12}CO 2 - 1 and ^{13}CO 2 - 1. The chemical conversion of CO into other species predominantly takes place around the midplane, while the CO emitting layer is higher up in the disk. For ^{12}CO 2 - 1 the emitting layer lies predominantly in the region of the disk, where the CO abundances are set by photodissociation and not grain-surface chemistry, and are therefore only slightly affected by CO chemistry after 10 Myr. The emitting layer of ^{13}CO 2 - 1 lies deeper in the disk and is therefore significantly affected by the conversion of CO.

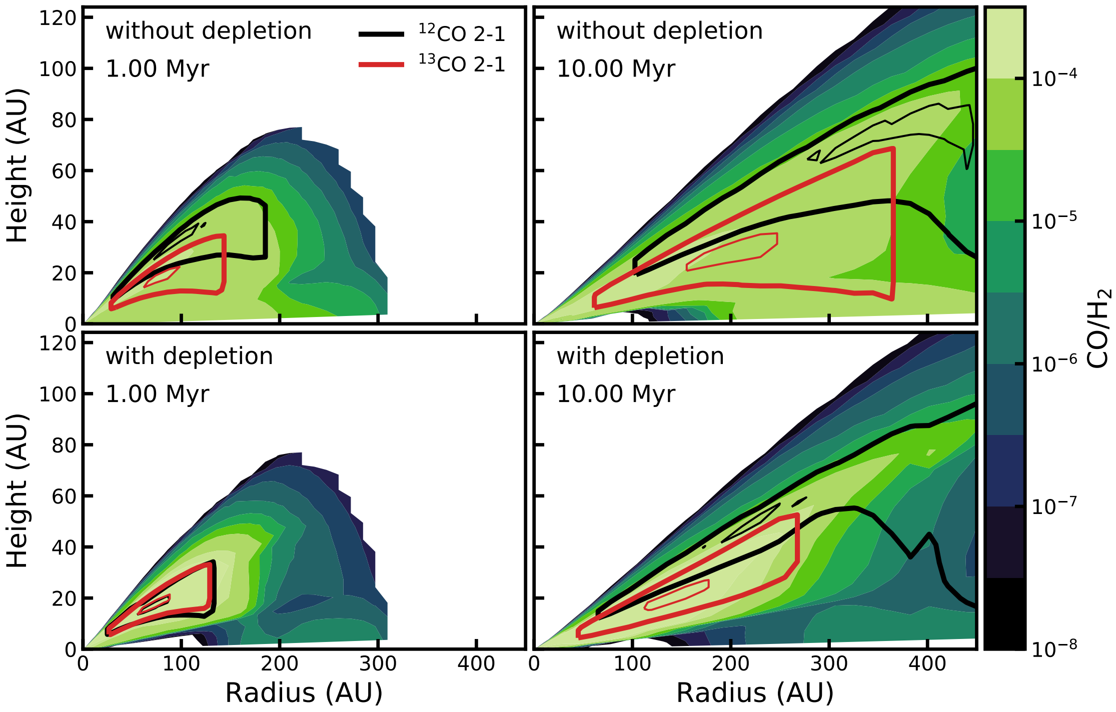

Figure 4.16: Effect of chemical depletion of CO through grain-surface chemistry on the CO abundance after 1 Myr (left panels) and 10 Myr (right panels). The example model shown has $M_* = 0.32$ M$_\odot$ and $\alpha_{\rm visc} = 10^{-3}$. The colors show the CO abundance with respect to H$_2$, where white indicates CO/H$_2 \leq 10^{-8}$. The black contours show the ^{12}CO 2-1 emitting region, enclosing 25% and 75% of the total ^{12}CO flux. Similarly, the red contours show the ^{13}CO 2-1 emitting region.

4.G Effect of CO depletion on the ^{13}CO emission

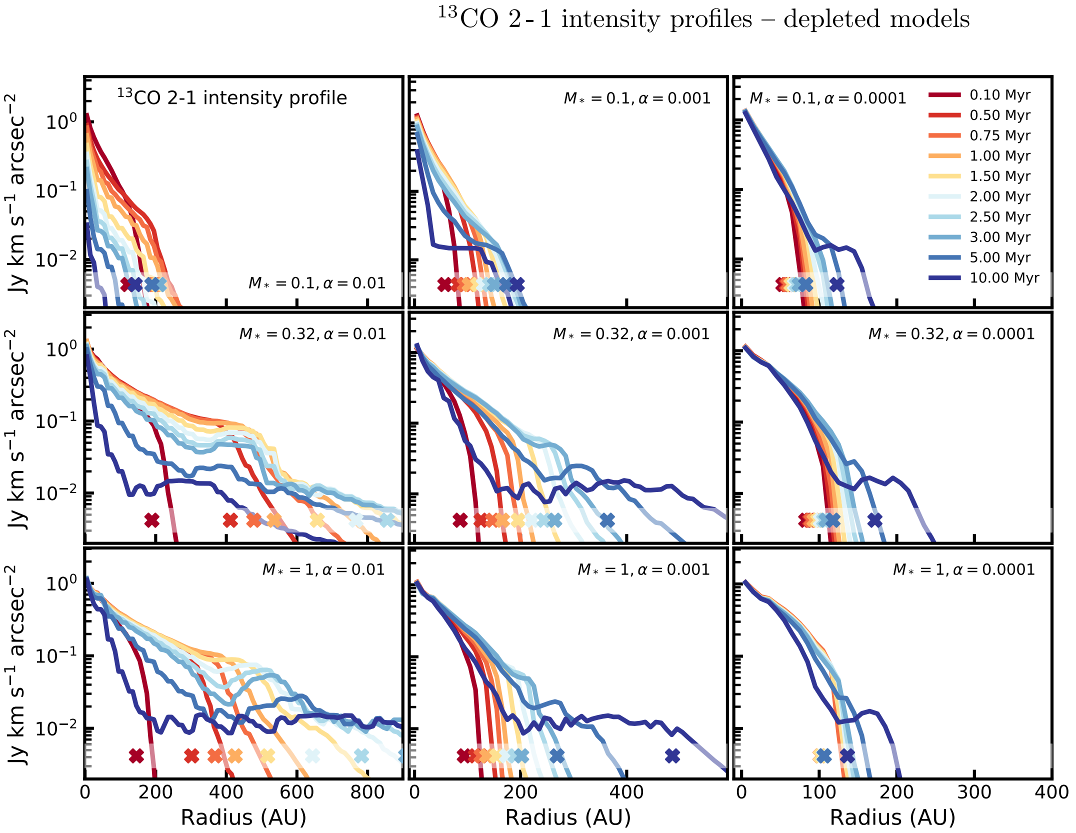

Figure 4.17: Time evolution of the ^{13}CO intensity profiles for our grid of models, after including the effects of chemical depletion of CO through grain surface chemistry (see Sections 4.4.3 and 4.F). The rows show models with equal stellar mass, columns show models with equal $\alpha_{\rm visc}$. The colors, going from red to blue, show the different time steps. For each model, the radius enclosing 90% of the total flux is indicated by a cross. A low stellar mass corresponds to a low stellar accretion rate, using the observational relation shown in Figure 6 in Alcalá et al. (2017). Also owing to the setup, a low $\alpha_{\rm visc}$ corresponds to a high viscous time ($t_{\rm visc}$) and a high initial mass ($M_{\rm init}$).

5 | CO ISOTOPOLOG LINE FLUXES OF VISCOUSLY EVOLVING DISKS: COLD CO CONVERSION INSUFFICIENT TO EXPLAIN OBSERVED LOW FLUXES

L. Trapman, A. D. Bosman, G. Rosotti, M. R. Hogerheijde and E. F. van Dishoeck,
subm. to A&A

Abstract

Context: Protoplanetary disks are thought to evolve viscously, where the disk mass - the reservoir available for planet formation - decreases over time as material is accreted onto the central star over a viscous timescale. Observations have shown a correlation between disk mass and stellar mass accretion rate, as expected from viscous theory. However, this happens only when using the dust mass as proxy of the disk mass, while the gas mass inferred from CO isotopolog line fluxes, which should be a more direct measurement, show no correlation with the stellar mass accretion rate.

Aims: We investigate how ^{13}CO and C^{18}O $J = 3 - 2$ line fluxes, commonly used as gas mass tracers, change over time in a viscously evolving disk and use them together with gas disk sizes, previously studied in Trapman et al. (2020), to provide diagnostics of viscous evolution. In addition, we aim to determine if CO conversion through grain surface chemistry combined with viscous evolution can explain observations of disks in Lupus.

Methods: We ran a series of thermochemical DALI models of viscously evolving disks, where the initial disk mass is derived from observed stellar mass accretion rates.

Results: While the disk mass $M_{\rm disk}$ decreases over time, the ^{13}CO and C^{18}O $J = 3 - 2$ line fluxes instead increase over time, due to their optically thick emitting regions growing in size as the disk expands viscously. For the disk structures examined here the C^{18}O emission becomes optically thin when $M_{\rm disk} \lesssim 3 \times 10^{-3}$ M$_\odot$, at which point the C^{18}O flux decreases with time similar to the disk mass. Based on the stellar mass-disk mass relation this corresponds to disks around stars with $M_* \lesssim 0.3$ M$_\odot$. Observed ^{13}CO and C^{18}O 3-2 fluxes of the most massive disks ($M_{\rm disk} \gtrsim 5 \times 10^{-3}$ M$_\odot$) in Lupus can be reproduced to within a factor of ~ 2 with viscously evolving disks where CO is converted into other species through grain-surface chemistry with a moderate cosmic-ray ionization rate $\zeta_{\rm cr} \sim 10^{-17}$ s^{-1}. The C^{18}O 3-2 fluxes for the bulk of the disks in Lupus (with $M_{\rm disk} \lesssim 5 \times 10^{-3}$ M$_\odot$) can be reproduced to within a factor of ~ 2 by increasing $\zeta_{\rm cr} \sim 5 \times 10^{-17} - 10^{-16}$ s^{-1}, although explaining the stacked upper limits requires a lower average abundance than our models can produce. In addition, increasing $\zeta_{\rm cr}$ cannot explain the observed ^{13}CO fluxes for lower mass disks, which are more than an order of magnitude fainter than what is predicted. In our models the optically thick ^{13}CO emission originates from a layer higher up in the disk ($z/r \sim 0.25 - 0.4$) where photodissociation stops the conversion of CO into other species. Reconciling the ^{13}CO fluxes of viscously evolving disks with the observations requires either efficient vertical mixing or low mass disks ($M_{\rm dust} \lesssim 3 \times 10^{-5}$ M$_\odot$) being much thinner and/or smaller than their more massive counterparts.

Conclusions The ^{13}CO model flux predominantly traces the disk size, but the C^{18}O model flux traces the disk mass of our viscously evolving disk models if chemical conversion of CO is included. The discrepancy between the CO isotopolog line fluxes of viscous evolving disk models and the observations suggests that CO is efficiently vertically mixed or that low mass disks are smaller and/or colder than previously assumed.

5.1 Introduction

With over 4200 exoplanets detected[1] in a multitude of planetary systems, it has become clear that the formation of planets around young stars is a common occurrence (see, e.g., Borucki et al. 2011; Winn & Fabrycky 2015; Morton et al. 2016). Understanding the processes behind the formation of planets has proven challenging. A key ingredient is the total amount of material available in the protoplanetary disks in which these planets form and grow (see, e.g., Benz et al. 2014; Armitage 2015; Mordasini 2018). The disk mass determines how much raw material can be accreted onto the forming planets. The disk mass is also not static, as accretion onto the central star slowly decreases its mass over time. Combined, the disk mass and the stellar mass accretion rate determine the lifetime of the disk and therefore set an upper limit to the duration of planet formation. Determining disk masses and how they evolve over time is therefore crucial for our understanding of planet formation.

It is commonly assumed that protoplanetary disks evolve viscously (see, e.g. Lynden-Bell & Pringle 1974; Shakura & Sunyaev 1973). Viscous stresses in the disk transport angular momentum outward, causing the outer parts of the disk to spread out. To conserve angular momentum this causes material to be transported inward where it is accreted onto the central star. While still debated, the physical process behind this effective viscosity is commonly assumed to be the magnetorotational instability (see, e.g. Balbus & Hawley 1991, 1998). In the framework of viscous evolution the disk mass $M_{\rm disk}$ and the stellar mass accretion rate $\dot{M}_{\rm acc}$ follow a linear relation, with the disk mass being accreted onto the star on a viscous timescale ($M_{\rm disk} \sim \dot{M}_{\rm acc} t_{\rm visc}$).

Alternatively, it has been suggested that the angular momentum in disks can be removed by magnetic disk winds rather than transported outward by viscous stresses (see, e.g Turner et al. 2014). These magnetic disks winds form in the presence of a vertical magnetic field in the disk and they are able to remove material from the disk surface, thus reducing the total angular momentum in the disk. What fraction of the angular momentum can be carried away by disk winds is still a matter of debate (see, e.g, Ferreira et al. 2006; Béthune et al. 2017; Zhu & Stone 2018). Magnetic disk winds have been detected in observations but predominantly in the inner part of the disk and it remains unclear how much disk winds affect disk evolution (see, e.g, Pontoppidan et al. 2011; Bjerkeli et al. 2016; Tabone et al. 2017; de Valon et al. 2020).

Recently, several combined observing campaigns have performed large surveys of the full disk population, allowing the simultaneously study of properties of protoplanetary disks and the young stellar objects that host them. Several star-forming regions have been covered by Atacama Large Millimeter/sub-millimeter Array (ALMA) disk surveys, providing high angular resolution observations of disk continuum emission and carbon monoxide (CO) rotational line emission (e.g Ansdell et al. 2016; Ansdell et al. 2017, 2018; Barenfeld et al. 2016, 2017; Pascucci et al. 2016; Long et al. 2017; Cazzoletti et al. 2019; Cox et al. 2017; Cieza et al. 2019; Williams et al. 2019. Using spectra from X-shooter spectrograph (Vernet et al. 2011) at the ESO Very Large Telescope, stellar properties such as stellar mass accretion rate have also been measured for a large fraction of disk-hosting stars in star-forming regions like Lupus, Chamaeleon I and Upper Sco (Alcalá et al. 2014, 2017; Manara et al. 2017, 2020).

Combining observations for the disk population in Lupus, Manara et al. (2016b) found a correlation between observed stellar mass accretion rate $\dot{M}_{\rm acc}$ and the disk dust

---

[1] `http://www.exoplanet.eu`

mass M_{dust} derived from millimeter continuum emission. If an interstellar medium (ISM) gas-to-dust mass ratio $\Delta_{\mathrm{gd}} = 100$ is assumed, the observations, i.e., $\dot{M}_{\mathrm{acc}}$ and $M_{\mathrm{disk}} = 100 \times M_{\mathrm{dust}}$, are consistent with viscous disks having evolved for 1-3 Myr, which matches the approximate age of the sources (see also Rosotti et al. 2017). Interestingly, they find no correlation between $\dot{M}_{\mathrm{acc}}$ and the disk gas mass M_{gas} derived from ^{13}CO $J = 3 - 2$ and C^{18}O $J = 3 - 2$ line fluxes. This seems to contradict their first finding, suggesting that the disk gas mass, which is expected to make up most of the total disk mass, is not related to the stellar mass accretion rate.

The cause for this discrepancy might lie with the tracer used to measure the disk gas mass. For most disks the gas masses derived from optically thin CO isotopologs like ^{13}CO and C^{18}O are found to be low compared to their dust mass, with $\Delta_{\mathrm{gd}} = M_{\mathrm{gas}}/M_{\mathrm{dust}} \approx 1 - 10$ for most disks (see, e.g. Ansdell et al. 2016; Miotello et al. 2017; Long et al. 2017). *Herschel* Space observatory observations of the hydrogen deuteride (HD) $J = 1 - 0$ rotational line towards a handful of disks has provided an independent measurement of the disk gas mass (Bergin et al. 2013; McClure et al. 2016; Trapman et al. 2017; Kama et al. 2020). These observations find a gas-to-dust mass ratio of ~ 100, suggesting that the low CO-based gas masses are a sign that disks are underabundant in CO. This underabundance is in addition to well-understood processes such as CO freeze-out and photodissociation. Several processes have been suggested to explain the extra underabundance of CO, such as chemical conversion of CO in the gas or on the grains into more complex species (e.g., Aikawa et al. 1997; Bergin et al. 2014; Bosman et al. 2018; Schwarz et al. 2018), or locking CO up in larger bodies (see, e.g., Bergin et al. 2010; Bergin et al. 2016; Kama et al. 2016b; Krijt et al. 2018).

In this work we use an alternative approach to investigate the lack of a correlation between $\dot{M}_{\mathrm{acc}}$ and the CO-based M_{gas}, by taking a step back and examine what ^{13}CO and C^{18}O line fluxes are expected for viscously evolving disks. Over time the disk spreads out and the disk mass decreases, changing ^{13}CO- and C^{18}O-column densities distributions and the resulting line fluxes. Furthermore, by using the initial gas masses that can explain the observed stellar mass accretion rates, we can examine if the observed ^{13}CO and C^{18}O line fluxes are consistent with viscous evolution.

Recently, Trapman et al. (2020) used the same modeling framework to examine if observed gas outer radii of disks in the Lupus and Upper Sco star-forming regions can be explained with viscous evolution (see also Ansdell et al. 2018; Barenfeld et al. 2017). They showed that gas outer radii of disks in Lupus are consistent with viscously evolving disks that start out small, i.e. an initial characteristic radius of ~ 10 AU, and that have a low viscosity ($\alpha_{\mathrm{visc}} = 10^{-4} - 10^{-3}$). Combining their results with our analysis of the CO isotopolog line fluxes, we can examine if disks are in agreement with viscous theory in terms of both their size and their mass.

The structure of this work is as follows: In Section 5.2 we discuss the setup and initial conditions of our models. Here we also outline the implementation of CO conversion through grain-surface chemistry. In Section 5.3 we first show how ^{13}CO and C^{18}O line fluxes change over time in a viscously evolving disk and how they shift if grain-surface chemistry converts CO into other species. Next we compare our models to observations in Lupus and discuss the cosmic-ray ionization rates that are required to match the observed fluxes. In Section 5.4 we look in more detail at the ^{13}CO and C^{18}O fluxes that are overproduced by our models and we discuss the impact of vertical mixing and alternative explanation such as small disks. We conclude in Section 5.5

that reconciling the ^{13}CO and C^{18}O fluxes of viscously evolving disks models with the observations requires either that CO is efficiently mixed vertically or that low mass disks are small.

5.2 Model setup

Our approach for setting up our models is the following. Based on observed stellar accretion rates we calculate what the initial disk mass must have been, assuming that the disk has evolved viscously. From the initial disk masses we compute the surface density profile ($\Sigma(R,t)$) analytically at 10 consecutive disk ages. At each time-step the thermochemical code Dust and Lines (`DALI`; Bruderer et al. 2012; Bruderer 2013) is used to calculate temperature and chemical structure of the disk and the model is ray-traced to obtain ^{13}CO $J = 3-2$ and C^{18}O $J = 3-2$ integrated line fluxes. This modeling approach was previously used by Trapman et al. (2020) to study the evolution of measured gas disk sizes.

5.2.1 Viscous evolution of the surface density

While the physical processes underlying the viscosity in disks are still an open question, it is common to describe the kinetic viscosity ν using the dimensionless parameter $\alpha_{\rm visc}$, defined as $\nu = \alpha c_s H$, where c_s is the sound speed and H is the height above the midplane (the $\alpha-$disk formalism, see Shakura & Sunyaev 1973; Pringle 1981). In this formalism a self-similar solution for the surface density Σ can be calculated (Lynden-Bell & Pringle 1974; Hartmann et al. 1998)

$$\Sigma_{\rm gas}(R) = \frac{(2-\gamma)\,M_{\rm disk}(t)}{2\pi R_{\rm c}(t)^2}\left(\frac{R}{R_{\rm c}(t)}\right)^{-\gamma}\exp\left[-\left(\frac{R}{R_{\rm c}(t)}\right)^{2-\gamma}\right], \tag{5.1}$$

where γ enters by assuming that the viscosity varies radially as $\nu \propto R^{\gamma}$ and $M_{\rm disk}$ and $R_{\rm c}$ are the disk mass and the characteristic radius, respectively.

The evolution of the surface density depends on how $M_{\rm disk}$ and $R_{\rm c}$ change over time (see, e.g. Hartmann et al. 1998)

$$\begin{aligned} M_{\rm disk}(t) &= M_{\rm disk}(t=0)\left(1+\frac{t}{t_{\rm visc}}\right)^{-\frac{1}{[2(2-\gamma)]}} && (5.2)\\ &= M_{\rm disk}(t=0)\left(1+\frac{t}{t_{\rm visc}}\right)^{-\frac{1}{2}} && (5.3)\\ R_{\rm c}(t) &= R_{\rm c}(t=0)\left(1+\frac{t}{t_{\rm visc}}\right)^{\frac{1}{(2-\gamma)}} && (5.4)\\ &= R_{\rm c}(t=0)\left(1+\frac{t}{t_{\rm visc}}\right). && (5.5) \end{aligned}$$

Here $t_{\rm visc}$ is the viscous timescale. For the second step and the rest of this work we have assumed $\gamma = 1$. For a typical temperature profile this corresponds to the case where $\alpha_{\rm visc}$ stays constant with radius. The time evolution of $M_{\rm disk}$ for our models can be seen in Figure 5.1.

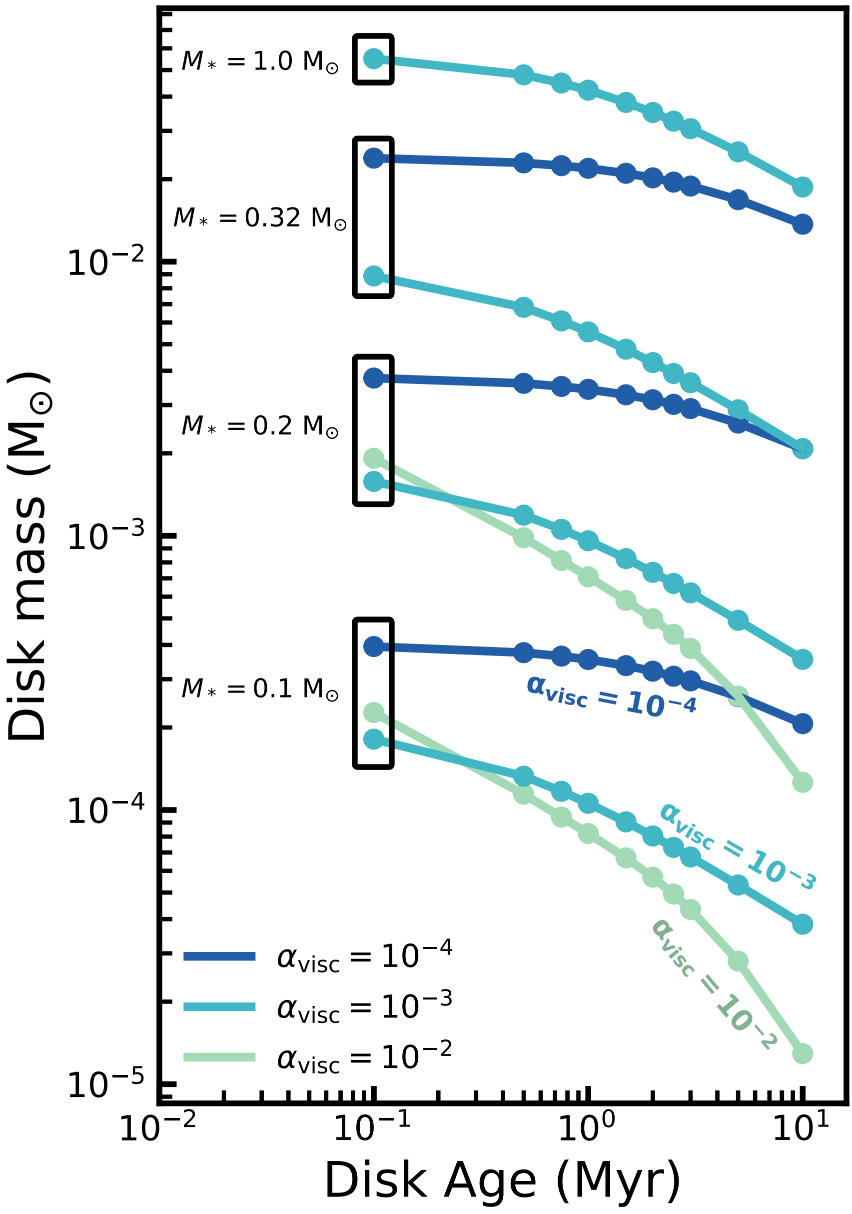

Figure 5.1: Time evolution of the disk mass $M_{\rm disk}$ of our models. Colours indicate the viscous alpha $\alpha_{\rm visc}$ of the models. The black boxes show which stellar mass, and therefore accretion rate, was used to calculate the initial disk mass of the models (see Table 5.1). Note that we exclude models with $\alpha_{\rm visc} = 10^{-2}$ for $M_* = [0.32, 1.0]$ M$_\odot$ as the gas disk sizes of these models can be ruled out by observations of disks in Lupus (Trapman et al. 2020). Also note that models with $M_* = 1.0$ M$_\odot$ and $\alpha_{\rm visc} = 10^{-4}$ are much more massive ($M_{\rm gas} \gtrsim 2 \times 10^{-1}$ M$_\odot$) than the disks observed in Lupus (cf. Ansdell et al. 2016; see Figure A.1 in Trapman et al. 2020).

5.2.2 Initial disk mass and disk size

Over time the mass of a disk decreases as material is accreted onto the central star. For a disk that is viscously evolving with a constant $\alpha_{\rm visc}$ the relation between the initial disk mass $M_{\rm disk}(t = 0)$ and the stellar mass accretion rate $\dot{M}_{\rm acc}$ at a given time t can be written such that the initial disk mass is a function of $\dot{M}_{\rm acc}$(t) (see, e.g. Hartmann et al. 1998)

$$M_{\rm disk}(t=0) \quad = 2\ t_{\rm visc}\ \dot{M}_{\rm acc}(t)\ \left(\frac{t}{t_{\rm visc}}+1\right)^{3/2}. \tag{5.6}$$

Stellar mass accretion rates have now been measured for multiple star-forming regions like Lupus, Chamealeon I and Upper Sco (Alcalá et al. 2014, 2017; Manara et al. 2017, 2020). Based on these accretion rates we can calculate what the initial disk masses would have been, given the viscous timescale and the average age of the star-forming region.

To determine the initial disk masses of the models, our approach is as follows. We take four stellar mass accretion rates ($4\times10^{-12}, 4\times10^{-11}, 2\times10^{-9}$ and 10^{-8} $\rm M_{\odot}\ yr^{-1}$) that span the range of the observations in Lupus (see, e.g. Alcalá et al. 2014, 2017). As observations have shown that $\dot{M}_{\rm acc}$ is correlated to M_{*} our selected $\dot{M}_{\rm acc}$ represent the average accretion rates for stars with $M_{*} = 0.1, 0.2, 0.32$ and 1.0 $\rm M_{\odot}$, respectively. For these stellar mass accretion rates we calculate what the initial disk mass must have been for three different viscous timescales, assuming an average age of 1 Myr for Lupus. The viscous timescales are calculated for three values of the dimensionless viscosity $\alpha_{\rm visc} = 10^{-2}, 10^{-3}, 10^{-4}$, assuming a characteristic radius of 10 AU (a choice which is discussed below) and a disk temperature $T_{\rm disk}$ of 20 K (see, e.g. equation 37 in Hartmann et al. 1998)

$$\frac{t_{\rm visc}}{\rm yr} = \frac{R_{\rm c}^2}{\nu} \simeq 8\times10^4 \left(\frac{10^{-2}}{\alpha_{\rm visc}}\right)\left(\frac{R_{\rm c}}{10\ \rm AU}\right)\left(\frac{M_{*}}{0.5\ \rm M_{\odot}}\right)^{1/2}\left(\frac{10\ \rm K}{T_{\rm disk}}\right). \tag{5.7}$$

The resulting initial disk masses, 12 in total, are summarized in Table 5.1. Figure 5.1 shows how these disk masses decrease over time. In our analysis we exclude three models. Trapman et al. (2020) showed that the gas disk sizes measured from models with $\alpha = 10^{-2}$ and $M_{*} = [\,0.32, 1.0\,]$ $\rm M_{\odot}$ can be ruled out based on observed gas disk sizes in Lupus. We also exclude the model with $M_{*} = 1.0$ $\rm M_{\odot}$ and $\alpha = 10^{-4}$ which has an initial disk mass of $M_{\rm disk} = 2.6\times10^{-1}$ $\rm M_{\odot}$. At all points during its evolution this model is factor of 5 more massive than the most massive disk observed in Lupus, but consistent with Class 0/1 disk masses (cf. Figure A.1 in Trapman et al. 2020; see also Tychoniec et al. 2018, 2020; Tobin et al. 2020).

For the initial disk size we assume that disks start out small, with an initial characteristic disk size $R_{\rm c}(t = 0) = 10$ AU. Recently, Trapman et al. (2020) showed that the observed gas outer radii of Class II disks in Lupus can be explained by viscously evolving disks that start out small ($R_{\rm c}(t = 0) = 10$ AU) and that have a low viscosity ($\alpha_{\rm visc} = 10^{-4} - 10^{-3}$). More importantly, they show that the bulk of the observed gas outer radii cannot be explained by disks that start out large ($R_{\rm c}(t = 0) \geq 30$ AU).

Observational constraints on the disk size of young Class 1 and 0 objects have only recently become available. In their VANDAM II survey Tobin et al. 2020 presented ALMA observations of 330 protostars in Orion at a resolution of $\sim 0\farcs1$ (~ 40 AU in diameter). Their observations suggest that the majority of disks are initially small ($\sim 37 - 45$ AU in radius), at least in the dust. It is worth mentioning that their radii are defined as half of the full with at half maximum (FWHM) of a 2D Gaussian fit to the observations, which is not the same as the characteristic radius of the disk. For the gas there is similar evidence that disks start out small, albeit from a smaller sample. Maret et al. (2020) presented NOEMA observations of 16 Class 0 protostars as part of the CALYPSO large program. They found only two sources that show a Keplerian disk larger than ~ 50 AU. This suggests that stars with a large Keplerian disk at a young age, such as found for VLA 1623 (Murillo et al. 2013), are uncommon. We therefore adopt an initial disk size of $R_{\rm init} = 10$ AU for our models.

Table 5.1: Initial conditions of our `DALI` models

M_*	$\dot{M}_{\rm acc}$	$\alpha_{\rm visc}$		
($M_\odot$)	($M_\odot$ yr^{-1})	10^{-2}	10^{-3}	10^{-4}
		$M_{\rm disk}$ ($M_\odot$) at $t = 0$		
0.1	4×10^{-11}	4.5×10^{-4}	2.1×10^{-4}	4.1×10^{-4}
0.2	4×10^{-10}	3.6×10^{-3}	1.8×10^{-3}	3.9×10^{-3}
0.32	2×10^{-9}	*2.0×10^{-2}*	1.0×10^{-2}	2.5×10^{-2}
1.0	1×10^{-8}	*6.9×10^{-2}*	5.9×10^{-2}	*2.6×10^{-1}*

Notes. Disk masses in italic are not included in our analysis (see Section 5.2.2). The viscous timescale in the models varies approximately as $t_{\rm visc} \simeq 0.5 \times \left(10^{-3}/\alpha_{\rm visc}\right) \times 10^6$ yr.

5.2.3 The `DALI` models

Using the initial conditions discussed previously we compute how $M_{\rm disk}$ decreases and $R_{\rm c}$ increases over time. For 10 points in the lifetime of the disk, starting at 0.1 Myr and ending at 10 Myr, we compute the current surface density $\Sigma_{\rm gas}(t)$ of the disk model.

We use the thermochemical code `DALI` to compute CO isotopolog abundances and line fluxes of our disk models. `DALI` is a 2D physical-chemical code that computes the thermal and chemical structure for a given physical disk structure. For each $\Sigma_{\rm gas}(t)$, the radiation field (from UV- to mm-wavelengths) at each point in the disk and dust temperature structure are determined from Monte Carlo radiative transfer. Next, the code computes atomic and molecular abundances by solving the time-dependent chemistry. The heating and cooling balance is solved to calculate the gas temperature. These two steps are solved iteratively until a self-consistent solution is obtained. Raytracing of the model then yields line fluxes. For a more detailed description of the code we refer the reader to Appendix A of Bruderer et al. (2012).

To obtain a 2D (i.e., R, z) density structure for our models we assume that in the vertical direction the disk follows a Gaussian density distribution, as motivated by hydrostatic equilibrium (see, e.g. Chiang & Goldreich 1997). The height of the disk is assumed to follow a powerlaw of the form $H = Rh = Rh_c \left(R/R_{\rm c}\right)^{\psi}$, where h_c is the opening angle at R_c and ψ is the flaring angle.

Dust settling is included in our models by splitting the dust grains into two populations. Most of the dust mass (90%) is in large grains with sizes of 1-10^3 μm. These large grains follow the gas radially but vertically they are confined to the midplane by reducing their scale height by a factor $\chi = 0.2$ with respect to the gas. A population of small grains (0.005-1 μm) make up the remaining 10% of the dust mass in the disk. These small grains follow the distribution of the gas both radially and vertically.

For the stellar spectrum we assume a blackbody with effective temperature for T_eff = 4000 K. A second blackbody with T_eff = 10000 K is added to simulate the excess UV radiation released by material accreted onto the star. To compute the luminosity of this second component we follow Kama et al. (2015) and assume that the gravitational potential energy of the accreted material is converted into radiation with a 100% efficiency. These parameters are summarized in Table 5.2.

Table 5.2: `DALI` parameters of the physical model.

Parameter	Range
Chemistry	
Chemical age	0.1-10 Myr*,†
Volatile [C]/[H]	1.35×10^{-4}
Volatile [O]/[H]	2.88×10^{-4}
Physical structure	
γ	1.0
ψ	0.15
h_c	0.1
R_c	$10 - 3 \times 10^3$ AU†
M_gas	$10^{-5} - 10^{-1}$ M$_\odot^\dagger$
Gas-to-dust ratio	100
Dust properties	
f_large	0.9
χ	0.2
composition	standard ISM^1
f_PAH	0.001
Stellar spectrum	
T_eff	4000 K + Accretion UV
L_*	0.28 L$_\odot$
L_X	10^{30} erg s^{-1}
ζ_cr	10^{-17} s^{-1}
Observational geometry	
i	0°
PA	0°
d	150 pc

Notes. *The age of the disk is taken into account when running the time-dependent chemistry. †These parameters evolve with time. ^{1}Weingartner & Draine 2001, see also Section 2.5 in Facchini et al. 2017.

Isotopolog chemical network

For less abundant isotopologs of CO like ^{13}CO, C^{18}O, and C^{17}O, isotope-selective photodissociation can have significant effect on their abundances (see, e.g. Visser et al. 2009; Miotello et al. 2014). Miotello et al. (2014) expanded the standard chemical network of DALI, based on the UMIST 06 network (Woodall et al. 2007; Bruderer et al. 2012; Bruderer 2013), to include the isotope-selective photodissociation and chemistry of ^{13}CO, C^{18}O, and C^{17}O. The chemical network includes the formation of H_2 on grains, freeze-out, thermal and non-thermal desorption of species, hydrogenation of simple species on ices, gas-phase reactions, photodissociation, X-ray- and cosmic-ray-induced reactions, polycyclic aromatic hydrocarbon (PAH) grain charge exchange and/or hydrogenation, and reactions with vibrationallly excited H_2^*. A detailed description of the implementation of these reactions can be found in Appendix A.3.1 of Bruderer et al. (2012). A full description of the isotopolog chemical network can be found in Miotello et al. (2014). For the initial volatile carbon and oxygen abundances, typical ISM values of $[\mathrm{C}]/[\mathrm{H}]_{\mathrm{ISM}} = 1.35 \cdot 10^{-4}$, $[\mathrm{O}]/[\mathrm{H}]_{\mathrm{ISM}} = 2.88 \cdot 10^{-4}$ were used (Bruderer et al. 2012).

Relevant for this work is that in the `DALI` chemical network CO is not further processed once it is frozen out on the grains. The only reaction included in the network that affects CO ice is desorption back into the gas-phase.

CO conversion through grain surface chemistry

Recent observations have shown that a large fraction of protoplanetary disks have unexpectedly low ^{13}CO and C^{18}O line fluxes (see, e.g., Ansdell et al. 2016; Miotello et al. 2017; Long et al. 2017). Gas masses derived from these line fluxes using models that include freeze-out and photodissociation suggest that the bulk of the protoplanetary disks are gas poor, with gas-to-dust mass ratios (Δ_{gd}) of the order of $\Delta_{\mathrm{gd}} \approx 1 - 10$. For a few disks the gas mass has been determined independently using HD (see, e.g., Bergin et al. 2013; McClure et al. 2016; Trapman et al. 2017; Kama et al. 2020). These observations suggest instead that CO is underabundant in disks (see, e.g. Favre et al. 2013; Du et al. 2015; Bergin et al. 2016; Kama et al. 2016b; Zhang et al. 2019). This requires some process currently not accounted for that removes CO from the gas-phase. Two such processes have been suggested: the first proposes that when CO freezes out on grain it can become locked up in larger bodies, preventing it from re-entering the gas-phase (see, e.g., Bergin et al. 2010; Bergin et al. 2016; Du et al. 2015; Kama et al. 2016b; Krijt et al. 2018; Krijt et al. 2020). Radial drift of these larger bodies can move the frozen out CO to smaller radii (see, e.g Booth et al. 2017). Several authors have also shown that grain-surface chemistry is capable of lowering the CO abundance in disks. In the gas collisions with He$^+$ can break apart CO molecules, allowing the available carbon to be locked up in hydrocarbons like CH_4 and C_2H_6 (see, e.g. Aikawa et al. 1997; Bergin et al. 2014; Schwarz et al. 2018). In the ice CO can be converted into other species like CO_2 and CH_3OH on a timescale of several Myr (see, e.g. Bergin et al. 2014; Bosman et al. 2018; Schwarz et al. 2019).

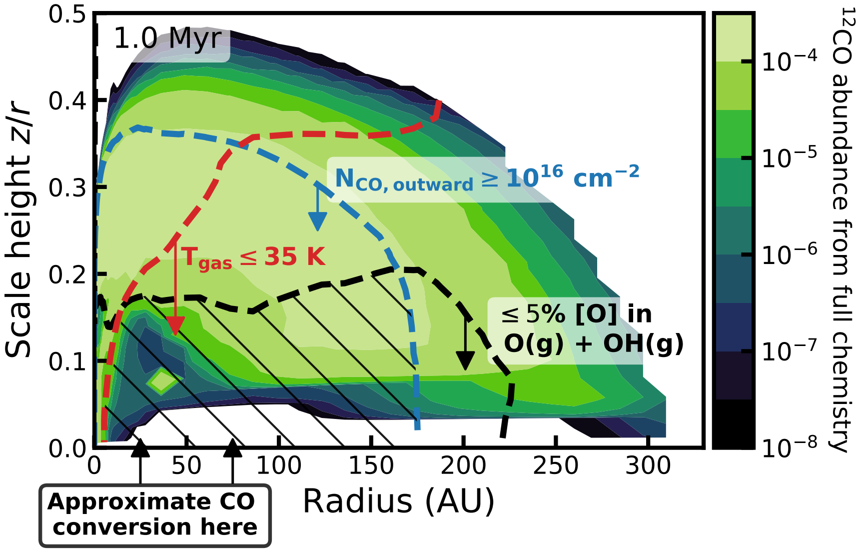

Figure 5.2: CO abundance computed using the full chemical network in Bosman et al. (2018) (see also Cridland et al. 2020) for the model with $M_* = 0.32$ M$_\odot$, $\alpha_{\rm visc} = 10^{-3}$ at 1 Myr. The chemistry was calculated using a $\zeta_{\rm cr} = 10^{-16}$ s^{-1} to show where CO can be transformed. Taken from the same model, but with the chemistry calculated within `DALI`, the blue dashed line shows where the CO outward column is 10^{16} cm^{-2}. The black contour shows where 5% of the total oxygen abundance is in OH(g) + O(g). The red contour shows where $T_{\rm gas} = 35$ K. The hatched region below the three dashed lines shows where the CO abundance is recalculated using the approximate grain surface chemistry.

In this work we have implemented the *chemical conversion of CO* using an approximate description for CO gas and grain surface chemistry based on the results of Bosman et al. (2018). The description simplifies the full chemical network in Bosman et al. (2018) by only tracing the main carbon carriers, i.e., CO, CH_3OH, CO_2 and CH_4. The chemistry is split up into the carrier species that have long ($> 10^4$ yr) chemical timescales and intermediates, radicals and ions, which have a short, < 100 yr, chemical timescales. The former are explicitly integrated while kinetic equilibrium is assumed for the latter. A more detailed description can be found in Appendix A in Krijt et al. (2020).

Using this approximate grain-surface chemistry, we recalculate the CO abundances computed by `DALI`. In doing so some thought has to be put in where in the disk our method gives an accurate approximation of the full chemical network in Bosman et al. (2018). Based on tests where the full chemistry is computed, we identify three boundaries beyond which the shielded midplane approximation is no longer valid: a low outward column of CO, the presence of oxygen in the gas-phase and a high temperature. The first is an outward column of CO of $N_{\rm CO,outward} = 10^{16}$ cm^{-2} (see also van Dishoeck & Black 1988; Heays et al. 2017). In regions with a lower outward column CO can be photodissociated by UV photons and the CO abundance is set by the balance between photodissociation and chemistry, which is included in DALI.

The second boundary is related to the fraction of oxygen in the gas-phase. The approximation assumes that all gas-phase oxygen directly transforms into OH ice where it can react with CO or H to form CO_2 ice or H_2O ice respectively. The presence of atomic oxygen in the gas-phase in the model indicates that photodissociation is still a significant driver of the chemistry. UV dissociation reactions will dissociate carbon carriers other than CO and push carbon back into the more photo-stable CO (see, e.g. van Dishoeck & Black 1988). Empirically we have found the boundary where 5% of the available oxygen exists as gas-phase O or OH encloses the region where in the full chemical network CO is transformed into other species (see Figure 5.2).

Finally we also exclude the parts of the disk where $T_{\mathrm{gas}} > 35$ K. Tests show that above this temperature the conversion of CO through grain-surface chemistry is negligible. At these temperatures CO is converted in CH_4 in the gas-phase (see, e.g. Aikawa et al. 1997; Schwarz et al. 2018. This is the dominant route above ~ 25 K and densities below $\lesssim 10^{10}$ cm^{-3}. It becomes less and less effective with increasing temperature due to the lower sticking of atomic oxygen on grains (see Figure 4 in Bosman et al. 2018). The increased time atomic oxygen spends in the gas-phase results in the reformation of CO through reactions of O and OH with hydrocarbon radicals and ions, for example: $CH_2^+ + O \rightarrow HCO^+ \rightarrow CO$.

It should be noted that efficiency of gas-phase conversion of CO depends directly on rate at which CO can be destroyed by He^+. Changes to the assumptions made to calculate this rate, for example increasing cosmic-ray ionization rate of He, could increase the efficiency of gas-phase CO conversion. To summarize, CO abundances are recalculated using the approximate grain-surface chemistry for regions in the disk where $N_{\mathrm{CO,outward}} > 10^{16}$, $\leq 5\%$ of [O] is in O(g)+OH(g) and $T_{\mathrm{gas}} \leq 35$ K. The abundances of the CO isotopologs ^{13}CO and C^{18}O are calculated by scaling their abundances by factor $X_{\mathrm{CO}}^{\mathrm{new}}/X_{\mathrm{CO}}^{\mathrm{old}}$, i.e. by how much the ^{12}CO abundance has decreased.

Figure 5.3 shows the effects of CO conversion through grain-surface chemistry on the CO abundances at 1, 3 and 10 Myr for one of our disk models. As discussed above, the CO abundances are only recalculated below the dashed black lines. At 1 Myr the CO abundance is still $CO/H_2 \sim 10^{-4}$ and CO has not been depleted significantly. By 3 Myr the CO abundance has dropped to $CO/H_2 \sim 5 \times 10^{-5}$ higher up in the disk and $CO/H_2 \sim 5 \times 10^{-6}$ close to the midplane. For ^{13}CO the effect of isotope-selective photodissociation is partly offset by the reaction $^{13}C^+ + {}^{12}CO \rightarrow {}^{13}CO + {}^{12}C^+ + 35$ K, which is energetically favored towards the production of ^{13}CO at low temperatures (see, e.g. Visser et al. 2009; Miotello et al. 2014 and references therein).

Having a lower abundance and lacking a similar back reaction, C^{18}O is much more affected by isotope-selective photodissociation. As a result, C^{18}O is confined to a layer deeper in the disk. This can be seen in the figure, with the ^{13}CO 3-2 emitting region lying higher up in the disk, fully above the black contour. The C^{18}O 3-2 emitting region lies closer towards the midplane and crosses the black contour. We can therefore expect the ^{13}CO 3-2 flux not to be affected by the chemical conversion of CO, whereas the C^{18}O 3-2 flux will be affected. After 10 Myr almost all of the available CO has been converted, with $CO/H_2 \lesssim 10^{-6}$ for the region where CO can be converted through cosmic-ray-driven chemistry. The ^{13}CO and C^{18}O emitting regions have moved inward and upward to regions of the disk that still have a high CO abundance.

In this work we raytrace the ^{13}CO and C^{18}O $J = 3 - 2$ lines, but tests show that the $J = 2 - 1$ lines show the same qualitative behavior (cf. Appendices 5.A and 5.B). As a rule of thumb if the $J = 3 - 2$ lines are optically thick, i.e., at early ages when the disk is most massive, the ^{13}CO 2-1 line is up to 5% fainter (in Jy km s^{-1}) and the C^{18}O 2-1 line is up to 15% fainter. If the $J = 3 - 2$ lines are optically thin, the

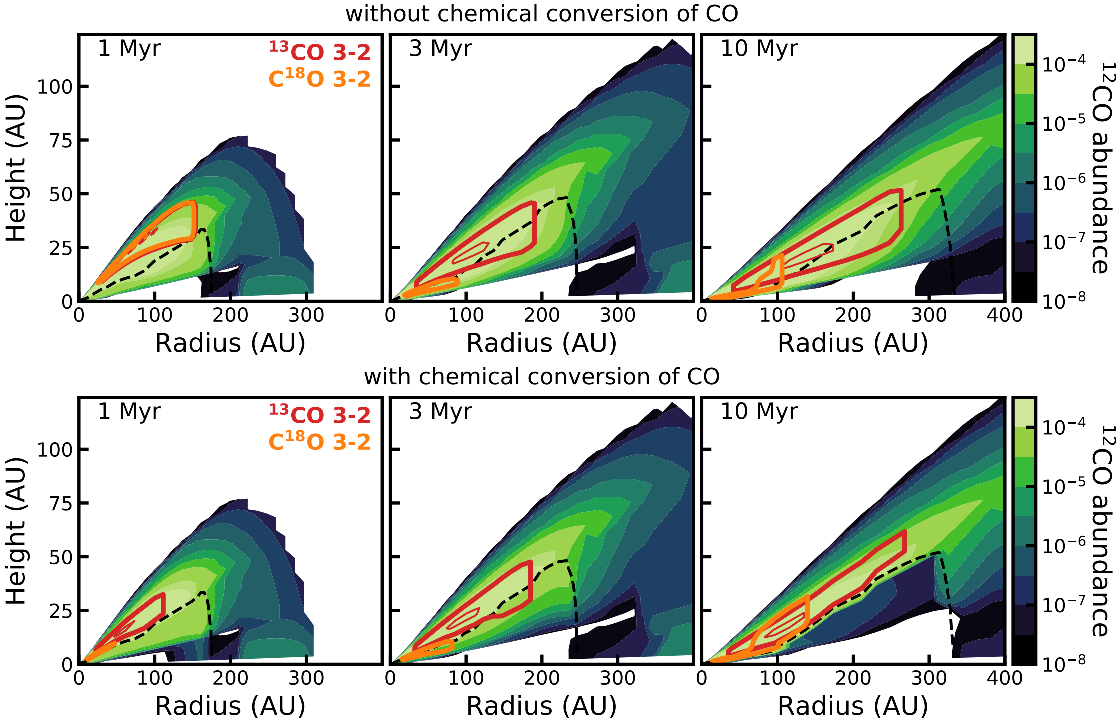

Figure 5.3: The effect of the chemical conversion of CO on the CO abundance after 1, 3 and 10 Myr. The example model shown here has $M_* = 0.32$ M$_\odot$ and $\alpha_{\rm visc} = 10^{-3}$. In the top panels CO abundances have been calculated using the DALI chemical network (see Section 5.2.3). In the bottom panels we have included the chemical conversion of CO into other species, as described in Section 5.2.3. Colors show the CO abundance with respect to H$_2$, where white indicates CO/H$_2 \leq 10^{-8}$. The black dashed line shows where $\leq$ 5% of the total amount of oxygen is in O(g)+OH(g), the gas temperature $T_{\rm gas} \leq 35$ K and outward CO column is $\geq 10^{16}$ cm^{-2}. Grain surface chemistry is calculated below this black dashed line. Red contours show the ^{13}CO $J = 3-2$ emitting region, enclosing 25% and 75% of the total ^{13}CO flux. Similarly, the orange contours show the C^{18}O $J = 3-2$ emitting region.

$J = 2 - 1$ fluxes are up to 30% lower for both ^{13}CO and C^{18}O.

5.3 Results

5.3.1 CO isotopolog line fluxes: a viscously evolving disk

As the disk evolves viscously, the disk mass decreases and the disk size increases. Figure 5.4 shows how the ^{13}CO and C^{18}O $J = 3 - 2$ line fluxes change over time in these circumstances. The ^{13}CO 3-2 flux, shown in the top panel, increases over time. This is found to be the case for all models except those with $M_* = 0.1$ M$_\odot$ and $\alpha_{\rm visc} \geq 10^{-3}$ (see also Figure 5.10). A closer inspection of the models reveals that the ^{13}CO emission is optically thick. As the disk expands this optically thick emitting region grows in size and the ^{13}CO flux increases. The ^{13}CO flux is therefore more of a disk size tracer than a disk mass tracer.

The C^{18}O flux, shown in the bottom panel of Figure 5.4, starts optically thick and also increases with time. For the model with $\alpha_{\rm visc} = 10^{-3}$ this changes at ~ 2 Myr, when the C^{18}O 3-2 flux starts to decrease rapidly. At this point the increasing disk size and decreasing disk mass have reduced the C^{18}O column densities to the point where the C^{18}O emission has become optically thin and therefore it traces the total CO mass.

As shown here, the behavior of the CO isotopolog lines in a viscously evolving disk depends strongly on whether the emission is optically thick or thin and therefore the mass of the disk. Based on an extensive grid of disk models, Miotello et al. (2016) determined that for disk masses below $M_{\rm disk} \lesssim 2 \times 10^{-4}$ M$_\odot$ the ^{13}CO 3-2 flux is optically thin and traces the disk mass (see also Miotello et al. 2017). If we compare this disk mass threshold to the disk masses required to explain the observed stellar mass accretion rates, the ^{13}CO 3-2 emission is expected to be optically thick for all viscously evolving disks, except for disks with $\alpha_{\rm visc} \geq 10^{-3}$ around stars with $M_* = 0.1$ M$_\odot$ (cf. Figure 5.1, see also Figure 5.10). For C^{18}O the emission is optically thin $M_{\rm disk} \lesssim 2.5 \times 10^{-3}$ M$_\odot$. Based on the disk masses required to explain observed stellar accretion rates, we expect C^{18}O emission to be optically thin, and thus trace the disk mass, for disks around stars with $M_* \lesssim 0.3$ M$_\odot$.

5.3.2 CO isotopolog line fluxes: effects of grain surface chemistry

Before we compare our models to the observations, we first look at the effects of conversion of CO through grain surface chemistry on CO isotopolog line fluxes. As lowering the CO abundance decreases the ^{13}CO and C^{18}O column densities, we expect the ^{13}CO and C^{18}O emission to become optically thin at an earlier disk age.

Figure 5.5 shows C^{18}O and ^{13}CO $J = 3 - 2$ integrated line fluxes for models with $M_* = 0.32$ M$_\odot$ and $\alpha_{\rm visc} = [10^{-3}, 10^{-4}]$. The line fluxes without grain surface chemistry, presented earlier in Figure 5.4, are included as dashed lines. Up to 1 Myr there is no discernible difference between the models with and without grain-surface chemistry, as it takes time for the chemistry to lower the gas-phase CO abundance. We note here that the timescale for the grain-surface chemistry depends directly on the assumed cosmic-ray ionization rate $\zeta_{\rm cr}$, which we have assumed to be $\zeta_{\rm cr} = 1 \times$

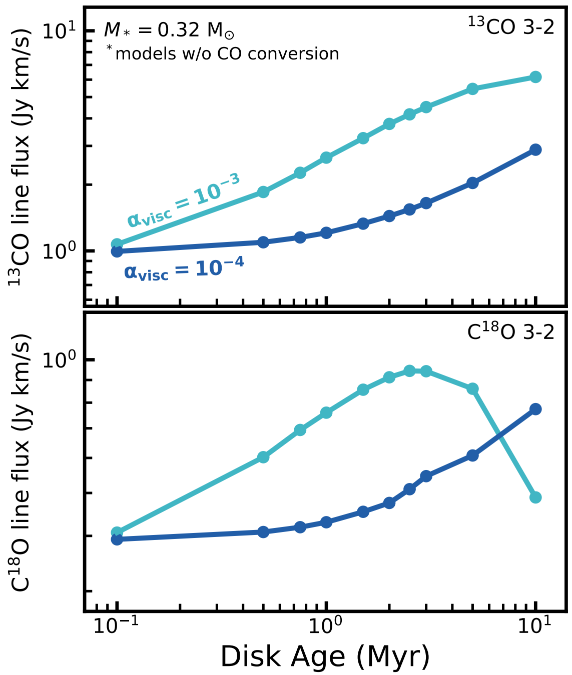

Figure 5.4: ^{13}CO and C^{18}O $J = 3 - 2$ line fluxes of a viscously evolving disk, shown in the top and bottom panel, respectively. Presented here are models with $M_* = 0.32$ M$_\odot$, $\alpha_{\rm visc} = 10^{-3} - 10^{-4}$ that have an initial disk mass $M_{\rm disk}(t = 0) = 2 \times 10^{-3} - 2 \times 10^{-2}$ M$_\odot$. Note that for these models CO conversion through grain-surface chemistry is not included.

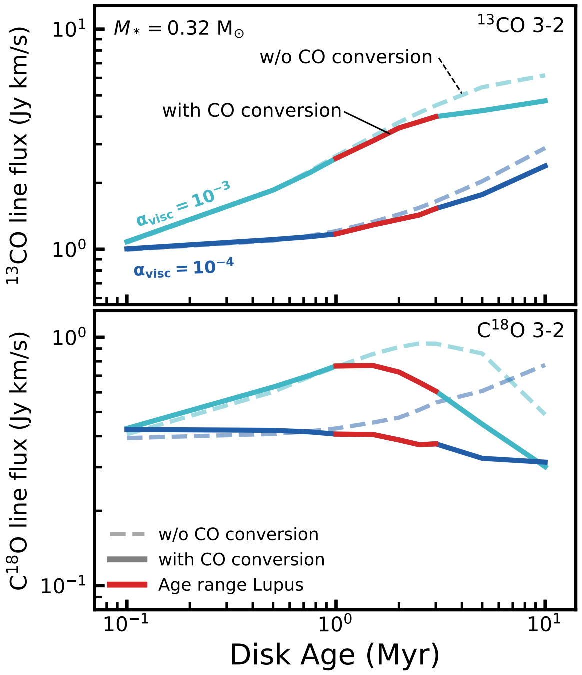

Figure 5.5: ^{13}CO and C^{18}O $J = 3 - 2$ line fluxes of a viscously evolving disk, shown in the top and bottom panel, respectively. Presented here are models with $M_* = 0.32$ M$_\odot$, $\alpha_{\rm visc} = 10^{-3} - 10^{-4}$ that have an initial disk mass $M_{\rm disk}(t = 0) = 2 \times 10^{-3} - 2 \times 10^{-2}$ M$_\odot$. A full overview of the model fluxes can be found in Figure 5.10. Solid lines show fluxes for models that include CO conversion through grain-surface chemistry. For comparison, dashed lines show fluxes for models without CO conversion as in Figure 5.4. The red line highlights the age range of disks in the Lupus star-forming region.

10^{-17} s^{-1}. For a higher $\zeta_{\rm cr}$ the conversion of CO into other species will occur on a shorter timescale (see also Section 5.3.4).

For ^{13}CO there is almost no difference when grain-surface chemistry is included even after 1 Myr. As can be seen in Figure 5.3 the ^{13}CO 3-2 emitting region lies almost completely above the region of the disk where CO can be transformed on the grains. Grain-surface chemistry has a larger effect on the C^{18}O fluxes, because the C^{18}O 3-2 emitting region lies closer to the midplane, where the conversion of CO is most efficient (see, e.g. Figure 5.3). For both $\alpha_{\rm visc} = 10^{-3}$ and 10^{-4} the C^{18}O 3-2 flux starts to decrease at a disk age of $\sim$ 1.5 Myr. This indicates that the C^{18}O emission is optically thin for a much larger disk masses (up to $M_{\rm disk} \sim 2 \times 10^{-2}$ M$_\odot$, cf. Figure 5.1). At 10 Myr grain surface chemistry has lowered the C^{18}O 3-2 fluxes by a factor of $\sim 2-3$ compared to the model without CO conversion.

5.3.3 Comparing to the Lupus disk population

Recently Ansdell et al. (2016) have carried out an ALMA survey of the protoplanetary disk population in the Lupus star-forming region, in both continuum and ^{12}CO, ^{13}CO and C^{18}O line emission (see also Ansdell et al. 2018). We examine whether the low ^{13}CO and C^{18}O 3-2 fluxes are compatible with viscous evolution.

Figure 5.6 shows the C^{18}O and ^{13}CO $J = 3-2$ integrated line fluxes of our models and observations of protoplanetary disks in Lupus (Ansdell et al. 2016; Yen et al. 2018). To have a useful comparison, we have aligned the models and observations based on total (estimated) disk mass. For the observations we use $100 \times M_{\rm dust}$ as a proxy for the disk mass. This is equivalent to assuming that disks have a gas-to-dust mass ratio $\Delta_{\rm gd} = 100$, the canonical value for the ISM. Note that due to radial drift, and subsequent accretion onto the star, of larger grains, disks will likely have a $\Delta_{\rm gd} > 100$, moving the observations to the right in Figure 5.6. This is discussed in more detail in Section 5.4.2. In our analysis we exclude transition disks with a resolved inner cavity in the dust continuum, as our models do no represent their disk structure (see van der Marel et al. 2018).

At the high mass end ($M_{\rm disk} \gtrsim 5 \times 10^{-3}$ M$_\odot$) ^{13}CO 3-2 is detected for all disks and C^{18}O 3-2 is detected for most disks in Lupus. The observed range of ^{13}CO fluxes is reasonably well reproduced by our models, although for individual objects the flux for the model with the corresponding mass might be a factor $2-4\times$ higher. There are two disks, IM Lup (Sz 82) and HK Lup (Sz 98) that are either significantly brighter or fainter than our models. These two disks are among the largest disks in Lupus. Interestingly, while these two disks are of similar size and dust mass, they differ in ^{13}CO 3-2 flux by more than an order of magnitude, suggesting that the processes that affect the abundance of CO can be very different in two very similarly looking disks. Note that our models are aimed at reproducing the average protoplanetary disk and we do not expect them to reproduce outliers. In a similar study Trapman et al. (2020) showed that a larger initial disk size of 30-50 AU is required to reproduce the gas disk size of these large disks.

The C^{18}O 3-2 fluxes detected for the high mass disks are reproduced by the models within a factor $\sim$ 2 for most disks. Four of the massive disks in Lupus, slightly less than half of the disks in this mass range, are not detected in C^{18}O 3-2. Our models overproduce these C^{18}O upper limits by a factor $\sim 2-4$, suggesting they either have a $\Delta_{\rm gd} \ll 100$ or that they have lower C^{18}O abundances than our models. The C^{18}O

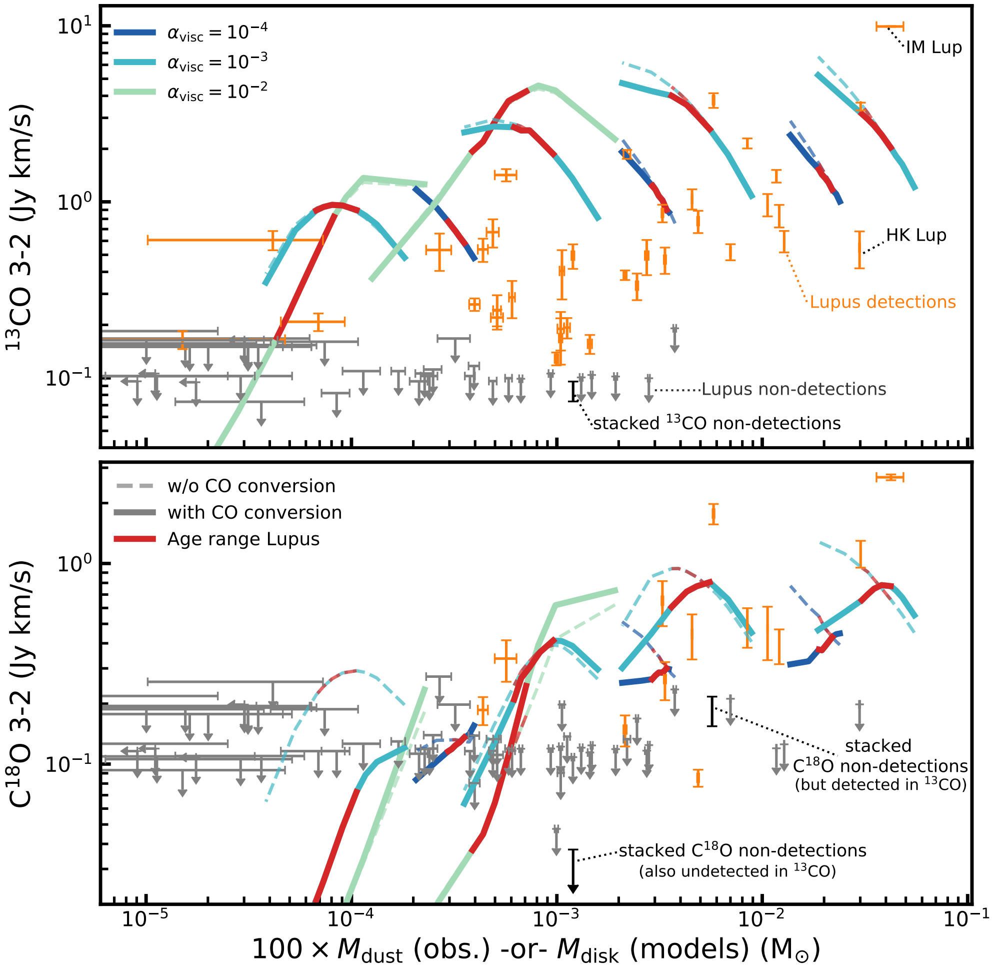

Figure 5.6: ^{13}CO (top) and C^{18}O (bottom) $J = 3 - 2$ line fluxes versus disk mass. Solid lines show models that include CO conversion through grain surface chemistry. For comparison, dashed lines show the models without grain surface chemistry. For the observations, shown in orange, we use $M_{\rm gas} \simeq 100 \times M_{\rm dust}$ as a proxy for the disk mass (see, e.g. Ansdell et al. 2016; Ansdell et al. 2018; Yen et al. 2018). Colours show models with different viscous alpha. Models with age between 1 and 3 Myr, the approximate age of Lupus, are highlighted in red. Note that in our models $M_{\rm disk}$ decreases with time, meaning that time runs right to left in this figure for our models. Observations for which we only have an upper limit on the ^{13}CO or C^{18}O line flux are shown in gray. Stacked non-detections are shown in black (cf. Section 5.3.3).

fluxes in our models can be reduced by increasing the cosmic-ray ionization rate (see Section 5.3.4 and Figure 5.12).

For lower disk masses (5×10^{-4} M$_\odot \lesssim M_{\rm disk} \lesssim 5 \times 10^{-3}$ M$_\odot$) the majority of disks in Lupus are still detected in ^{13}CO but only a few are also detected in C^{18}O. Here the ^{13}CO fluxes of our models and the observations start to diverge. While the brightest observed ^{13}CO fluxes are still reproduced by the models, there is up to an order of magnitude difference between the model ^{13}CO fluxes and the bulk of the ^{13}CO detections and the ^{13}CO upper limits.

For C^{18}O, comparing the models to the observations becomes more difficult due to the low number of C^{18}O 3-2 detections in Lupus. The few C^{18}O detections in this mass range are reproduced by the models. However, these are the same disks whose bright ^{13}CO emission is also reproduced by the models. The C^{18}O fluxes of the models do get low enough to match the observed C^{18}O upper limits ($\sim$ 0.1 Jy km s^{-1}), but only when the disk models are $\sim$ 10 Myr old. This is much older than most disks in Lupus, which are estimated to be 1-3 Myr old.

Ansdell et al. (2016) stacked the disks that were detected in the continuum but not in ^{13}CO 3-2 and C^{18}O 3-2. First, stacking the 25 sources that were detected in the continuum and ^{13}CO resulted in a mean continuum flux of 70 mJy, corresponding to a dust mass of $\sim 5 \times 10^{-5}$ M$_\odot$, with a detected mean C^{18}O 3-2 flux of 206 ± 31 mJy km s^{-1}. Stacking the 26 sources detected in the continuum but not detected in both ^{13}CO 3-2 and C^{18}O 3-2 provided a much deeper mean C^{18}O 3-2 upper limit of 42 mJy km s^{-1}. Note that we have scaled the fluxes to a distance of 160 pc, the average distance to the Lupus clouds based on Gaia DR2 measurements (Brown et al. 2018; Bailer-Jones et al. 2018), instead of the 200 pc used by Ansdell et al. (2016). This stacked upper limit lies a factor 5-10 lower than our model fluxes, similar to what was found for ^{13}CO, suggesting that both ^{13}CO 3-2 and C^{18}O 3-2 fluxes are overproduced by our models, even if chemical conversion of CO is included.

For disks with $M_{\rm disk} = 100 \times M_{\rm dust} \lesssim 5 \times 10^{-4}$ M$_\odot$ only a handful of disks are detected in ^{13}CO and none are detected in C^{18}O. While the ^{13}CO fluxes of the models have decreased for these lower gas masses, the model fluxes are still at least a factor of 5 higher than the observed ^{13}CO upper limits. In comparison the C^{18}O fluxes of the model have decreased with $M_{\rm disk}$ and are consistent with the observed C^{18}O upper limits.

To summarize, our viscously evolving disk models that include CO conversion are able to explain most observed ^{13}CO and C^{18}O fluxes for high mass disks ($M_{\rm disk} \gtrsim 5 \times 10^{-5}$ M$_\odot$) in Lupus. For lower mass disks the model ^{13}CO and C^{18}O fluxes are up to an order of magnitude higher than what has been observed.

5.3.4 Cosmic-ray ionization rate required to match observed CO isotopolog fluxes

The previous Section showed that for disk masses below $\sim 5 \times 10^{-3}$ M$_\odot$ the model ^{13}CO and C^{18}O fluxes are a factor $5-10\times$ higher than what is observed in Lupus. The cosmic-ray ionization rate $\zeta_{\rm cr}$ is one of the main factors that determines the rate at which CO is converted into CO$_2$, CH$_4$ and CH$_3$OH. Here we examine if increasing $\zeta_{\rm cr}$ would allow us to reproduce the observations and what $\zeta_{\rm cr}$ would be needed to do so in a 1-3 Myr time period. We focus on the mass range between $M_{\rm disk} = 5 \times 10^{-4}$ M$_\odot$ and $M_{\rm disk} = 10^{-2}$ M$_\odot$ where the difference in fluxes between the models and the

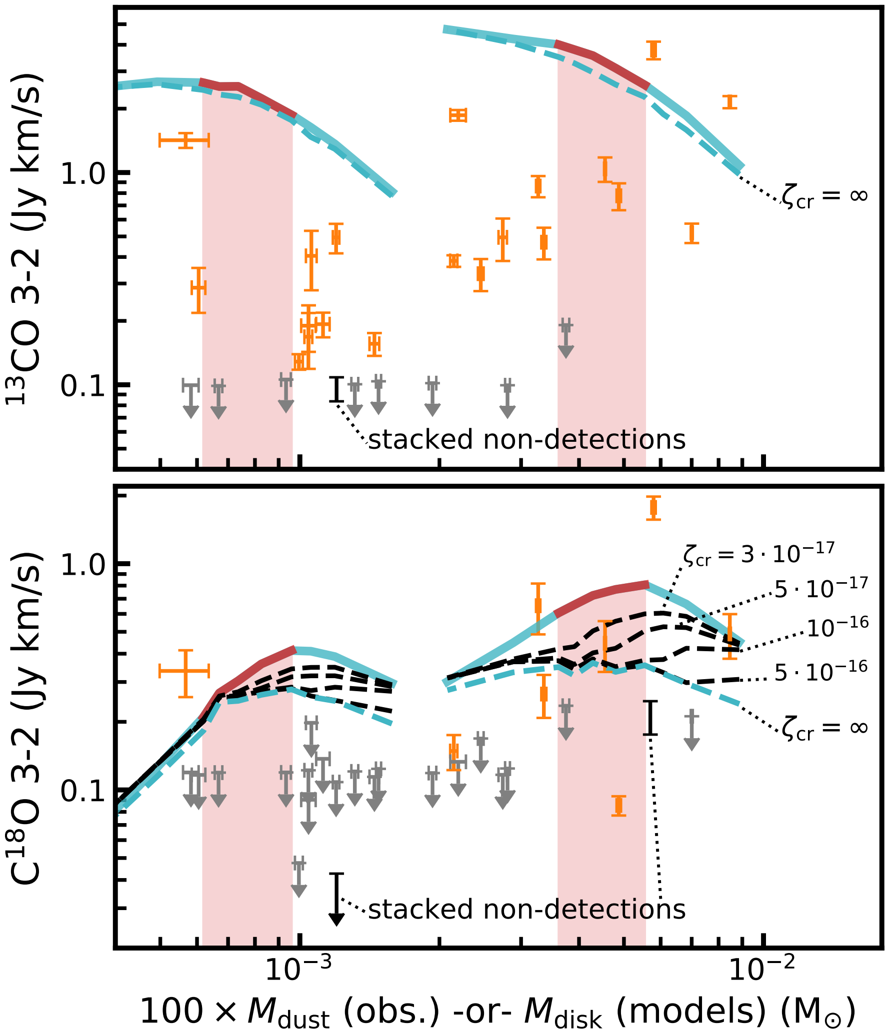

Figure 5.7: The effect of the cosmic ray ionization rate on ^{13}CO and C^{18}O $J = 3 - 2$ line fluxes, shown in the top and bottom panel respectively. Models shown here have $\alpha_{\rm visc} = 10^{-3}$ and $M_* = [0.2, 0.32]$ M$_\odot$. Solid light blue lines show the model line fluxes where CO conversion through grain surface chemistry is calculated with a cosmic ray ionization rate $\zeta_{\rm cr} = 1 \times 10^{-17}$ s^{-1}. For the black dashed lines $\zeta_{\rm cr}$ is increased up to 5×10^{-16} s^{-1}. The dashed blue line shows the upper limit of the effect of grain surface chemistry, where we have removed all CO in the region of the disk where CO conversion by grain surface chemistry is effective. Observations in Lupus are shown in orange if detected and in gray if an upper limit (Ansdell et al. 2016; Yen et al. 2018). The stacked non-detections are shown in black (see also Section 5.3.3). The red shaded lane highlights the age range of the Lupus star-forming region.

observations is the largest. Similarly, we focus on models with $\alpha_{\rm visc} = 10^{-3}$ and $M_* = [0.2, 0.32]$ $M_\odot$, which span a similar disk mass range.

Figure 5.7 shows the ^{13}CO and C^{18}O 3-2 fluxes after CO abundances were recalculated using a higher $\zeta_{\rm cr}$ than is used in the models presented previously ($\zeta_{\rm cr} = 1 \times 10^{-17}$ s^{-1}, see Table 5.2.) The ^{13}CO 3-2 emission is only weakly dependent on the cosmic-ray ionization rate, with less than $\sim 10\%$ differences in flux. Again, this is due to the ^{13}CO emitting region ($z/r \sim 0.2 - 0.35$) being higher than the region of CO removal ($z/r \lesssim 0.15$) In Section 5.4.1 we discuss alternative ways to reconcile the ^{13}CO 3-2 observations with our models.

The bottom panel of Figure 5.7 shows that, in contrast to ^{13}CO, increasing $\zeta_{\rm cr}$ has a larger effect on the C^{18}O fluxes, but not enough. Increasing $\zeta_{\rm cr}$ from 1×10^{-17} s^{-1} to $5 \times 10^{-17} - 10^{-16}$s^{-1} is sufficient to explain almost all of the C^{18}O detections for disks with $100 \times M_{\rm dust} \gtrsim 2 \times 10^{-3}$ $M_\odot$. However, the figure also shows that by increasing $\zeta_{\rm cr}$ the C^{18}O 3-2 fluxes can reduced to at most ~ 0.2 Jy km s^{-1}, which is still a factor ~ 2 higher than the observed C^{18}O upper limits in Lupus. Moreover, the fluxes obtained from our models remain a factor ~ 5 higher than the stacked C^{18}O 3-2 upper limits. This indicates that increasing the amount of cosmic-ray ionization by itself cannot explain the faintest C^{18}O 3-2 fluxes.

5.4 Discussion

5.4.1 Reproducing ^{13}CO 3-2 line fluxes observed in Lupus

In Section 5.3.3 it was found that our models overproduce the ^{13}CO 3-2 and C^{18}O 3-2 observation in Lupus by a factor of 5-10 for disks with $M_{\rm disk} \lesssim 5 \times 10^{-3}$ $M_\odot$. By increasing the cosmic-ray ionization rate from $\zeta_{\rm cr} = 1 \times 10^{-17}$ s^{-1} to 10^{-16} s^{-1} it is possible to decrease the C^{18}O 3-2 fluxes of our models to within a factor two of the observed upper limits. However, the ^{13}CO 3-2 emission originates predominantly from a layer higher up in the disk where CO is not being efficiently converted into other species. As such, the ^{13}CO 3-2 fluxes of our models remain a factor $10 - 30\times$ higher than the observations, even after removing all CO from region of the disk where CO grain-surface chemistry is effective. Here, we examine the emitting regions of ^{13}CO 3-2 and C^{18}O 3-2 and we discuss processes that could reduce the ^{13}CO and C^{18}O fluxes to the point where they are in agreement with both detections and upper limits seen in observations.

Figure 5.8 shows an example of the ^{13}CO and C^{18}O emitting regions in a model with maximum CO conversion. The ^{13}CO emitting region is located high up in the disk ($z/r \sim 0.25 - 0.4$), fully above the region where CO can be removed ($z/r \lesssim 0.15$). The presence of oxygen in the gas-phase in this layer indicates that it cannot be locked up efficiently in H_2O, meaning it is available to react with the carbon released from the destruction of CO to reform CO (see also Schwarz et al. 2018). The C^{18}O emitting region, shown in the bottom panel of Figure 5.8 lies much deeper in the disk, at a height of $z/r \sim 0.18$. With efficient CO conversion the C^{18}O emitting region is very compact and extends only slightly above the oxygen-threshold. Unlike for ^{13}CO it is therefore plausible that a slight change in for example the height of the disk will push the C^{18}O abundant region below the oxygen-threshold, thus drastically reducing the observed C^{18}O 3-2 fluxes. In the rest of this section we therefore focus on lowering the ^{13}CO 3-2 fluxes, which are in stronger violation with the observations.

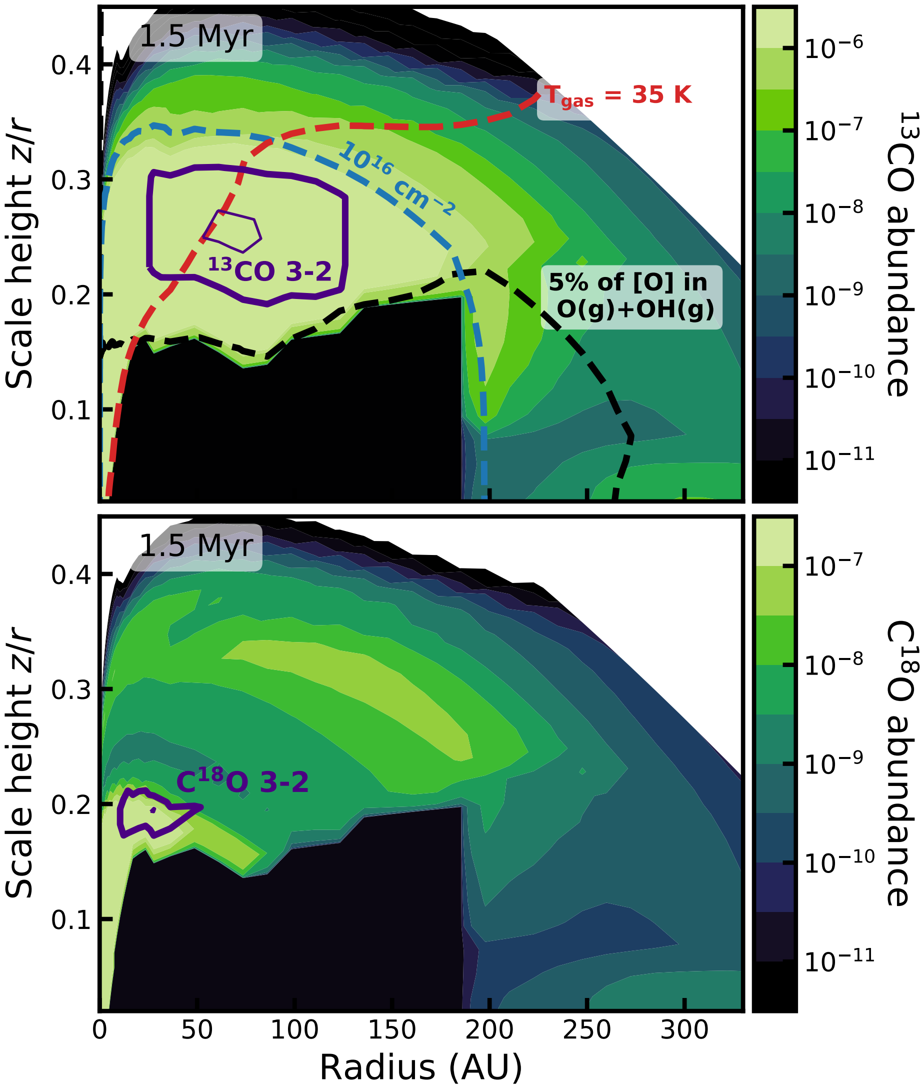

Figure 5.8: ^{13}CO (top) and C^{18}O (bottom) abundance structure (colors) and $J = 3-2$ emitting regions (purple contours) for an example disk model ($M_* = 0.32$ M$_\odot$, $\alpha_{\rm visc} = 10^{-3}$ and a disk age of 1.5 Myr). The contours shown are the same as in Figure 5.2.

Knowing the location of the ^{13}CO emission, we can discuss processes by which the emission can be reduced.

A colder disk: Given that the ^{13}CO 3-2 emission is optically thick, a lower disk temperature could potentially explain the low ^{13}CO 3-2 emission in Lupus. Lowering $T_{\rm gas}$ would decrease the brightness of the optically thick line. The temperature of a disk is predominantly set by its vertical structure. The vertical structure that is assumed in our disk models is thought to be a good representation of the average disk vertical structure, but here are only a few disks, biased towards high disk masses, for which the disk height has been estimated using the scattering surface observed in scattered light (see, e.g. Avenhaus et al. 2018; Garufi et al. 2020). It is therefore possible that lower mass disks are much flatter, and therefore colder, than previously thought. Reducing the scale height of the disk would concentrate the mass in the shielded midplane, where the cosmic-ray-driven conversion of CO is efficient.

A colder disk cannot explain all of the disks observed to be underabundant in CO. The TW Hya disk is thought to be underabundant in CO by a factor 10-100 (see, e.g. Favre et al. 2013; Du et al. 2015; Bergin et al. 2016; Kama et al. 2016b; Trapman et al. 2017). This disk is also known to be much more flared ($\Psi \sim 0.3$), and therefore warmer, than the disk models presented here (see, e.g., Kama et al. 2016b; van Boekel et al. 2017; Schwarz et al. 2016). Although anecdotal, the example of TW Hya shows that a colder disk cannot be the sole explanation for the low observed ^{13}CO 3-2 fluxes (see also Fedele et al. 2016).

Smaller disks: Another way to explain the low ^{13}CO 3-2 fluxes would be that disks are smaller than our models. Trapman et al. (2020) showed that our models are consistent with observed gas disk sizes in Lupus, measured from the extent of the ^{12}CO $J = 2 - 1$ emission. However, these observations are biased towards the most massive disks around the most massive stars in the Lupus disk population. Comparing their results with the observations presented in Figure 5.6 reveals that there are only three disks below $M_{\rm disk} = 3 \times 10^{-3}$ M$_\odot$ for which the gas disk size has been measured: Sz 133 (238 AU), Sz 65 (172 AU) and Sz 73 (103 AU). Of these, only Sz 73 has a ^{13}CO flux that lies a factor ~ 2 below the predictions of our models. For the remaining disks of similar or lower mass the gas disk size is unknown. Without knowing their gas disk size, it could be possible that the low ^{13}CO fluxes can be explained by a compact gas disk.

The optically thick emitting region of our disk models with $M_{\rm disk} \lesssim 5 \times 10^{-3}$ M$_\odot$ has a radius of $\sim 30 - 150$ AU, depending on the mass and $R_{\rm c}$ of the disk model. The ^{13}CO 3-2 flux scales with emitting area ($F \propto R^2$). To reduce the ^{13}CO 3-2 flux of these models by a factor $10 - 30$ and bring them in line with the observations, the disk size has to be reduced by a factor $3 - 5$, to $\sim 10 - 50$ AU. Note that this is the disk size as measured from the ^{13}CO 3-2 emission. Trapman et al. (2019) found that the gas disk size measured from ^{12}CO is 30-35% larger than the gas disk size measured from ^{13}CO, assuming that both ^{12}CO and ^{13}CO are optically thick. This would suggest that disks with dust masses $\lesssim 3 \times 10^{-4}$ M$_\odot$ need to have gas disk sizes on the order of $\sim 40 - 70$ AU as measured from ^{12}CO if small disks are the explanation for the low ^{13}CO fluxes. It should be noted however that disks with similar ^{13}CO flux can have very different gas disk sizes (e.g. Sz 129 (140 AU) and HK Lup (358 AU)), suggesting that ^{13}CO might not always be optically thick and that compact disks might not be the sole explanation for the faint ^{13}CO emission seen in observations. Deeper high resolution ^{12}CO and ^{13}CO observations of low mass disks are required to test this theory.

Vertical mixing: It is very likely that turbulence in protoplanetary disks mixes material both vertically and radially. Through vertical mixing the CO-rich material higher up in the disk would be moved down toward the midplane, where the CO can then be converted into other species via grain-surface chemistry. If the mixing timescale is much shorter than the lifetime of the disk the CO will be well mixed and the CO abundance higher up in the disk will match that of the CO-poor material close to the midplane (see, e.g. Willacy et al. 2006; Semenov & Wiebe 2011; Krijt et al. 2018; Krijt et al. 2020).

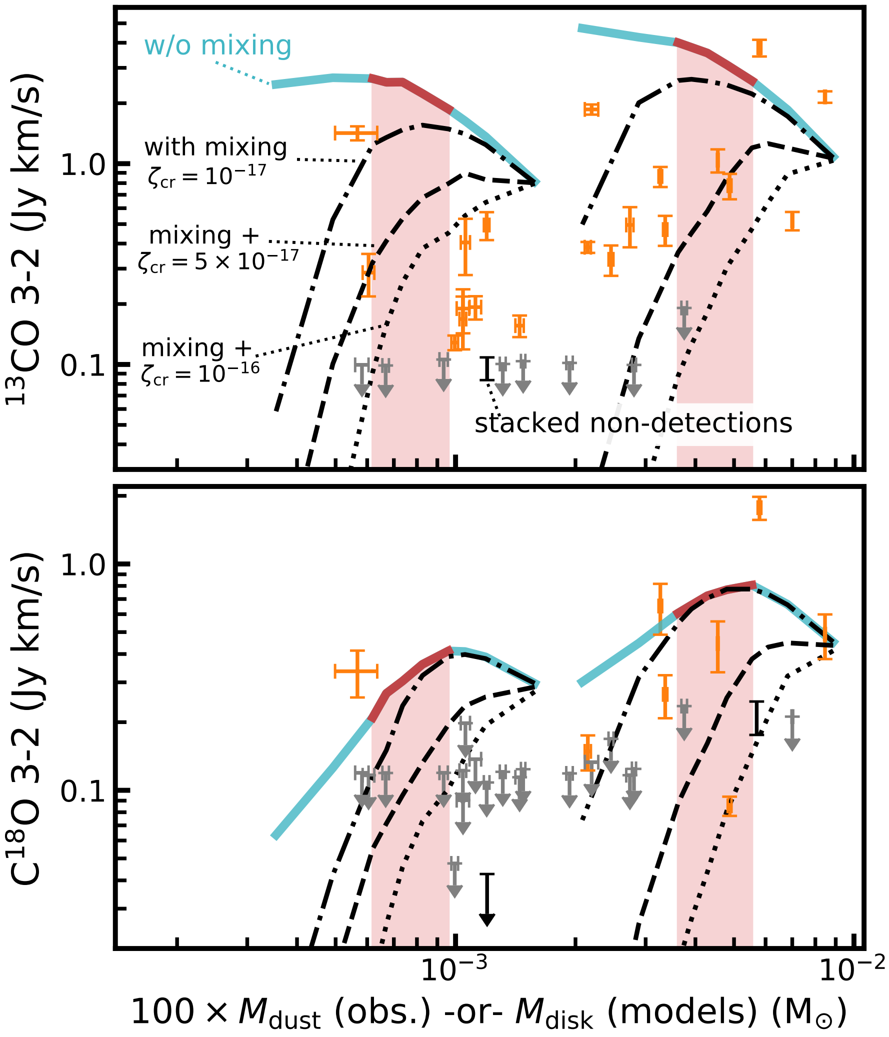

Figure 5.9: ^{13}CO 3-2 model fluxes after applying vertical mixing (black dash-dotted lines) compared the observation in Lupus (orange markers). Upper limits are shown in gray. The stacked non-detections are shown in black (see also Section 5.3.3). Shown here are disk models with $\alpha_{visc} = 10^{-3}$ and $M_* = [0.2, 0.32]$ M$_\odot$. For reference, the model fluxes without vertical mixing are shown in light blue. The black dashed and dotted lines show models where mixing is combined with higher cosmic-ray ionization rates (see also Section 5.3.4). The red shaded lane highlights the age range of the Lupus star-forming region.

Figure 5.9 shows the effect of vertical mixing on the ^{13}CO and C^{18}O 3-2 fluxes. Here we have approximated the effect of mixing by setting the CO abundance higher up in the disk equal to the mass-weighted average CO abundance in the region where we compute the grain-surface chemistry. To obtain such efficient mixing requires a mixing timescale that is much shorter than the chemical timescale of the disk, which is likely to be the case. Based on turbulent diffusion, Krijt et al. (2020) calculate a vertical mixing timescale of $t_z \approx 2.5 \times 10^5$ yr for one scale height at 30 AU assuming a turbulent strength corresponding to $\alpha = 10^{-4}$. We have also assumed that mixing goes up to the ^{13}CO emitting layer at $z/r \sim 0.25 - 0.4$.

Up to 3 Myr vertical mixing does not significantly affect the ^{13}CO and C^{18}O fluxes for the standard case of $\zeta_{\rm cr} = 1 \times 10^{-17}$ s^{-1}. While the material in the upper layer of the disk is now well mixed with the material below, the grain-surface chemistry has not had enough time to decrease the mass-averaged CO abundance to the point where it has a noticeable effect on the isotopolog line fluxes. After 3 Myr both the ^{13}CO flux has started to decrease rapidly and by 10 Myr the fluxes from the our models are at or below the level of the observed upper limits in Lupus.

The effect of mixing on the ^{13}CO and C^{18}O 3-2 fluxes is limited to how quickly the chemistry is able to decrease the mass-averaged CO abundance. It is therefore interesting to examine whether a combination of vertical mixing and a higher cosmic-ray ionization rate $\zeta_{\rm cr}$ can explain the ^{13}CO 3-2 observations in Lupus within 1-3 Myr age of the region. We have included vertical mixing in our models with $\zeta_{\rm cr} = 5{\times}10^{-17}{-}10^{-16}$ s^{-1} and present the resulting fluxes in Figure 5.9. With CO conversion now occurring at an increased rate, vertical mixing has a much larger impact at earlier disk ages. Within 3 Myr the model fluxes have decreased to the same level as the faintest ^{13}CO and C^{18}O detections and upper limits in Lupus. By combining vertical mixing with a high cosmic-ray ionization rate of $\zeta_{\rm cr} = 5 \times 10^{-17} - 10^{-16}$ s^{-1} we can explain all ^{13}CO 3-2 and C^{18}O 3-2 observations in Lupus.

This is in agreement with recent results of Krijt et al. (2020), who investigated processes that have been invoked to explain low CO abundances inferred for disks, such as chemical conversion of CO, turbulent diffusion of gas and small grains and locking up CO in large bodies. They show that a combination of vertical mixing and the chemical conversion of CO can decrease the CO abundance to $10^{-6} - 10^{-5}$ up to $z/r \sim 0.2$, which is the upper edge of their model. This is similar to the mass-weighted average CO abundance of the viscous disk models that reproduce the observed ^{13}CO and C^{18}O 3-2 upper limits (see Figure 5.9). We should note however that to lower the ^{13}CO flux mixing must be efficient up to at least $z/r \sim 0.3$ (see Figure 5.8). Krijt et al. (2020) also show that including the locking up of CO ice into larger bodies in addition to the chemical conversion of CO can further decrease the CO abundance to below 10^{-6} at $z/r \sim 0.2$ for $\zeta_{\rm cr} = 1 \times 10^{-17}$ s^{-1}. The combination of these processes could therefore potentially explain the low observed fluxes without having to invoke a high cosmic-ray ionization.

5.4.2 Alternative explanations

Assumed gas-to-dust mass ratio: In Section 5.3.3 we compared our models to observations of disks in Lupus. In this comparison we used $M_{\rm disk} \approx 100 \times M_{\rm dust}$, which is equivalent to assuming that the disk has inherited the ISM gas-to-dust mass ratio of $\Delta_{\rm gd} = 100$. However, most of the dust mass in protoplanetary is made up of large grains, which are expected to radially drift inward where they are accreted onto the star. This process would lead to $\Delta_{\rm gd} \gg 100$, with simulations of dust evolution in protoplanetary disks showing values as high as $\Delta_{\rm gd} = 10^3 - 10^4$ (see, e.g. Birnstiel et al. 2012). Increasing the assumed gas-to-dust mass ratio would shift the observations to the right in Figure 5.6, as it would increase the gas mass we associate with each of the sources. While this could change which models the observations are compared to, it would not significantly affect our results. A small increase ($\Delta_{\rm gd} = 200 - 300$) might help the comparison between the observations and our models at the high mass end. The main effect of increasing $\Delta_{\rm gd}$ would be increasing the gas mass threshold, currently $M_{\rm disk} \lesssim 5 \times 10^{-3}$ M$_{\odot}$, below which we require a higher cosmic-ray ionization rate to match our models to the observations (see also Figure 5.12).

We note here that lowering the gas-to-dust mass ratio of the observed sources to $\Delta_{\rm gd} = 1 - 10$ would also allow us to reproduce the observed ^{13}CO and C^{18}O fluxes with our models. This is in essence the same result as was obtained by Ansdell et al. (2016) and Miotello et al. (2017), who showed that gas masses derived from the ^{13}CO and C^{18}O fluxes suggests that disks have low gas-to-dust mass ratios. However, these lower gas masses would no longer be consistent with observed stellar mass accretion rates under the assumption of viscous evolution (see Manara et al. 2016b).

The other side of this comparison are the initial disk masses used for our models. As outlined in Section 5.2.2 the initial disk mass $M_{\rm disk}(t = 0)$ is set by the stellar accretion rate $\dot{M}_{\rm acc}$, for which we have taken representative $\dot{M}_{\rm acc}$ for four stellar masses $M_* = [0.1, 0.2, 0.32, 1.0]$ M$_{\odot}$ from observations. As the observations show a spread in $\dot{M}_{\rm acc}$ there should be a similar spread in $M_{\rm disk}(t = 0)$. Changing the initial disk mass would, to first order, move the model curves to the left or right in Figure 5.6. While the gas masses of both the models and observations can be varied to some degree, changing the gas masses alone cannot explain the order of magnitude difference between the ^{13}CO fluxes of models and the observations.

The assumption of viscous evolution: Throughout this work we have assumed that protoplanetary disks evolve viscously and calculated the time evolution of ^{13}CO and C^{18}O 3-2 line fluxes based on this premise. However, it is also possible disk evolution is instead driven by magnetic disk winds. While a quantitative analysis of this scenario is beyond the scope of this work, we can discuss the expected differences. In our models we saw that the ^{13}CO fluxes, and to some degree the C^{18}O fluxes, increase with time while the disk mass instead decreases with time. This is attributed to a combination of the ^{13}CO emission being mostly optically thick and the disk viscously spreading as it evolves. If disk evolution is instead driven by disk winds the disk is not expected to spread out and the ^{13}CO and C^{18}O line fluxes will not increase over time. Instead, the ^{13}CO and C^{18}O fluxes are expected to remain constant with time while the emission is optically thick. To drive the observed stellar mass accretion the disk mass has to decrease over time. At some point the ^{13}CO and C^{18}O emission will become optically thin and the line fluxes will start to decrease over time, similarly to what is seen for C^{18}O at 2 Myr in Figure 5.4. It might take more time for the emission to become optically thin, because in contrast to a viscously spreading disk, the disk mass is not distributed out over an increasingly larger area. Indeed, if disks start out small as suggested by observations (e.g Tobin et al. 2020; Maury et al. 2019), it is possible that the ^{13}CO emission remains optically thick as most of the mass is concentrated in a small area.

5.5 Conclusions

In this work we have used the thermochemical code `DALI` to run a series of viscously evolving disk models with initial disk masses based on observed stellar mass accretion rates. Using these models we examined how CO isotopolog line fluxes, commonly used as to measure disk gas masses, change over time in a viscously evolving disk. We also compared our models to ^{13}CO $J = 3 - 2$ and C^{18}O $J = 3 - 2$ observations of disks in the Lupus star-forming region, to investigate if they are consistent with disks evolving viscously. Here we present our conclusions:

- ^{13}CO and C^{18}O 3-2 fluxes of viscously evolving disks increase over time due to the lines being optically thick and their optically thick emitting area increasing in size as the disk expands. For disks around stars with $M_* \lesssim 0.3$ M$_\odot$ the C^{18}O 3-2 emission is expected to be optically thin and thus trace the disk mass.

- Including the conversion of CO through grain-surface chemistry does not affect the ^{13}CO flux. Initially the C^{18}O is also not affected, but from $\sim$ 1 Myr onward it starts to decrease up to a factor $\sim 2 - 3$ at 10 Myr. This also ensures that from $\sim$ 1 Myr and onward C^{18}O 3-2 emission decreases with time in a viscously evolving disk.

- The observed ^{13}CO 3-2 and C^{18}O 3-2 line fluxes of the most massive disks ($M_{\mathrm{disk}} \gtrsim 5 \times 10^{-3}$ M$_\odot$) in Lupus are consistent to within a factor of 2 with our viscously evolving disk models where CO is converted into other species through grain-surface chemistry, assuming a moderate cosmic-ray ionization rate $\zeta_{\mathrm{cr}} \sim 10^{-17}$ s^{-1}.

- Increasing the cosmic-ray ionization rate to $\zeta_{\mathrm{cr}} \gtrsim 5 \times 10^{-17} - 10^{-16}$ s^{-1} decreases the C^{18}O fluxes to within a factor $\sim$ 2 of the observed upper limits for disks in Lupus with $M_{\mathrm{disk}} \lesssim 5 \times 10^{-3}$ M$_\odot$. Reproducing the stacked C^{18}O upper limit observed in Lupus requires a lower average abundance, which could be obtained with efficient vertical mixing.

- Our models overpredict the observed ^{13}CO 3-2 fluxes by a factor $10 - 30$ for most disks with $M_{\mathrm{disk}} \lesssim 5 \times 10^{-3}$ M$_\odot$ because the ^{13}CO 3-2 emission originates from a layer at $z/r \sim 0.25 - 0.4$, which is much higher up than the region where CO can be efficiently converted into other species ($z/r \lesssim 0.15$).

- The ^{13}CO 3-2 observations can be reproduced by our models by assuming efficient vertical mixing in addition to a higher cosmic-ray ionization rate $\zeta_{\mathrm{cr}} \sim 5 \times 10^{-17} - 10^{-16}$ s^{-1}. Alternatively, the observations can be explained if less massive ($M_{\mathrm{dust}} \lesssim 3 \times 10^{-5}$ M$_\odot$) disks are either much flatter and colder or much smaller ($R_{\mathrm{CO,\ 90\%}} \sim 40 - 70$ AU) than their more massive counterparts.

Our models show that the observed C^{18}O fluxes in Lupus are consistent with these disks having evolved viscously, if CO has been converted into other species under a high cosmic-ray ionization rate. The observed ^{13}CO fluxes are also consistent with this picture, provided that the material in the disk is well mixed vertically. However, alternative explanations for the low observed ^{13}CO fluxes such as the disks being colder or smaller than assumed cannot be discarded based on current observations. Deeper observations that resolve the CO isotopolog emission of low mass disks are needed to conclusively demonstrate whether these disks are evolving viscously.

Appendix

5.A Model ^{13}CO and C^{18}O $J = 3 - 2$ fluxes

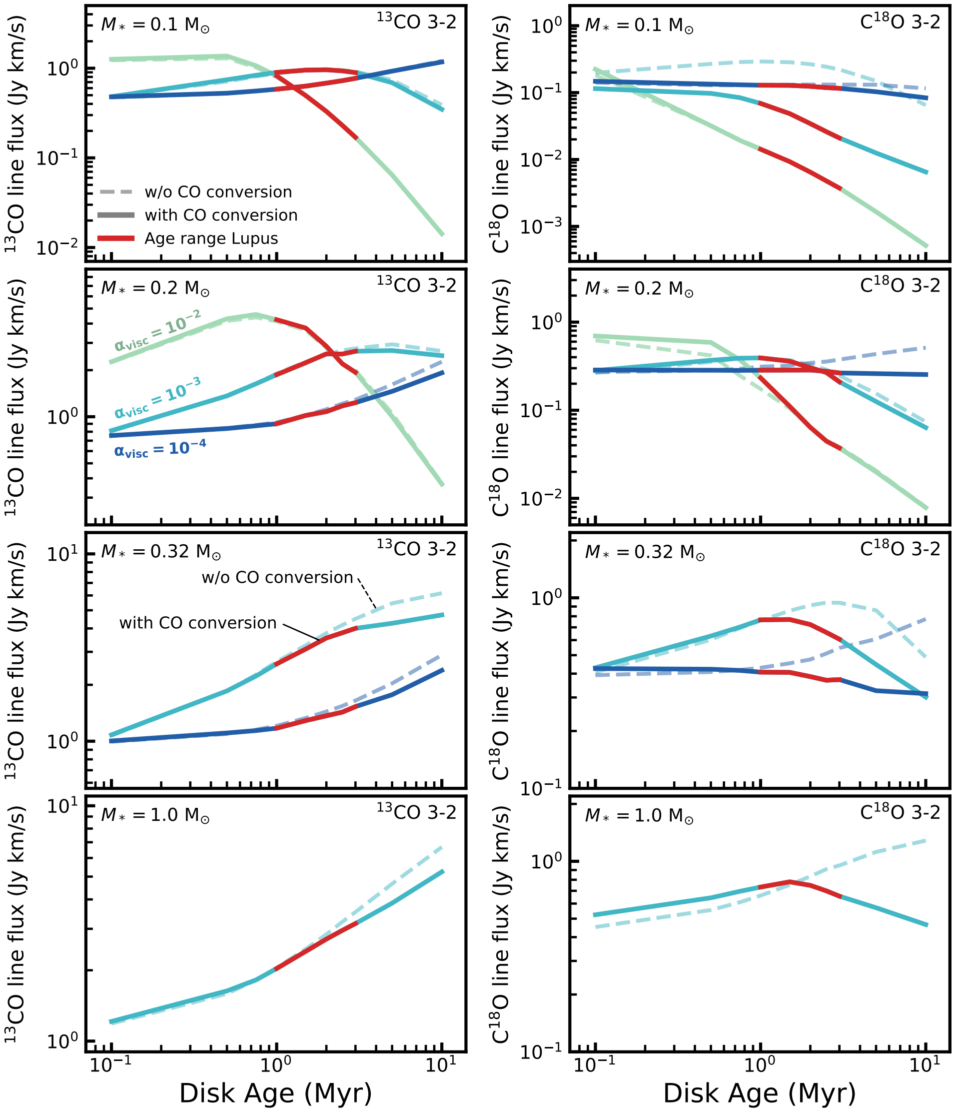

Figure 5.10: As Figure 5.5, but showing the ^{13}CO (left) and C^{18}O (right) $J = 3 - 2$ fluxes for all models. Colors indicate different $\alpha_{\rm visc}$. Models with and without CO conversion through grain-surface chemistry are shown with solid and dashed lines, respectively. The age range for disks in Lupus is highlighted in red. Few models show a significant decrease in ^{13}CO line fluxes, except for models with $\alpha_{\rm visc} = 10^{-2}$ that have low disk masses. The C^{18}O line fluxes do show a decrease with age, especially at later disk ages.

5.B Model ^{13}CO and C^{18}O $J = 2 - 1$ fluxes

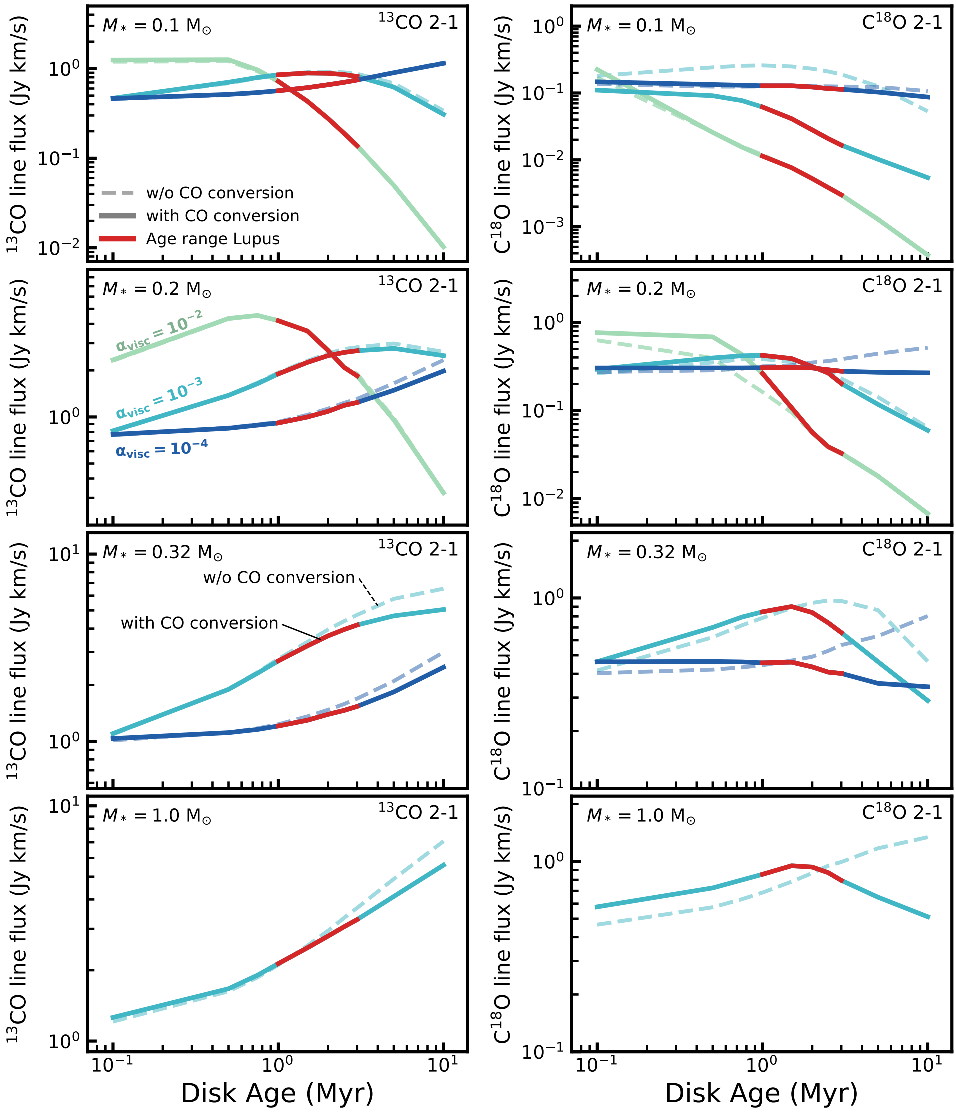

Figure 5.11: As Figure 5.10, but showing the ^{13}CO (left) and C^{18}O (right) $J = 2 - 1$ fluxes for all models. Note that the range of the y-axes are the same as for Figure 5.10.

5.C Comparing maximum CO conversion models to observed CO isotopolog line fluxes

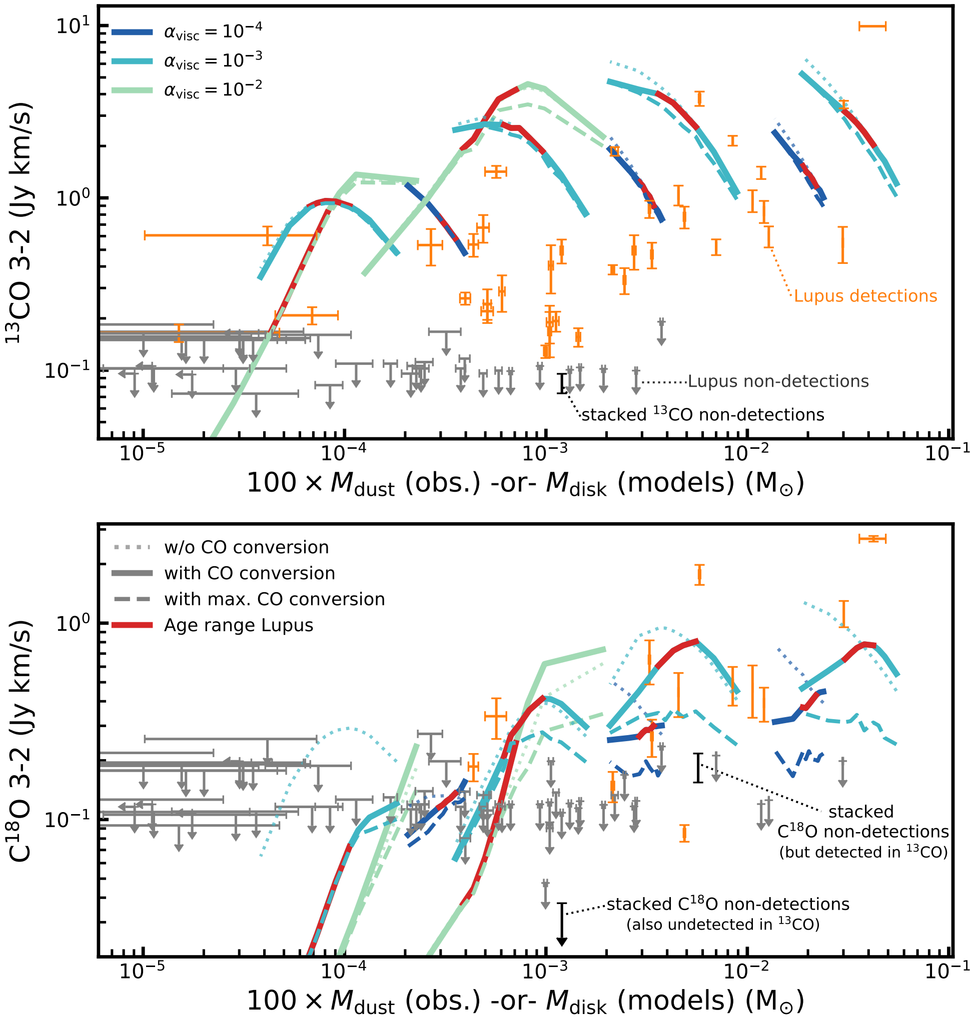

Figure 5.12: As Figure 5.5, but now showing three sets of models. The dotted lines show the ^{13}CO (top) and C^{18}O (bottom) $J = 3 - 2$ line fluxes for models with standard DALI chemistry, i.e. without CO conversion. The solid lines show line fluxes for the models where CO has been chemically converted into other species, as described in Section 5.2.3. The dashed lines show line fluxes for models with maximal CO conversion, i.e. where we have removed all CO in the region where CO conversion through grain-surface chemistry occurs (see also Section 5.7). Observations in Lupus are shown in orange if detected and gray if an upper limit (Ansdell et al. 2016; Yen et al. 2018). Stacked non-detections are shown in black (see Section 5.3.3).

6

Mass constraints for 15 protoplanetary disks from HD 1–0

M. Kama, L. Trapman, D. Fedele, S. Bruderer, M. R. Hogerheijde, A. Miotello, E. F. van Dishoeck, C. Clarke and E. A. Bergin, 2020, A&A, 634, 88

Abstract

Context: Hydrogen deuteride (HD) rotational line emission can provide reliable protoplanetary disk gas mass measurements, but it is difficult to observe and detections have been limited to three T-Tauri disks. No new data have been available since the *Herschel* Space Observatory mission ended in 2013.

Aims: We set out to obtain new disk gas mass constraints by analyzing upper limits on HD $1-0$ emission in *Herschel*/PACS archival data from the DIGIT key program.

Methods: With a focus on the Herbig Ae/Be disks, whose stars are more luminous than T Tauris, we determine upper limits for HD in data previously analyzed for its line detections. Their significance is studied with a grid of models run with the DALI physical-chemical code, customized to include deuterium chemistry.

Results: Nearly all the disks are constrained to $M_{\mathrm{gas}} \leq 0.1\,\mathrm{M}_{\odot}$, ruling out global gravitational instability. A strong constraint is obtained for the HD 163296 disk mass, $M_{\mathrm{gas}} \leq 0.067\,\mathrm{M}_{\odot}$, implying $\Delta_{\mathrm{gd}} \leq 100$. This HD-based mass limit is towards the low end of CO-based mass estimates for the disk, highlighting the large uncertainty in using only CO and suggesting that gas-phase CO depletion in HD 163296 is at most a factor of a few. The M_{gas} limits for HD 163296 and HD 100546, both bright disks with massive candidate protoplanetary systems, suggest disk-to-planet mass conversion efficiencies of $M_{\mathrm{p}}/(M_{\mathrm{gas}}+M_{\mathrm{p}}) \approx 10$ to $40\,\%$ for present-day values. Near-future observations with SOFIA/HIRMES will be able to detect HD in the brightest Herbig Ae/Be disks within 150 pc with ≈ 10 h integration time.

6.1 Introduction

The elusive total gas mass of a protoplanetary disk is relevant for planet formation, dust dynamics, and for testing disk evolution models. Due to difficulties in observing H_2, $M_{\rm gas}$ has been robustly measured in only three cases. In this work, we use *Herschel* archival data to constrain $M_{\rm gas}$ in a sample of 15 Herbig Ae/Be disks, and determine the mass of HD 163296 to within a factor of a few.

The gas mass is dominated by H_2, which has a large energy spacing between its lowest rotational levels (*para*-H_2 $J = 2-0$, $\Delta E = 512\,$K) and lacks a dipole moment. As such, H_2 is not emissive at the 10-100 K temperatures typical for disks. Dust continuum emission at millimeter wavelengths is often used to estimate $M_{\rm gas}$. Gas and dust are linked through a mass ratio, canonically $\Delta_{\rm gd} = 100$ for solar-composition material below $\sim 10^3$ K (e.g. Lodders 2003). While dust emission is easy to detect, the different dust and gas evolution as well as uncertain opacity values limit its reliability in measuring $M_{\rm gas}$. The most precise $M_{\rm gas}$ measurements to-date are from hydrogen deuteride (HD) rotational lines. The relative abundance of this deuterated isotopolog of H_2 is set by the local absolute D-to-H ratio ($(2.0 \pm 0.1) \times 10^{-5}$, Prodanović et al. 2010) and minimally affected by disk chemistry (Trapman et al. 2017). As the $J = 1$ rotational level is at $E/k_B = 128.5\,$K, HD emits from warm gas ($T_{\rm gas} \approx 30$ to 50 K, Bergin et al. 2013; Trapman et al. 2017). This is sufficient to constrain the total $M_{\rm gas}$, especially if the temperature structure is constrained via other observables. The HD $J = 1-0$ line at 112 μm, is however impossible to observe from the ground due to atmospheric absorption and requires air- or spaceborne telescopes.

After the pioneering HD $1-0$ detection in TW Hya (Bergin et al. 2013; Trapman et al. 2017), facilitated by the PACS spectrometer (Poglitsch et al. 2010b) on the *Herschel Space Observatory* (Pilbratt et al. 2010b), further detections were only made in DM Tau and GM Aur (McClure et al. 2016) before the instrument expired. The masses of these T Tauri disks are $M_{\rm gas} = (6-9) \times 10^{-3}$, $(1-4.7) \times 10^{-2}$, and $(2.5-20.4) \times 10^{-2}\,{\rm M}_\odot$, respectively. An upper limit $M_{\rm gas} \leq 8 \times 10^{-2}\,{\rm M}_\odot$ was obtained for the Herbig Ae/Be system HD 100546 (Kama et al. 2016b, revised down from the published value due to a mistake in the D/H ratio).

In this work, we use the 2D physical-chemical code `DALI` (Bruderer et al. 2012; Bruderer 2013) to constrain $M_{\rm gas}$ in 15 disks by analyzing *Herschel* archival data covering the HD $1-0$ and $2-1$ lines. The data and models are discussed in Sections 6.2 and 6.3, respectively. In Section 6.4, we explore the disk mass constraints, with a focus on HD 163296, and discuss the potential for gravitational instability. In Section 6.5, we compare the mass of disks, stars, and planetary systems for stars over $1.4\,{\rm M}_\odot$. We also discuss future observations of HD with SOFIA/HIRMES (Richards et al. 2018) and SPICA/SAFARI (Nakagawa et al. 2014; Audley et al. 2018).

6.2 Observations and sample

We use archival data from the *Herschel Space Observatory* (Pilbratt et al. 2010b) key program DIGIT (PI N.J. Evans), which targeted 30 protoplanetary disks with the PACS (Poglitsch et al. 2010b) instrument at 50–210 μm. Detected gaseous species in this data were presented in Fedele et al. (2013) and Meeus et al. (2013). We analyze upper limits on HD $J = 1-0$ and $2-1$ lines at 112 and 56 μm for the 15 Herbig Ae/Be disks in the sample. Due to the intrinsically higher luminosity of their host stars ($\sim$ 10-100 $L_\odot$), these disks are warmer, and brighter in continuum and line emission than those around T Tauri stars. This enables tighter constraints for disks at equivalent distance.

Table 6.1: HD line flux upper limits (3σ) for the sample.

Name	$L_\star$ ($L_\odot$)	$T_{\rm eff}$ (K)	d (pc)	HD 112 μm ($10^{-17}\,\frac{\rm W}{\rm m^2}$)	HD 56 μm ($10^{-17}\,\frac{\rm W}{\rm m^2}$)	$F_{\rm 1.3mm}$ (mJy)	Meeus group
HD 104237	$26^{\rm F15}$	$8000^{\rm F15}$	$108^{\rm GDR2}$	≤ 0.9	≤ 2.4	$92 \pm 19^{\rm M14}$	IIa
HD 144668	$58^{\rm F15}$	$8500^{\rm F15}$	$161^{\rm GDR2}$	≤ 0.8	≤ 7.8	$20 \pm 16^{\rm M14}$	IIa
HD 163296	$31^{\rm F12}$	$9200^{\rm F12}$	$101^{\rm GDR2}$	≤ 0.6	≤ 3.0	$743 \pm 15^{\rm M14}$	IIa
HD 31293	$59^{\rm F15}$	$9800^{\rm F12}$	$139^{\rm F12}$	≤ 4.2	≤ 22.4	$136 \pm 15^{\rm M14}$	Ia
HD 36112	$22^{\rm M14}$	$8190^{\rm F12}$	$160^{\rm GDR2}$	≤ 0.6	≤ 7.6	$72 \pm 13^{\rm M14}$	Ia
HD 38120	$123^{\rm S13}$	$10471^{\rm S13}$	$406^{\rm GDR2}$	≤ 0.9	≤ 5.6	-	Ia
HD 100546	$36^{\rm K16b}$	$10390^{\rm K16b}$	$110^{\rm GDR2}$	≤ 2.7	≤ 16.0	$465 \pm 20^{\rm M14}$	Ia
HD 139614	$6.6^{\rm F15}$	$7750^{\rm F15}$	$135^{\rm GDR2}$	≤ 1.2	≤ 8.5	$242 \pm 15^{\rm M14}$	Ia
HD 142527	$7.9^{\rm F15}$	$6500^{\rm F15}$	$157^{\rm GDR2}$	≤ 4.0	≤ 13.0	$1190 \pm 33^{\rm M14}$	Ia
HD 179218	$110^{\rm F12}$	$9640^{\rm F12}$	$266^{\rm GDR2}$	≤ 1.1	≤ 7.0	$71 \pm 7^{\rm M14}$	Ia
HD 97048	$33^{\rm F15}$	$10500^{\rm F15}$	$171^{\rm F15}$	≤ 2.4	≤ 2.4	$454 \pm 34^{\rm M14}$	Ib
HD 100453	$8.5^{\rm F15}$	$7250^{\rm F15}$	$104^{\rm GDR2}$	≤ 1.3	≤ 5.5	$200 \pm 21^{\rm M14}$	Ib
HD 135344B	$7.1^{\rm F15}$	$6375^{\rm F15}$	$136^{\rm GDR2}$	≤ 0.6	≤ 8.2	$142 \pm 19^{\rm M14}$	Ib
HD 169142	$10^{\rm F12}$	$7500^{\rm F12}$	$114^{\rm GDR2}$	≤ 2.4	≤ 13.5	$197 \pm 15^{\rm M14}$	Ib
Oph IRS 48*	$14.3^{\rm S13}$	$9000^{\rm S13}$	$134^{\rm GDR2}$	≤ 1.2	≤ 8.3	$60 \pm 10^{\rm M14}$	Ib

Notes. * – WLY 2-48.
References: F12 – Folsom et al. (2012); S13 – Salyk et al. (2013); M14 – Maaskant et al. (2014) and references therein; F15 – Fairlamb et al. (2015); K16b – Kama et al. (2016b); GDR2 – Brown et al. (2018).

We selected disks around stars of spectral type mid-F to late-B, including well-known targets such as HD 100546 and HD 163296. HD 50138 was excluded as it is likely an evolved star (Ellerbroek et al. 2015), and HD 35187 because it is a binary of two intermediate-mass stars and not directly comparable to our model grid. The data are spectrally unresolved, with $\delta v \approx 100\,{\rm km\,s^{-1}}$ ($\lambda/\delta\lambda = 3000$) at the shortest wavelengths (51 μm), while expected linewidths are $\leq$ 10 km s^{-1}. Exposure times ranged from 4356 s to 8884 s. The system parameters and 3σ line flux upper limits are given in Table 6.1.

We obtained flux limits for the HD transitions from the 1σ noise reported for the nearest lines of other molecules from Fedele et al. (2013): OH $^2\Pi_{1/2}\, J = 9/2^{-}$–$7/2^{+}$ at 55.89 μm for the 56 μm line and OH $^2\Pi_{3/2}\, J = 5/2^{-}$–$3/2^{+}$ at 119.23 μm for the 112 μm line. With a typical 1σ uncertainty of 5×10^{-18} W m^{-2} at 112 μm and 2×10^{-17}W m^{-2} at 56 μm, neither of the HD lines is detected in the targets, individually or stacked. For comparison, the HD $1-0$ detections Bergin et al. (2013) and McClure et al. (2016) had respective uncertainties of roughly 7×10^{-19} W m^{-2} and 5×10^{-19} W m^{-2}, which illustrates the difference between those targeted, deep integrations and the survey-type observations analyzed here.

The disks fall into two categories, cold (flat, group II in the Meeus classification, Meeus et al. 2001) and warm (flaring, group I). This characterizes the shape of the radial optically thick surface, where starlight is effectively absorbed. Starlight impinges at a shallow angle on flat disks, and heating is inefficient compared to that above the same midplane location in a flaring disk. In addition, among the Herbig Ae/Be systems flaring, group I disks have resolved cavities or gaps 10–100 au scales in their millimeter dust emission (Maaskant et al. 2013; Kama et al. 2015).

6.3 Modeling

6.3.1 DALI

To determine the behavior of the HD $1-0$ line and 1.3 millimeter continuum flux as a function of disk structure parameters, we run a grid of models with the 2D physical-chemical disk code DALI (Bruderer et al. 2012; Bruderer 2013). The surface density is parameterized following the viscous accretion disk formalism (Lynden-Bell & Pringle 1974; Hartmann et al. 1998):

$$\Sigma_{\rm gas} = \Sigma_c \left(\frac{R}{R_c}\right)^{\gamma} \exp\left[-\left(\frac{R}{R_c}\right)^{2-\gamma}\right], \tag{6.1}$$

where Σ_c is the surface density at the characteristic radius R_c, and γ the power-law index which is generally 1. Assuming an isothermal structure in hydrostatic equilibrium, the vertical structure is given by a Gaussian density distribution (Kenyon & Hartmann 1987):

$$\rho_{\rm gas}(R,z) = \frac{\Sigma_{\rm gas}(R)}{\sqrt{2\pi}Rh} \exp\left[-\frac{1}{2}\left(\frac{z}{Rh}\right)^{2}\right]. \tag{6.2}$$

Here $h = h_c(R/R_c)^{\psi}$, ψ is the flaring index and h_c is the disk opening angle at R_c.

A population of small grains (0.005-1 μm), with a mass fraction $f_{\rm small}$, follows the gas density distribution given in Eq. (6.2). A second population, consisting of large grains (1 μm - 1 mm), has a mass fraction $f_{\rm large}$. Their scale height is χh, where $\chi \in (0,1]$ is the settling parameter.

Table 6.2: `DALI` model grid parameters.

Parameter	Range
Chemistry	
Chemical age	1 Myr
HD/H_2	$4 \cdot 10^{-5}$
Physical structure	
γ	1.0
ψ	[0.0, 0.3]
h_c	[0.05, 0.15] rad
R_c	[50, 150] au
M_{gas}	$[10^{-3}, 10^{-2}, 10^{-1}]$ $M_\odot$
Dust properties	
Gas-to-dust ratio	[10, 50, 100, 300]
f_{large}	[0.8, 0.95]
χ	[0.2, 0.5]
f_{PAH}	0.001
Stellar properties[1]	
T_{eff}	10390 K
L_X	$8 \cdot 10^{28}$ erg s^{-1}
T_X	$7 \cdot 10^{7}$ K
L_*	[10, 50, 115] $L_\odot$
ζ_{cr}	10^{-17} s^{-1}
Observational geometry	
i	60°
d	150 pc

Notes. Standard `DALI` parameter names as in Bruderer et al. (2012). Deuterium abundance from Prodanović et al. (2010).[1]HD 100546 (Bruderer et al. 2012).

For the dust opacities of both small and large grain populations we assume a standard interstellar composition following Weingartner & Draine (2001), in line with Bruderer (2013). The absorption coefficient for the small (large) grains is $29.9\,cm^2\,g^{-1}$ ($30.0\,cm^2\,g^{-1}$) at 112 μm and $154\,cm^2\,g^{-1}$ ($46.3\,cm^2\,g^{-1}$) at 56 μm.

First, the radiation field and dust temperature are determined from Monte Carlo radiative transfer. Next, the gas temperature (heating-cooling balance) and chemical composition (steady-state) are solved for iteratively. Raytracing then yields simulated line and continuum observations.

HD chemical network *versus* fixed abundance

The HD abundance (HD/H_2) can be prescribed as a constant or obtained from solving a chemical reaction network. In the parametric approach, the HD abundance is determined by the local D/H ratio, which for the local ISM (within ≈ 2 kpc) is measured to be $(D/H)_{ISM} = (2.0 \pm 0.1) \times 10^{-5}$ (Prodanović et al. 2010). Assuming all deuterium is in HD, this gives $HD/H_2 = 4 \times 10^{-5}$.

A more refined approach is to calculate the HD abundance using a reaction network which includes deuterium. Trapman et al. (2017) extended the standard DALI chemical network (originally based on the UMIST06 database Woodall et al. 2007) to include the species HD, D, HD^+, and D^+. HD formation on dust and ion-exchange reactions were included, in addition to HD self-shielding. The details of the implementation are described in Section 2.3 of Trapman et al. (2017).

Using the chemical network approach, we find that all of the available deuterium is locked up in HD for the vast majority of the disk, and the parametric abundance of $HD/H_2 = 4 \times 10^{-5}$ is appropriate to use. The network produces less HD in only two regions: the uppermost layers of the disk where HD is photodissociated, and in a thin intermediate layer, where the HD abundance is decreased by a factor of ~ 2. Tests determined that neither of these significantly affects the disk-integrated HD line flux.

Given the very close match between the two approaches, we opt for simplicity and fix the HD/H_2 ratio at 4×10^{-5}.

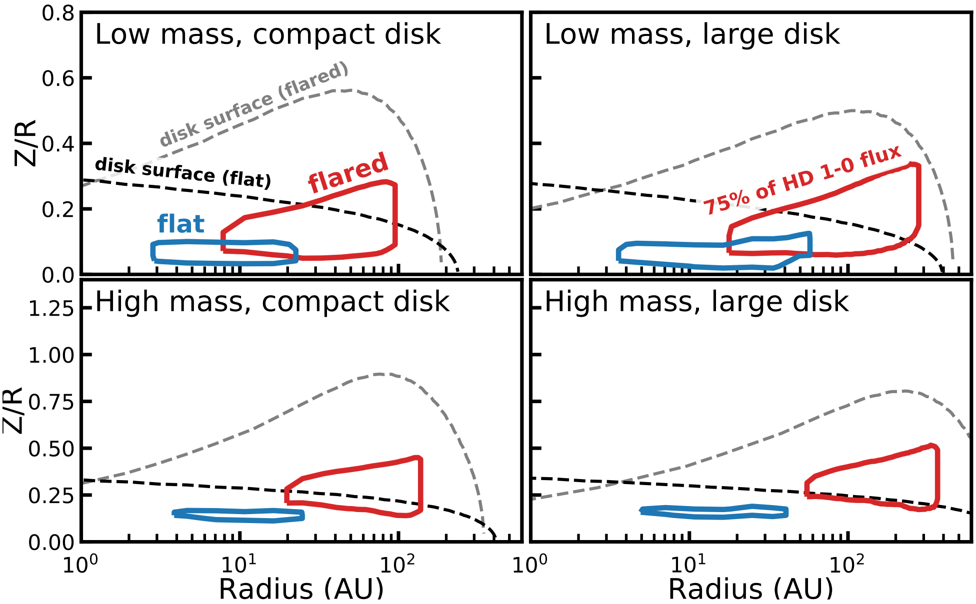

Figure 6.1: HD 1–0 line emitting regions in our flat/cold (blue) and flared/warm (red) disk models. Solid contours contain the middle 75% of vertically cumulative line emission. Dashed lines are gas number density iso-contours for $n_{\rm gas} = 10^6$ cm^{-3}, acting as a disk "outline".

6.3.2 Model grid

To investigate the range of disk properties constrained by the *Herschel* upper limits on the HD $1-0$ line, we run a grid of Herbig Ae/Be disk models covering a wide range of parameters, summarized in Table 6.2. The disk gas masses are $M_{\rm gas} = 10^{-3}, 10^{-2}$, and 10^{-1} M$_\odot$. Dust mass is defined by the gas-to-dust mass ratio, with values $\Delta_{\rm gd} = 10, 50,$ 100, and 300, and ranges from $M_{\rm dust} = 3 \times 10^{-6}$ to 10^{-2} M$_\odot$. The shape of the stellar spectrum, including UV excess, is based on HD 100564 from Bruderer et al. (2012). The spectrum is scaled to the total stellar luminosity, $L_\star \in [10, 50, 115]$ L$_\odot$. This covers the sources in our sample, as given in Table 6.1. In total we run 2304 models, with parameters given in Table 6.2. Our fiducial model has $h_c = 0.15$, $R_c = 50\,\mathrm{au}$, $\Delta_{\mathrm{gd}} = 100$, $f_{\mathrm{large}} = 0.95$, $\chi = 0.2$, and $L_\star = 10\,\mathrm{L}_\odot$.

Figure 6.1 shows the HD 1 − 0 emitting regions and disk mass outline for models representing extremes in flaring ($\Psi = 0.0$ and $h_{\mathrm{c}} = 0.05$ for flat, and $\Psi = 0.3$ and $h_{\mathrm{c}} = 0.15$ for flared), radial extent ($R_{\mathrm{c}} = 50$ and $125\,\mathrm{au}$), and total disk mass. From the figure it is clear that the flared disk ($\psi = 0.3, h_c = 0.15$), shown in red, has a much large emitting region than the flat disk ($\Psi = 0.0, h_c = 0.05$), shown in blue. In both cases the HD 1 − 0 emission originates from the warm layer above the midplane.

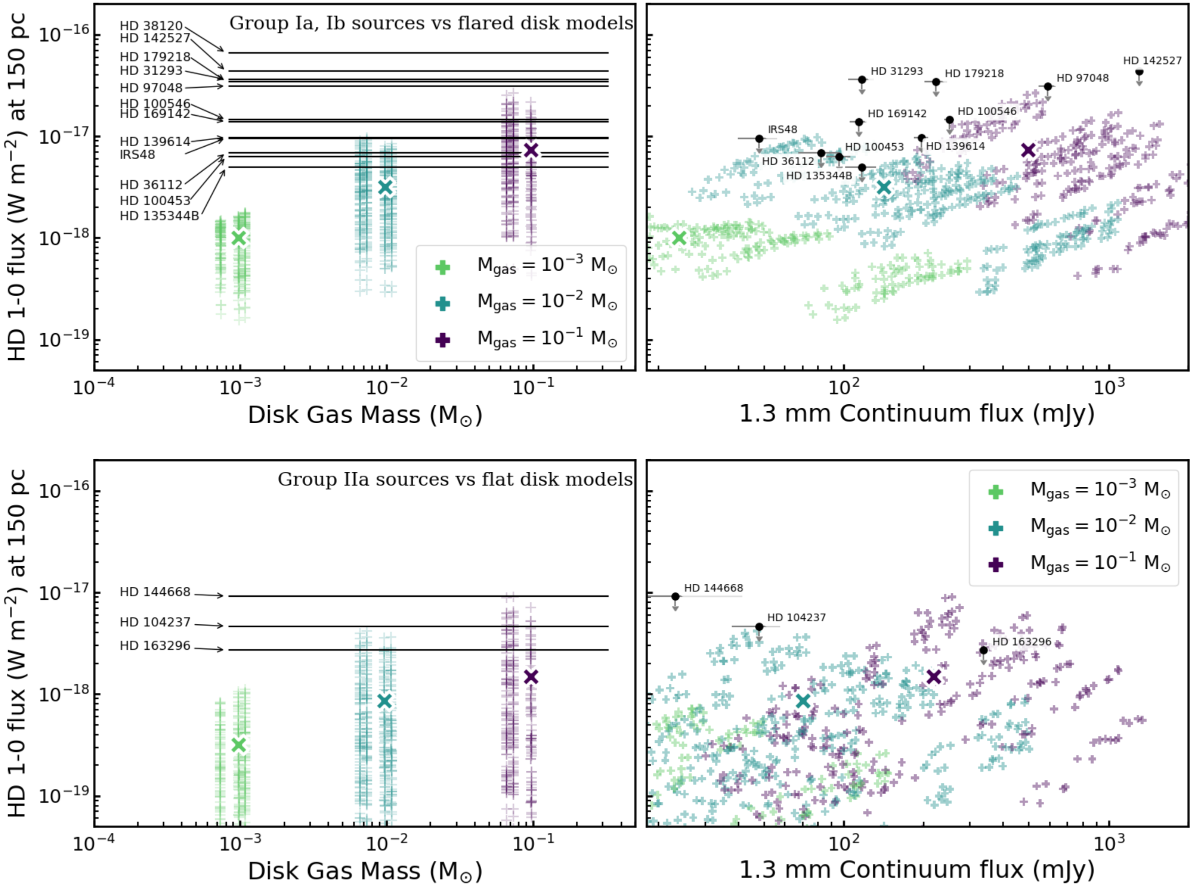

Figure 6.3: Distance-normalized 3σ upper limits on HD 112 μm line flux for the disk sample (black lines and circles) compared with our grid of DALI disk models (colored crosses). Highlighted crosses show the HD 112 μm line flux of our fiducial model. The top panels show the group I sources compared to models with flaring angle $\psi = 0.3$. The bottom panels show the group II sources compared to models with $\psi = 0.0$. **Left:** models are separated based on gas mass. **Right:** HD $1-0$ upper limits set against 1.3 mm continuum fluxes for both observations and models.

6.4 Results

In Figure 6.3, we show the HD $J = 1-0$ flux as a function of $M_{\rm gas}$ and 1.3 millimeter continuum flux. The warm, flaring, group I disks and cold, flat, group II disks are highlighted separately for clarity.

6.4.1 Parameter dependencies in the grid

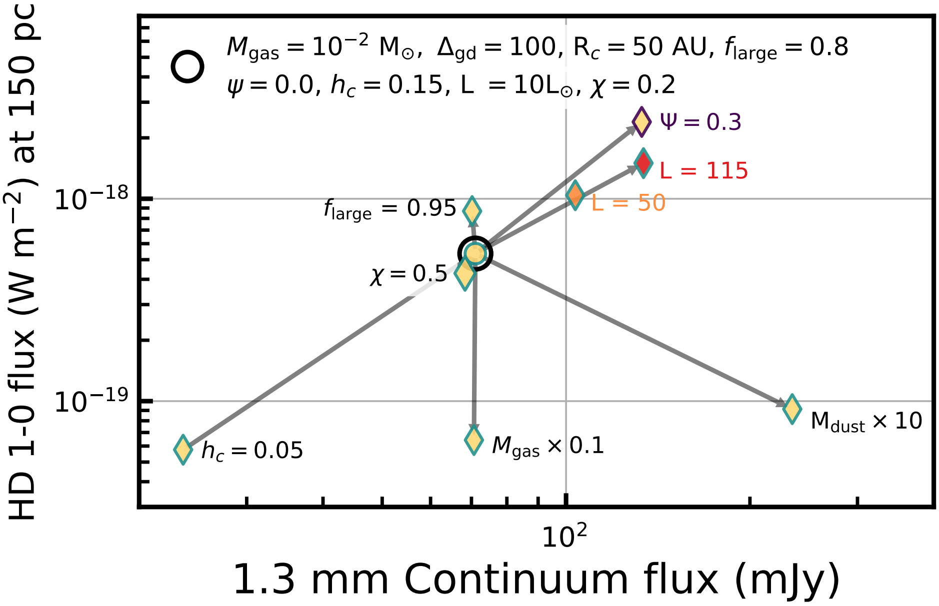

Figure 6.4: HD 1 − 0 line and dust continuum flux dependencies on disk and stellar parameters.

Dependencies of the HD 1 − 0 line and 1.3 millimeter continuum flux on the main model parameters are shown in Figure 6.4. The HD line flux depends linearly on $M_{\rm gas}$, which has only a marginal effect on the dust emission. For a fixed $M_{\rm gas}$, a 1 dex increase in $M_{\rm dust}$ leads to a factor 6.7 lower HD and 2.5 higher continuum flux. The flaring structure of the disk has the largest influence, as the HD line flux increases by a factor of 26 when the flaring parameter Ψ goes from 0 (height is linear with radius, inefficient heating) to 0.3 (very flared and efficiently heated). The Meeus group corresponds to the flaring structure (group I disks are flared, II flat).

A near-linear dependence of HD line flux on $M_{\rm gas}$ arises because the HD line emission in the models is vertically limited by the dust optical depth τ at 112 μm out to ≈ 100 au radii, beyond which the surface density drops rapidly. Thus the HD contribution from the gas above and radially outside the dust scales linearly with the total gas mass. Dust emission, to first order, is optically thin at 1.3 mm, and thus scales linearly with the total dust mass. Again due to the dust optical depth dominating at the 112 μm wavelength of HD 1 − 0, increasing the dust mass in a given column lifts the vertical $\tau(112\,\mu\mathrm{m}) = 1$ surface, hiding a larger fraction of the HD molecules.

6.4.2 Constraints on M_{gas} across the sample

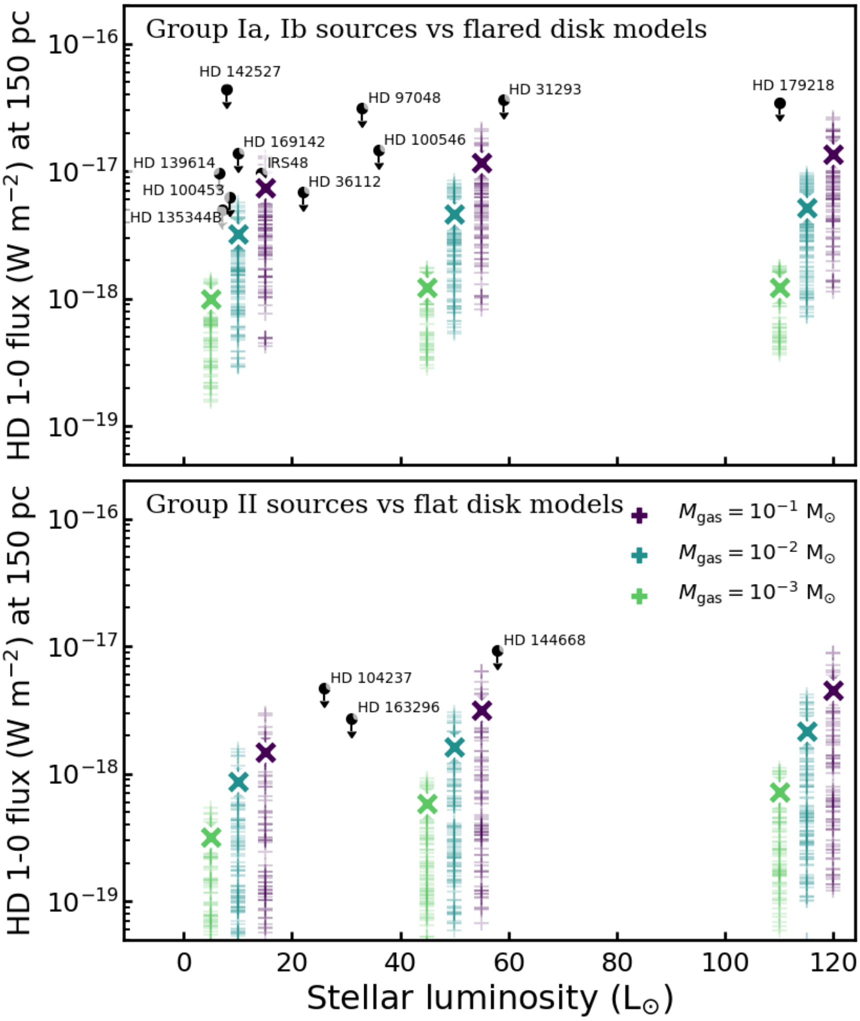

Figure 6.5: HD 1 − 0 line flux versus the stellar luminosity. Observed stellar luminosities taken from Table 6.1. Model stellar luminosities were given a small offset for clarity. Highlighted crosses show our fiducial model ($h_c = 0.15$, $R_c = 50\,\mathrm{au}$, $\Delta_{\mathrm{gd}} = 100$, $f_{\mathrm{large}} = 0.95$, $\chi = 0.2$).

A comparison of the HD upper limits from *Herschel* with our DALI model grid (Figures 6.3 and 6.5) places an upper limit of approximately $M_{\mathrm{gas}} \leq 0.1\,\mathrm{M}_\odot$ for the disks in our sample. Among the flared, group I disks (Fig. 6.3, upper row), we find $M_{\mathrm{gas}} < 0.02$–$0.03\,\mathrm{M}_\odot$ for IRS 48, HD 36112, HD 100453, and HD 135344B, while among the flat, group II disks HD 163296 has a limit at $< 0.1\,\mathrm{M}_\odot$.

Source-specific models can tighten the mass limit for individual disks. We run a small grid of models for HD 163296, where we have a strong HD upper limit and a wide comparison range of indirect gas mass estimates from the literature based on various isotopologs of CO.

6.4.3 HD 163296

We constrain the gas mass in the HD 163296 disk to $M_{\rm gas} \leq 0.067\,{\rm M}_\odot$ (Figure 6.6). Given that the disk-integrated dust mass in our model is $6.7 \times 10^{-4}\,{\rm M}_\odot$, this constrains the gas-to-dust ratio to $\Delta_{\rm gd} \leq 100$ and has implications for the gas-phase volatile abundances, which we discuss below. This source-specific model matches the continuum spectral energy distribution, ^{12}CO rotational ladder and isotopolog lines, and several other key volatile species. The full details of this modeling are outside the scope of this paper and will be published separately, below we focus on the main outcomes of the continuum, CO, and HD modeling.

Table 6.3: Adopted model for HD 163296

Parameter	Value
γ	0.9
ψ	0.05
$h_{\rm c}$	0.075
$R_{\rm c}$	125 au
$\Sigma_{\rm c}$ $R_{\rm cav}$	0.41 au
$M_{\rm gas}$	$6.7 \times 10^{-2}\,{\rm M}_\odot$
$M_{\rm dust}$	$6.6 \times 10^{-4}\,{\rm M}_\odot$
$\Delta_{\rm gd}$	100
$f_{\rm large}$	0.9
χ	0.2
L_* (L$_\odot$)	37.7
i (°)	45
d (pc)	101 pc

HD 163296 is one of the largest known disks, with a CO $J = 3-2$ gas emission radius of 540 au (Rosenfeld et al. 2013). Fitting of CO and 850 μm continuum emission, observed by ALMA, with a tapered surface density powerlaw yielded $\gamma = 0.9$ and $R_c = 125$ au (Tilling et al. 2012; de Gregorio-Monsalvo et al. 2013). We model HD 163296 with the stellar spectrum from the PRODiMo project (Woitke et al. 2019), fixing the shape of the dust surface density profile to the above parameters and varying the gas mass. To satisfy the radial profile of CO 3 − 2 emission simultaneously with the spectral energy distribution, we find the density profile flaring index in Eq. 6.2 is around $\psi = 0.05$, consistent with the range of 0.019 to 0.066 found by Tilling et al. (2012). The morphology of the ^{12}CO 3 − 2 channel maps, in which both the near and far side of the disk can be seen, suggest HD 163296 is more flared ($\psi \approx 0.12$, de Gregorio-Monsalvo et al. 2013) than our model ($\psi = 0.05$). However, these two ψ-s differ in physical meaning: the CO-based one measures the observed shape of the CO-emitting surface, while the disk structure parameter ψ characterizes the shape of the total gas mass distribution (see Eq. 6.2).

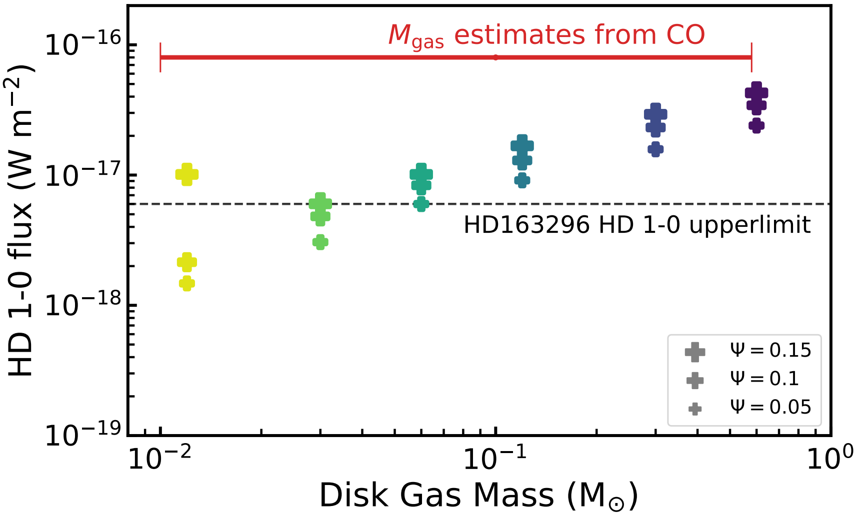

Figure 6.6: Comparing the HD 163296 specific models to the HD $1-0$ upper limit (Fedele et al. 2013). All models have a dust mass $M_{\rm dust} = 6.6 \times 10^{-4}$ M$_\odot$ (Table 6.3). The red bar shows the range of gas masses inferred from CO in the literature.

Our model which hits the HD upper limit reproduces the observed dust emission across the far-infrared and sub-millimeter wavelengths as well as various spatially resolved and unresolved emission lines of ^{12}CO and its isotopologs, and has a gas-to-dust ratio $\Delta_{\rm gd} = 100$.

Most previous estimates of the HD 163296 gas mass relied on low-J emission lines of CO isotopologs, and used a range of modeling approaches from generic model grids to tailored modeling with physical-chemical codes. Those $M_{\rm gas}$ estimates range from 8×10^{-3} to 5.8×10^{-1} M$_\odot$ (Isella et al. 2007; Williams & Best 2014; Boneberg et al. 2016; Miotello et al. 2016; Williams & McPartland 2016; Powell et al. 2019; Woitke et al. 2019; Booth et al. 2019). The mass obtained from the most optically thin isotopolog among these, ^{13}C^{17}O, was 2.1×10^{-1}M$_\odot$ (Booth et al. 2019).

Above, we assumed an undepleted solar abundance for elemental gas-phase carbon and oxygen. Our model matching the HD upper limit over-produces the low-J line fluxes of CO isotopologs by a factor of a few. Since the rarer isotopologs are progressively more optically thin, we can reproduce their line fluxes by decreasing the gas-phase elemental carbon and oxygen abundance proportionately to the flux mismatch. Since the millimeter-wave dust emission and HD upper limit constrain the gas-to-dust mass ratio to be ≤ 100, we can combine the above considerations to arrive at three distinct hypotheses for HD 163296:

1. $M_{\rm gas}$ is just sufficiently below our upper limit of 6.7×10^{-2} M$_\odot$ for HD not to be detected. If so, then as the dust mass is fixed, it follows from our models that $\Delta_{\rm gd} = 100$ and that total gas-phase elemental C and O are depleted by up to a factor of a few.

2. $M_{\rm gas}$ is a factor of a few below our HD limit, and the total gas-phase elemental C and O abundances are not depleted with respect to their interstellar values.

If so, the implication is that $\Delta_{\mathrm{gd}} \approx 20$–$50$. This relative depletion of gas over dust is supported by the hydrostatic MCMax modeling of the SED and low-J ^{12}CO, ^{13}CO, and C^{18}O lines by Boneberg et al. (2016), whose best models had $9.2 < \Delta_{\mathrm{gd}} < 18$. It is also consistent with the inner disk value $\Delta_{\mathrm{gd}} \approx 55$, measured using accretion onto the central star by Kama et al. (2015, their Figure 2).

3. M_{gas} is far below our upper limit. In this hypothesis, the total C and O abundance in the gas must be enhanced above the interstellar baseline, in order to still match the optically thin CO isotopologs. This would be the first known case of C and O enhancement, however the inner disk composition analysis by Kama et al. (2015) does not show evidence for a strong enhancement of gas-phase volatile elements over total hydrogen.

Thus $\Delta_{\mathrm{gd}} > 100$ is ruled out by the HD $1-0$ upper limit for HD 163296, independently of assumptions about the precise abundance of gas-phase volatiles.

The abundance of volatile elements in the HD 163296 disk may be depleted or enhanced by up to a factor of a few, depending on the true value of M_{gas} and on the somewhat uncertain underlying number abundance ratios of ^{12}CO and its various isotopologs. We note that even with the flat, cold disk structure of HD 163296, our $\Delta_{\mathrm{gd}} = 100$ model somewhat over-predicts the CO emission outside of ~ 100 au for an undepleted elemental carbon abundance (C/H $= 1.35 \times 10^{-4}$). A more flared surface would aggravate this over-prediction, while globally reducing the elemental C under-predicts the CO $3-2$ inside ~ 100 au. This may indicate that any depletion of gas-phase volatile elemental C and O, reflected in the CO abundance in the warm molecular layer, is restricted to the region beyond the CO snowline, which has been observed to be at ≈ 90 au (Qi et al. 2015). The same conclusion was recently reached by Zhang et al. (2019) through an analysis of spatially resolved C^{18}O data, which yielded a factor of ten depletion of gas-phase CO outside the CO snowline.

6.4.4 HD 100546

HD 100546 was previously modeled with DALI by Bruderer et al. (2012) who determined the radial and vertical structure of the disk mainly from CO lines and continuum emission. A refined version of this modeling effort included the *Herschel* HD upper limits, the C^0 and C$_2$H fluxes, and the spatially resolved CO $3-2$ emission, constraining the gas mass to $8.1 \times 10^{-3} \leq M_{\mathrm{gas}} \leq 2.4 \times 10^{-1}\,\mathrm{M}_\odot$ (Kama et al. 2016b). The highest-mass model had $\Delta_{\mathrm{gd}} = 300$, with a dust mass anchored by the continuum spectral energy distribution. Due to a factor of four error in the D abundance used in that model, we revise those numbers to $\lesssim 100$ and thus $M_{\mathrm{gas}} \lesssim 0.08\,\mathrm{M}_\odot$ from the Kama et al. (2016b) model. This is about a factor of two stronger than the constraint from our general model grid, so in Figure 6.7 we adopt $M_{\mathrm{gas}} \lesssim 0.08\,\mathrm{M}_\odot$.

6.4.5 Other individual disks

HD 97048 hosts a massive dust disk, $M_{\mathrm{dust}} \simeq 6.7 \times 10^{-4}\,\mathrm{M}_\odot$ (Walsh et al. 2016), so it is likely the gas mass is also high. The disk surface is highly flared ($\Psi = 0.5 - 0.73$, see e.g. Lagage et al. 2006; Walsh et al. 2016; Ginski et al. 2016; van der Plas et al. 2019)). This exceeds the largest Ψ in our general grid, but we note again that the

CO-surface Ψ and the density structure Ψ differ in physical meaning. From our grid we find $M_{\rm gas} \leq 9.4 \cdot 10^{-2}\,{\rm M}_\odot$ ($\Delta_{\rm gd} \leq 200$).

HD 104237. For this disk, Hales et al. (2014) determined $M_{\rm dust} = 4 \times 10^{-4}\,{\rm M}_\odot$, which assuming $\Delta_{\rm gd} = 100$ implies a total mass $M_{\rm gas} = 4 \times 10^{-2}\,{\rm M}_\odot$. This is consistent with our upper limit from HD $1-0$, which yields an upper limit of $\Delta_{\rm gd} \leq 300$ (Figure 6.3).

HD 36112 (MWC 758). Based on millimeter continuum interferometry, Guilloteau et al. (2011) inferred a disk mass of $(1.1 \pm 0.2) \times 10^{-2}\,{\rm M}_\odot$. Our analysis of the 1.3 mm continuum flux and the HD $1-0$ upper limit matches both datapoints for $\Delta_{\rm gd} \approx 100$ and a disk mass of order $10^{-2}\,{\rm M}_\odot$. A substantially lower gas mass would imply a very low $\Delta_{\rm gd}$ mass ratio.

HD 31293 (AB Aurigae). From 1.3 millimeter continuum observations performed using the SMA, Andrews et al. (2013) inferred a dust mass of $(1.56 \pm 0.09) \times 10^{-4}\,{\rm M}_\odot$, implying $M_{\rm gas} = 1.56 \times 10^{-2}\,{\rm M}_\odot$ assuming $\Delta_{\rm gd} = 100$. The high upper limit of HD 1 - 0 for this source does not allow us to put any meaningful constraints on the gas mass based on HD.

HD 135344B has been modeled by van der Marel et al. (2016b) to determine the physical structure. Using ALMA observations of ^{13}CO $J = 3-2$, C^{18}O $J = 3-2$, ^{12}CO $J = 6-5$ and dust 690 GHz continuum, they determined a gas mass $M_{\rm gas} = 1.5 \times 10^{-2}\,{\rm M}_\odot$. We run models based on their physical structure and find the resulting HD $1-0$ flux to be in agreement with the upper limit (see Figure 6.9 in Appendix 6.A).

HD 142527. Modeling interferometric 880 μm continuum and ^{13}CO 3–2 and C^{18}O 3–2 line observations, Boehler et al. (2017) determine a dust mass of $1.5 \times 10^{-3}\,{\rm M}_\odot$ and a gas mass of $5.7 \times 10^{-3}\,{\rm M}_\odot$ (see also Muto et al. 2015). This gives $3 \leq \Delta_{\rm gd} \leq 5$ and suggests the gas is either strongly depleted in elemental C and O, or dissipating entirely. Due to the loose HD $1-0$ upper limit for this source, we cannot provide an independent check of the low $\Delta_{\rm gd}$ derived from CO.

HD 179218. From the integrated 1.3 millimeter flux Mannings & Sargent (2000) infer a dust mass of $(1.5 \pm 0.15) \times 10^{-4}\,{\rm M}_\odot$, implying $M_{\rm gas} = 1.5 \times 10^{-2}\,{\rm M}_\odot$ assuming $\Delta_{\rm gd} = 100$. Again the HD $1-0$ upper limit provides no meaningful constraint on the gas mass.

HD 100453. Based on millimeter continuum interfermotric observations, van der Plas et al. (2019) inferred a dust mass of $6.7 \times 10^{-5}\,{\rm M}_\odot$. By comparing the ^{13}CO $2-1$ and C^{18}O $2-1$ to the disk model grid in Williams & Best (2014), they determine a gas mass of $(1 - 3\times) \times 10^{-3}\,{\rm M}_\odot$. Combining both disk masses implies a gas-to-dust mass ratio of $\Delta_{\rm gd}$ $15 - 45$. From our analysis of the 1.3 mm continuum flux and the HD $1-0$ upper limit we constrain gas mass to $M_{\rm gas} \leq 10^{-2}\,{\rm M}_\odot$ and the gas-to-dust mass ratio $\Delta_{\rm gd} \leq 300$. Both constraints are in agreement with the results of van der Plas et al. (2019).

HD 169142. From interferometric 1.3 millimeter continuum and ^{12}CO $2-1$, ^{13}CO $2-1$ and C^{18}O $2-1$ line observations, Panić et al. (2008) derived a dust mass of $2.16 \times 10^{-4}\,{\rm M}_\odot$ and a gas mass of $(0.6 - 3.0) \times 10^{-2}\,{\rm M}_\odot$. Fedele et al. (2017) find similar disk masses based on higher resolution observations. Constraints based on our analysis of the 1.3 mm continuum flux and the HD $1-0$ upper limit put the gas mass at $M_{\rm gas} \leq 4 \times 10^{-2}\,{\rm M}_\odot$ and $\Delta_{\rm gd} \leq 300$, both of which are in good agreement with previous results.

Oph IRS 48 (WLY 2-48). van der Marel et al. (2016b) modeled the resolved 440 μm continuum and ^{13}CO $6-5$ and C^{18}O $6-5$ line observations. They derived a dust mass of $1.5 \times 10^{-5}\,\mathrm{M_\odot}$ and a gas mass of $5.5 \times 10^{-4}\,\mathrm{M_\odot}$, giving a gas-to-dust mass ratio of $\Delta_{\rm gd} \approx 37$. Constraints from our analysis of the HD $1-0$ line flux and 1.3 millimeter continuum give $M_{\rm gas} \lessapprox 10^{-2}\,\mathrm{M_\odot}$ and $\Delta_{\rm gd} \lessapprox 300$. These upper limits agree with previous results.

6.4.6 Are the disks stable?

Constraints on $M_{\rm gas}$ allow to test whether the disks in our sample are currently gravitationally stable. Gravitational instability, leading to spirals or fragmentation, occurs in disk regions which are dense and cold, and have low orbital shearing on the timescale of the instability (i.e. at large radii). This is quantified with the Toomre Q parameter, $Q = \Omega_K\, c_{\rm s}\, (\pi\, G\, \Sigma)^{-1}$ (Toomre 1964), which simplifies to

$$Q = 21 \times \left(\frac{\Sigma}{10\,\mathrm{kg\,m^{-2}}}\right)^{-1} \times \left(\frac{r}{100\,\mathrm{au}}\right)^{-3/2}, \tag{6.3}$$

following Kimura & Tsuribe (2012). If $Q < 1$, the disk will fragment. For $1 < Q < 2$, the disk will be marginally stable, developing transient spirals and clumps, while for $Q > 2$ it is stable against gravitational collapse. Assuming a surface density profile $\Sigma = \Sigma_0 \times (r/r_0)^{-1}$ and $M_{\rm disk} \approx M_{\rm gas}$, we obtain

$$Q = 2.44 \times 10^{22}\,\pi\, r_0^{1/2}\, M_{\rm disk}^{-1}, \tag{6.4}$$

Our most massive disk models have $M_{\rm gas} = 0.1\,\mathrm{M_\odot}$. Taking a characteristic radius $r_0 = 100\,\mathrm{au}$, we find $Q = 1.5$, which is marginally stable. The disks for which we have the weakest upper limits relative to the massive disk models – HD 142527, HD 144668, HD 179218, and HD 31293 – may potentially be gravitationally unstable within the limits of the *Herschel* HD data. For the rest of the sample, a gravitationally unstable $M_{\rm gas}$ is effectively ruled out, i.e. they are most likely stable.

6.5 Discussion

6.5.1 Mass of disks, stars, and planets

Intermediate-mass stars (spectral types B9 to F5, masses 1.5 to $3\,\mathrm{M_\odot}$) host some of the best-studied protoplanetary disks and high-mass planetary systems. Several Herbig Ae/Be protoplanetary disks have also yielded detections of protoplanet candidates. This presents an opportunity to investigate equivalent planetary systems at different stages of evolution. While radial velocity surveys

In Figure 6.7, we compare the disk mass reservoir with the host star and the mass of candidate protoplanets in the disk. We show two Herbig Ae/Be systems with strong mass limits, HD 163296 ($M_{\rm gas} \leq 0.067\,\mathrm{M_\odot}$, this work) and HD 100546 ($M_{\rm gas} \leq 0.08\,\mathrm{M_\odot}$, Kama et al. 2016b).

For HD 163296, our HD-based upper limit rules out a large fraction of the wide range of CO isotopolog based $M_{\rm gas}$ estimates from the literature. Of those still possible, the lowest is $M_{\rm gas} = 8 \times 10^{-3}\,\mathrm{M_\odot}$. The presence of five giant planets has been inferred from dust gaps and gas kinematics: at 10 au with a mass $(0.53 \pm 0.18)\,\mathrm{M_{Jup}}$ for $\alpha_{\rm visc} = 10^{-4}$ to 10^{-3} (Zhang et al. 2018); at 48 au with $0.46\,\mathrm{M_{Jup}}$ (Isella et al. 2016; Liu et al. 2018); at 86 au with $(1 \pm 0.5)\,\mathrm{M_{Jup}}$ (Liu et al. 2018; Teague et al.

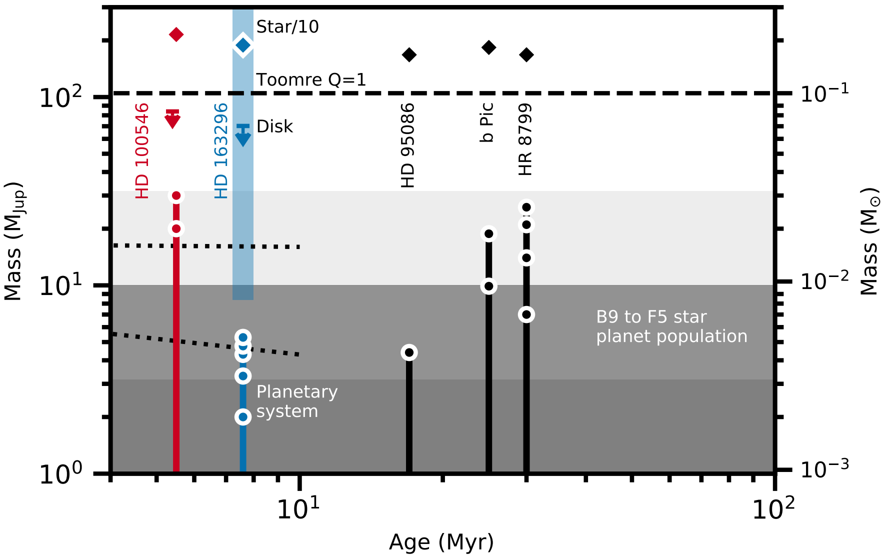

Figure 6.7: Mass of selected disks and planets around B9 to F5 type stars. Vertical lines show the cumulative mass of each planetary system, with dots highlighting planets from the most massive at bottom. Disk gas mass upper limits from HD lines are from this work (HD 163296) and from Kama et al. (2016b, HD 100546). For HD 163296, the range of CO-isotopolog based disk mass estimates is shown by a light blue bar (8×10^{-3} to 5.8×10^{-1} $M_\odot$; references in text). Also shown are the stellar mass divided by 10 and age; the mass limit for a gravitationally unstable disk (dashed line); an extrapolated dust-based disk mass range (dotted lines, Pascucci et al. 2016); and a population density colormap for planets around B9 to F5 type stars (data retrieved from `exoplanets.org` on 2019.07.16; bins contain from bottom to top 7, 6, and 1 planet). See text for individual planet and stellar mass references.

2018); at 145 au with 1.3 $M_{\rm Jup}$ (Liu et al. 2018; Teague et al. 2018); and at 260 au with 2 $M_{\rm Jup}$ (Pinte et al. 2018). Using the HD- and CO-based $M_{\rm gas}$ limits, and taking the combined mass of all published protoplanets in this disk as $\approx 5\,M_{\rm Jup}$, we find the HD 163296 disk has converted 10 to 40 % of its mass into giant planets.

For HD 100546, the planet masses were constrained to be $\approx 10\,M_{\rm Jup}$ at 10 au and $\sim 10\,M_{\rm Jup}$ at 70 au by Pinilla et al. (2015). The mass of the outer planet could be $< 5\,M_{\rm Jup}$ ($> 15\,M_{\rm Jup}$) if it formed very early (late), so we adopt 10 $M_{\rm Jup}$. The HD-based $M_{\rm gas}$ upper limit and the combined mass of the candidate planets yield a lower limit on the disk-to-planet mass conversion efficiency, $\gtrsim 30\,\%$.

Such high disk-to-planet mass conversion efficiencies combined with the presence of several gas giants per star raise the question of whether the planets formed through gravitational instability. Adding the $M_{\rm gas}$ upper limit and combined mass of proposed planets in either disk gives a result close to 0.1 $M_\odot$. This is approximately at the gravitationally unstable limit, so such a formation pathway may be feasible even with the current total mass in the system, although the local Toomre Q varies with radius and may leave the outer disk still far from instability (e.g. Booth et al. 2019).

We also show in Figure 6.7 three somewhat older stars of similar mass (HD 95086,

β Pic, and HR 8799) and their planets; standard disk mass estimates for stars of 1.5 and 3 $M_\odot$ based on $M_{\rm dust}$ relations from Pascucci et al. (2016) and scaled up with $\Delta_{\rm gd} = 100$; and a shaded log-scale histogram of the mass distribution of known planets around early-type stars[1]. Stellar masses are from the GAIA DR2 analysis by Vioque et al. (2018), and from David & Hillenbrand (2015, β Pic) and Stassun et al. (2018, HD 95086). Planet masses for individual systems are plotted as cumulative bars, with the highest-mass planet at the base. We compiled planet data from Teague et al. (2018), Pinte et al. (2018, 2019), Pinilla et al. (2015), Liu et al. (2018), Zhang et al. (2018), Rameau et al. (2013a,b), De Rosa et al. (2016), and Marois et al. (2008, 2010). Individual stellar masses are from Rhee et al. (2007), David & Hillenbrand (2015), Stassun et al. (2018), and Vioque et al. (2018).

The two HD-based disk $M_{\rm gas}$ limits in Fig. 6.7 exceed the combined mass of planets around HR 8799, the most massive known planetary system, by a factor of only three. The disk mass limits are also only a factor of three above combined mass of candidate protoplanets in the HD 100546 disk. Either A-type star disks can, in some cases, convert as much as 25 % or more of their mass into giant planets, or these planetary systems formed at a very early stage, perhaps while the central protostar and massive initial disk were still heavily accreting from the protostellar envelope in which they were embedded. The mass distribution of giant planets around main-sequence A and B stars (Fig. 6.7) is strongly skewed towards lower masses, suggesting that such extreme mass conversion events are either rare, or that the high-mass planetary systems are not stable on timescales beyond a few times 10 Myr.

6.5.2 Observing HD in Herbig disks with SOFIA/HIRMES, SPICA/SAFARI and emphOrigins Space Telescope

In the coming years, several facilities will or may become available for observing HD rotational lines. The HIRMES instrument for SOFIA is currently undergoing commissioning and is due to be delivered at the end of 2020 (Richards et al. 2018). HIRMES will have a high spectral resolution of R $\sim$ 100000, allowing us, for the first time to spectrally resolve the HD 1 - 0 line. The sensitivity of HIRMES will be similar to Herschel/PACS. Our models suggest some Herbig Ae/Be disks will be detectable with this instrument, assuming the necessary hours per source are available.

Figure 6.8 shows the detectability of our disk models with a 10 h SOFIA/HIRMES observation, assuming a distance of 150 pc. Of the flat models (group II disks), only the most massive ($M_{\rm gas} \sim 0.1\,M_\odot$) around stars with the highest stellar luminosity ($L_* \geq 50\,L_\odot$) are detectable. Among the flared models (group I), a larger fraction of disks is observable. All of the disk models $M_{\rm gas} = 0.1$ $M_\odot$ where $\Delta_{\rm gd} > 10$ should be detectable in 10 hrs with SOFIA/HIRMES. For those disks with $M_{\rm gas} = 0.01$ $M_\odot$, all systems with $L_* = 125$ $L_\odot$ and most systems with $L_* = 50$ $L_\odot$ are detectable. To maximize the chance of success, future SOFIA/HIRMES observations should select group I sources with high stellar luminosity.

Based on the stellar luminosities in Table 6.1 there are four group I sources that match these criteria best for SOFIA/HIRMES to detect the HD $1-0$ line: HD 31293 (AB Aur), HD 100546, HD 179218 and HD 97048. For these sources a 10 h observation with SOFIA/HIRMES would improve the current upper limits by a factor 3–10 and constrain the gas-to-dust mass ratio to $\Delta_{\rm gd} \leq 50-100$ if the sources remain undetected.

---

[1] Planets retrieved from `exoplanets.org` on 2019.07.16.

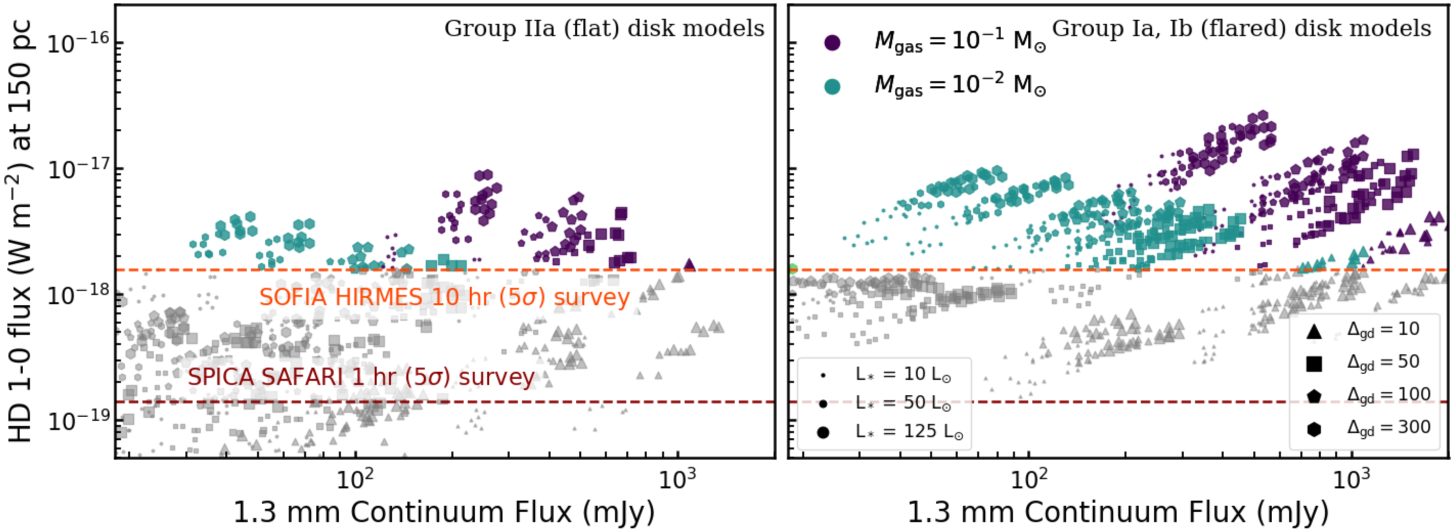

Figure 6.8: Observability of Group Ia,Ib (left) and Group IIa (right) models with SOFIA HIRMES. Colored disk models are detectable ($\geq 5\sigma$) with a 10 hr integration. Dark red dashed line shows the SPICA/SAFARI 1 hr detection limit. The *Origins Space Telescope* 1 hr detection limit ($\sim 1 \times 10^{-20}$ W m^{-2}) lies below the limits of the figure. Note that the fluxes are calculated for a distance of 150 pc.

Beyond SOFIA/HIRMES there are two proposed space missions focusing on far-infrared observations: SPICA/SAFARI and *Origin Space Telescope*. SPICA is one of the competitors for ESA's M5 opportunity, with a resolving power R $\sim$ 3000 and a 5σ 1 hr sensitivity of $1.3 \times 10^{-19}\,\mathrm{W\,m^{-2}}$ at $112\,\mu$m (Audley et al. 2018) . The *Origin Space Telescope* is a NASA mission concept. It would have high spectral resolution (R $\sim$ 43000) and sensitivity ($\sim 1 \times 10^{-20}\,\mathrm{W\,m^{-2}}$ in 1 hr) at $112\,\mu$m (Bonato et al. 2019). Hydrogen deuteride in all Herbig Ae/Be disks, and many T Tauris, within $\sim$ 200 pc will be detectable with these missions. However, both still require final approval and would only become available at the end of the 2020's at the earliest.

6.6 Conclusions

1. We find an overall gas mass upper limit of $M_{\mathrm{gas}} \leq 0.1\,\mathrm{M}_{\odot}$ is a strong conclusion for most of the disks studied. None of the disks are very likely to be strongly gravitationally unstable, although the constraints for HD 142527, HD 144668, HD 179218, and HD 31293 (AB Aur) are weak enough to allow for the possibility.

2. The HD 163296 disk mass is $M_{\mathrm{gas}} \leq 6.7 \times 10^{-2}\,\mathrm{M}_{\odot}$, based on the HD 1 − 0 upper limit. The CO-based literature lower limit is $M_{\mathrm{gas}} = 8 \times 10^{-3}\,\mathrm{M}_{\odot}$, contingent on the true level of gas-phase volatile depletion. The gas-to-dust ratio is thus $12 \leq \Delta_{\mathrm{gd}} \leq 100$, indicating gas dissipation may be proceeding faster than dust removal in this disk.

3. Comparing the HD 163296 and HD 100546 M_{gas} constraints with their protoplanet candidates and the HR 8799 giant planet system, we find that at least some Herbig Ae/Be disks convert the equivalent of $> 25\,\%$ of their present-day mass into giant planets.

4. Near-future SOFIA/HIRMES observations will probe the mass of flaring disks and large flat disks around A-type stars within ≈ 150 pc with $\gtrsim 10$ h integrations. SPICA/SAFARI will be crucial for larger sample studies of M_{gas} in disks. OST, if approved, would further revolutionise the field.

Appendix

6.A HD 1 - 0 fluxes for HD 135344B

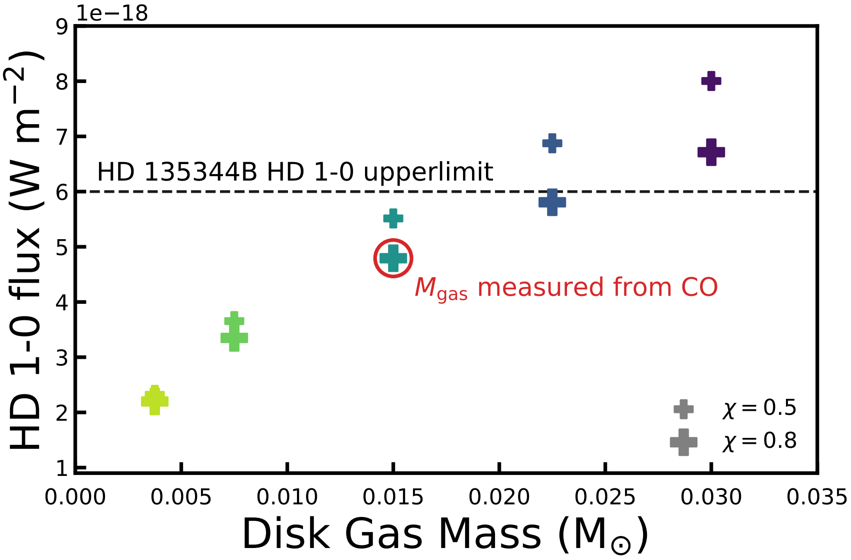

Figure 6.9: Comparing the HD135344B specific models from van der Marel et al. (2016b) to HD 1 - 0 upper limit (Fedele et al. 2013). All models have a dust mass $M_{\rm dust} = 1.3 \times 10^{-4}$ M$_\odot$ (cf. Table 3 in van der Marel et al. 2016b). The red circle shows the gas mass inferred from CO by van der Marel et al. (2016b).

Based on the HD135344B source-specific model from van der Marel et al. (2016a,b), we run a series of 10 models, varying the disk gas mass between 3.75×10^{-3} M$_\odot$ and 3×10^{-2} M$_\odot$. Figure 6.9 compares the HD 1 - 0 line fluxes of these models to the observed upper limit (Table 6.1). From the CO isotopolog observations van der Marel et al. (2016b) infer $M_{\rm gas} = 1.5 \times 10^{-2}$ M$_\odot$. This gas mass is in agreement with the gas mass upper limit inferred from HD 1 - 0, $M_{\rm gas} \leq 2.3 \times 10^{-2}$ M$_\odot$. Note that both gas masses are much lower than 0.1 M$_\odot$, making it highly unlikely that HD 135344B is gravitationally unstable (Section 6.4.6).

6.B HD 2-1 upper limits versus the model fluxes

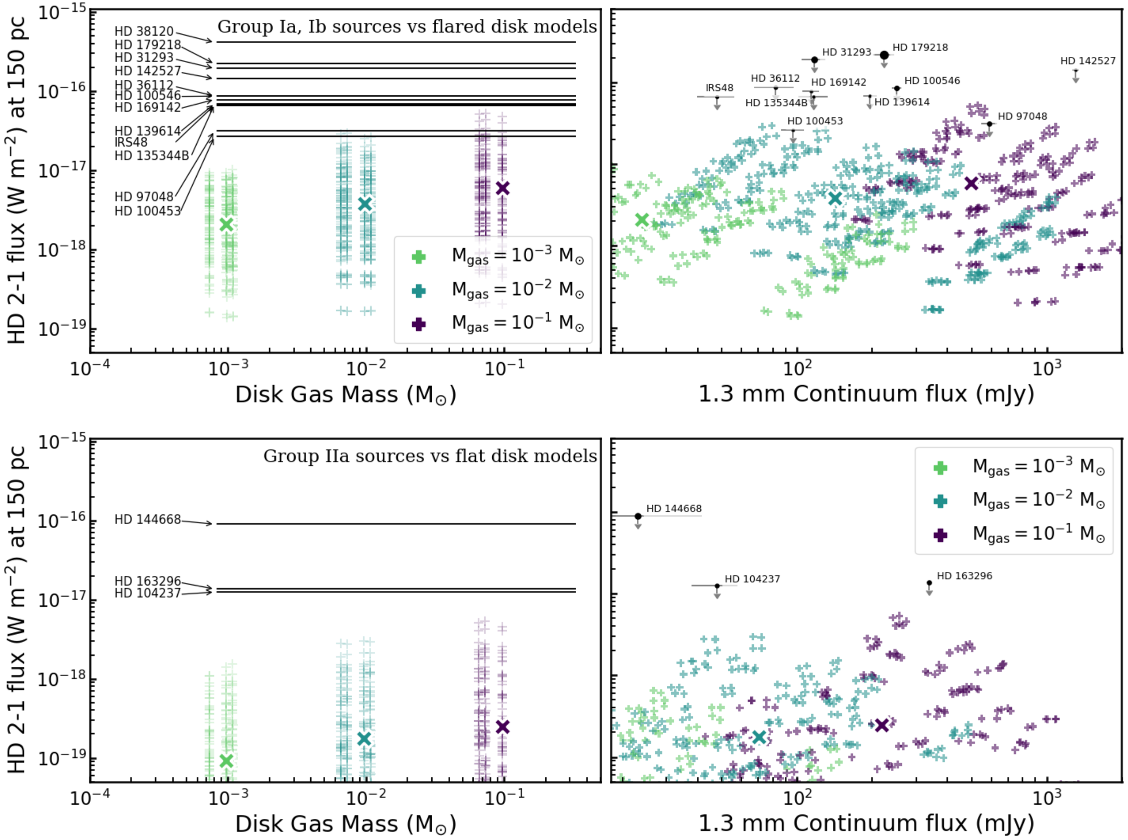

Figure 6.10: Upper limits on HD 56 μm line flux for the sample of Herbig Ae/Be disk systems (black lines) compared with our grid of DALI disk models (crosses). The top panels show the group I sources compared to models with flaring angle $\psi = 0.3$. The bottom panels show the group II sources compared to models with $\psi = 0.0$. **Left:** models are separated based on gas mass. **Right:** HD 2-1 upper limits set against 1.3 mm continuum fluxes for both observations and models.

6.C HD 1-0 line versus 1.3 mm continuum fluxes, showing gas-to-dust ratios and stellar luminosities

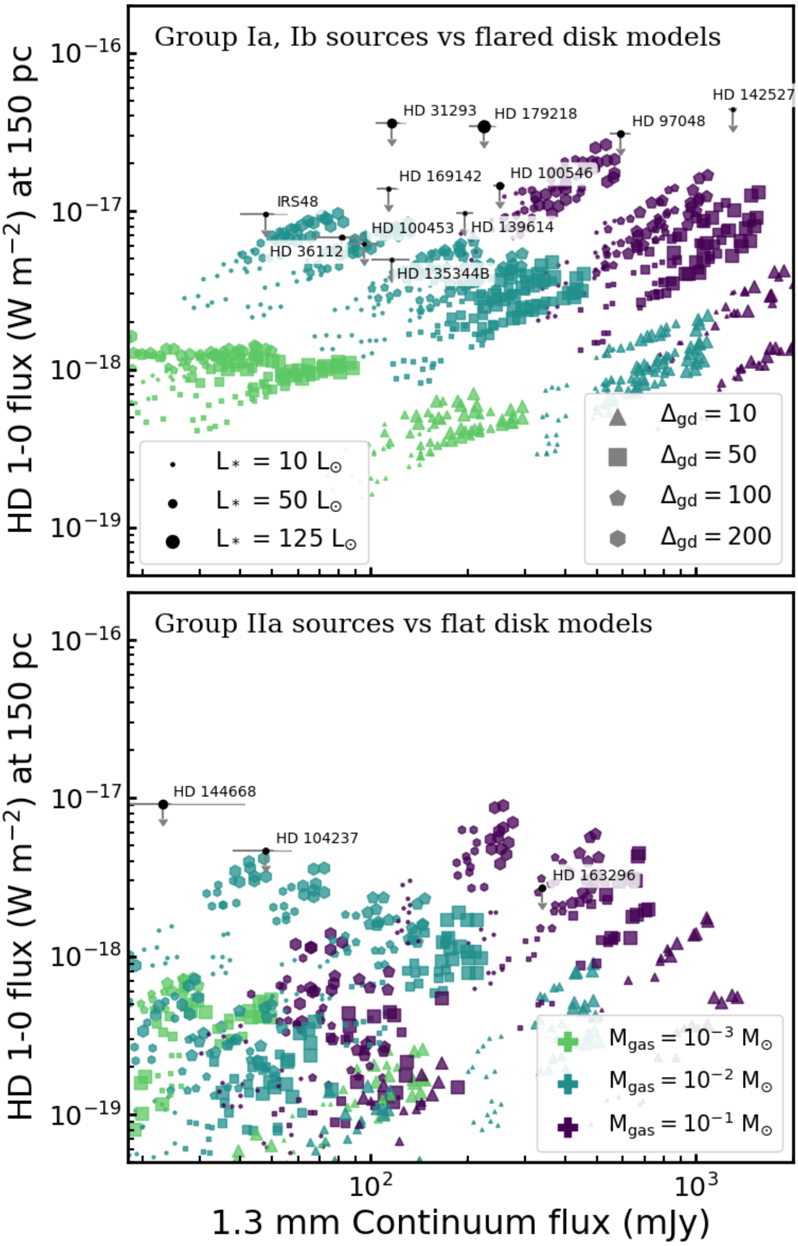

Figure 6.11: HD 1-0 line flux versus 1.3 continuum fluxes for both observations and models. Panels shown here are similar to right panels of Figure 6.3, but also showing the model gas-to-dust mass ratios (marker shape) and stellar luminosities (marker size).

BIBLIOGRAPHY

Adams, F. C., Hollenbach, D., Laughlin, G., & Gorti, U. 2004, ApJ, 611, 360

Aikawa, Y., Umebayashi, T., Nakano, T., & Miyama, S. M. 1997, The Astrophysical Journal Letters, 486, L51

Aikawa, Y., van Zadelhoff, G., van Dishoeck, E. F., & Herbst, E. 2002, A&A, 386, 622

Akimkin, V., Zhukovska, S., Wiebe, D., et al. 2013, ApJ, 766, 8

Alcalá, J., Manara, C., Natta, A., et al. 2017, Astronomy & Astrophysics, 600, A20

Alcalá, J., Natta, A., Manara, C., et al. 2014, Astronomy & Astrophysics, 561, A2

Alcalá, J. M., Manara, C. F., France, K., et al. 2019, A&A, 629, A108

Alexander, R., Pascucci, I., Andrews, S., Armitage, P., & Cieza, L. 2014, in Protostars and Planets VI, ed. H. Beuther, R. S. Klessen, C. P. Dullemond, & T. Henning, 475

ALMA Partnership, Brogan, C. L., Pérez, L. M., et al. 2015, ApJ, 808, L3

André, P., Men'shchikov, A., Bontemps, S., et al. 2010, A&A, 518, L102

Andrews, S. M., Huang, J., Pérez, L. M., et al. 2018a, ApJ, 869, L41

Andrews, S. M., Rosenfeld, K. A., Kraus, A. L., & Wilner, D. J. 2013, The Astrophysical Journal, 771, 129

Andrews, S. M., Terrell, M., Tripathi, A., et al. 2018b, ApJ, 865, 157

Andrews, S. M. & Williams, J. P. 2005, AJ, 631, 1134

Andrews, S. M. & Williams, J. P. 2007, AJ, 671, 1800

Andrews, S. M., Wilner, D., Hughes, A., Qi, C., & Dullemond, C. 2009, AJ, 700, 1502

Andrews, S. M., Wilner, D. J., Espaillat, C., et al. 2011, ApJ, 732, 42

Andrews, S. M., Wilner, D. J., Hughes, A., et al. 2011, The Astrophysical Journal, 744, 162

Andrews, S. M., Wilner, D. J., Zhu, Z., et al. 2016, The Astrophysical Journal Letters, 820, L40

Ansdell, M., Williams, J. P., Manara, C. F., et al. 2017, AJ, 153, 240

Ansdell, M., Williams, J. P., Trapman, L., et al. 2018, ApJ, 859, 21

Ansdell, M., Williams, J. P., van der Marel, N., et al. 2016, The Astrophysical Journal, 828, 46

Antonellini, S., Kamp, I., Lahuis, F., et al. 2016, A&A, 585, A61

Antonellini, S., Kamp, I., Riviere-Marichalar, P., et al. 2015, A&A, 582, A105

Armitage, P. J. 2015, ArXiv e-prints [`arXiv:1509.06382`]

Armitage, P. J. 2019, Saas-Fee Advanced Course, 45, 1

Audard, M., Ábrahám, P., Dunham, M. M., et al. 2014, in Protostars and Planets VI, ed. H. Beuther, R. S. Klessen, C. P. Dullemond, & T. Henning, 387

Audley, M. D., de Lange, G., Gao, J.-R., et al. 2018, in Society of Photo-Optical Instrumentation Engineers (SPIE) Conference Series, Vol. 10708, Proc. SPIE, 107080K

Avenhaus, H., Quanz, S. P., Garufi, A., et al. 2018, ApJ, 863, 44

Bai, X.-N. 2017, ApJ, 845, 75

Bai, X.-N. & Stone, J. M. 2013, ApJ, 769, 76

Bailer-Jones, C. A. L., Rybizki, J., Fouesneau, M., Mantelet, G., & Andrae, R. 2018, AJ, 156, 58

Balbus, S. A. & Hawley, J. F. 1991, ApJ, 376, 214

Balbus, S. A. & Hawley, J. F. 1998, Reviews of Modern Physics, 70, 1

Balbus, S. A. & Papaloizou, J. C. B. 1999, ApJ, 521, 650

Barenfeld, S. A., Carpenter, J. M., Ricci, L., & Isella, A. 2016, The Astrophysical Journal, 827, 142

Barenfeld, S. A., Carpenter, J. M., Sargent, A. I., Isella, A., & Ricci, L. 2017, The Astrophysical Journal, 851, 85

Barnard, E. E. 1919, ApJ, 49, 1

Beckwith, S. V. W. & Sargent, A. I. 1991, ApJ, 381, 250

Beckwith, S. V. W., Sargent, A. I., Chini, R. S., & Guesten, R. 1990, AJ, 99, 924

Benz, W., Ida, S., Alibert, Y., Lin, D., & Mordasini, C. 2014, in Protostars and Planets VI, ed. H. Beuther, R. S. Klessen, C. P. Dullemond, & T. Henning, 691

Bergin, E., Cleeves, L. I., Crockett, N., & Blake, G. 2014, Faraday discussions, 168, 61

Bergin, E., Hogerheijde, M., Brinch, C., et al. 2010, Astronomy & Astrophysics, 521, L33

Bergin, E., Pontoppidan, K., Bradford, C., et al. 2019, BAAS, 51, 222

Bergin, E. A., Aikawa, Y., Blake, G. A., & van Dishoeck, E. F. 2007, in Protostars and Planets V, ed. B. Reipurth, D. Jewitt, & K. Keil, 751

Bergin, E. A., Cleeves, L. I., Gorti, U., et al. 2013, Nature, 493, 644

Bergin, E. A., Du, F., Cleeves, L. I., et al. 2016, ApJ, 831, 101

Bergner, J. B., Guzmán, V. G., Öberg, K. I., Loomis, R. A., & Pegues, J. 2018, ApJ, 857, 69

Béthune, W., Lesur, G., & Ferreira, J. 2017, A&A, 600, A75

Birnstiel, T. & Andrews, S. M. 2013, The Astrophysical Journal, 780, 153

Birnstiel, T., Andrews, S. M., Pinilla, P., & Kama, M. 2015, ApJ, 813, L14

Birnstiel, T., Klahr, H., & Ercolano, B. 2012, Astronomy & Astrophysics, 539, A148

Birnstiel, T., Ricci, L., Trotta, F., et al. 2010, Astronomy & Astrophysics, 516, L14

Bjerkeli, P., van der Wiel, M. H. D., Harsono, D., Ramsey, J. P., & Jørgensen, J. K. 2016, Nature, 540, 406

Blandford, R. D. & Payne, D. G. 1982, MNRAS, 199, 883

Blum, J., Gundlach, B., Mühle, S., & Trigo-Rodriguez, J. M. 2014, Icarus, 235, 156

Blum, J. & Wurm, G. 2008, ARA&A, 46, 21

Boehler, Y., Weaver, E., Isella, A., et al. 2017, ApJ, 840, 60

Bok, B. J. 1948, Dimensions and Masses of Dark Nebulae, Vol. 7, 53

Bonato, M., De Zotti, G., Leisawitz, D., et al. 2019, PASA, 36, e017

Boneberg, D. M., Panić, O., Haworth, T. J., Clarke, C. J., & Min, M. 2016, MNRAS, 461, 385

Bontemps, S., Motte, F., Csengeri, T., & Schneider, N. 2010, A&A, 524, A18

Booth, A. S., Walsh, C., Ilee, J. D., et al. 2019, arXiv e-prints, arXiv:1908.05045

Booth, R. A., Clarke, C. J., Madhusudhan, N., & Ilee, J. D. 2017, MNRAS, 469, 3994

Borucki, W. J., Koch, D. G., Basri, G., et al. 2011, ApJ, 736, 19

Bosman, A. D., Walsh, C., & van Dishoeck, E. F. 2018, A&A, 618, A182

Brauer, F., Henning, T., & Dullemond, C. P. 2008, A&A, 487, L1

Brauer, R., Wolf, S., Reissl, S., & Ober, F. 2017, A&A, 601, A90

Brinch, C. & Hogerheijde, M. R. 2010, A&A, 523, A25

Brown, A., Vallenari, A., Prusti, T., et al. 2018, arXiv preprint arXiv:1804.09365

Bruderer, S. 2013, A&A, 559, A46

Bruderer, S., Doty, S. D., & Benz, A. O. 2009, ApJS, 183, 179

Bruderer, S., van Dishoeck, E. F., Doty, S. D., & Herczeg, G. J. 2012, A&A, 541, A91

Buser, R. & Kurucz, R. L. 1992, A&A, 264, 557

Cabrera, J., Csizmadia, S., Lehmann, H., et al. 2014, ApJ, 781, 18

Cambrésy, L. 1999, A&A, 345, 965

Carmona, A., van der Plas, G., van den Ancker, M. E., et al. 2011, A&A, 533, A39

Carney, M. T., Hogerheijde, M. R., Loomis, R. A., et al. 2017, A&A, 605, A21

Carpenter, J. M., Mamajek, E. E., Hillenbrand, L. A., & Meyer, M. R. 2006, ApJ, 651, L49

Cassan, A., Kubas, D., Beaulieu, J.-P., et al. 2012, Nature, 481, 167–169

Cazzoletti, P., Manara, C. F., Baobab Liu, H., et al. 2019, A&A, 626, A11

Cazzoletti, P., van Dishoeck, E. F., Visser, R., Facchini, S., & Bruderer, S. 2018, A&A, 609, A93

Chaparro Molano, G. & Kamp, I. 2012, A&A, 547, A7

Chiang, E. I. & Goldreich, P. 1997, ApJ, 490, 368

Ciesla, F. J. & Cuzzi, J. N. 2006, Icarus, 181, 178

Cieza, L. A., Ruíz-Rodríguez, D., Hales, A., et al. 2019, MNRAS, 482, 698

Cieza, L. A., Ruíz-Rodríguez, D., Perez, S., et al. 2018, MNRAS, 474, 4347

Cleeves, L. I., Öberg, K. I., Wilner, D. J., et al. 2016, ApJ, 832, 110

Costigan, G., Vink, J. S., Scholz, A., Ray, T., & Testi, L. 2014, MNRAS, 440, 3444

Cox, E. G., Harris, R. J., Looney, L. W., et al. 2017, ApJ, 851, 83

Cridland, A. J., Bosman, A. D., & van Dishoeck, E. F. 2020, A&A, 635, A68

Cuppen, H. M., van Dishoeck, E. F., Herbst, E., & Tielens, A. G. G. M. 2009, A&A, 508, 275

D'Alessio, P., Cantö, J., Calvet, N., & Lizano, S. 1998, ApJ, 500, 411

Damiani, F., Prisinzano, L., Pillitteri, I., Micela, G., & Sciortino, S. 2019, A&A, 623, A112

David, T. J. & Hillenbrand, L. A. 2015, ApJ, 804, 146

de Boer, J., Salter, G., Benisty, M., et al. 2016, A&A, 595, A114

de Bruijne, J. H. J. 1999, MNRAS, 310, 585

de Gregorio-Monsalvo, I., Ménard, F., Dent, W., et al. 2013, A&A, 557, A133

De Rosa, R. J., Rameau, J., Patience, J., et al. 2016, ApJ, 824, 121

de Valon, A., Dougados, C., Cabrit, S., et al. 2020, A&A, 634, L12 de Zeeuw, P. T., Hoogerwerf, R., de Bruijne, J. H. J., Brown, A. G. A., & Blaauw, A. 1999, AJ, 117, 354

Dodson-Robinson, S. E., Evans, II, N. J., Ramos, A., Yu, M., & Willacy, K. 2018, ArXiv e-prints [`arXiv:1811.05934`]

Draine, B. 2006, AJ, 636, 1114

Draine, B. T. 2003, ARA&A

Du, F. & Bergin, E. A. 2014, ApJ, 792, 2

Du, F., Bergin, E. A., & Hogerheijde, M. R. 2015, ApJ, 807, L32

Dubrulle, B., Morfill, G., & Sterzik, M. 1995, Icarus, 114, 237

Dullemond, C. P., Birnstiel, T., Huang, J., et al. 2018, ApJ, 869, L46

Dullemond, C. P. & Dominik, C. 2004, A&A, 421, 1075

Dullemond, C. P. & Dominik, C. 2005, A&A, 434, 971

Dullemond, C. P., Isella, A., Andrews, S. M., Skobleva, I., & Dzyurkevich, N. 2020, A&A, 633, A137

Dullemond, C. P., Juhasz, A., Pohl, A., et al. 2012, RADMC-3D: A multi-purpose radiative transfer tool

Dunham, M. M., Stutz, A. M., Allen, L. E., et al. 2014, in Protostars and Planets VI, ed. H. Beuther, R. S. Klessen, C. P. Dullemond, & T. Henning, 195

Dutrey, A., Guilloteau, S., Prato, L., et al. 1998, Astronomy and Astrophysics, 338, L63

Dutrey, A., Semenov, D., Chapillon, E., et al. 2014, Protostars and Planets VI, 317

Eistrup, C., Walsh, C., & van Dishoeck, E. F. 2016, A&A, 595, A83

Eistrup, C., Walsh, C., & van Dishoeck, E. F. 2018, A&A, 613, A14

Ellerbroek, L. E., Benisty, M., Kraus, S., et al. 2015, A&A, 573, A77

Ercolano, B. & Pascucci, I. 2017, Royal Society Open Science, 4, 170114

Facchini, S., Birnstiel, T., Bruderer, S., & van Dishoeck, E. F. 2017, A&A, 605, A16

Facchini, S., Clarke, C. J., & Bisbas, T. G. 2016, MNRAS, 457, 3593

Facchini, S., van Dishoeck, E. F., Manara, C. F., et al. 2019, A&A, 626, L2

Fairlamb, J. R., Oudmaijer, R. D., Mendigutía, I., Ilee, J. D., & van den Ancker, M. E. 2015, MNRAS, 453, 976

Favre, C., Cleeves, L. I., Bergin, E. A., Qi, C., & Blake, G. A. 2013, ApJ, 776, L38

Fedele, D., Bruderer, S., van Dishoeck, E. F., et al. 2013, A&A, 559, A77

Fedele, D., Carney, M., Hogerheijde, M. R., et al. 2017, A&A, 600, A72

Fedele, D., van Dishoeck, E. F., Kama, M., Bruderer, S., & Hogerheijde, M. R. 2016, A&A, 591, A95

Ferreira, J., Dougados, C., & Cabrit, S. 2006, A&A, 453, 785

Flaherty, K., Hughes, A. M., Simon, J. B., et al. 2020, ApJ, 895, 109

Flaherty, K. M., Hughes, A. M., Rose, S. C., et al. 2017, ApJ, 843, 150

Flaherty, K. M., Hughes, A. M., Rosenfeld, K. A., et al. 2015, ApJ, 813, 99

Folsom, C. P., Bagnulo, S., Wade, G. A., et al. 2012, MNRAS, 422, 2072

Foreman-Mackey, D., Hogg, D. W., Lang, D., & Goodman, J. 2013, Publications of the Astronomical Society of the Pacific, 125, 306

Frank, A., Ray, T. P., Cabrit, S., et al. 2014, in Protostars and Planets VI, ed. H. Beuther, R. S. Klessen, C. P. Dullemond, & T. Henning, 451

Frasca, A., Biazzo, K., Alcalá, J. M., et al. 2017, A&A, 602, A33

Fromang, S. & Papaloizou, J. 2006, A&A, 452, 751

Gärtner, S., Gundlach, B., Headen, T. F., et al. 2017, ApJ, 848, 96

Garufi, A., Avenhaus, H., Pérez, S., et al. 2020, A&A, 633, A82

Gillon, M., Triaud, A. H. M. J., Demory, B.-O., et al. 2017, Nature, 542, 456

Ginski, C., Stolker, T., Pinilla, P., et al. 2016, A&A, 595, A112

Goodman, A. A., Benson, P. J., Fuller, G. A., & Myers, P. C. 1993, ApJ, 406, 528

Gorti, U. & Hollenbach, D. 2009, ApJ, 690, 1539

Gressel, O., Turner, N. J., Nelson, R. P., & McNally, C. P. 2015, ApJ, 801, 84

Guilloteau, S. & Dutrey, A. 1998, Astronomy and Astrophysics, 339, 467

Guilloteau, S., Dutrey, A., Piétu, V., & Boehler, Y. 2011, Astronomy & Astrophysics, 529, A105

Guilloteau, S., Simon, M., Piétu, V., et al. 2014, A&A, 567, A117

Gundlach, B., Kilias, S., Beitz, E., & Blum, J. 2011, Icarus, 214, 717

Güttler, C., Blum, J., Zsom, A., Ormel, C. W., & Dullemond, C. P. 2010, A&A, 513, A56

Habing, H. J. 1968, Bull. Astron. Inst. Netherlands, 19, 421

Hales, A. S., De Gregorio-Monsalvo, I., Montesinos, B., et al. 2014, AJ, 148, 47

Harries, T. 2014, TORUS: Radiation transport and hydrodynamics code

Harries, T. J., Haworth, T. J., Acreman, D., Ali, A., & Douglas, T. 2019, Astronomy and Computing, 27, 63

Harries, T. J., Monnier, J. D., Symington, N. H., & Kurosawa, R. 2004, MNRAS, 350, 565

Harsono, D., Bjerkeli, P., van der Wiel, M. H. D., et al. 2018, Nature Astronomy, 2, 646

Hartmann, L., Calvet, N., Gullbring, E., & D'Alessio, P. 1998, ApJ, 495, 385

Hartmann, L. & Kenyon, S. J. 1996, ARA&A, 34, 207

Haworth, T. J., Clarke, C. J., Rahman, W., Winter, A. J., & Facchini, S. 2018, MNRAS, 481, 452

Haworth, T. J., Facchini, S., Clarke, C. J., & Cleeves, L. I. 2017, MNRAS, 468, L108

Heays, A. N., Bosman, A. D., & van Dishoeck, E. F. 2017, A&A, 602, A105

Helling, C., Woitke, P., Rimmer, P. B., et al. 2014, Life, 4, 142

Henning, T. & Semenov, D. 2013, Chemical Reviews, 113, 9016

Herbig, G. H. 1977, ApJ, 217, 693

Herbst, E. & Klemperer, W. 1973, ApJ, 185, 505

Hildebrand, R. H. 1983, QJRAS, 24, 267

Hill, T., Motte, F., Didelon, P., et al. 2011, A&A, 533, A94

Hillenbrand, L. A. & White, R. J. 2004, ApJ, 604, 741

Huang, J., Andrews, S. M., Dullemond, C. P., et al. 2018, ApJ, 869, L42

Hughes, A., Wilner, D., Qi, C., & Hogerheijde, M. 2008, The Astrophysical Journal, 678, 1119

Isella, A., Guidi, G., Testi, L., et al. 2016, Phys. Rev. Lett., 117, 251101

Isella, A., Testi, L., Natta, A., et al. 2007, A&A, 469, 213

Jones, M. G., Pringle, J. E., & Alexander, R. D. 2012, MNRAS, 419, 925

Kama, M., Bruderer, S., Carney, M., et al. 2016a, A&A, 588, A108

Kama, M., Bruderer, S., van Dishoeck, E. F., et al. 2016b, A&A, 592, A83

Kama, M., Folsom, C. P., & Pinilla, P. 2015, A&A, 582, L10

Kama, M., Trapman, L., Fedele, D., et al. 2020, A&A, 634, A88

Kamp, I., Thi, W. F., Woitke, P., et al. 2017, A&A, 607, A41

Kamp, I., Tilling, I., Woitke, P., Thi, W. F., & Hogerheijde, M. 2010, A&A, 510, A18

Kenyon, S. J. & Hartmann, L. 1987, ApJ, 323, 714

Kimura, S. S. & Tsuribe, T. 2012, PASJ, 64, 116

Klahr, H. H. & Henning, T. 1997, Icarus, 128, 213

Königl, A. & Salmeron, R. 2011, The Effects of Large-Scale Magnetic Fields on Disk Formation and Evolution, ed. P. J. V. Garcia, 283–352

Könyves, V., André, P., Men'shchikov, A., et al. 2010, A&A, 518, L106

Kothe, S., Güttler, C., & Blum, J. 2010, ApJ, 725, 1242

Kretke, K. A. & Lin, D. N. C. 2007, The Astrophysical Journal, 664, L55

Krijt, S., Bosman, A. D., Zhang, K., et al. 2020, CO Depletion in Protoplanetary Disks: A Unified Picture Combining Physical Sequestration and Chemical Processing

Krijt, S. & Kama, M. 2014, A&A, 566, L2

Krijt, S., Ormel, C. W., Dominik, C., & Tielens, A. G. G. M. 2015, A&A, 574, A83

Krijt, S., Schwarz, K. R., Bergin, E. A., & Ciesla, F. J. 2018, ApJ, 864, 78

Kurtovic, N. T., Pérez, L. M., Benisty, M., et al. 2018, ApJ, 869, L44

Lacy, J., Knacke, R., Geballe, T., & Tokunaga, A. 1994, ApJ, 428, L69

Lagage, P.-O., Doucet, C., Pantin, E., et al. 2006, Science, 314, 621

Li, Z. Y., Banerjee, R., Pudritz, R. E., et al. 2014, in Protostars and Planets VI, ed. H. Beuther, R. S. Klessen, C. P. Dullemond, & T. Henning, 173

Liu, S.-F., Jin, S., Li, S., Isella, A., & Li, H. 2018, ApJ, 857, 87

Lodato, G., Scardoni, C. E., Manara, C. F., & Testi, L. 2017, MNRAS, 472, 4700

Lodders, K. 2003, ApJ, 591, 1220

Lommen, D., Wright, C. M., Maddison, S. T., et al. 2007, A&A, 462, 211

Long, F., Herczeg, G. J., Harsono, D., et al. 2019, ApJ, 882, 49

Long, F., Herczeg, G. J., Pascucci, I., et al. 2017, The Astrophysical Journal, 844, 99

Long, F., Pinilla, P., Herczeg, G. J., et al. 2018, ApJ, 869, 17

Loomis, R. A., Cleeves, L. I., Öberg, K. I., et al. 2018, ApJ, 859, 131

Luhman, K. L. & Mamajek, E. E. 2012, ApJ, 758, 31

Lynden-Bell, D. & Pringle, J. E. 1974, MNRAS, 168, 603

Lyra, W., Johansen, A., Zsom, A., Klahr, H., & Piskunov, N. 2009, A&A, 497, 869

Maaskant, K. M., Honda, M., Waters, L. B. F. M., et al. 2013, A&A, 555, A64

Maaskant, K. M., Min, M., Waters, L. B. F. M., & Tielens, A. G. G. M. 2014, A&A, 563, A78

Manara, C. F., Morbidelli, A., & Guillot, T. 2018, A&A, 618, L3

Manara, C. F., Natta, A., Rosotti, G. P., et al. 2020, arXiv e-prints, arXiv:2004.14232

Manara, C. F., Rosotti, G., Testi, L., et al. 2016a, A&A, 591, L3

Manara, C. F., Rosotti, G., Testi, L., et al. 2016b, A&A, 591, L3

Manara, C. F., Testi, L., Herczeg, G. J., et al. 2017, A&A, 604, A127

Mannings, V. & Sargent, A. I. 2000, The Astrophysical Journal, 529, 391

Maret, S., Maury, A. J., Belloche, A., et al. 2020, arXiv e-prints, arXiv:2001.06355

Marois, C., Macintosh, B., Barman, T., et al. 2008, Science, 322, 1348

Marois, C., Zuckerman, B., Konopacky, Q. M., Macintosh, B., & Barman, T. 2010, Nature, 468, 1080

Mathis, J. S., Rumpl, W., & Nordsieck, K. H. 1977, ApJ, 217, 425

Maury, A. J., André, P., Men'shchikov, A., Könyves, V., & Bontemps, S. 2011, A&A, 535, A77

Maury, A. J., André, P., Testi, L., et al. 2019, A&A, 621, A76

Mayor, M. & Queloz, D. 1995, Nature, 378, 355

McClure, M. K., Bergin, E. A., Cleevs, L. I., et al. 2016, AJ

McKee, C. F. & Ostriker, E. C. 2007, ARA&A, 45, 565

Meeus, G., Salyk, C., Bruderer, S., et al. 2013, A&A, 559, A84

Meeus, G., Waters, L. B. F. M., Bouwman, J., et al. 2001, A&A, 365, 476

Megier, A., Strobel, A., Galazutdinov, G. A., & Krełowski, J. 2009, A&A, 507, 833

Menu, J., Van Boekel, R., Henning, T., et al. 2014, Astronomy & Astrophysics, 564, A93

Merín, B., Jørgensen, J., Spezzi, L., et al. 2008, ApJS, 177, 551

Min, M., Dullemond, C. P., Dominik, C., de Koter, A., & Hovenier, J. W. 2009, A&A, 497, 155

Miotello, A., Bruderer, S., & van Dishoeck, E. F. 2014, A&A, 572, A96

Miotello, A., Facchini, S., van Dishoeck, E. F., & Bruderer, S. 2018, A&A, 619, A113

Miotello, A., Facchini, S., van Dishoeck, E. F., et al. 2019, A&A, 631, A69

Miotello, A., Robberto, M., Potenza, M. A. C., & Ricci, L. 2012, ApJ, 757, 78

Miotello, A., van Dishoeck, E., Williams, J., et al. 2017, Astronomy & Astrophysics, 599, A113

Miotello, A., van Dishoeck, E. F., Kama, M., & Bruderer, S. 2016, Astronomy & Astrophysics, 594, A85

Miville-Deschênes, M. A., Martin, P. G., Abergel, A., et al. 2010, A&A, 518, L104

Molyarova, T., Akimkin, V., Semenov, D., et al. 2017, ApJ, 849, 130

Mordasini, C. 2018, Planetary Population Synthesis, 143

Morton, T. D., Bryson, S. T., Coughlin, J. L., et al. 2016, ApJ, 822, 86

Mulders, G. D. & Dominik, C. 2012, A&A, 539, A9

Murillo, N. M., Lai, S.-P., Bruderer, S., Harsono, D., & van Dishoeck, E. F. 2013, A&A, 560, A103

Muto, T., Tsukagoshi, T., Momose, M., et al. 2015, PASJ, 67, 122

Najita, J. R. & Bergin, E. A. 2018, ApJ, 864, 168

Najita, J. R. & Kenyon, S. J. 2014, MNRAS, 445, 3315

Nakagawa, T., Shibai, H., Onaka, T., et al. 2014, in SPIE Astronomical Telescopes+ Instrumentation, International Society for Optics and Photonics, 91431I–91431I

Nakamura, F. & Li, Z.-Y. 2008, ApJ, 687, 354

Natta, A., Testi, L., Neri, R., Shepherd, D. S., & Wilner, D. J. 2004, A&A, 416, 179

Öberg, K. I., Murray-Clay, R., & Bergin, E. A. 2011, ApJ, 743, L16

Palmeirim, P., André, P., Kirk, J., et al. 2013, A&A, 550, A38

Panić, O., Hogerheijde, M. R., Wilner, D., & Qi, C. 2008, A&A, 491, 219

Pantin, E., Bouwman, J., & Lagage, P. O. 2005, A&A, 437, 525

Pascucci, I., Herczeg, G., Carr, J., & Bruderer, S. 2013, AJ, 779, 178

Pascucci, I., Testi, L., Herczeg, G., et al. 2016, The Astrophysical Journal, 831, 125

Paszun, D. & Dominik, C. 2009, A&A, 507, 1023

Pecaut, M. J., Mamajek, E. E., & Bubar, E. J. 2012, ApJ, 746, 154

Peretto, N., André, P., Könyves, V., et al. 2012, A&A, 541, A63

Pérez, L. M., Carpenter, J. M., Chandler, C. J., et al. 2012, The Astrophysical Journal Letters, 760, L17

Pérez, L. M., Chandler, C. J., Isella, A., et al. 2015, The Astrophysical Journal, 813, 41

Piétu, V., Dutrey, A., & Guilloteau, S. 2007, Astronomy & Astrophysics, 467, 163

Piétu, V., Guilloteau, S., Di Folco, E., Dutrey, A., & Boehler, Y. 2014, Astronomy & Astrophysics, 564, A95

Piétu, V., Guilloteau, S., & Dutrey, A. 2005, A&A, 443, 945

Pilbratt, G. L., Riedinger, J. R., Passvogel, T., et al. 2010a, A&A, 518, L1

Pilbratt, G. L., Riedinger, J. R., Passvogel, T., et al. 2010b, A&A, 518, L1

Pinilla, P., Birnstiel, T., Ricci, L., et al. 2012, A&A, 538, A114

Pinilla, P., Birnstiel, T., & Walsh, C. 2015, A&A, 580, A105

Pinilla, P., Tazzari, M., Pascucci, I., et al. 2018, ApJ, 859, 32

Pinte, C., Ménard, F., Duchêne, G., & Bastien, P. 2006, A&A, 459, 797

Pinte, C., Ménard, F., Duchêne, G., et al. 2018, A&A, 609, A47

Pinte, C., van der Plas, G., Menard, F., et al. 2019, arXiv e-prints, arXiv:1907.02538

Poglitsch, A., Waelkens, C., Geis, N., et al. 2010a, A&A, 518, L2

Poglitsch, A., Waelkens, C., Geis, N., et al. 2010b, A&A, 518, L2

Pontoppidan, K. M., Blake, G. A., & Smette, A. 2011, ApJ, 733, 84

Pontoppidan, K. M., Meijerink, R., Dullemond, C. P., & Blake, G. A. 2009, ApJ, 704, 1482

Powell, D., Murray-Clay, R., Pérez, L. M., Schlichting, H. E., & Rosenthal, M. 2019, ApJ, 878, 116

Preibisch, T., Brown, A. G. A., Bridges, T., Guenther, E., & Zinnecker, H. 2002, AJ, 124, 404

Preibisch, T. & Mamajek, E. 2008, The Nearest OB Association: Scorpius-Centaurus (Sco OB2), Vol. 5, 235

Pringle, J. E. 1981, ARA&A, 19, 137

Prodanović, T., Steigman, G., & Fields, B. D. 2010, MNRAS, 406, 1108

Qi, C., Öberg, K. I., Andrews, S. M., et al. 2015, ApJ, 813, 128

Qi, C., Öberg, K. I., Espaillat, C. C., et al. 2019, ApJ, 882, 160

Qi, C., Öberg, K. I., Wilner, D. J., et al. 2013, Science, 341, 630

Rameau, J., Chauvin, G., Lagrange, A. M., et al. 2013a, ApJ, 772, L15

Rameau, J., Chauvin, G., Lagrange, A. M., et al. 2013b, ApJ, 779, L26

Reipurth, B., Clarke, C. J., Boss, A. P., et al. 2014, in Protostars and Planets VI, ed. H. Beuther, R. S. Klessen, C. P. Dullemond, & T. Henning, 267

Reissl, S., Wolf, S., & Brauer, R. 2016, A&A, 593, A87

Rhee, J. H., Song, I., Zuckerman, B., & McElwain, M. 2007, ApJ, 660, 1556

Ricci, L., Testi, L., Natta, A., et al. 2010, A&A, 512, A15

Richards, S. N., Moseley, S. H., Stacey, G., et al. 2018, arXiv preprint arXiv:1811.11313

Riols, A. & Lesur, G. 2018, A&A, 617, A117

Robitaille, T. P. 2011, A&A, 536, A79

Rodmann, J., Henning, T., Chandler, C. J., Mundy, L. G., & Wilner, D. J. 2006, A&A, 446, 211

Rosenfeld, K. A., Andrews, S. M., Hughes, A. M., Wilner, D. J., & Qi, C. 2013, ApJ, 774, 16

Rosotti, G. P., Benisty, M., Juhász, A., et al. 2020, MNRAS, 491, 1335

Rosotti, G. P., Booth, R. A., Tazzari, M., et al. 2019a, MNRAS, 486, L63

Rosotti, G. P., Clarke, C. J., Manara, C. F., & Facchini, S. 2017, MNRAS, 468, 1631

Rosotti, G. P., Tazzari, M., Booth, R. A., et al. 2019b, MNRAS, 486, 4829

Ruíz-Rodríguez, D., Cieza, L. A., Williams, J. P., et al. 2018, MNRAS, 478, 3674

Sakai, N., Sakai, T., Hirota, T., et al. 2014, Nature, 507, 78

Salinas, V. N., Hogerheijde, M. R., Bergin, E. A., et al. 2016, Astronomy & Astrophysics, 591, A122

Salyk, C., Herczeg, G. J., Brown, J. M., et al. 2013, ApJ, 769, 21

Schaefer, G. H., Dutrey, A., Guilloteau, S., Simon, M., & White, R. J. 2009, ApJ, 701, 698

Schaller, G., Schaerer, D., Meynet, G., & Maeder, A. 1992, A&AS, 96, 269

Schwarz, K. R., Bergin, E. A., Cleeves, L. I., et al. 2016, AJ, 823, 91

Schwarz, K. R., Bergin, E. A., Cleeves, L. I., et al. 2018, ApJ, 856, 85

Schwarz, K. R., Bergin, E. A., Cleeves, L. I., et al. 2019, ApJ, 877, 131

Semenov, D. & Wiebe, D. 2011, ApJS, 196, 25

Shakura, N. I. & Sunyaev, R. A. 1973, A&A, 24, 337

Simon, M., Guilloteau, S., Di Folco, E., et al. 2017, ApJ, 844, 158

Stassun, K. G., Oelkers, R. J., Pepper, J., et al. 2018, AJ, 156, 102

Stevenson, D. J. & Lunine, J. I. 1988, Icarus, 75, 146

Suzuki, D., Bennett, D., Sumi, T., et al. 2016, The Astrophysical Journal, 833, 145

Suzuki, T. K. & Inutsuka, S.-i. 2009, ApJ, 691, L49

Tabone, B., Cabrit, S., Bianchi, E., et al. 2017, A&A, 607, L6

Tabone, B., Cabrit, S., Pineau des Forêts, G., et al. 2020, arXiv e-prints, arXiv:2004.08804

Tafalla, M. & Hacar, A. 2015, A&A, 574, A104

Takeuchi, T. & Lin, D. N. C. 2002, ApJ, 581, 1344

Tazzari, M., Beaujean, F., & Testi, L. 2018, MNRAS, 476, 4527

Tazzari, M., Testi, L., Ercolano, B., et al. 2016, Astronomy & Astrophysics, 588, A53

Tazzari, M., Testi, L., Natta, A., et al. 2017, Astronomy & Astrophysics, 606, A88

Teague, R., Bae, J., & Bergin, E. A. 2019, Nature, 574, 378

Teague, R., Bae, J., Bergin, E. A., Birnstiel, T., & Foreman-Mackey, D. 2018, ApJ, 860, L12

Teague, R., Guilloteau, S., Semenov, D., et al. 2016, A&A, 592, A49

Testi, L., Natta, A., Shepherd, D. S., & Wilner, D. J. 2003, A&A, 403, 323

Thi, W. F., van Dishoeck, E. F., Blake, G. A., et al. 2001, ApJ, 561, 1074

Thi, W. F., Woitke, P., & Kamp, I. 2011, MNRAS, 412, 711

Tilling, I., Woitke, P., Meeus, G., et al. 2012, A&A, 538, A20

Tobin, J. J., Sheehan, P. D., Megeath, S. T., et al. 2020, ApJ, 890, 130

Toomre, A. 1964, ApJ, 139, 1217

Trapman, L., Facchini, S., Hogerheijde, M. R., van Dishoeck, E. F., & Bruderer, S. 2019, A&A, 629, A79

Trapman, L., Miotello, A., Kama, M., van Dishoeck, E. F., & Bruderer, S. 2017, A&A, 605, A69

Trapman, L., Rosotti, G., Bosman, A. D., Hogerheijde, M. R., & van Dishoeck, E. F. 2020, A&A, 640, A5

Tripathi, A., Andrews, S. M., Birnstiel, T., et al. 2018, ApJ, 861, 64

Tripathi, A., Andrews, S. M., Birnstiel, T., & Wilner, D. J. 2017, ApJ, 845, 44

Turner, N. J., Fromang, S., Gammie, C., et al. 2014, Protostars and Planets VI, 411

Tychoniec, Ł., Manara, C. F., Rosotti, G. P., et al. 2020, arXiv e-prints, arXiv:2006.02812

Tychoniec, Ł., Tobin, J. J., Karska, A., et al. 2018, ApJS, 238, 19

van Boekel, R., Henning, T., Menu, J., et al. 2017, ApJ, 837, 132

van der Marel, N., van Dishoeck, E. F., Bruderer, S., et al. 2016a, A&A, 585, A58

van der Marel, N., van Dishoeck, E. F., Bruderer, S., et al. 2016b, A&A, 585, A58

van der Marel, N., van Dishoeck, E. F., Bruderer, S., et al. 2013, Science, 340, 1199

van der Marel, N., Williams, J. P., Ansdell, M., et al. 2018, ApJ, 854, 177 van der Marel, N., Williams, J. P., Ansdell, M., et al. 2018, The Astrophysical Journal, 854, 177

van der Plas, G., Ménard, F., Gonzalez, J. F., et al. 2019, A&A, 624, A33

van Dishoeck, E. F. & Black, J. H. 1988, ApJ, 334, 771

van Dishoeck, E. F., Jonkheid, B., & van Hemert, M. C. 2006, Faraday Discussions, 133, 231

van 't Hoff, M. L. R., Tobin, J. J., Harsono, D., & van Dishoeck, E. F. 2018, A&A, 615, A83

van 't Hoff, M. L. R., Walsh, C., Kama, M., Facchini, S., & van Dishoeck, E. F. 2017, A&A, 599, A101

van Terwisga, S. E., van Dishoeck, E. F., Ansdell, M., et al. 2018, A&A, 616, A88

van Terwisga, S. E., van Dishoeck, E. F., Cazzoletti, P., et al. 2019, A&A, 623, A150

van Zadelhoff, G. J., van Dishoeck, E. F., Thi, W. F., & Blake, G. A. 2001, A&A, 377, 566

Venuti, L., Bouvier, J., Irwin, J., et al. 2015, A&A, 581, A66

Vernet, J., Dekker, H., D'Odorico, S., et al. 2011, A&A, 536, A105

Vioque, M., Oudmaijer, R. D., Baines, D., Mendigutía, I., & Pérez-Martínez, R. 2018, A&A, 620, A128

Visser, R., Bruderer, S., Cazzoletti, P., et al. 2018, A&A, 615, A75

Visser, R., van Dishoeck, E. F., & Black, J. H. 2009, A&A, 503, 323

Wada, K., Tanaka, H., Suyama, T., Kimura, H., & Yamamoto, T. 2008, ApJ, 677, 1296

Walsh, C., Loomis, R. A., Öberg, K. I., et al. 2016, ApJ, 823, L10

Walsh, C., Nomura, H., Millar, T. J., & Aikawa, Y. 2012, ApJ, 747, 114

Ward-Duong, K., Patience, J., Bulger, J., et al. 2018, AJ, 155, 54

Ward-Thompson, D., Kirk, J. M., André, P., et al. 2010, A&A, 518, L92

Watanabe, N. & Kouchi, A. 2002, ApJ, 571, L173

Weidenschilling, S. J. 1977, MNRAS, 180, 57

Weidling, R., Güttler, C., & Blum, J. 2012, Icarus, 218, 688

Weingartner, J. C. & Draine, B. 2001, The Astrophysical Journal, 548, 296

Whipple, F. L. 1972, in From Plasma to Planet, ed. A. Elvius, 211

Willacy, K., Langer, W., Allen, M., & Bryden, G. 2006, ApJ, 644, 1202

Williams, J. P. & Best, W. M. J. 2014, ApJ, 788, 59

Williams, J. P., Cieza, L., Hales, A., et al. 2019, The Astrophysical Journal, 875, L9

Williams, J. P. & McPartland, C. 2016, ApJ, 830, 32

Windmark, F., Birnstiel, T., Ormel, C. W., & Dullemond, C. P. 2012, A&A, 544, L16

Winn, J. N. & Fabrycky, D. C. 2015, ARA&A, 53, 409

Winter, A. J., Clarke, C. J., Rosotti, G., et al. 2018, MNRAS, 478, 2700

Woitke, P., Kamp, I., Antonellini, S., et al. 2019, PASP, 131, 064301

Woitke, P., Kamp, I., & Thi, W.-F. 2009, A&A, 501, 383

Woitke, P., Min, M., Pinte, C., et al. 2016, A&A, 586, A103

Woitke, P., Min, M., Thi, W. F., et al. 2018, A&A, 618, A57

Woodall, J., Agúndez, M., Markwick-Kemper, A., & Millar, T. 2007, Astronomy & Astrophysics, 466, 1197

Wright, N. J. & Mamajek, E. E. 2018, MNRAS, 476, 381

Yen, H.-W., Koch, P. M., Manara, C. F., Miotello, A., & Testi, L. 2018, A&A, 616, A100

Yen, H.-W., Koch, P. M., Takakuwa, S., et al. 2015, ApJ, 799, 193

Yen, H.-W., Liu, H. B., Gu, P.-G., et al. 2016, The Astrophysical Journal Letters, 820, L25

Yen, H.-W., Takakuwa, S., Gu, P.-G., et al. 2019, A&A, 623, A96

Youdin, A. N. & Chiang, E. I. 2004, ApJ, 601, 1109

Yu, M., Evans, Neal J., I., Dodson-Robinson, S. E., Willacy, K., & Turner, N. J. 2017, ApJ, 841, 39

Zhang, K., Bergin, E. A., Blake, G. A., Cleeves, L. I., & Schwarz, K. R. 2017, Nature Astronomy, 1, 0130

Zhang, K., Bergin, E. A., Schwarz, K., Krijt, S., & Ciesla, F. 2019, ApJ, 883, 98

Zhang, S., Zhu, Z., Huang, J., et al. 2018, ApJ, 869, L47

Zhu, Z., Hartmann, L., & Gammie, C. 2009, ApJ, 694, 1045

Zhu, Z. & Stone, J. M. 2018, ApJ, 857, 34

Zhu, Z., Zhang, S., Jiang, Y.-F., et al. 2019, ApJ, 877, L18

SAMENVATTING

De vraag "waar komen we vandaan?" is er één die ons al sinds mensenheugenis bezig houdt. Een belangrijk onderdeel daarvan is "hoe is onze aarde ontstaan?" Een antwoord op deze vraag kan ons helpen met begrijpen hoe leven zich hier heeft kunnen vormen. En het geeft ons misschien ook een idee waar in het heelal we zouden kunnen gaan zoeken naar leven op andere planeten.

Onze aarde is net iets minder oud dan de zon. Dit vertelt ons dat de aarde gevormd is toen de zon nog vrij jong was. Het liefst zouden we de tijd terugspoelen naar dit moment om het vormen van de aarde en de andere planeten in ons zonnestelsel bij te kunnen wonen. Dit is natuurlijk niet mogelijk. Wat we wel kunnen doen is op zoek gaan jonge zon-achtige sterren die nog bezig zijn met het vormen van hun eigen planetenstelsel. Door onze telescopen op deze sterren te richten kijken we als het ware terug in de tijd, naar de babyfoto's van onze zonnestelsel. Of in ieder geval iets wat hier dicht bij in de buurt komt.

De telescoop die we hier het meeste voor gebruiken is de Atacama Large Millimeter/ sub-millimeter Array, voor het gemak afgekort tot ALMA (zie figuur 1). Deze telescoop staat op het Chajnantor plateau, een hoogvlakte op meer dan 5000 meter boven zeeniveau, in de Atacamawoestijn in Noord-Chili. Wanneer we ALMA op deze jonge sterren richten zien we dat ze omringd zijn door dunne schijven van gas en stof. Aangezien we denken dat planeten in deze schijven gevormd worden noemen we ze "protoplanetaire schijven". Door deze schijven te bestuderen en te achterhalen wat er zich binnenin deze schijf afspeelt krijgen we een beter beeld van hoe planeten zoals onze aarde gevormd kunnen worden.

Dit proefschrift richt zich op deze protoplanetaire schrijven, waarbij twee vragen centraal staan. Hoeveel massa hebben deze schijven, oftewel hoeveel bouwmateriaal is er beschikbaar om planeten mee te kunnen vormen? En hoe groot zijn protoplanetaire schijven? Zijn ze heel groot en is dus al dat bouwmateriaal dun uitgesmeerd? Of zijn ze juist heel compact, met al het materiaal opgepropt in een klein gebied?

Van gaswolk tot ster

Het vormen van planeten is maar een klein deel van het grotere proces van hoe sterren gevormd worden. Het is daarom een goed idee om dit proces eerst globaal door te lopen. Sterren worden geboren in grote wolken van gas en stof. In deze wolken kunnen verdichtingen ontstaan, een soort klonten, die zwaar genoeg zijn dat ze onder hun eigen zwaartekracht bezwijken. De klont van gas en stof blijft ineenstorten en vormt een veel dichtere kern, totdat het in het midden van deze kern heet genoeg is voor kernfusie. Deze bron van energie zorgt ervoor dat het binnenste van de kern niet verder kan instorten en daarmee is de ster geboren. De buitenste delen van de kern willen ook

Figuur 1: De ALMA telescoop is een verzameling van 66 radio antennes, elk met een doorsnede van 7 of 12 meter, die wordt gebruikt voor waarnemingen van protoplanetaire schijven. Door de signalen van alle antennes te combineren kunnen plaatjes met ongekend scherpte worden gemaakt. Credit: Y. Beletsky/ESO

op de ster vallen, maar kunnen dat niet direct doen. De kern heeft namelijk een klein beetje draaiing. Dit is haast niet merkbaar aan de buitenrand van de wolk, maar zodra deze buitenste delen naar binnen vallen zorgt het behoud van hoekmoment er voor dat ze steeds sneller om de ster beginnen te draaien.[2] De doorsnede van de kern is meer dan 100 000 keer groter dan die van de ster, dus tegen de tijd dat materiaal van de oorspronkelijke buitenrand van de kern bij de ster aangekomen is, draait het 100 000 keer sneller om de ster heen. Als de ster dit materiaal zou willen opslokken dan moet hij zo snel om zijn eigen as draaien dat hij zichzelf kapot draait.

De oplossing hiervoor is dat het materiaal uit de buitenste delen niet op de ster valt, maar in plaats daarvan om de ster heen gaat draaien. Zoals eerder gezegd noemen we deze schijf van gas en stof de protoplanetaire schijf. In deze schijf kan het materiaal genoeg afgeremd worden om door de ster opgeslokt te worden. Hoe dit precies gebeurd is nog niet helemaal duidelijk en daarom gaan we daar in hoofdstukken 4 en 5 dieper op in. Na ongeveer 5 tot 10 miljoen jaar is het grootste deel van het materiaal in de schijf opgegaan in de ster of omgezet in planeten. De restjes die zijn overgebleven worden weggeblazen door straling van de ster. Tien miljoen jaar klinkt misschien als een lange tijd, maar voor het vormen van een planeet is dit vrij krap. Om het ontstaan van planeten te begrijpen is het daarom zaak dat we goed begrijpen hoe de protoplanetaire schijf in elkaar zit.

De protoplanetaire schijf

Net als het materiaal waaruit hij gevormd is bestaat de schijf uit twee componenten. Veruit het meeste van de schijf is gas, naar schatting zo'n 99%. De andere 1% zijn stofdeeltjes die klein beginnen maar uiteindelijk uit moeten groeien tot planeten. Omdat er zoveel meer gas dan stof in de schijf is, bepaalt het gas hoe de schijf verandert

---

[2] Je kunt dit zelf ook uitproberen: ga op een bureaustoel zitten (die kan draaien), voeten van de vloer en draai langzaam rond met uitgestrekte armen. Als je je armen nu naar binnen trekt zul je merken dat je sneller gaat draaien.

met de tijd. En, zoals we zo dadelijk zullen zien, heeft het gas ook een grote invloed op hoe de stofdeeltjes samenklonteren en groeien.

Het gas is een mengsel van voornamelijk waterstof moleculen[3] en helium atomen[4]. Het gas bevat ook kleine hoeveelheden (1-0.1 promille) koolstofmonoxide (CO), stikstof (N_2) en water (H_2O). Vooral de aanwezigheid van CO is fijn voor sterrenkundigen. Waterstof en helium zenden maar heel weinig licht uit en zijn daarom heel moeilijk te zien. CO daarentegen zendt wel veel licht uit en wordt daarom veel ingezet om indirect het gas te kunnen volgen.

Ondanks het feit dat het in de ruimte vele malen kouder en leger is dan hier op aarde vinden er toch nog steeds chemische reacties plaats. Deze zorgen er onder andere voor dat het percentage CO niet overal in de schijf hetzelfde is. Dit is problematisch wanneer we CO gebruiken om te achterhalen wat de waterstof moleculen aan het doen zijn. Zien we nou ver van de ster weinig CO omdat daar weinig gas zit? Of juist omdat CO door middel van een chemische reactie is omgezet in een ander molecuul? Het is daarom voor sterrenkundigen de moeite waard om goed te begrijpen hoe de chemie van CO in protoplanetaire schijven in elkaar zit.

Chemisch gezien kun je een protoplanetaire schijf opdelen in drie lagen. De bovenste laag van de schijf wordt blootgesteld aan directe straling van de ster. Moleculen in deze laag, waaronder CO, worden binnen de kortste keren kapot gemaakt door deze straling. De bovenste laag bestaat daarom vooral uit losse atomen. De middelste laag ligt diep genoeg in de schijf dat het grootste deel van de straling van de ster er niet bij kan komen. Deze laag is daarom rijk aan moleculen. In onze waarnemingen zien wij vooral licht afkomstig van CO moleculen uit deze laag. De onderste laag ligt in het midden van de schijf en is heel erg koud. De temperatuur is hier zo laag dat moleculen zoals CO vastvriezen op de stofdeeltjes. In de ijslaag op de stofdeeltjes gaat de chemie door en worden simpele moleculen omgezet in complexere moleculen zoals methaan en methanol. Het feit dat de meeste moleculen hier bevroren zijn betekent ook dat we deze laag van de schijf moeilijk kunnen zien in onze waarnemingen.

Van stofdeeltje tot planeet

Hoewel het stof maar 1 % is van de totale hoeveelheid materiaal in de schijf zijn het wel deze stofdeeltjes die uiteindelijk uitgroeien tot de planeten waar we in geïnteresseerd zijn. Ook gasreuzen zoals Jupiter en Saturnus hebben naar alle waarschijnlijkheid een rotsachtige kern die ongeveer 10 keer zo zwaar is als onze aarde. De stofdeeltjes beginnen heel klein, ongeveer een duizendste van een millimeter. In de schijf kunnen deze deeltjes op elkaar botsen en blijven plakken, om op die manier te groeien tot het formaat van een zandkorrel (±1 mm) of zelfs een kleine kiezel (±1 cm). Dit gaat extra goed in het midden van de schijf, omdat de stofdeeltjes hier bedekt zijn met een ijslaag. Deze maakt ze plakkerig, waardoor ze beter aan elkaar blijven kleven.

Één van de grootste vragen op het gebied van het vormen van planeten is hoe deze zandkorrels en kiezels verder groeien. We hebben een vrij goed beeld van hoe rotsblokken met een doorsnede van meer dan honderd meter op elkaar kunnen botsen en langzaam kunnen uitgroeien tot het formaat van een planeet, enkele duizenden kilometers in doorsnede. Wat we niet goed weten is hoe deze rotsblokken kunnen

---

[3] het gas in zeppelins

[4] het gas in ballonnen

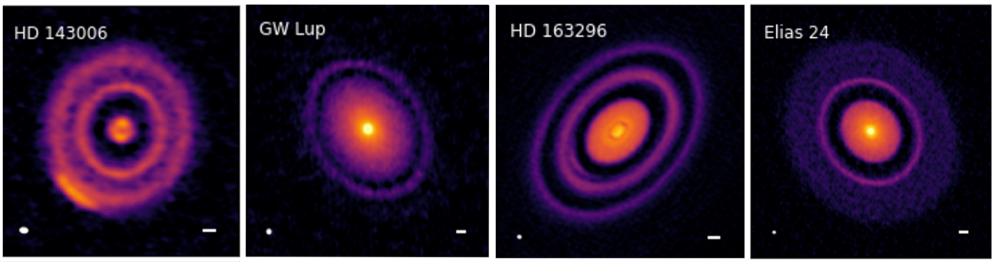

Figuur 2: Een selectie van waarnemingen gedaan met ALMA van het stof in protoplanetaire schijven. Hoe lichter de kleur in het plaatje, hoe meer stof er op dat punt van de schijf zit. Hier is goed te zien dat het stof zich heeft verzameld in 1 of meer ringen rond de ster. Credit: Andrews et al. (2018a)

ontstaan uit de stofdeeltjes van millimeter formaat.

Er zijn twee hindernissen die de stofdeeltjes moeten over komen om uit te kunnen groeien tot rotsblok. De eerste heeft te maken met wat er gebeurt wanneer twee stofdeeltjes op elkaar botsen. Wanneer dit plaatsvindt bij lage snelheden is de kans groot dat ze aan elkaar blijven plakken. Echter als de snelheid waarmee ze botsen groter wordt dan kunnen ze ook van elkaar af stuiteren of zelfs kapot breken. In de meeste gevallen voorkomt dit dat de stofdeeltjes groter kunnen worden dan ongeveer 1 meter in doorsnede.

De tweede hindernis is dat het gas de grotere stofdeeltjes afremt, waardoor ze naar binnen vallen en op de ster terecht komen. In het begin zijn de stofdeeltjes klein genoeg dat ze door het gas worden meegevoerd. Wanneer de stofdeeltjes groter geworden zijn is dit niet meer het geval. De snelheid waarmee de stofdeeltjes rond de ster bewegen wordt bepaald door zwaartekracht. Het gas daarentegen kan voor een deel steunen op zijn eigen gasdruk en beweegt daarom met een iets lagere snelheid rond de ster. Voor het stof voelt dit als een “tegenwind” terwijl het zich een weg baant door het langzaam bewegende gas. Hierdoor wordt het stof afgeremd en begint het naar binnen richting de ster te vallen. Hoe groter het stofdeeltje, hoe sneller deze wordt afgeremd: een kei met een doorsnede van 1 meter die begint op de afstand die de aarde van de zon staat verdwijnt binnen 100 jaar.

Een mogelijke oplossing om te voorkomen dat alle grote stofdeeltjes in de ster verdwijnen is de aanwezigheid van een planeet in de schijf. Deze vervormd de schijf buiten zijn baan op zo’n manier dat er een soort blokkade ontstaat die voorkomt dat de stofdeeltjes verder naar binnen kunnen vallen. Daarom begint het zich hier op te hopen. Deze ophoping van stof is een ideale plek om planeten te kunnen vormen. De ALMA telescoop heeft ons recent in staat gesteld om protoplanetaire schijven waar te nemen met een zeer hoge resolutie. In figuur 2 zien we een aantal van deze waarnemingen. Daarin lijkt het stof zich inderdaad te verzamelen in één of meer ringen rond de ster. Het feit dat er al een planeet moet zijn om deze ringen te vormen lijkt een beetje het kip en ei probleem, maar er zijn ook andere processen die een vergelijkbare barrière kunnen maken.

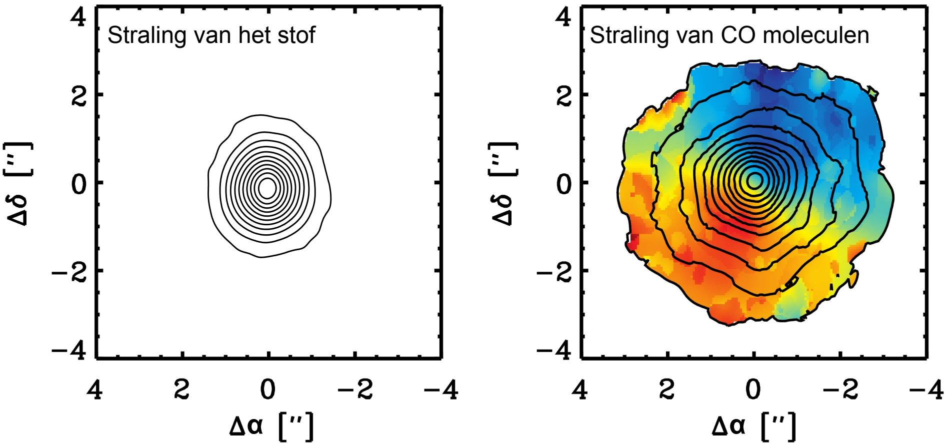

Figuur 3: Waarnemingen van de nabij gelegen protoplanetaire schijf TW Hya. Links zien we de straling van stofdeeltjes van ongeveer 1 millimeter in doorsnede. We zien hier een bovenaanzicht van de schijf, met de ster (niet zichtbaar bij deze golflengte) in het midden. De contouren laten zien dat straling minder wordt naarmate we verder van de ster komen. Rechts zien we de straling van de CO moleculen, die nog tot op veel grotere afstanden van de ster te zien is. De kleuren hier laten zien dat de schijf draait: een deel van de straling is blauw verschoven en komt naar ons toe, terwijl een ander deel van de straling rood verschoven is en van ons af beweegt. Credits: Andrews et al. (2011)

Dit proefschrift

In dit proefschrift richten we ons op drie onderwerpen: In hoofdstukken 2 en 3 kijken we naar wat de waarnemingen ons vertellen over hoeveel het stof naar binnen gedreven is. Hoofdstukken 4 en 5 proberen vast te stellen welk proces verantwoordelijk is voor hoe een protoplanetaire schijf verandert over de tijd. Hoofdstuk 6, en tot op zekere hoogte hoofdstuk 5, richt zich op de vraag: hoeveel gas zit er in totaal in een protoplanetaire schijf? Om de waarnemingen te kunnen interpreteren en om voorspellingen te kunnen maken gebruiken we geavanceerde computer modellen. Zo'n computermodel kun je zien als een protoplanetaire schijf in het klein: gegeven een beschrijving van een schijf rekent het model uit hoeveel de schijf opgewarmd wordt door straling van de ster en hoeveel de schijf afkoelt door straling uit te zenden. Ook rekent het model de chemie in de schijf uit, om bijvoorbeeld te bepalen wat het percentage CO is op verschillende plekken in de schijf. Als laatste berekent het model hoe onze schijf er uit zou zien als we hem zouden waarnemen.

Wanneer we ALMA op een protoplanetaire schijf richten dan zien we de straling van zowel het stof als van de CO moleculen in het gas. In figuur 3 zijn deze twee componenten naast elkaar geplaatst. In deze waarnemingen lijkt het alsof het gas zich veel verder van de ster uitstrekt dan de stofdeeltjes. De straling die we hier zien komt van stofdeeltjes van ongeveer een millimeter in doorsnede. De waarnemingen lijken dus te suggereren dat het deze stofdeeltjes naar binnen zijn gedreven richting de ster. Het gas is daarentegen op dezelfde plek gebleven. Hoeveel kleiner de stofschijf is in vergelijking met de gasschijf zou ons dus kunnen vertellen hoeveel de stofdeeltjes naar binnen zijn gedreven.

Dit is echter niet het enige proces wat kan verklaren wat we hier zien. CO zendt ook bij lage dichtheden nog straling uit en is daarom nog steeds zichtbaar op grote afstanden van de ster. Dit is in tegenstelling tot de straling van het stof, die al veel eerder te zwak wordt om waar te kunnen nemen. Wat we zien in figuur 3 is dus ook wat we verwachten waar te nemen als het stof niet naar binnen gedreven is.

In hoofdstuk 2 gebruiken we computermodellen van een protoplanetaire schijf om onderscheid te kunnen maken tussen deze twee processen. In ons computermodel kunnen we er voor kiezen of het stof wel of niet naar binnen laten drijven. Voor beide gevallen kunnen we dan berekenen hoe we deze schijf zouden zien met onze telescoop. Uit ons onderzoek blijkt dat we met zekerheid kunnen zeggen dat het stof naar binnen gedreven is als de doorsnede van de gasschijf, gemeten van de straling van de CO moleculen, meer dan 4 keer zo groot is als de doorsnede van de stofschijf. In het geval dat het verschil kleiner is kunnen we dit niet met zekerheid zeggen zonder eerst in meer detail naar de schijf in kwestie te kijken. Ook laten we zien dat het niet mogelijk is iets te zeggen over hoe snel het stof naar binnen gedreven is aan de hand van hoeveel kleiner de stofschijf is ten opzichte van de gasschijf. Er spelen hier simpelweg teveel andere factoren een rol.

Deze bevindingen worden in hoofdstuk 3 toegepast op waarnemingen van 10 protoplanetaire schijven. De sterren waar deze schijven om heen draaien liggen allemaal in dezelfde wolk en zijn allemaal rond dezelfde tijd gevormd. Door deze schijven tegelijk te onderzoeken en met elkaar te vergelijken krijgen we een beeld van de overeenkomsten en verschillen binnen één generatie van sterren. Deze schijven hebben allemaal een gasschijf die groter is dan hun stofschijf, maar het verschil in doorsnede is kleiner dan 4. Er is dus geen duidelijk teken dat het stof naar binnen gedreven is voor deze schijven. Voor ons onderzoek maken we voor elk van de 10 schijven een computermodel op zo'n manier dat het precies de waarnemingen van het stof nabootst, waarbij we het stof niet naar binnen laten drijven. Er vanuit gaande dat dit klopt zou dit model ook de waargenomen grootte van de gasschijf moeten nabootsen. Als het stof in de waargenomen schijf wel naar binnen gedreven is dan zal ons model een te kleine gasschijf hebben in vergelijking met de waarnemingen. Dit blijkt voor 5 van de 10 het geval te zijn. Voor deze 5 schijven moet het stof naar binnen gedreven zijn om te verklaren wat we zien. Voor de andere 5 is de gasschijf van ons model even groot als de waargenomen schijf en lijkt het stof dus niet naar binnen gedreven te zijn.

Voor hoofdstuk 4 stappen we over naar gas en kijken we hoe de protoplanetaire schijf verandert met de tijd. Ondanks de aantrekkende werking van de zwaartekracht van de ster kan materiaal van de schijf niet zomaar op de ster vallen. Het behoud van hoekmoment zegt dat hoe meer een deeltje naar binnen richting de ster beweegt, hoe sneller het om de ster moet gaan draaien. Toch zien we wel dat er materiaal op de ster valt. Één van de mogelijke theorieën om dit te verklaren is dat het gas dichter bij de ster wordt afgeremd door het gas verder weg van de ster. Stel je voor dat de schijf is opgebouwd uit een opeenvolging van steeds grotere ringen die rond de ster draaien. Een ring dichter bij de ster beweegt sneller rond dan de volgende ring in de rij. Dit zorgt voor wrijving tussen de twee ringen. De binnenste ring wordt hierdoor afgeremd en valt naar binnen, terwijl de buitenste ring juist versnelt en naar buiten geslingerd wordt. Globaal gezien over de hele schijf betekent dit dat het gas vlak bij de ster op de ster valt, terwijl het gas aan de buitenrand van de schijf steeds verder weg van de ster komt te staan.

In ons onderzoek hebben we gekeken naar hoe goed dit effect te zien zou moeten zijn in onze waarnemingen. Gebruikmakende van een computermodel kijken we naar een opeenvolging van momentopnames uit het leven van een protoplanetaire schijf die steeds groter wordt. Van elk van deze momentopnames berekenen we hoe groot de schijf er uit zou zien in onze waarnemingen. Hieruit blijkt dat het groeien van de schijf inderdaad terug te zien is in de waarnemingen. Echter, puur uitgaande van deze waarnemingen overschat je met een factor 10 hoe snel de schijf daadwerkelijk groeit. Wanneer we onze computermodellen vergelijken met daadwerkelijke waarnemingen blijkt dat deze overeenkomen mits de schijven heel klein begonnen zijn en heel langzaam groeien.

In de laatste twee hoofdstukken gaan we aan de slag met de vraag: Hoeveel gas zit er in totaal in een protoplanetaire schijf. De totale gas massa van de schijf geeft ons de totale hoeveelheid bouwmateriaal die beschikbaar is om planeten, specifiek gasreuzen, mee te vormen. Hoeveel gas er is heeft ook invloed op hoe snel het stof naar binnen drijft en het is één van de factoren die bepaalt hoe lang de schijf kan blijven bestaan. Het bepalen van de totale gas massa van de schijf is zeer lastig, omdat het gas voornamelijk bestaat uit waterstof moleculen die haast geen straling uitzenden. Het “wegen” van een protoplanetaire schijf kan daarom niet direct. In plaats daarvan maken we gebruik van computermodellen om de waargenomen straling van CO te vertalen naar de totale hoeveelheid waterstof in de schijf.

Hoofdstuk 5 ligt in het verlengde van hoofdstuk 4. De theorie dat protoplanetaire schijven groeien naarmate ze ouder worden doet ook een voorspelling over een verband tussen hoe snel materiaal uit de schijf op de ster valt en hoeveel materiaal er in de schijf zit. Huidige waarnemingen laten dit verband echter niet zien, zij suggereren dat schijven veel minder gas bevatten dan verwacht. Een mogelijke verklaring hiervoor is dat we een proces niet hebben meegenomen in onze omrekening van het aantal CO moleculen naar het aantal waterstof moleculen. Één van de mogelijkheden is dat we de chemie van CO die we in onze modellen stoppen niet compleet is. Recente onderzoeken hebben bijvoorbeeld laten zien dat CO door middel van chemische reacties kan worden omgezet in grotere moleculen zoals methanol, een proces dat momenteel niet in onze modellen zit.

In dit onderzoek nemen we de computermodellen van hoofdstuk 5 en breiden ze uit met een beschrijving van hoeveel CO er wordt omgezet in andere moleculen. Door op deze manier CO uit onze modellen weg te halen proberen we de waargenomen lage hoeveelheden straling van CO na te bootsen. Deze toevoeging lijkt inderdaad iets te helpen, maar bij lange na niet genoeg om de modellen op één lijn te krijgen met de waarnemingen. Hoewel CO efficiënt wordt weggehaald dieper in de schijf gebeurt er vrij weinig in de laag van CO die we zien in onze waarnemingen. Wat hier een uitweg zou kunnen bieden is als het CO-arme gas van dieper in de schijf op efficiënte wijze gemengd kan worden met het CO-rijke gas in de laag waar de waargenomen straling vandaan komt.

In het laatste hoofdstuk kijken we naar een andere manier om de totale hoeveelheid gas in een protoplanetaire schijf te meten. Hiervoor maken we gebruik van HD, een waterstof molecuul (H_2) waarbij één van de waterstof atomen vervangen is met een net iets zwaarder deuterium atoom. In tegenstelling tot zijn lichtere, symmetrische broertje H_2 zendt HD wel straling uit. Omdat HD zoveel lijkt op H_2 is het heel makkelijk om de vertaling te maken van de waargenomen hoeveelheid HD moleculen naar de totale hoeveelheid gas in de schijf. Waarnemingen van de straling van HD zijn niet makkelijk en kunnen alleen met een telescoop vanuit de ruimte gedaan worden. De *Herschel Space Observatory* is er in geslaagd om HD te detecteren in een handjevol protoplanetaire schijven, maar is sinds 2011 gestopt met waarnemen.

In dit onderzoek kijken we naar een serie waarnemingen van 15 protoplanetaire schijven waarbij er naar straling van HD gezocht is, waarbij helaas niks is gevonden. Desalniettemin kunnen we hier nog steeds iets van leren, door met behulp van computermodellen te berekenen wat de maximale hoeveelheid gas is die deze schijven kunnen hebben voordat we ze hadden moeten zien in onze waarnemingen. Dit blijkt ongeveer 10% van de massa van onze zon te zijn. Dit blijkt een relevante grens te zijn, want dit betekent dat ze niet zo zwaar zijn dat delen van de schijf onder hun eigen zwaartekracht kunnen bezwijken en ter plekke een planeet of dwergster kunnen vormen. Voor 1 van de 15 schijven kunnen we zelfs zeggen dat de schijf niet zwaarder kan zijn dan 7% van de massa van onze zon. Dit maximum is lager dan sommige eerdere berekeningen van de massa van deze schijf gedaan aan de hand van CO. Tenslotte hebben we onze resultaten ook vergeleken met twee waargenomen planetenstelsels rond sterren die lijken op de jonge sterren waar wij naar gekeken hebben. Wanneer we de massa's van deze planeten optellen komen we dicht in de buurt (±40%) van de maximale hoeveelheid gas van onze schijven. Dit betekent dat deze planeten of heel efficiënt gevormd zijn of dat ze al eerder zijn gevormd, toen er nog meer gas in de schijf zat.

Toekomstperspectief

Telescopen zoals ALMA hebben ons de afgelopen jaren in staat gesteld om protoplanetaire schijven in ongelofelijk detail te kunnen bestuderen. Dit heeft tot veel nieuwe inzichten geleid. We hebben echter nog een lange weg te gaan voordat we precies begrijpen hoe protoplanetaire schijven in elkaar zitten en hoe zich hierin planeten kunnen vormen. Vooral over het gas in protoplanetaire schijven zijn nog veel vraagtekens. ALMA kan ons helpen deze weg te nemen, vooral door dieper te staren en de zwakke straling van het gas in meer detail waar te nemen. Het is hierbij ook belangrijk dat we dit doen voor een groot aantal schijven. Zo kunnen we een beeld krijgen van wat normaal is in een protoplanetaire schijf, of anders gezegd, hoe ziet de gemiddelde schijf er uit? Want dit is uiteindelijk de omgeving waarin de gemiddelde planeet gevormd gaat worden.

Het is nog steeds onduidelijk wat de totale hoeveelheid gas is in protoplanetaire schijven, ondanks de grote hoeveelheid aandacht voor dit onderwerp waaronder delen van dit proefschrift. Alles wijst erop dat de straling van HD moleculen de meest betrouwbare manier is om protoplanetaire schijven te wegen. Om deze straling waar te kunnen nemen moeten we een telescoop in de ruimte hebben. De huidige waarnemingen van HD zijn gedaan met de *Herschel Space Observatory*, maar helaas is deze sinds 2013 niet meer te gebruiken voor deze waarnemingen door een gebrek aan koelvloeistof. Er zijn momenteel plannen voor twee potentiële opvolgers: de *Space Infrared Telescope for Cosmology and Astrophysics* (SPICA) die hopelijk wordt goedgekeurd in het voorjaar van 2021 en de *Origin Space Telescope* (OST). Als de plannen voor deze telescopen worden goedgekeurd dan duurt het waarschijnlijk nog wel tot ongeveer 2035 voordat ze gelanceerd kunnen worden, maar het zal uiteindelijk het wachten waard zijn.

LIST OF PUBLICATIONS

Refereed publications

1. Far-infrared HD emission as a measure of protoplanetary disk mass
   Trapman, L., Miotello, A., Kama, M., van Dishoeck, E. F., Bruderer, S. 2018, A&A, 605, A69
2. Gas versus dust sizes of protoplanetary discs: effects of dust evolution
   Trapman, L., Facchini, S., Hogerheijde, M. R., van Dishoeck, E. F., Bruderer, S. 2019, A&A, 629, A79 [Chapter 2]
3. Constraining the radial drift of millimeter-sized grains in the protoplanetary disks in Lupus
   Trapman, L., Ansdell, M., Hogerheijde, M. R., Facchini, S., Manara, C. F., Miotello, A., Williams, J. P., Bruderer, S. 2020, A&A, 638, A38 [Chapter 3]
4. Observed sizes of planet-forming disks trace viscous spreading
   Trapman, L., Rosotii, G., Bosman, A. D., Hogerheijde, M. R., van Dishoeck, E. F. 2020, A&A, 640, A4 [Chapter 4]
5. Mass constraints for 15 protoplanetary disks from HD 1-0
   Kama, M., **Trapman, L.,**, Fedele, D., Bruderer, S., Hogerheijde, M.R., Miotello, A., van Dishoeck, E. f., Clarke, C., Bergin, E. A. 2020, A&A, 638, A88 [Chapter 6]
6. ALMA Survey of Lupus protoplanetary disks. II. Gas disk radii
   Ansdell, M., Williams, J. P., **Trapman, L.**, van Terwisga, S. E., Facchini, S., Manara, C. F., van der Marel, N., Miotello, A., Tazzari, M., Hogerheijde, M., Guidi, G., Testi, L., van Dishoeck, E. F. 2018, ApJ, 859, 21
7. V1094 Scorpii: A rare giant multi-ringed disk around a T Tauri star
   van Terwisga, S. E., van Dishoeck, E. F., Ansdell, M., van der Marel, N., Testi, L.; Williams, J. P., Facchini, S., Tazzari, M., Hogerheijde, M. R., **Trapman, L.**, Manara, C. F., Miotello, A., Maud, L. T., Harsono, D. 2018, A&A, 616, A88
8. Methanol and its relation to the water snowline in the disk around the young outbursting star
   van 't Hoff, M. L. R., Tobin, J. J., **Trapman, L.**, Harsono, D., Sheehan, P. D., Fischer, W. J., M., Thomas, S., van Dishoeck, E. F.2018, ApJL, 864, L23

9. The ALMA Lupus protoplanetary disk survey: evidence for compact gas disks and molecular rings from CN
   van Terwisga, S. E., van Dishoeck, E. F., Cazzoletti, P., Facchini, S., **Trapman, L.**, Williams, J. P., Manara, C. F., Miotello, A., van der Marel, N., Ansdell, M., Hogerheijde, M. R., Tazzari, M., Testi, L. 2019, A&A, 623, A150

CURRICULUM VITAE

I was born on Februari 5th in Amsterdam to Joris Trapman en Rita Bakker. Before my second birthday we had already moved on to Lelystad, which is where I would spend most of my childhood. Here I would be joined by a younger brother, Bart, who was and has remained a constant source of excitement (and some headaches). As it turns out, it would take a while for my interest in Astronomy to fully manifest itself. As a kid I had many interests over the years that are common to many at that age: firetrucks, astronauts and space, knights. It was my interest with dinosaurs, fueled by documentaries like Walking With Dinosaurs, that made it clear to me that I wanted to be a paleontologist (or an archaeologist in a pinch).

This changed during my years at the Scholengemeenschap Lelystad where I followed my secondary education. During primary education it had already become clear that I had a knack for arithmetic, and now physics, chemistry and mathematics could be added to that list. Despite that, I was still convinced that I wanted to become a paleontologist until, during a visit to a job/study market, it became clear that my childhood vision of the job did not fully match with the real world. It was at this point that my brain decided to pick astronomy as the logical alternative. It is still not fully clear to me what made me pick astronomy, but I have not regretted it since.

I started my Bachelor in Astronomy at the Leiden University in 2011. For someone who breezed through secondary education without having to put much effort in, the transition to university was a bit of a shock but also a welcome challenge. I finished my Bachelor doing a research project together with Leindert Boogaard, under the supervision of Michiel Hogerheijde. Together we looked at ALMA data of transition disks, which are protoplanetary disks with a clear inner cavity. It is obvious that I enjoyed this topic, as I would eventually return to it.

After my Bachelor I decided to continue with a Master in Astronomy in Leiden. During my Masters I shared an office with Arthur, Bavo, David, David[5], Kasper, Matthias and Leindert, with whom I formed a tightly-knit group for studying, scientific discussions and the odd christmas tree decorating. For my first research project I looked at methods for measuring gravitational lensing, under the supervision of Henk Hoekstra, Massimo Viola and Ricardo Herbonnet. I did my second research project in the group of Ewine van Dishoeck. Here I returned to the topic of protoplanetary disks. Under the supervision of Anna Miotello and Mihkel Kama I dove into the world of thermochemical modeling and investigated hydrogen deuteride as potential disk gas mass tracer. I was very happy to find out that I finished my Masters cum laude.

By the end of my Master it was clear to me that I wanted to continue in research and in astronomy. I was fortunate to be invited for the PhD interviews in both Leiden and Amsterdam. Over the five years of my Bachelor and Master I kept my fascination

---

[5] no that's not a typo, there were two Davids

for protoplanetary disks, so when Michiel Hogerheijde offered me a PhD position to work with him on this topic I did not hesitate to accept it.

When I started in 2016, the plan for my PhD was to work on the so-called "icelines", locations in protoplanetary disks where molecules transition from being mostly gaseous to being frozen out on dust grains. Obtaining the necessary observations turned out to be difficult. While we successfully got our observing proposal(s) accepted each year (currently a three-year streak) it has so far not resulted in any observations. Instead I joined the Lupus collaboration - Jonathan Williams, Megan Ansdell, Stefano Facchini, Carlo Manara, Anna Miotello, Marco Tazzari, Leonardo Testi, Michiel Hogerheijde, Ewine van Dishoeck and others - just as they were starting to look at their new ALMA observations. I worked together with Megan Ansdell on measuring gas and dust outer radii of protoplanetary disks in the Lupus star-forming region. This turned out to be a rich vein of interesting science, which lead directly and indirectly to several articles you can find elsewhere in this thesis. Also early in my PhD I started working together with Mihkel Kama on a side project involving unpublished HD 1-0 flux upper limits. This turned out to be a long and eventful journey that at some point reached near mythical status. Having clearly found my home in modeling, I finished of my PhD with two projects on the evolution of protoplanetary disks. During my PhD I also had the opportunity to travel abroad and visit other scientific institutes. I made several work trips to the MPE in Germany, attended schools in the Netherlands and France, and presented my work at conferences in Göteborg and Boston.

As part of my PhD I also had the pleasure to supervise two Master students, Lisa Dombrovsky and Yapeng Zhang and two bachelor students, Ivana van Leeuwen and Yke Rusticus. In addition, I worked as a teaching assistent for the course Pre-university college Astronomy[6], where we presented high school students with an overview of astronomy and gave them a taste of what it is like to study astronomy at Leiden University. Finally, I was part of the Education Committtee of the Astronomy Master, where we gather feedback from the students and use that to provide advice to the University on how to improve the astronomy Master. After completing my PhD I will work as a postdoc researcher with Ke (Coco) Zhang at the University of Wisconsin-Madison in the United States.

---

[6] previously known as Laptopp

ACKNOWLEDGEMENTS

The thesis that you see here before has been four years in the making. That sounded like a long time when I started working on it, but now that I am at the end I am amazed at how quickly it all has gone by. These four years have been a journey, with twists and turns, ups and downs. But more than the work itself, it is also a collection of memories: of challenges, places, but most importantly, of people. Without the people around me it would not nearly have been this much fun. Thank you all for helping to make this happen.

First of all, I want to thank my supervisor, Michiel, for taking me on this journey. Throughout my PhD you have taught me a great deal of science, but also life lessons that will be useful wherever I might end up. And most importantly, your door was always open for any questions, no matter what the topic was. And thank you Ewine, for your positive attitude as well as your detailed insights. Our meetings were always invaluable for keeping my research focused on the big questions, especially when I sometimes got lost in the details.

Anna and Mihkel, thank you for supervising my master project, which introduced me to the wondrous world of disk modeling. Our project together made it clear to me that this is what I wanted to do for the next four years. And Mihkel, who would have guessed where that conversation in a cafe in Cambridge would lead to? I am looking forward to our next, hopefully slightly shorter, project. To Megan, Jonathan, Anna, Carlo, Stefano, Marco, Leonardo, Sierk, Michiel, Ewine and all the others on the Lupus team: I could not think of a better group for my first international collaboration. I would also like to thank the LKBF for funding three of my work visits abroad, two of which where instrumental for my development as a researcher, while the third was unfortunately canceled due to the current situation in the world.

My fellow group members, Eva, Nico and Mason, you welcomed me with open arms into the group. Thanks for helping me to get started with my PhD. Eva, I enjoyed our shared lunches, which came with their own eleven-flights-of-stairs exercise regime. Jeroen, it was nice to have a fellow partner in crime (i.e. group member) again. Thanks for all your energy, humor and borrel conversations.

I also became an honorary member of Ewine's research group, where I was so readily accepted that people kept forgetting that I was not actually a member of the group. I cannot thank you guys enough for that. I have enjoyed our many scientific discussions, but also the myriad of topics that were discussed over beers during our Friday afternoon borrels. Arthur, you were a constant stream of knowledge, tech-support and (in-)jokes. I'm convinced you probably are a wizard [citation needed]. Merel, I enjoyed our conversations both N_2H^+ related or otherwise. And I still owe you that thing we discussed during our bike ride. Giovanni, thanks for kick-starting my interest in the evolution of disks. I have thoroughly enjoyed working together so far, and based on our current plans, I have the feeling that we will continue to do so for a while. Alex, your positive attitude is infectious. Please keep reminding me that planets are important, not just for the introduction of my papers. On the flip side, thank you Alvaro for reminding me of the big picture. Łukasz, what about outflows? Joking aside, I always enjoyed our conversations, especially over one of your special coffee brews. Benoit, thank you for explaining to me the dark arts of MHD disk wind simulations. Beside that, it was always gezellig to join you for beers at the borrel. Sierk, it was really nice to have someone from the Lupus team also in Leiden, especially in the beginning. Margot, supervising you and answering your many questions over the last year has been fun and has also kept me sharp. Good luck with the rest of your doctorate. Martijn, thanks for the smooth organization of the telecons, but more importantly, thanks for providing ample beers during the Friday borrels. Pooneh, it has always been great to see your excitement on all matters inside and outside of science. To all of the new people in Leiden, Alice, Lucas and Ardjan: good luck and have fun, I know that you are in good hands.

And to the Garching side of the group, Stefano, Paolo, Lisa and now also Andres, you made me immediately feel at home whenever I came to visit the MPE. Stefano, you helped making my second project go smoothly while my first project was stuck in the dirt. Thank you Paolo for letting me see a PhD defense from the front row before I have to do my own. Lisa, I hope that you will enjoy Leiden next year as much as I have. And good luck Andres, I have no doubt that you can make it to the end of your PhD.

The observatory is of course much bigger than just two research group. To my fellow PhDs on the 11th floor, David, Steven, Maaike, Alex, Rob, Emiel, Sebas, thanks for all of our morning coffees. And thanks Leindert, Stijn and Kirsty for being willing to come up to the 11th floor to join said coffees. Leindert, in terms of astronomy topic you and I have somewhat diverged after our Bachelor research project. You have nevertheless remained a constant source of friendship and scientific discourse. Arthur, Bavo, David, David, Kasper, Matthias and Leindert: check out the latest release of 101 productions™! And to all of the others at the observatory that I might be forgetting right now: thanks for creating this amazing atmosphere that is both stimulating to work in and relaxing when at the end of the week we all join for the Friday borrel.

Last but not least, there are also some people outside of the astronomy world that I would like to thank. It is quite special to not only live in the same house for nine years, but also to do so with basically the same group of housemates. Kay, Maartje, Marijke, thanks for all the late night conversations, our movie nights, our shared dinners and just all of our adventures in general. Maartje, you and I have lived in the same house now for close to nine years and I have enjoyed every minute of it. Kay, with you around there is never a dull moment. Marijke, thanks for reminding me that there is more than one point of view on life. Als laaste wil ik ook mijn ouders en mijn broer bedanken. Jullie zijn er altijd voor me geweest en hebben me altijd gesteund, zelf wanneer dat lastig was. Dankjulliewel voor alles.